Microstructural and Chemical Behaviour of Irradiated Graphite Waste under Repository Conditions

A thesis submitted to the University of Manchester for the degree Doctor of Philosophy in the Faculty of Engineering and Physical Sciences

2013

Bereket Hagos

School of Mechanical, Aerospace and Civil Engineering

The University of Manchester

Word: 43,358

TABLE OF CONTENTS

TABLE OF CONTENTS 2
DECLARATION 6
COPYRIGHT STATEMENT 6
TABLE OF FIGURES 7
LIST OF TABLES 12
ABSTRACT 14
GLOSSARY OF TERMS 15
ACKNOWLEDGEMENTS 18
1. INTRODUCTION 19
1.1 NUCLEAR GRAPHITE WASTE 19
1.2 HISTORICAL PROBLEMS 19
1.3 ISSUES AND OBJECTIVES OF RESEARCH 21
1.4 RESEARCH PROPOSAL 22
1.5 RESEARCH PLACEMENT 23
1.6 PROJECT AIMS 24
2. LITERATURE REVIEW 24
2.1 GRAPHITE MODERATED NUCLEAR REACTORS 24
2.2 NUCLEAR GRAPHITE 26
2.3 MANUFACTURING PROCESS 31
2.4 OPERATIONAL CONDITIONS 34
2.5 RADIOLYTIC OXIDATION 34
2.6 IRRADIATION DAMAGE IN GRAPHITE 35
2.7 DEFECTS IN GRAPHITE 35
2.7.1 Point Defects 35
2.7.2 Dislocation Loops 37
2.7.3 Vacancy Lines 38
2.8 RADIOACTIVE GRAPHITE WASTE 39

2.8.1 Location and types of waste 39
2.8.2 Classification 45
2.8.3 Leaching 45
2.9 DECOMMISSIONING SOLUTIONS 45
2.9.1 Incineration 46
2.9.1.1 Conventional Incineration under Air 47
2.9.1.2 Fluidised Bed Incineration 47
2.9.1.3 Power Laser Driven Incineration 47
2.9.2 Recycling 47
2.9.3 Encapsulation 48
3. MATERIALS AND METHODS 52
3.1 MATERIALS 52
3.1.1 Virgin Sample Providence 52
3.1.2 Irradiated Graphite Providence 52
3.2 MICROSTRUCTURAL METHODS 57
3.2.1 Sample preparation 57
3.3 ANALYTICAL INSTRUMENTATION 57
3.3.1 Polarised Light Optical Microscopy 58
3.3.2 Scanning Electron Microscopy (SEM) 59
3.3.3 Transmission Electron Microscopy (TEM) 61
3.3.4 X – Ray Diffraction 62
3.3.5 Tomography 63
3.4 RADIOCHEMICAL METHODS 64
3.4.1 Sample Preparation for Leaching test on active graphite samples 64
3.4.2 Counting Efficiency 67
3.4.2.1 Quench Correction Methods 68

3.4.2.2 ^{3}H Counting Efficiency Determination 71
3.4.2.3 ^{14}C Counting Efficiency Determination 72
3.4.2.4 Window Selection and Widow Optimisation 74
3.4.3 Cocktail Selection 75
3.4.4 Estimate of the Counting Error 76
3.4.5 Detection Limit Determination 77
3.4.5.1 ^{3}H Minimal Detectable Activity 78
3.4.5.2 ^{14}C Minimal Detectable Activity 78
3.5 ANALYTICAL INVESTIGATION 79
3.5.1 Gamma Spectroscopy 79
3.5.2 Liquid Scintillation Counting 79
3.5.3 Total Alpha and Beta 80
3.5.4 Total Alpha and Beta without Tritium Analysis 81
3.5.5 Measurement of ^{3}H by digestion and distillation of leachant 81
3.5.6 Measurement of ^{14}C by digestion (wet oxidation) of leachant methods 82
4. RESULTS AND DISCUSSIONS 85
4.1 MICROSTRUCTURAL RESULTS 85
4.1.1 Polarised Light Microscopy 85
4.1.2 Scanning Electron Microscopy 87
4.1.3 Transmissions Electron Microscopy 90
4.1.4 X-ray diffraction 97
4.1.5 Tomography 102
4.1.6 EDX analysis 114
4.2 LEACHING RESULTS 128
4.2.1 Measurement of Total Gamma Activity 128
4.2.2 Measurement of total alpha and beta radiation by liquid scintillation 139

4.2.3 Measurement of total alpha and beta radiation without ^{3}H using liquid scintillation ... 139

4.2.4 Measurement of ^{3}H by digestion and distillation of leachant ... 140

4.2.5 Measurement of ^{14}C by digestion (wet oxidation) of leachant ... 142

4.2.6 Leaching Rate of Graphite Specimens ... 143

4.2.6.1 Determination of leaching mechanism ... 149

4.2.6.2 Leaching Factor/ Effective Diffusion Coefficient ... 153

4.2.6.3 Comparison with previous studies ... 156

5. CONCLUSIONS ... 158

6. RECOMMENDATION ... 161

7. REFERENCE ... 162

8. APPENDIX ... 169

Terminologies ... 169

9. PAPERS AND JOURNALS ... 172

DECLARATION

What portion of the work referred to in the thesis has been submitted in support of an application for another degree or qualification of this or any other university or other institute of learning.

COPYRIGHT STATEMENT

i. The author of this thesis (including any appendices and/or schedules to this thesis) owns certain copyright or related rights in it (the “Copyright”) and s/he has given The University of Manchester certain rights to use such Copyright, including for administrative purposes.

ii. Copies of this thesis, either in full or in extracts and whether in hard or electronic copy, may be made only in accordance with the Copyright, Designs and Patents Act 1988 (as amended) and regulations issued under it or, where appropriate, in accordance with licensing agreements which the University has from time to time. This page must form part of any such copies made.

iii. The ownership of certain Copyright, patents, designs, trademarks and other intellectual property (the “Intellectual Property”) and any reproductions of copyright works in the thesis, for example graphs and tables (“Reproductions”), which may be described in this thesis, may not be owned by the author and may be owned by third parties. Such Intellectual Property and Reproductions cannot and must not be made available for use without the prior written permission of the owner(s) of the relevant Intellectual Property and/or Reproductions.

iv. Further information on the conditions under which disclosure, publication and commercialisation of this thesis, the Copyright and any Intellectual Property and/or Reproductions described in it may take place is available in the University IP Policy (see http://documents.manchester.ac.uk/DocuInfo.aspx?DocID=487), in any relevant Thesis restriction declarations deposited in the University Library, The University Library’s regulations (see http://www.manchester.ac.uk/library/aboutus/regulations) and in The University’s policy on Presentation of Theses.

TABLE OF FIGURES

Figure 1: The ideal crystal structure of graphite....26

Figure 2: a) Structure of hexagonal graphite projected on to the (0001) plane, (b) Part of the central reciprocal lattice plane. The size of the spot represents the structure factor....27

Figure 3: Basal-plane projection for hexagonal and rhombohedral lattices. The Burgers vectors of partial dislocations are of the type A α = a/3 [10$\bar{1}$0] or A β= -a [01$\bar{1}$0]. Total dislocations are of the type AB = ⅓[11$\bar{2}$0]. 28

Figure 4: Schematic diagram showing manufacturing processes of nuclear graphite 33

Figure 5: Schematic of crystallite imperfection in graphite showing unfilled lattice or vacancy....36

Figure 6: Simple edge dislocation in a cubic material illustrating FS/RH Burger vector convention. 37

Figure 7: The criteria for loop shear for interstitial and vacancy loops 38

Figure 8: Possible configurations of vacancy lines along (a) <11$\bar{2}$0> and (b) <10$\bar{1}$0>....39

Figure 9: Nuclear waste encapsulated with cement 49

Figure 10: Scheme of sampling from graphite core brick (not to scale) 55

Figure 11: Temperatures and Doses as a function of Trepanned Samples height for Oldbury Reactor 1 from Flattened Region Channels 56

Figure 12: Weight Loss and Dose as a function of Temperature of the Samples of Oldbury Reactor 1 graphite from Flattened Region Channels....57

Figure 13: Schematic diagram of Polarised Light Microscopy....59

Figure 14: Schematic diagram of secondary electron microscope 60

Figure 15: Schematic diagram of signals produced by SEM when the incident beam interacts with opaque material 61

Figure 16: Schematic of scattering beam of x-rays 62

Figure 17: Schematic Diagram of Computed Tomography System 64

Figure 18: Leaching experiment set -up 67

Figure 19: Effect of Quenching on an Energy Spectrum [71] 68

Figure 20: LSC energy spectrum of ^{3}H, ^{14}C and ^{32}P showing activity contribution of neighbouring radionuclides....71

Figure 21: The effect of quench on counting efficiency of ^{14}C 73
Figure 22: ^{14}C Distillation Apparatus Schematic Diagram 84
Figure 23: Polarised light optical micrographs of nuclear grade graphites: (a) PGA (b) NBG-10 and (c) NBG-18 all scaled to 500µm 85
Figure 24: Polarised light optical micrographs of nuclear grade graphites: (a) PGA (b) NBG-10 and (c) NBG-18 all scaled to 100µm 86
Figure 25: Scanning electron micrographs (Secondary Electron Image (SEI)) of nuclear grade graphites: (a) PGA (b) NBG-10 and (c) NBG-18. 88
Figure 26: Scanning electron micrographs of unirradiated NBG-10 graphite. Scale: 100 -10µm 89
Figure 27: Scanning electron micrographs of NBG-10 graphite irradiated at 9.16dpa....90
Figure 28: Transmission electron micrographs of NGB-10 nuclear grade graphite (a) Microcracks (b) graphitised and non-graphitised regions and (c) Quinoline Insoluble Particles (coalescence of quinoline insoluble (QI) particles) The scale bar is 100nm 91
Figure 29: TEM micrograph of NBG-10 showing the coalescence of quinoline insoluble (QI) particles of coal tar pitch and cracks between the lamellas and bridged by crystallite – Scale bar 200 - 100nm 92
Figure 30: TEM micrograph of NBG-10 showing (a) crystallisation disturbance caused by QI particles and (b) arrow showing randomly oriented microstructures 93
Figure 31: TEM micrograph of NBG-10 showing randomly oriented microstructures indicated by arrows and incomplete process of carbonisation indicated by the letter M – Scale bar 100nm 93
Figure 32: TEM micrograph of PGA showing (a) Quinoline Insoluble Particles (coalescence of quinoline insoluble (QI) particles) - scale bar 200nm (b) QI Particles - scale bar 100nm and (c) Microcracks - scale bar 20nm 94
Figure 33: Transmission electron microscopy micrographs of irradiated PGA nuclear grade graphite (a) Large thin fragment scale bar is 0.5µm, (b) thin area labeled ‘β’ section from (a) scale bar is 100nm and (c)Diffraction pattern of thin area labeled ‘β’....96
Figure 34: Transmission electron microscopy micrographs showing defects in PGA nuclear grade graphite irradiated at 6.69dpa at a temperature of 338°C together with corresponding diffraction pattern 97
Figure 35: X-ray diffraction pattern of nuclear grade graphites PGA, NBG -10 and NBG -18, all normalised to the [002] peak 98

Figure 36: X-ray diffraction pattern of nuclear grade graphites PGA, NBG -10 and NBG -18 at [002] peaks, all normalised to the [002] peak of PGA 99
Figure 37: X-ray diffraction pattern of PGA, NBG -10 and NBG -18 nuclear grade graphites excluding [002] peak, all normalised to the [004] peak 101
Figure 38: Hexagonal lattice structure showing (112) plane of a rhombohedral 102
Figure 39: Micrograph of PGA nuclear graphite (a) SEM (b) µCT 105
Figure 40 : Thresholding value with respect to greyscale distribution: (a) A greyscale value histogram of the median filtered raw image data (Figure 39b). (b) A profile of the greyscale values across the distance of the same image. 106
Figure 41: Impurities in PGA graphite 107
Figure 42: Labelling of PGA graphite (a) Reduced cube cut out of the main specimen (b) 2D radiographic cross-sectional image of the XY-plane), (c) YZ-plane, (d) XZ plane, (e) label of features and (f) 3D bounding box showing high attenuation impurities 108
Figure 43: Segmentation and Skeletonisation of PGA graphite (a) reconstructed specimen, (b) Reconstructed slice, (c) virtual model, (d) all pores, (e) small pores, (f) gas evolution pores, (g) lenticular pores and (h) impurities 109
Figure 44: Radiographs of (a) PGA and (b) Gilsocarbon graphites 111
Figure 45: The Distribution of High Attenuation Impurities and Porosity. 113
Figure 46: Back scattered electrons (BSE) micrograph of PGA graphite showing impurities as white dots - Scale bar 1 mm 115
Figure 47: Back scattered electrons (BSE) micrograph of PGA graphite showing a selected impurity – Scale bar 50 µm 116
Figure 48: Back scattered electrons (BSE) micrograph of PGA graphite showing a selected impurity – Scale bar 10 µm 117
Figure 49: Secondary electrons micrograph of PGA graphite showing a selected impurity – Scale bar 10 µm 117
Figure 50: Energy dispersive x-ray spectrum of elements in an impurity from graphite showing K_α series peaks of Carbon (C), Oxygen (O), Magnesium (Mg) and Silicon (Si). 118
Figure 51: Back scattered electrons (BSE) micrograph of PGA graphite showing a selected impurity – Scale bar 50 µm 119
Figure 52: Back scattered electrons (BSE) micrograph of PGA graphite showing a selected impurity – Scale bar 5 µm 120

Figure 53: Secondary electrons micrograph of PGA graphite showing a selected impurity – Scale bar 5 µm.....120
Figure 54: Energy dispersive x-ray spectrum of elements in an impurity from graphite showing K series peaks of Aluminium (Al).....121
Figure 55: Back scattered electrons (BSE) micrograph of PGA graphite showing a selected impurity – Scale bar 10 µm.....122
Figure 56: Secondary electrons micrograph of PGA graphite showing a selected impurity – Scale bar 10 µm.....123
Figure 57: Energy dispersive x-ray spectrum of elements in an impurity from graphite showing K_{α} series peaks of Iron (Fe).....123
Figure 58: Back scattered electrons (BSE) micrograph of PGA graphite showing a selected impurity – Scale bar 10 µm.....125
Figure 59: Secondary electrons micrograph of PGA graphite showing a selected impurity – Scale bar 10 µm.....126
Figure 60: Energy dispersive x-ray spectrum of elements in an impurity from graphite showing K series peaks of Carbon (C), Oxygen (O), Calcium (Ca), Silicon (Si), Aluminium (Al), Iron (Fe), Titanium (Ti), Sulphur (S), Potassium (K), Sodium (Na), Magnesium (Mg), Chlorine (Cl) and Zinc (Zn).....126
Figure 61: Bar graph showing gamma emitter radionuclides and corresponding activity release measured using Gamma Spectroscopy for all six samples.....129
Figure 62: Cumulative total activity release of ^{60}Co measured using gamma spectroscopy.....136
Figure 63: Cumulative total activity release of ^{134}Cs measured using gamma spectroscopy.....136
Figure 64: Cumulative total activity release of ^{133}Ba measured using gamma spectroscopy.....137
Figure 65: Cumulative total activity release of ^{137}Cs measured using gamma spectroscopy.....137
Figure 66: Cumulative total activity release of ^{155}Eu measured using gamma spectroscopy.....138
Figure 67: Cumulative total activity release of ^{46}Sc measured using gamma spectroscopy.....138
Figure 68: Cumulative total beta activity release measured using liquid scintillation.....139
Figure 69: Cumulative total beta without ^{3}H activity release measured using liquid scintillation....140
Figure 70: Cumulative total ^{3}H activity release measured using liquid scintillation.....141
Figure 71: Graph showing result found by interpolating cumulative total alpha and beta and total alpha and beta without ^{3}H activity release.....141
Figure 72: Cumulative total ^{14}C activity release measured using Liquid Scintillation.....142

Figure 73: Cumulative Fraction of ^{3}H Activity Leached in Simulated Groundwater at 20 ± 5°C 146

Figure 74: Cumulative Fraction of ^{14}C Activity Leached in Simulated Groundwater at 20 ± 5°C ...146

Figure 75: Fractional Leach Rate of ^{3}H in Simulated Groundwater at 20 ± 5°C.....148

Figure 76: Fractional Leach Rate of ^{14}C in Simulated Groundwater at 20 ± 5°C 148

Figure 77: Linear Regression Graph of the Logarithm of Cumulative Leach Fraction of ^{3}H versus the Logarithm of Time.....152

Figure 78: Linear Regression Graph of the Logarithm of Cumulative Leach Fraction of ^{14}c versus the Logarithm of Time.....153

Figure 79: Cumulative Fraction of ^{3}H Activity Leached in Simulated Groundwater at 20 ± 5°C 155

Figure 80: Cumulative Fraction of ^{14}C Activity Leached in Simulated Groundwater at 20 ± 5°C ...155

LIST OF TABLES

Table 1 : Types of radiation and typical half life for the found radioisotopes in nuclear graphite 20

Table 2 : Former UKAEA Gas Cooled Reactors 25

Table 3 : Magnox Reactors 25

Table 4 : Advanced Gas Cooled Reactors 25

Table 5: Typical virgin properties of pile grade A (PGA) and NBG 10 graphites 30

Table 6: Operational Conditions of UK Reactors 34

Table 7: LIST OF UK GRAPHITE MODERATED REACTORS 40

Table 8: Classification of Radiological Waste 45

Table 9 : Initial Evaluation by BNFL of Processing Options for Graphite in the UK 50

Table 10: Temperatures and Fast Neutron Dose for Oldbury Reactor 1 (2009) Trepanned Samples from Flattened Region Channels [56] 54

Table 11: Leachant Renewal Schedule 65

Table 12: Original Simulated Groundwater Composition (Wilkins) [64] 66

Table 13: ^{3}H counting efficiency determination 72

Table 14: ^{14}C counting efficiency determination 73

Table 15 : Crystallite dimensions (*c* and *a*) of nuclear grade graphites calibrated at (002) and (110) 100

Table 16 : Lattice spacing of nuclear grade graphites calibrated using XRD 100

Table 17: Quantitative analysis of PGA graphite features 108

Table 18: Quantitative analysis of Gilsocarbon graphite features 112

Table 19: Energy dispersive x-ray semi-quantitative measurement of elements in an impurity from graphite 118

Table 20: Energy dispersive x-ray semi-quantitative measurement of elements in an impurity from graphite 121

Table 21: Energy dispersive x-ray semi-quantitative measurement of elements in an impurity from PGA graphite 124

Table 22: Energy dispersive x-ray semi-quantitative measurement of elements in an impurity from PGA graphite 127

Table 23: Solubility, origin and possible entrainment of radionuclides 130

Table 24: Time for cumulative release to plateau versus Cumulative release to plateau 131

Table 25: Characterisation Results 145
Table 26: Temperatures and Fast Neutron Dose for Oldbury Reactor 1 (2009) Trepanned Samples from Flattened Region Channels [56] 145
Table 27: Incremental Leach Rates at Day 91 147
Table 28: Cumulative Fraction of Activity Leached at day 91 147
Table 29: Diffusion coefficient value ^{14}C radionuclide leached from irradiated graphite waste 154
Table 30: Average Cumulative Fraction and Average Incremental Leach Rate of Activity Leached at day 91 from all samples 157
Table 31: Cumulative Fraction and Incremental Leach Rate of Activity Leached at day 100 obtained by White et al. 157

ABSTRACT

A procedure to evaluate the leaching properties of radionuclides from irradiated graphite waste has been developed by combining ANSI 16.1 (USA) and NEN 7345 (Netherlands) standardised diffusion leaching techniques. The ANSI 16.1 standard has been followed to the acquire the leachates and to determine the leach rate/ diffusion coefficient and NEN 7345 standard technique has been used to determine the diffusion mechanism of radionuclides. The investigation employs simulated Drigg groundwater as a leachant using semi-dynamic technique for the production of leachate specimens. From gamma spectroscopy analysis the principal radionuclides present in terms of activity were ^{60}Co, ^{137}Cs, ^{134}Cs, ^{155}Eu, ^{133}Ba and ^{46}Sc. The dominant radionuclides are ^{60}Co, ^{134}Cs and ^{133}Ba which together account for about 91 % of the total activity. The 91 % can be broken down into 73.4 % ^{60}Co, 9.1 % ^{134}Cs and 8.1 % ^{133}Ba. Analysis of total beta and total beta without tritium activity release from Magnox graphite was measured using liquid scintillating counting. Preliminary results show that there is an initial high release of activity and decreases when the leaching period increases. This may be due to the depletion of contaminants which were absorbed by the internal pore networks and the surface. During the leaching test approximately 275.33 ± 18.20 Bq of ^{3}H and 106.26 ± 7.01 Bq of ^{14}C was released into the leachant within 91 days.

Irradiation induced damages to the nuclear graphite crystal structure have been shown to cause disruption of the bonding across the basal planes. Moreover, the closures of Mrozowski cracks have been observed in nuclear graphite, the bulk property are governed by the porosity, in particular, at the nanometre scale. Therefore, knowledge of the crystallite structure and porosity distribution is very important; as it will assist in understand the affects of irradiated damage and location and the mechanism of the leaching of radionuclides.

The work reported herein contributed several key findings to the international work on graphite leaching to offer guidance leading toward obtaining leaching data in the future: (a) the effective diffusion coefficient for ^{14}C from graphite waste has been determined. The diffusion process for ^{14}C has two stages resulting two different values of diffusion coefficient, i.e., for the fast and slow components; (b) the controlling leaching mechanism for ^{3}H radionuclide from graphite is shown to be surface wash–off; and for that of ^{14}C radionuclide the initial controlling leaching mechanism is surface wash-off following by diffusion which is the major transport mechanism ; (c) The weight loss originates from the open pore structure which has been opened up by radiolytic oxidation; at the higher weight losses much of the closed porosity in the graphite has been opened. The investigation indicates that weigh loss has a major influence on the leaching of elements from the irradiated graphite; and (d) the analysis of the pores in nuclear graphite can be categorised into three types. These three types of pores are: (1) small pores narrow which are slit-shaped pores in the binder phase or matrix, (2) gas evolution pores or gas entrapment pores within the binder phase or matrix and (3) lenticular pores which are large cracks within the filler particles. It is shown in this thesis that by using tomography to study the morphology of the different pores coupled with the distribution of impurities an understanding of the role of porosity in leaching is possible.

GLOSSARY OF TERMS

Abbreviation/ Acronym	Symbol/	Definition
AGL		Anglo Great Lakes
AGR		Advanced Gas Reactors
ANSI		American National Standards Institute
A		Area
B		Channel B
BAEL		British Acheson Electrodes Ltd
BEPO		British Experimental Pile ‘0’
BNFL		British Nuclear Fuels Limited
Bq		Becquerel
cm		centimetre
CEGB		Central Electricity Generating Board
COSHH		Control of Substances Hazardous to Health
CPM		Count per Minute
CPS		Count per Second
CPSB		Count per Second in Channel B
CT		Computed Tomography
D		Diffusion Coefficient
DIDO		Di-Deuterium Oxide Reactor
DPA		Displacement per Atom
DPM		Disintegrations per Minute
EDND		Equivalent DIDO Nickel Dose
EDS		Energy Dispersive Spectroscopy

EDX	Energy Dispersive X-ray
F	Fraction
g	Gram
GLEEP	Graphite Low Energy Experimental Pile
HOPG	Highly Orientated Pyrolytic Graphite
HTR	High Temperature Reactor
IAEA	International Atomic Energy Agency
i-graphite	Irradiated Graphite
ICRP	International Commission on Radiological Protection
ID	Identification
ILW	Intermediate Level Waste
log	Logarithm
LLD	Lower Limit of detection
LLW	Low Level Waste
LLWR	Low Level Waste Repository
LSC	Liquid Scintillation Counter
MTR	Material Test Reactor
m	Metre
m	Gradient/ Slope
M	Mega
µ	Micro
MDA	Minimum Detectable Activity
MW	Mega Watt
MW	Megawatt
n	neutron

NBG	Nuclear Block Graphite
NDA	Nuclear Decommissioning Authority
NNL	National Nuclear Laboratory
PGA	Pile Grade A
PGB	Pile Grade B
pH	the acidity or basicity measure of an aqueous solution
PMT	Photo-multiplier tube
QI	Quinoline Insoluble
SEI	Secondary Electron Image
SEM	Scanning Electron Microscopy
S	Surface Area
t	Time
TEM	Transmission Electron Microscopy
tSIE	Transformed Spectral Index of the External Standard
UG	Ultima Gold
UKAEA	United Kingdom Atomic Energy Authority
V	Volume
VLLW	Very Low Level Waste
XRD	X-ray Diffraction
α	Alpha
β	Beta
γ	Gamma

ACKNOWLEDGEMENTS

I would like to take this opportunity to express my sincere gratitude to my supervisors Prof. Barry Marsden, and Dr. Abbie Jones for giving me the chance to work with them, for their constant guidance and invaluable advice and for reviewing my work throughout the process of conducting the experiments. Since the beginning of the project they always had opened their door for all questions I had and discussions concerning all aspects of the work. I must also thank Prof. James Marrow who was there to discuss my ideas and provide timely motivation while he was at UoM.

I would also like to extend my acknowledgements to Ms. Judith Shackleton, Mr. Teruo Hashimoto, and Ms. Xiangli Zhong, Dr. Alan Harvey, Mr. Chris, Mr. Michel Faulkner and Mr. Paul Townsend for their advice and help during preparation and evaluation of the samples.

Thanks are given to the National Nuclear Laboratory (NNL) for facilitating a long-term placement in their laboratories at Sellafield Ltd., Cumbria, where part of the research was undertaken. I found working at NNL to be a very exciting and intellectual environment. I have benefited a lot from the professional excellence of the many scientists working there, particularly Mr. Ed Butcher, Dr. Martine Metcalfe, Mrs Nassia Tzelepi, Mr. John Rawcliffe, Dr. Simon Woodbury, and Dr. Simon Dumbill, and National Decommissioning Agency (NDA) for funding the project. Financial support from EPSRC for funding this work under the Diamond Project, Grant Number EP/F055412/1 is gratefully acknowledged.

Last, but not least, I thank my family and friends particularly my fiancée Dagi for being patient and providing unconditional support and encouragement to pursue my interests. Without the generous help of these individuals all my studies would not have been possible. I am greatly indebted to my mum, who inspired me to pursue higher education and achieve my full potential.

1. INTRODUCTION

1.1 NUCLEAR GRAPHITE WASTE

The most obvious source of irradiated graphite is from reactor moderators and reflectors. This graphite is exposed to a very high irradiation resulting very high potential activation of impurity isotopes. There are also other sources of graphite components, in addition to the moderator and reflector, such as thermal columns, channel sleeves, graphite plugs, outer circumferential fuel sleeves and side locating struts.

On the basis of gross activity, nuclear graphite waste from many of the reactors is classified as Low Level Waste (LLW). British Nuclear Fuels Limited (BNFL) at Drigg in Cumbria placed a limit on the disposal of LLW. For nuclear waste to be classified as LLW, it should have an activity below 4G Bq/te alpha and 12G Bq/te beta/gamma however, there are further radiological restrictions. The ^{14}C content of the waste is the main restriction associated with the disposal of graphite as LLW. The radiological limit of the residual Drigg for ^{14}C is 1.5 TBq. This gives a limit of 0.05 TBq per year (30 year operating life). Considering the Windscale Pile 1 reactor, the total ^{14}C content of the graphite is 6.9 TBq; this exceeds the total radiological capacity of Drigg for ^{14}C by a factor of 4.6. This fact shows that it will not be possible to dispose of radioactive graphite as low level waste. [1]

1.2 HISTORICAL PROBLEMS

Graphite has many special features that make it a unique waste form. There are a number of technical issues associated with the packaging for disposal of graphite. The main areas of concern are the levels of Wigner energy and the activity associated with the graphite. Wigner energy is produced as a consequence of the presence of defects.[2] The annealing of this stored energy was responsible for the fire in the Windscale Piles in 1957.[3] To relieve the build-up of stored energy of the graphite moderator, accumulated as a result of neutron irradiation, the air blowers were shut down and the core was heated up to encourage self-annealing. This heating initiated the Wigner release that caused the graphite temperature to increase further and fire broke out. The fire was due to damage of the fuel cladding and oxidation of uranium metal fuel. Therefore, the possibility of a large spontaneous temperature rise in the graphite moderator is the main source of concern associated with the accumulation of stored energy in an operating reactor. The total amount of stored energy can be determined by measuring the heat of combustion of samples of unirradiated and irradiated graphite.[4]

The activity associated with the graphite or the possible release of radioisotopes during decommissioning is also a major concern. The radioactive isotopes, which are considered the most of potential concern to the environmental, are ^{3}H, ^{14}C, ^{36}Cl, ^{60}Co, ^{137}Cs and ^{152}Eu. Table 1 shows typical half life and types of radioisotope species which are found in nuclear graphite.[5] Some of the radionuclides arise from the activation of impurities which are integral with the

material. Other isotopes may arise from the neutron flux from reactor material, which has then been activated in the core and are associated with the surfaces and inside the graphite crystal lattice transported via the porosity. One of the most important isotope of concern is ^{14}C because it has a long half life of 5730 years [6]. This radionuclide is produced in three principal ways, by transmutation of the $^{14}N(n, p) \rightarrow {}^{14}C$, via the reaction $^{13}C(n,\gamma) \rightarrow {}^{14}C$ or/and the reaction $^{16}O(n,\gamma) \rightarrow {}^{17}O(n,\alpha) \rightarrow {}^{14}C$ during irradiation. The radionuclides ^{3}H and ^{60}Co have half-lives of 12.3 years and 5.3 years respectively. Their concentration is negligible because most reactors are decommissioned after probably 30 – 150 years of shut down.[4]

Table 1 : Types of radiation and typical half life for the found radioisotopes in nuclear graphite

Radioisotope	Radiation Energy				Half Life (Years)
	α	β	γ	ε	
^{3}H		√			12.3
^{14}C		√			5730
^{36}Cl		√			300000
^{41}Ca				√	130000
^{60}Co		√	√		5.3
^{85}Kr		√			10.8
^{94}Nb		√	√		20000
^{95}Nb		√	√		0.096
^{133}Ba			√	√	10.5
^{134}Cs		√	√		2.06
^{137}Cs		√	√		30.2
^{152}Eu			√	√	13.3
^{154}Eu		√	√	√	8.5
^{155}Eu		√	√		4.96
^{238}Pu	√				87.75
^{239}Pu	√				24390
^{240}Pu	√				6537
^{241}Am	√		√		433
^{241}Pu	√	√			14.89

Recent work suggests that the majority of ^{14}C does not appear to be integrated into the graphite crystal lattice but only bound on the surface of the graphite crystallites and pores following neutron activation [7-9]. Therefore, further characterisation of the graphite before and after irradiation is required in order to gain understanding of the transportation mechanism of ^{14}C in terms of leaching and particulate gaseous release and stability of the final immobilisation matrix.

In a recent review, it was concluded that it may be possible to reduce the activity of the radioactive graphite waste by up to 60% using thermal treatment with Argon/oxygen [5]. This would lead to the reduction in volume of intermediate level waste, and significantly decrease the cost of decommissioning.

1.3 ISSUES AND OBJECTIVES OF RESEARCH

The largest source of irradiated graphite within the UK originates from reactor moderators and reflector material. The majority of this graphite has been exposed to very high levels of neutron irradiation resulting in activation of impurity radionuclides. There are also other sources of irradiated graphite components, in addition to the moderator and reflector, such as Material Test Reactor (MTR) thermal columns, fuel channel sleeves, graphite plugs, outer circumferential fuel sleeves, graphite boats and side locating struts. Once all the graphite moderated reactors have closed, the UK will have a graphite waste inventory amounting to approximately 100,000 tonnes. Therefore graphite waste treatment and behaviour in typical geological conditions is an increasingly important issue that the UK has to address and fully understand.

On the basis of gross activity, nuclear graphite waste from many of the reactors is classified as Low Level Waste (LLW) however the ^{14}C content of the waste is the main restriction associated to the disposal of graphite as LLW. To support the measures which are going to be taken to dispose of the large volume of irradiated graphite, it is necessary to understand fully the microstructural and radioisotopic character of the graphite and the consequent effectiveness of the various proposed preparative and immobilisation treatments. The current UK plan for graphite disposal is that this material will be packaged as Intermediate Level Waste (ILW) for deep geological repository disposal. It has not yet been shown that the current baseline represents effective solution in terms of safety, cost and protection of the environment.

The main objectives of the research program are to study the rate of the diffusion of radionuclides into groundwater from irradiated graphite waste in order to assess the possibility of isotopic release to the environment. The leachability of the contaminants from the waste under repository conditions will be studied in order to assist the evaluation of encapsulation methods as a possible disposal route and identify the parameters that need to be taken into account for its implementation. Irradiated graphite samples from the Oldbury Magnox Reactor 1 core were used for this study. A related pair of matching samples, in terms of irradiation history and properties was immersed in solution, representing typical repository conditions. The data collected will be used to relate the leach rate of the leachant and the graphite irradiation history.

The surface and porosity of the graphite are considered to influence the diffusion of radionuclides from the graphite waste. Therefore, the microstructure of both unirradiated and irradiated graphite are analysed by state-of-the-art materials characterisation techniques.

1.4 RESEARCH PROPOSAL

The following research questions gave course to this research:

- How does irradiation damage affect the leaching of radionuclides from the waste?
- What method should be used to assess leaching of radionuclides from graphite waste incineration residues? How is a leaching test carried out to get representative data with regard to long-term leaching predictions?
- How accurate are leaching predictions made derived from diffusion leaching test data?
- What is the mechanism of leaching of radionuclides from the waste?
- What is the origin of the radionuclides released during leaching tests? Is it from the activation of impurities which are integral with the original graphite or are they arise from other reactor materials or fission products?
- How irradiation does affect the graphite? How does it affects/ influence the leaching of radionuclides?

First, a method to assess the leaching properties of radionuclides form irradiated graphite waste was developed based on a standardised diffusion leaching tests. The United States ANSI 16.1 standard is used to acquire the leachates and to determine the leach rate/ diffusion coefficient. Second, The Dutch NEN 7345 standard technique has been used to determine the diffusion mechanism of radionuclides. Third, based on diffusion leaching test data, long-term leaching predictions were made and evaluated. Predictions were compared with the leaching tests performed by other scientists.

Then, the affect of irradiated damage to the graphite lattice, change in lattice parameters and the arrangement of crystallites within the microstructure and the distribution of microporosity contained within the graphite structure are studied using Polarised Light Microscopy (PLM), X-ray Diffraction (XRD), Scanning Electron Microscopy (SEM) and Transmission Electron Microscopy (TEM).

Finally, the distribution of porosity and impurities in graphite are also assayed using X-ray Computed Tomography (CT) and Energy Dispersive Spectroscopy (EDS). Nuclear grade graphites, namely PGA form UK Magnox reactors, Gilsocarbon from AGRs (Advanced Gas Cooled Reactors) and NBG-10 and NBG-18 from future HTRs (High Temperature Reactors) were chosen for investigation. The manufacturing processes of these graphite grades are distinct, which results different microstructures, including differences in crystal orientations, in the final product.

1.5 RESEARCH PLACEMENT

A unique opportunity was granted for a University of Manchester student to conduct research at the National Nuclear laboratory (NNL) Sellafield. The National Decommissioning Authority (NDA) through the Engineering and Physical Sciences Research Council (EPSRC) funded this research placement. This research is a pilot study aimed at determining the leaching rate of the major nuclides found in irradiated graphite; the work was carried out as part of a research placement at the National Nuclear Laboratory (NNL), Sellafield underwritten by the NDA. The work placement was undertaken over for a period of nine months at the National Nuclear Central Laboratory as part of the NNL/University of Manchester (UoM) access agreement. The aims of the agreement were to enable this research to perform physical, microstructural and radiochemical analysis in order to determine and understand the isotopic leachability of Magnox graphite under deep waste repository conditions to determine critical leaching parameters for further encapsulation tests. The research was performed at the Technology Department at NNL Sellafield between June 2011 and April 2012.

To support research in the field of nuclear waste management and decommissioning the NDA has dedicated £4.3M of funding to the EPSRC over a four year period. The award granted to a consortium consisting of the University of Manchester, University of Leeds, Imperial College of London, Loughborough University, University College of London and the University of Sheffield. This consortium operates under the acronym DIAMOND (Decommissioning, Immobilisation and Management of Nuclear waste for Disposal). Through this consortium the Nuclear Graphite Research Group (NGRG) at the University of Manchester have forged strong collaborations with NNL. Over many years NNL has established valuable experience in encapsulation of non-irradiated graphite waste combined with an understanding of the microstructural and radioisotopic character of irradiated graphite.

The National Nuclear Laboratory (NNL) Central laboratory is based at Sellafield in Cumbria. NNL deals with many varied aspects of decommissioning, from decontamination to vitrification and develops high quality nuclear solutions for all customers across the fuel cycle The company develops products traditionally on a pure research basis and also sells its expertise to a large commercial market, with its cutting edge technology. Its customer base is both national and international.

The project was based within the NNL Reactor Operations Support Group and to ensure safety, a detailed training programme was undertaken by the student before the experimental programme could be carried out. The aims of training were to ensure safety and quality resulting in the trainer becoming a fully Suitably Qualified and Experienced Person (SQEP) in the analytical methods used for leaching tests and radiochemical analysis, as well as other work in active laboratory conditions without the need for supervision. The student successfully achieved this.

The research programme was successful in determining the ^{14}C and ^{3}H leachability of Magnox Oldbury graphite. In addition, total Beta, total Beta – ^{3}H and Gamma spectroscopy has been evaluated. Microstructural analyses, including preliminary Transmission Electron Microscopy (TEM) studies, were carried out. Due to the extent of the training program required, and constraints in access to NNL equipment it was not possible to perform ^{36}Cl analysis as was originally intended.

1.6 PROJECT AIMS

- To assess the leachability of contaminants of radioactive radionuclides, which are considered of potential concern to the environment such as ^{3}H, ^{14}C, ^{36}Cl, ^{60}Co, ^{137}Cs and ^{155}Eu, from the irradiated graphite waste under repository conditions in order to assist the evaluation of encapsulation methods as a possible disposal route and identify the parameters that need to be taken into account for its implementation;

- To determine the rate of diffusion of radionuclides into groundwater from irradiated graphite waste in order to assess the possibility of isotopic release to the environment;

- To understand the effects on microstructure of graphite that is induced by fast neutron irradiation. The aims are to understand the microstructure of unirradiated and irradiated graphite, the arrangement of crystallites within the microstructure and the types and distribution of microporosity contained within the graphite structure and the effect on structural integrity.

- To determine the distribution and amount of impurities in the graphite

2. LITERATURE REVIEW

2.1 GRAPHITE MODERATED NUCLEAR REACTORS

Worldwide, there are more than 100 nuclear power plants and many research and plutonium-production reactors which have been using graphite as a moderator and neutron reflector [10]. In the United Kingdom, there are about 42 nuclear power stations and 19 are still working. When all shut down, in total, they will produce about 100,000 tons of irradiated graphite waste [11]. Table 2, Table 3 and Table 4 shows UK reactors which use graphite. Table 2 show details of the UK Gas Cooled Reactors which were owned by the former UKAEA, now all shut down. Table 3 lists the UK Magnox Reactors and Table 4 shows list of advanced gas cooled reactors [5].

Table 2 : Former UKAEA Gas Cooled Reactors

Reactor	Site	Type	Power (MW)
GLEEP	Harwell	Graphite moderated air cooled	0.05
BEPO	Harwell	Graphite moderated air cooled	6.5
PILE 1 & 2	Windscale	Graphite moderated air cooled	160
WAGR	Windscale	Graphite moderated CO_2 cooled	110
DRAGON	Winfrith	Graphite moderated He cooled	20

Table 3 : Magnox Reactors

Station	No. of Reactors	Start of operation	Total electrical power (MW)	Shutdown	Expected closure
Calder Hall	4	1956-1959	200	2003	
Chapelcross	4	1959-1960	200	2005	
Berkley	2	1962	276	1988-1989	
Bradwell	2	1962	246	2002	
Hunterston A	2	1964	300	1990	
Trawsfynydd	2	1965	390	1993	
Hinkley Point A	2	1965	470	2000	
Dungeness A	2	1965	440	2006	
Sizewell A	2	1966	420	2006	
Oldbury on Severn	2	1968	434	2012	
Wylfa	2	1971	950		2014

Table 4 : Advanced Gas Cooled Reactors

Station	Reactors	Total electrical power (MW)	Start of operation	Graphite Manufacturer
Hinkley Point B	2	1220	1976	AGL
Hunterston B	2	1190	1977	AGL
Dungeness B	2	1210	1984	AGL
Heysham 1	2	1150	1984	BAEL
Hartlepool	2	1110	1985	BAEL
Torness	2	1250	1988	GrafTech
Heysham 2	2	1250	1989	GrafTech

2.2 NUCLEAR GRAPHITE

Graphite is one of the eight allotropes of carbon and is thermodynamically very stable, as the atoms are arranged in parallel, in a hexagonal network. The chemical element carbon, has an atomic number of six and is indicated by the symbol C. Carbon is a member of group IV on the periodic table, it is non metallic and has four electrons available to form covalent chemical bonds. It has three naturally occurring isotopes. ^{12}C and ^{13}C are stable isotopes, while ^{14}C is radioactive, with a half-life of about 5730 years.[12]

The ideal crystal structure of graphite is shown in Figure 1, where one atom in the lattice has three adjoining atoms.[13] Graphite occurs in two forms of close-packed structures, the hexagonal with a stacking sequence ABAB… as shown in Figure 2 [14] and the face-centred cubic or rhombohedral with a sequence ABCABC….(shown in Figure 3).[14] This rhombohedral arrangement however is thermodynamically unstable.[14] The adjacent parallel planes are arranged relative to each other and are arranged in alternating sequence. Delocalised electrons form a weak binding force (Van der Waals force) between the layers (c - direction), compared to the bonds between the atoms within the layers (a – direction) and due to this weak attraction bond between basal layers, graphite has a cohesive strength only one direction.[13, 15]

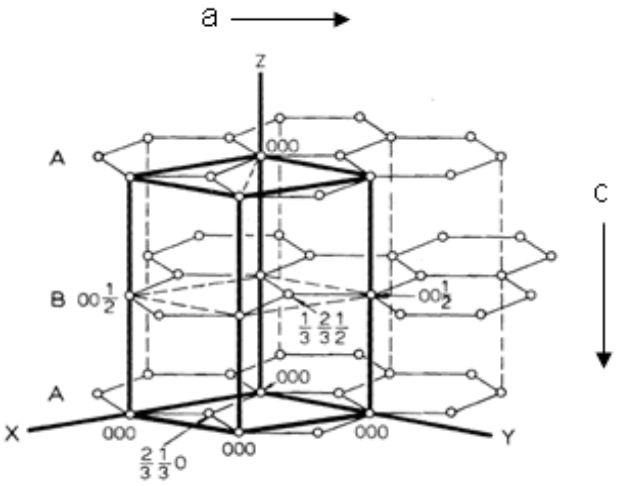

Figure 1: The ideal crystal structure of graphite

Graphite, which is close to the ideal crystal structure, occurs naturally in flakes. One method for manufacture of high purity artificial graphite is the decomposition of solid hydrocarbons or coke and can be graphitised by sufficient heat treatments to encourage crystal growth.[16, 17] Highly Orientated Pyrolytic Graphite (HOPG) has a planar morphology and a shining silvery surface. It is very soft and will therefore sheer along the C_{44} and collapse very easily.[16, 17] Polycrystalline form of graphite is dark grey, porous and soft. Ideal crystal graphite density is significantly greater than that of the polycrystalline graphite because it contains a large number of pores and impurities.[18, 19]

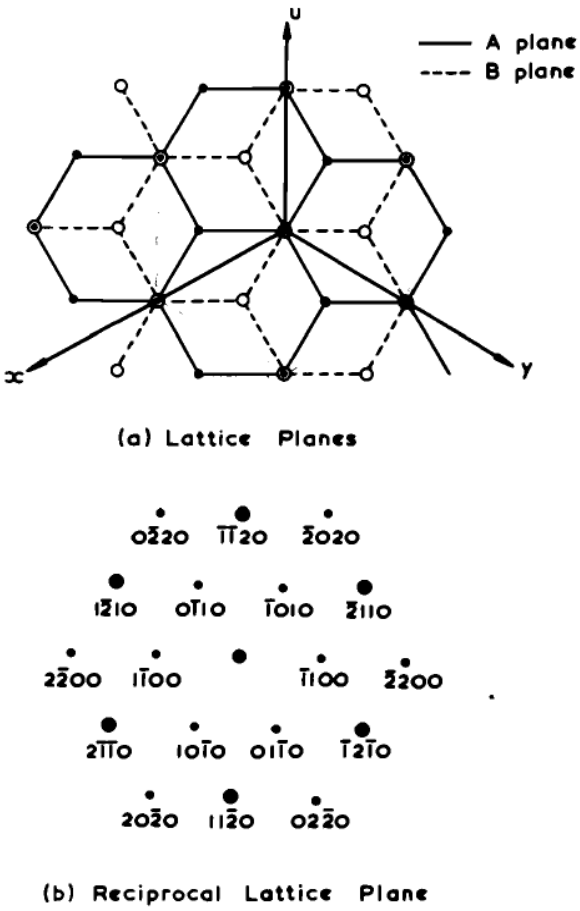

Figure 2: a) Structure of hexagonal graphite projected on to the (0001) plane, (b) Part of the central reciprocal lattice plane. The size of the spot represents the structure factor

Both natural and artificial of graphites have identical crystalline structures, however natural graphite has significantly larger crystals, which orient themselves in one direction, resulting in lamination.[15] Artificial graphite has similar properties to those of natural graphite however it is considerably higher purity as natural graphite contains a lot of naturally occurring impurities. As the degree of graphitisation of the artificial polycrystalline graphite increases, the average distance between lattices of artificial becomes smaller and nearer to the value for a perfect crystal.[15, 18]

The packing of crystallites has never been perfect in the binder and filler phases as there are always a cluster of pores. These pores structure are related to the voids in the graphite. The method by which the crystallites are packed, and the type of the bonding between the filler and binder phases, determine the number and size of the pores. Thus, understanding of the size distribution of pores is useful in characterising the structure of graphite. The physical properties of polycrystalline graphite depend on the method of preparation. Different methods of production result in different sizes of crystal orientation of the graphite. In addition, the graphite is anisotropic; i.e. its properties are different in perpendicular and parallel directions relative to the principal alignment of the basic planes. [15, 18]

By taking into account the first basal plane and taking any atomic position as origin, it may be possible to determine the hexagonal unit cell. The unit cell edge joins its nearest neighbours, as shown in Figure 3.[13] The magnitude of the pair of such vectors is equal, are at an angle of 60° and defines the basal structure.[13, 19] The neighbouring planes are reciprocally oriented in such a way that they cannot be overlaid by a simple linear displacement, so the c-axis vector is twice the interplanar spacing. There are four atoms per unit cell and two completely different kinds of atomic site: those situated between the neatest neighbours above and below and those with open hexagons immediately above and below. The positions of the four atoms are: (0, 0, 0); (0, 0, ½); *(⅔, ⅓,* 0) and (⅓, ⅔, ½). There are three corresponding directions in any basal plane, and to emphasise this type of symmetry Bravais-Miller system of structural notation is sometimes used, these three crystal axes in the basal plane of graphite are the $[2\bar{1}\bar{1}0]$, $[1\bar{2}10]$ and the $[\bar{1}2\bar{1}0]$ respectively.[12, 13]

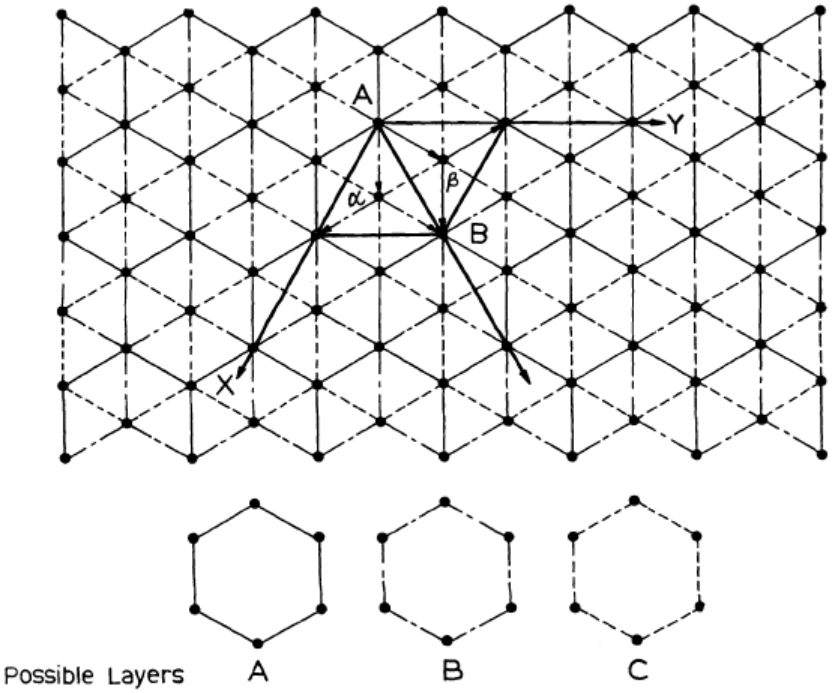

Figure 3: Basal-plane projection for hexagonal and rhombohedral lattices. The Burgers vectors of partial dislocations are of the type A α = a/3 $[10\bar{1}0]$ or A β= -a $[01\bar{1}0]$. Total dislocations are of the type AB = ⅓$[11\bar{2}0]$.

Pure graphite is a chemically inert material and resistant to most acids, alkaline and corrosive gases. The chemical reactivity of graphite is considerably influenced by its crystallographic structure [18, 19]. The irradiation behaviour of graphite is strongly influenced by the source of the pitch, the coke and the manufacturing process. Nuclear graphite is used within reactors as a moderator, reflector and other structural components. In nuclear reaction, the moderation of neutron flux depends on the density of the graphite [18, 19]. The greater the density, the greater it's slowing down power.

For nuclear graphite to be used as a moderator, there are two basic requirements. First, it must be efficient in slowing fast neutrons down and second, it must have a small cross-section for neutron absorption. The energy transfer during elastic collisions between the neutrons and the moderator atoms results in the slowing down of the neutrons. The collision rate per unit volume must be relatively high for a material to be an effective moderator. The number of moderator nuclei per unit volume is proportional to the rate of collision, and due to this, if the volume of the reactor core is to be minimised, the density of the moderator graphite should not be very low.[18] Moderator graphite is required to absorb very few neutrons during the moderating process, this is due to the neutrons that are absorbed will be considered as a loss, as they will be not be involved in the chain reaction. Distinctive impurities, which are found inside the graphite, have a greater tendency for absorbing neutrons than the carbon atoms; therefore, it is necessary to produce graphite which is free from impurities as far as possible. [13, 18, 19]

During manufacturing of graphite the most important characteristic which must monitored very closely, is its dimensional stability. At the time of dismantling, the graphite components in the reactor cores may experience distortions, cracking, or jamming.[13] These issues must be studied during the design of the reactor and the components must be manufactured accordingly. Any significant design problems may lead to severe problems during decommissioning.[13] These are the main factors which force us to vary manufacturing techniques to get a desired set of physical properties.

Nuclear graphites are usually manufactured with the end objectives of high thermal conductivity, high purity, and as far as possible, to have maximum resistance to irradiation damage [13]. To produce specialised grades of graphites with high strength, low permeability, minimum gas content, high density, or with other specific requirements, however, there may be sacrifices from other properties to attain these results.[13] Due to this, it is not possible to provide a comprehensive set of properties for all nuclear graphites, because each application may have unique issues. As sophistication of reactor design increases, so does the manufacturing method of graphite grades to a particular end use.

The degree of orientation of crystallites is dependent on the raw material used and techniques used in fabrication. The geometry of the end product and the physical properties will vary as the size and shape of the graphite are changed. Moderator graphites bulk density and purity are typically used as control properties. Mechanical properties (Table 5) [4, 13], such as strength, thermal conductivity, and thermal expansion, however, are usually monitored and altered for specific functions. These properties have a significant role in understanding the structure and irradiation resistance of nuclear graphites.

Table 5: Typical unirradiated properties of pile grade A (PGA), Gilsocarbon, NBG 10 and NBG 18 graphites

Property	Units	Pile Grade A graphite (Anisotropic)	Gilsocarbon (Isotropic)	NBG 10 (Near Isotropic)	NBG 18 (Near Isotropic)
Density	$g.cm^{-3}$	1.74	1.81	1.81	1.87
Thermal expansion coefficient (20-120) 10^{-6} °C	K^{-1}	0.9 * 28.3 **	4.3	4.2* 4.3**	4.5* 4.6**
Thermal conductivity(20°C)	$W.m^{-1}K^{-1}$	200 * 109 **	131	161* 157**	145* 141**
Young's modulus(20°C)	$GN.m^{-2}$	11.7 * 5.4 **	10.85	10.3* 9.9**	11.7* 11.6**
Tensile Strength	$MN.m^{-2}$	17 * 11 **	17.5	18* 21**	20.8* 20.4**
Flexural Strength	$MN.m^{-2}$	19 * 12 **	30	30* 27**	31.1* 29.7**
compression Strength	$MN.m^{-2}$	27 * 27 **	70	70* 60**	77.4* 78.5**
Electrical resistivity	μ ohm.cm^{-1}	620 * 1100 **	900	840* 860**	870* 890**

* With grain – parallel to the basal plane

** Against Grain – perpendicular to the basal plane

2.3 MANUFACTURING PROCESS

Graphites are manufactured from pitch coke and pitch derived from the crude oil. A schematic diagram of the manufacturing processes of nuclear graphite is shown in Figure 4. During manufacturing the first procedure is calcination, where the coke is crushed and calcined at temperatures in the range 900 – 1400°C. [13, 18] The aim of this process is to reduce the volatile content and to avoid excessive shrinkage in later heat treatments.

After calcinations, the coke is milled and mixed with the filler particles (coke) together with the binder. The shape of the filler particles is important in the forming process because extrusion preferentially tend to orient anisometric particles. This makes long particles to be positioned parallel to the direction of the extrusion, then, heated to ensure homogeneity of mixing, it will be extruded or moulded into blocks. Unlike extrusion, in moulding technique operation the elongated filler particles align themselves with their long dimension normal to the direction of moulding. The blocks are baked at a temperature of about 800°C. To allow expansion and to give mechanical support during this heating process, the blocks will normally be packed in sacrificial coke to fill the pores which may be produced by the release of gases. The manufactured blocks may require heating for up to 70 days. This is due to the poor thermal conductivity of the coke and to make the process effective. During this stage of graphite manufacturing, the population of porosity may increase, which may arise from the loss of volatile materials from the binder.[13, 18]

The density of these blocks depends on the size of the filler particles and the source of the coke. If the density of the blocks are not high enough, they are re-impregnated with pitch under pressure and re-baked.[15, 18, 19] Density and strength improvements may be achieved after two or three impregnations but sometimes it may take up to six repetitions.[20] Finally, the blocks are graphitised at a temperature of around 3000°C. In earlier days, graphitisation was accompanied by purification with chlorine containing gases, however, nowadays Fluorine is used instead of Chlorine.[14] The reason for this is chlorine, which might have been trapped in pores during manufacturing, may be released during irradiation and can act as a source of ^{36}Cl radionuclide.[3] The anisotropy of graphite depends on the alignment of the graphite crystallites and the orientation of the filler particles.[18, 19]

The final product chemical purity can be achieved is in three stages during manufacturing. The first step is ensuring the purity of the raw materials during the initial stage of manufacturing. The second involves the use of high graphitisation temperatures to encourage impurities to diffuse out. Finally, halogen treatments are used to produce removable volatile halides. In particular, Fluorine is useful in bringing the Boron content down to the very low values, which is required in nuclear applications.[13, 18]

Graphitisation causes a loss of weight. This may be attributed to the removal of interlayer chemical species, mainly interstitial carbon. Full graphitisation can achieved by heating the blocks in the absence of air to temperatures in the range 2800 – 3000 °C followed by slow cooling over several days.[13] This thermal shock and slow cooling process from high temperatures to room temperature induces Mrozowski cracking and porosity. The process of graphitisation increases the interlayer spacing, L_c and decreases the distance between atoms, L_a within the hexagon. Moreover, graphitization has other importance such as the ABAB stacking order growth, diffusion and growth of the crystallites, cross-linking bonds elimination, elimination of defects within each graphite layers, and diffusion of atoms to occupy vacancies and removal of defect.[13, 14]

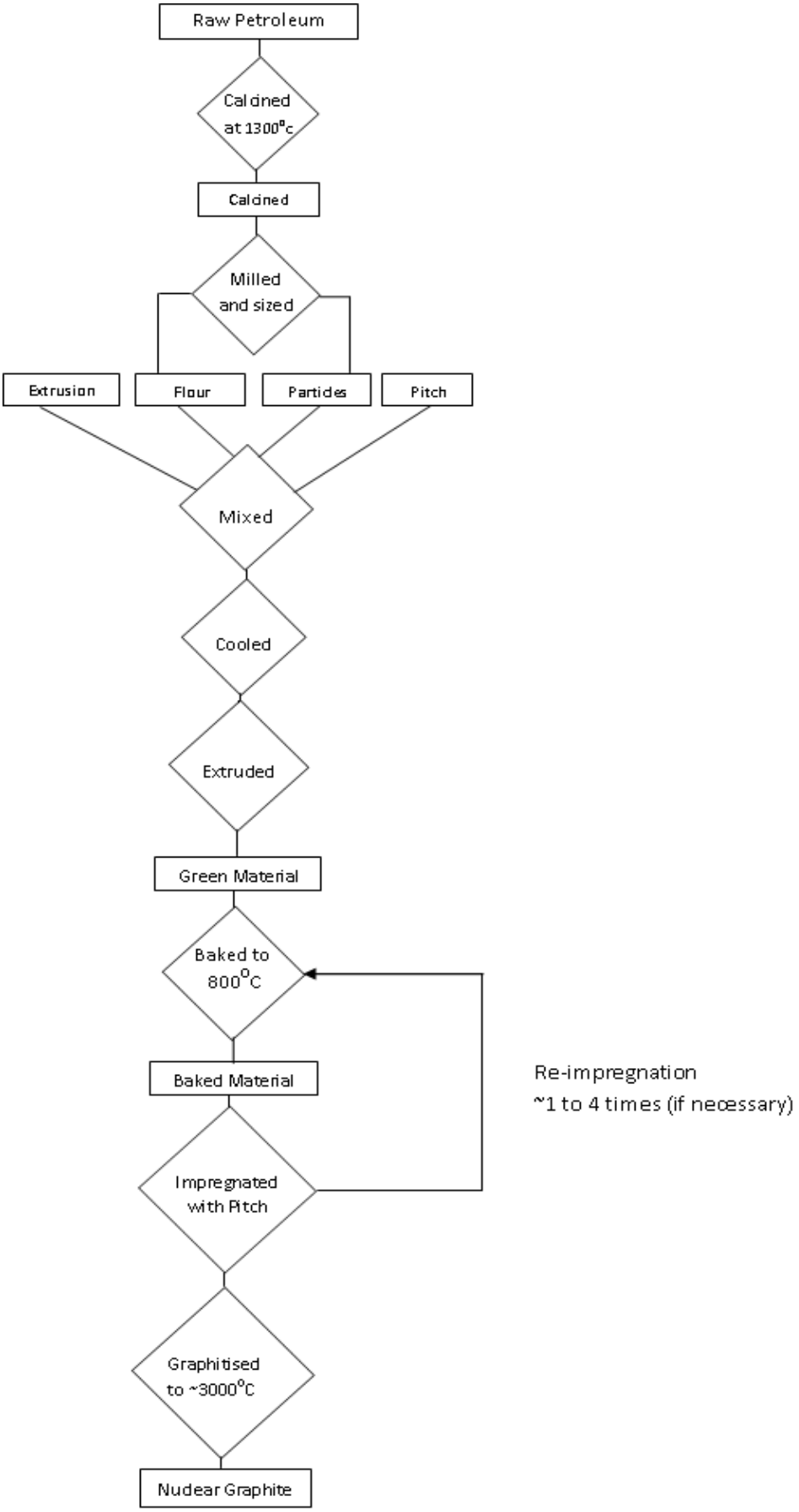

Figure 4: Schematic diagram showing manufacturing processes of nuclear graphite

2.4 OPERATIONAL CONDITIONS

An operational condition for a reactor refers to the safety requirements for operational limits and operating procedures for a reactor. For a reactor to operate safely the requirements made in the final design and any consequent alterations to the design must be taken into account in specifying the limits on operating limitations and the requirements on the equipment and personnel of the reactor facility. These operating limits and operating requirements are developed in the assessment of the design safety. Table 6 describes the operational condition of some of UK reactors [21-26].

Table 6: Operational Conditions of UK Reactors

Reactor	Pressure, (bar) (absolute)	Thermal Power (MWt)	Neutron Dose (n/cm^2. EDND)	Inlet Temperature (°C)	Outlet Temperature (°C)
GLEEP	27	0.003	1.00×10^{14}	240	350
BEPO	No Pressure Variance	6.5	11.00×10^{20}	160	180
PILE 1 & 2	No Pressure Variance	180	0.40×10^{20}	Room temperature	180
WAGR	40	110	1.97×10^{18}	250	325
DRAGON	20	20	1.52×10^{21}	350	750
Magnox	8-27	270-1760	7.00×10^{21}	~160	414
AGR	40	1496 - 1600	2.00×10^{21}	278	640

2.5 RADIOLYTIC OXIDATION

When carbon dioxide reacts with ionising radiation, it will generate an oxidizing species and this process is called Radiolytic oxidation [27]. These reactive oxidising species will be absorbed on a graphite surface and will cause graphite oxidation. The physical and mechanical properties of the graphite will be affected considerably due to this. Radiolytic oxidation is not a problem in reactors where the graphite operates in an inert atmosphere. Gas or air-cooled reactors may, however, exhibit various degrees of radiolytic oxidation, and may experience up to 45% peak weight loss at the end of the reactor life [3]. The gamma energy absorbed by the carbon dioxide within the pores of the graphite determines the rate of radiolytic oxidation of the graphite. Methane injection has been used to reduce the rate of graphite weight loss [3].

2.6 IRRADIATION DAMAGE IN GRAPHITE

The generally accepted model for irradiation damage [12] proposes that during irradiation, the weak bonding between the graphite basal planes and the large interlayer spacing make it relatively easy for neutrons and fast charged particles to displace atoms from the graphite lattice to generate a large number of interstitial atoms or vacant atom sites.[28] The meeting and amalgamation of interstitials causes large interstitial loops, which thus causes swelling of the graphite. Fast neutrons may also knock out carbon atoms from the lattice and form vacancies. The coalescence of these vacancies forms large vacancy loops. Therefore, when graphite crystals are irradiated with fast neutrons it expands in the direction perpendicular to the basal planes of the crystal, while at all temperatures of irradiation, the basal planes shrink.[2, 29, 30].

During neutron irradiation the growth of the c-axis of graphite and contraction of the a-axis occurs.[12, 31] In early low temperature reactors, radiation-damage effects caused problems, including swelling in the Hanford and Brookhaven reactors and accumulation of stored energy in the Windscale, BEPO, and X-10 reactors.[32] Irradiation-induced dimensional change is also an underlying cause of the lifetime limits for higher temperature reactors, characterised by the formation and accumulation of large numbers of point defects which change and distort the surrounding lattice.[33] This can lead to significant bulk dimensional changes and considerably alters the physical properties such as thermal conductivity, Young's modulus, Poisson's ratio, irradiation creep and electrical conductivity.

2.7 DEFECTS IN GRAPHITE

Structural characteristics of ideal three dimensional graphite lattices are subject to defects.[19] The diversity and the stability of various defect structures in graphite are of fundamental importance in explaining the wide range of properties exhibited by graphites. X-ray diffraction and electron microscope are the most widely used techniques for characterising defects. As discussed above, in graphite, the bond strength between the corresponding layers atoms is very weak compared with the bonding between the nearest neighbour carbon atoms within the carbon network. This makes it suitable to distinguish between the different types of defects, whether they cause interlayer disorder or real network bond defects.

2.7.1 Point Defects

There are two types of crystal lattice defects, the vacancy and the interstitial atom. Interstitial and vacancy defects together form Frenkel defect. Figure 5 illustrates a schematic representation of crystallite imperfection in graphite showing vacancy.[14] In electron microscope, diffraction contrast is produced by the phase contrast mechanism, whereas the phase difference is formed by atomic displacement. The lattice strains produced by defects make them visible in the electron microscope. It is the strain field of the defect, and not the defect itself, that is observed.[34, 35] All dislocation patterns observed so far by electron

microscopy were lying in the basal plane. Optical observations, however, suggest the existence of dislocations intersecting the c-planes.[36]

The lattice strains caused by an interstitial appear to be quite large. Henson and Reynolds estimated that a single interstitial occupies between two and four atomic volumes, [37] due to which the neighbouring basal planes are pushed apart. They also demonstrated that a single vacancy causes contraction of basal planes due to a change in the energy of the π– bond electrons and the Poisson's ratio effect as a result of a slight expansion in the *c* direction, as suggested by Kelly. [34] Strains which are produce by a vacancy are, therefore, relatively small and the distortion of the lattice resulting from a single interstitial, even if it is large, is not large enough to be visible in the electron microscope.[18]

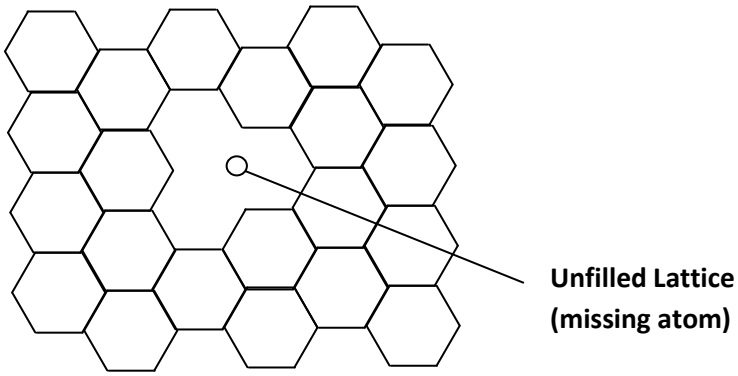

Figure 5: Schematic of crystallite imperfection in graphite showing unfilled lattice or vacancy

In each graphitic material, the size, shape, and degree of imperfection of the basic crystallite, the general orientation of these crystallites, as well as the bulk characteristics such as porosity and amount of impurities, may vary considerably from one material to another. As a result, the properties of these various materials may show considerable differences.

The displacement at any point due to dislocation or defects in the crystal is proportional to the *Burger vector* ***b***. This quantity is defined by constructing a circuit in the perfect material around the dislocation core and measuring the closure failure (Figure 6).[35]

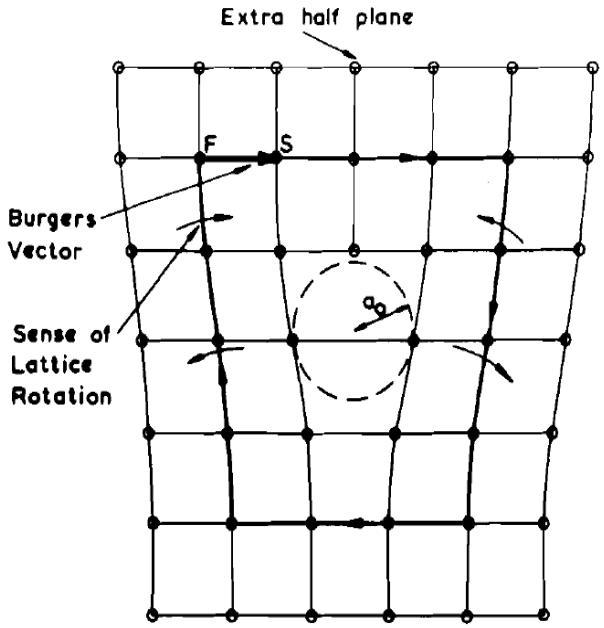

Figure 6: Simple edge dislocation in a cubic material illustrating FS/RH Burger vector convention.

From Figure 6 it can be seen that the rotation of lattice planes are both in opposite direction and on opposite sides of the dislocation.[35]

2.7.2 Dislocation Loops

Migration energies of point defects indicate that they should be quite mobile at low temperatures. Interstitials form a well ordered lattice plane which is inserted as a *c* plane into the normal …ABABA… stacking sequence. The accumulation of vacancies produce a large hole in the basal plane that neighbouring plane collapse into. Dislocation loops are large dislocation clusters. When the radius *r* of these loops is very large, the magnitude of the strains produced by interstitial and vacancy types are equal.[35, 38]

Figure 7 shows the structures of dislocation loops in graphite.[35] The interstitial loop contains the following stacking sequence

… ABACBAB…

with three second nearest neighbour misfits and a stacking fault energy of about **3γ**. This energy can reduce to **γ** by nucleation of partial dislocation which sweep across the loop to produce

…ABABACA…

This in turn increases the line energy of dislocation. Similarly, the very high stacking fault energy **Γ** of a collapsed vacancy loop due to “A over A” stacking may be reduced to **γ** by an identical process.[35]

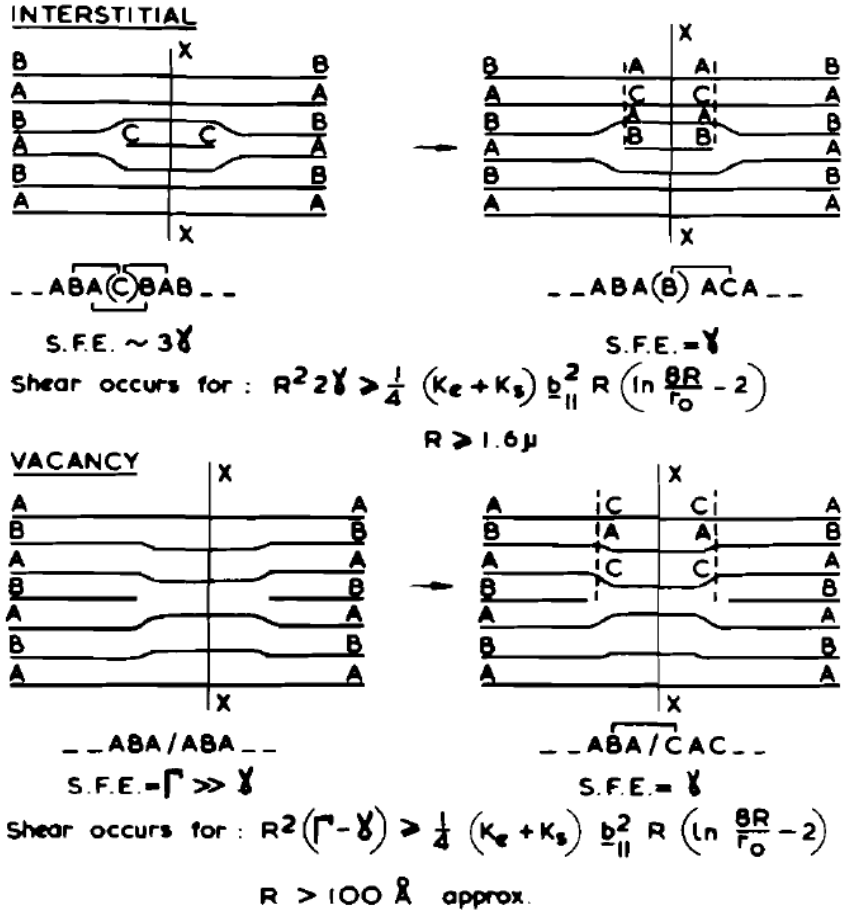

Figure 7: The criteria for loop shear for interstitial and vacancy loops

The conversion of an unsheared loop to a sheared loop was recently shown by Thrower.[35] These may be either sheared, with a basal plane component in the Burgers vector, or unsheared when the Burgers vector lies along the c-axis. They have been observed in both quenched and annealed [35] and high-dose neutron irradiated [39] materials, and may be of interstitial or vacancy type. Such dislocations may be also be found in rather imperfect natural crystals.[40]

2.7.3 Vacancy Lines

The study of lattice parameters and dimensional changes suggested [34, 38] that groups of vacancies collapse in lines in the basal planes. Figure 8 shows the possible structures of these lines [34] and they are well separated edge dislocation dipoles along the *c* axis of length c/2 and Burgers vector $a/3\langle 11\bar{2}0\rangle$. The collapse of these edge dislocation was investigated by Kelly [34], who suggested that in order to not accept diffusing interstitial atoms, a divacancy may collapse, and consequently very small vacancy line may be created.

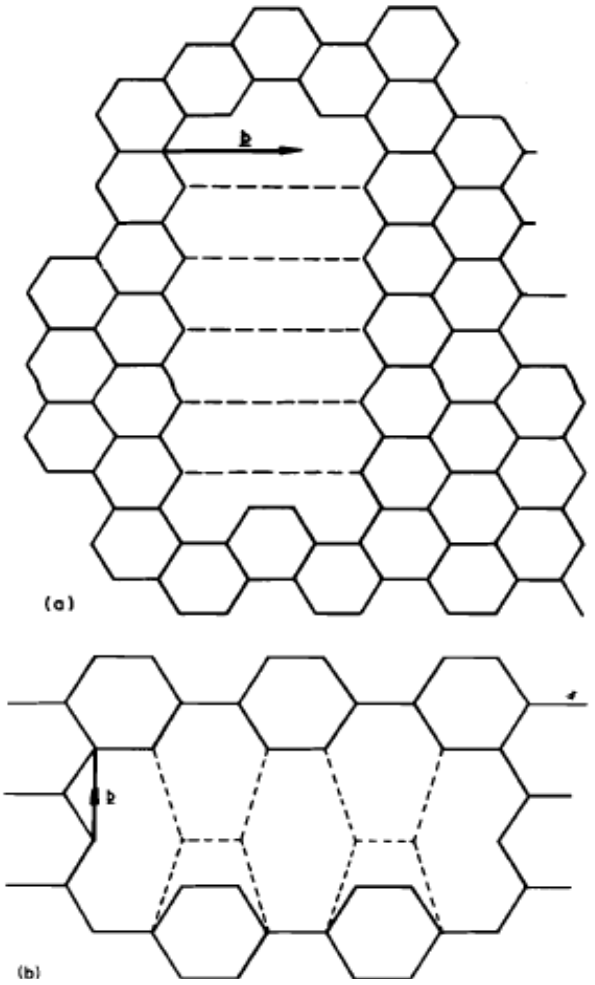

Figure 8: Possible configurations of vacancy lines along (a) <11$\bar{2}$0> and (b) <10$\bar{1}$0>

The strains at the ends of such a line would not be very large and would be confined mainly to the basal plane. If the line is divided into two partial lines in an similar way to a dislocation line, then the strain may be expected to produce some weak diffraction contrast in the same way as a monolayer loop.[35]

2.8 RADIOACTIVE GRAPHITE WASTE

2.8.1 Location and types of waste

The list of graphite-moderated reactors and the quantity of the graphite involve is shown in Table 7.[26] In addition, basic technical data of the reactors reported and the current status of the reactors is also reported.

Table 7: LIST OF UK GRAPHITE MODERATED REACTORS

Location	Reactor	Type	Graphite in reactor (Tonnes)	Graphite total (Tonnes)	Commissioned	Expected Shutdown Date	Shutdown Date	Decommissioning Stage
Dungeness	B1	AGR	850	ND	1983	2018	-	-
Dungeness	B2	AGR	850	ND	1985	2018	-	-
Hartlepool	1	AGR	1360	ND	1983	2014	-	-
Hartlepool	2	AGR	1360	ND	1984	2014	-	-
Heysham	Unit I-1	AGR	1520	ND	1983	2014	-	-
Heysham	Unit I-2	AGR	1520	ND	1984	2014	-	-
Heysham	Unit II-1	AGR	1520	ND	1988	2023	-	-
Heysham	Unit II-2	AGR	1520	ND	1988	2023	-	-
Hunterston	B1	AGR	970	ND	1976	2016	-	-
Hunterston	B2	AGR	970	ND	1977	2016	-	-
Hinkley Point	B1	AGR	970	ND	1976	2016	-	-

Location	Reactor	Type	Graphite in reactor (Tonnes)	Graphite total (Tonnes)	Commissioned	Expected Shutdown Date	Shutdown Date	Decommissioning Stage
Hinkley Point	B2	AGR	970	ND	1976	2016	-	-
Torness	1	AGR	1520	ND	1988	2024	-	-
Torness	2	AGR	1520	ND	1989	2024	-	-
Bradwell	Unit 1	Magnox	1810	1931	1962	-	2002	Decommissioning
Bradwell	Unit 2	Magnox	1810	1931	1962	-	2002	Decommissioning
Calder Hall	Unit 1	Magnox	1164	1630	1956	-	2004	Defueling
Calder Hall	Unit 2	Magnox	1164	1630	1957	-	2004	Defueling
Calder Hall	Unit 3	Magnox	1164	1630	1958	-	2004	Defueling
Calder Hall	Unit 4	Magnox	1164	1630	1959	-	2004	Defueling
Chapelcross	Unit 1	Magnox	1164	1630	1959	-	2004	Defueling and Decommissioning
Chapelcross	Unit 2	Magnox	1164	1630	1959	-	2004	Defueling and Decommissioning

Location	Reactor	Type	Graphite in reactor (Tonnes)	Graphite total (Tonnes)	Commissioned	Expected Shutdown Date	Shutdown Date	Decommissioning Stage
Chapelcross	Unit 3	Magnox	1164	1630	1959	-	2004	Defueling and Decommissioning
Chapelcross	Unit 4	Magnox	1164	1630	1960	-	2004	Defueling and Decommissioning
Dungeness	A1	Magnox	2150	2237	1965	-	2006	Defueling
Dungeness	A2	Magnox	2150	2237	1965	-	2006	Defueling
Hinkley Point	A1	Magnox	2210	2457	1965	-	2000	Decommissioning
Hinkley Point	A2	Magnox	2210	2457	1965	-	2000	Decommissioning
Oldbury	Unit 1	Magnox	2061	2090	1967	-	2012	Defueling
Oldbury	Unit 2	Magnox	2061	2090	1968	-	2012	Defueling
Sizewell	A1	Magnox	2237	2240	1966	-	2006	Defueling
Sizewell	A2	Magnox	2237	2240	1966	-	2006	Defueling
Wylfa	A1	Magnox	3470	3740	1971	2014	-	-

Location	Reactor	Type	Graphite in reactor (Tonnes)	Graphite total (Tonnes)	Commissioned	Expected Shutdown Date	Shutdown Date	Decommissioning Stage
Trawsfynydd	Unit 1	Magnox	1900	1980	1965	-	1991	Decommissioning
Wylfa	A2	Magnox	3470	3740	1971	2014	-	-
Berkeley	Unit 1	Magnox	1938	1650	1962	-	1989	Decommissioning
Berkeley	Unit 2	Magnox	1938	1650	1962	-	1988	Decommissioning
Hunterston	A1	Magnox	1780	2150	1964	-	1990	Decommissioning
Hunterston	A2	Magnox	1780	2150	1964	-	1989	Decommissioning
Trawsfynydd	Unit 2	Magnox	1900	1980	1965	-	1991	Decommissioning
Windscale	WAGR	AGR	285	285	1963	-	1981	Decommissioning
Winfrith	Dragon	HTR	40	40	1964	-	1976	Decommissioning
Windscale	Pile 1	Air cooled	<2000	<2000	1950	-	1957	Defueling and Decommissioning
Windscale	Pile 2	Air cooled	2000	2000	1951	-	1958	Defueling and Decommissioning

Harwell	BEPO	Air cooled	766	766	1962	-	1968	Decommissioning
Harwell	Gleep	Air cooled	505	505	1947	-	1990	Decommissioning

Key:-

Graphite in reactor = moderator + shielding blocks

Graphite total = graphite in reactor + graphite sleeves + graphite from maintenance/refurbishment

ND - data non-available or classified

Defueling - 1st stage of decommissioning,

Decommissioning – dismantling of peripheral structures

2.8.2 Classification

On the basis of radioactive inventory radioactive wastes are classified in three categories, namely low level, intermediate level and high level waste. The waste classification system is based on disposal options and is shown in Table 8.[41]

Table 8: Classification of Radiological Waste

Waste Category	Activity concentration, kBq/kg			
	Alpha bearing waste		Beta-gamma bearing waste	
	Group 1	Group 2	Group 3	Group 4
Low level	$10^{-1} – 10^{1}$	$10^{0} – 10^{2}$	$10^{1} – 10^{3}$	$10^{3} – 10^{5}$
Intermediate level	$10^{1} – 10^{5}$	$10^{2} – 10^{6}$	$10^{3} – 10^{7}$	$10^{5} – 10^{8}$
High level	$>10^{5}$	$>10^{6}$	$>10^{7}$	$>10^{8}$

2.8.3 Leaching

This technique employs the process of decontamination of graphite waste with the use of chemical treatments. The main aim is to remove the surface layer of the graphite which may contain the majority of the bulk activity by dissolution. The waste removed will be collected and the liquid will be separated from the solid, then the radioactive waste will be discarded in solid form. Several chemical decontamination treatments have been identified by CARBOWASTE [42, 43] including, acid treatment, liquid decontamination agents and aggressive leaching.

In the United States, the most widely used chemical treatment is Freon-12 or chlorine. Several other gases, including sulphur hexafluoride, carbon tetrafluoride, and carbon tetrachloride have also been tested. Here, the halides will penetrate into both bulk graphite and graphite crystals and then react with the radionuclide impurities and will remove them as volatile halide salts. This technique has long been known and has been used to produce samples for chemical analysis.[7]

2.9 DECOMMISSIONING SOLUTIONS

One of the main issues associated with the disposal of irradiated graphite is the large volume of relatively low active waste to be dealt with.[44, 45] The Nuclear Decommissioning Authority (NDA) reports that decommissioning of the UK's Magnox and Advanced Gas Cooled reactors, research reactors and plutonium production reactors will produce approximately 100,000 tonnes of graphite waste.[46] The major challenge for the nuclear industry is finding the best solution for this graphite

waste. In order to reduce the volume, and evaluate the possibility of reducing costs, it is important to consider alternative methods.

Due to the diverse range of graphite radioactive waste with a wide range of potential radioactive content and volume, it will undoubtedly require complex planning and a number of different treatment solutions. Therefore, dismantling of nuclear reactors and the management of radioactive graphite waste is an important concern in the UK.[47] The current UK plan for graphite disposal is that this material will be packaged as Intermediate Level Waste (ILW) for deep geological repository disposal. It has not yet been shown that the current baseline represents the optimum solution in terms of safety, cost and protection of the environment. To make effective choices to dispose of this large volume of irradiated graphite waste, it is necessary to understand fully its microstructural and radioisotopic character and the consequent effectiveness of the various proposed decommissioning solutions. These include various methods of encapsulation, and alternative preparative treatments for radiological reduction to LLW including decontamination, disposal and reprocessing.[8, 48, 49]

2.9.1 Incineration

Thermal treatment of contaminated structural graphite from the high temperature reactor core and thermal columns of the research reactors was investigated as a possible decontamination process.[1] Reprocessing of the graphite, based on graphite gasification, offers the opportunity to separate the radionuclides from the main graphite which could then be reused or disposed conventionally. The experiments were performed in an argon flow and steam in the temperature range of 870 – 1200°C. Comparison of the release rate ratios of the volatilised radionuclides ^{14}C and ^{3}H, with the release of ^{12}C, showed that under all experimental conditions, tritium and ^{14}C were released faster than the graphite sample was oxidised (about 5 % of ^{12}C). In general, this separation of carbon isotopes is only possible because ^{14}C may be mainly located on the surface of the graphite and its concentration profile decreases with the depth inside the graphite grains.

FZJ Jülich [43] studied the removal of tritium and ^{14}C from graphite during heating. This study concluded that the carbon fraction, enriched in ^{14}C and tritium, can be released by heating. The graphite was subjected to a temperature of about 1100 °C in different Ar / O_2 atmospheres. The amount of ^{14}C and tritium enriched is directly proportional to the temperature profile and the gas composition; however this was difficult to remove more than about 60 % of the ^{14}C and 80 % of the tritium within in the first few per cent of carbon lost. Pilot investigations, which were performed on blocks removed from the UK GLEEP reactor, have supported this observation.[43]

UKAEA has carried out a number of investigations on the incineration of reactor graphite. [50] Incineration resolves the problem associated with stored Wigner energy completely. It also greatly cut down the volume of graphite waste, i.e. for example 1400 m^3 of graphite could be reduced to as little as 35 m^3 of cemented ash product and filters. The various possible methods of incineration are discussed below.[1]

2.9.1.1 Conventional Incineration under Air

This method involves controlled incineration of the graphite. First of all, the graphite is crushed into pieces of typical dimension 2.5 cm. The graphite is then placed in a blast furnace, where it is subjected to a temperature about 1000 ^{o}C. This reduces CO production while allowing reasonably rapid boundary layer diffusion controlled combustion. The disadvantages of this process are the milling effort required, the production of active dust and the difficulties of the incinerator design.[1]

2.9.1.2 Fluidised Bed Incineration

This method involves combustion of the graphite in a fluidised bed.[1] For this process to provide enough surface area for reaction with oxygen at incineration temperatures, the graphite would be ground to a powder. The grinding would make a dust that would have to be controlled. This process could also lead to explosion if considerable stored Wigner energy and air were present. The disadvantages of this process include: the grinding prior to combustion produces waste itself, irradiated graphite can be very hard, making grinding more difficult and other materials can combine with the ash and increases the ash volume. This may cause inefficiency during combustion.[1]

2.9.1.3 Power Laser Driven Incineration

An alternative method of incineration is by power laser. Advantages of this method are that no prior milling or crushing of the graphite is required before incineration, thus the bricks can be loaded straight from the reactor core. The laser beam heats the graphite surface to about 1500 ^{o}C and rapid burning occur when O_2 is available. The laser can be outside the furnace area so it does not want handling within an active area. The process is entirely controlled by the presence of the laser beam. Any Winger energy in the block is only a few percent of the total energy release and so does not contribute any problem.[1]

2.9.2 Recycling

Within the context of any solution, reducing volume and cost of recycling and reuse of graphite waste is inevitable. Without recycling, the disposition of graphite waste will increase significantly and this may bring much more difficult and expensive problems in the future. The easiest solution is to use the decontaminated graphite to manufacture new graphite. The main disadvantage of this solution is, even if the graphite is cleaned with the decontamination treatments mentioned above prior to recycling, it is not possible to get a complete and clean bulk of the carbon from ^{14}C. For this reason, most likely all products made from recycled graphite will be restricted to controlled uses in the nuclear industry.[3]

Another possible technique is to develop new graphite or other products from the gaseous products of the graphite waste after gasifying it. The gasification process permits efficient decontamination for radionuclides other than ^{14}C. There are many potential uses for recycled graphite waste other than new reactor graphite. For example, it could be used to manufacture graphite electrodes for the immobilisation by high temperature processing of certain nuclear wastes, or activated charcoal filters.[3]

2.9.3 Encapsulation

Geological disposal of nuclear wastes requires that waste packages are designed to prevent the leaching of trapped radionuclides into the local groundwater over an extended time period.[51] The invention of appropriate packages for direct disposal of radioactive graphite wastes after their conditioning, surface decontamination and coating is dependent on the overall requirements of the disposal system. This may last for many thousands of years and is expected that during this timeframe, groundwater will penetrate the repository and interact with the wastes.[4, 52] Table 9 shows the various encapsulation materials which are used for immobilising graphite wastes in the UK [4].

Waste encapsulation using cementitious materials is widely used within the nuclear industry worldwide. Nuclear waste encapsulated with cement is shown in Figure 9. For many materials it is a suitable method of encapsulation for storage and disposal. A number of basic criteria will be applicable for each disposal facility, regardless of the waste type. These include the size of package and weight, surface dose rate of package, heat output and surface contamination and package radioactivity release under normal and accident conditions of handling, transport, and disposal. In addition, for graphite wastes, the guidelines to develop and test states that a wasteform must be structurally stable and must be able to maintain physical dimension and form under expected disposal conditions. These include the weight of overload and equipment, presence of moisture and microbial activity, and internal factors such as radiation effects and chemical changes.

Accordingly, an appropriate wasteform should remain stable if it is: solid and stable after disposal, has no free standing or corrosive liquid, resists degradation caused by radiation effects, resists biodegradation; remains stable under compressive loads in the disposal environment, remains stable if exposed to moisture or water after disposal and is compatible with the solidification medium used or container in which it is placed.[53] There are a number of specific properties of the material which need to be well thought-out in the invention and demonstration of packaging materials.

In the UK intermediate level waste (ILW) disposal package is a concrete disposal box into which a stillage containing four 500 litre drums, void space within the box is backfilled with cementitious grout. The disposal boxes form the basic disposal unit and fit exactly into the disposal tunnels (i.e. the tunnel liner is sized to ensure a good fit). The primary barrier to release

in this system is provided by the host rock which is of sufficiently low permeability that solute transport within it is primarily by diffusion. The waste form and the chemical barrier provided by the backfill around the waste drums provide additional containment and retardation.[52]

Figure 9: Nuclear waste encapsulated with cement

Table 9 : Initial Evaluation by BNFL of Processing Options for Graphite in the UK

ENCAPSULANT	PROCESS		PRODUCT	
	Advantages	**Disadvantages**	**Advantages**	**Disadvantages**
Cement	• Simple process • Proven technology • Low temperature process • Removes residual water	• Low initial strength • Potential for presetting in pipework • Hydrophobic properties of graphite	• High strength product • High radiation stability • Good self shielding • High pH matrix • Non-combustible product	• Relatively permeable • Increase the volume of waste to be stored • Leaching rate may not be acceptable
Modified cement	• Simple process • Proven technology • Low temperature process • Removes residual water	• Potential fire hazard • Increasingly expensive as polymer content increases • Organic solvents required for plant wash down	• Improved strain resistance • Reduced permeability • Good self shielding • High pH matrix	• Reduced radiation stability • Organic components may enhance equilibrium leaching
Polymer	• Relatively simple process • Proven technology • Low temperature process	• Potential fire hazard • Expensive • Organic solvents required for plant wash down • Less tolerant to residual water	• High Strain resistance • Low permeability • Self-supporting matrix	• Potential fire hazard • Reduced radiation stability • Organic components or filler may enhance equilibrium leaching • Life of polymer may be much less than ^{14}C
Resin sand	• Potentially simple process • Curing and dewatering • combined	• May prove difficult to infill wet waste • Requires high temperature for curing	• High strength produce • Self-supporting matrix • Good self shielding	• Potential fire hazard • High porosity product • Probable poor leaching characteristics • Reduced radiation stability

Table 9 (cont'd.): Initial Evaluation by BNFL of Processing Options for Graphite in the UK

ENCAPSULANT	PROCESS		PRODUCT	
	Advantages	**Disadvantages**	**Advantages**	**Disadvantages**
Bitumen	• Incorporates dewatering	• Potential fire hazard • High temperature process • May result in poor grouting	• Good leaching resistance	• Potential fire hazard • Low radiation stability • Non-self supporting • Low self-shielding • Reference production
Glass	• None	• High temperature process • Very expensive • Highly complex process • Complex off-gas treatment • Probably require pre-drying	• Good self shielding • Non-combustible • High radiation stability	• Probably fractured due to thermal incompatibility • Low thermal stability • Fracturing may result in low leach resistance
Low melting point metals	• Probably use proven casting technology	• High temperature process • Very expensive • Probably toxic • Probably require pre-drying	• Good self shielding • Non-combustible • Self supporting matrix • Good leaching properties • High radiation stability	• Probably toxic following disposal • Melt under fire conditions • High density may make transport difficult
Ceramic	• None	• Requires high temperature and pressure • Expensive • Highly complex process	•Good self-shielding • Non-combustible • Self supporting matrix • High radiation stability	• Probably sustain thermal stress damage on heating • Uncertain performance on drop testing

3. MATERIALS AND METHODS

3.1 MATERIALS

3.1.1 Virgin Sample Providence

For the investigations nuclear grade graphites, namely PGA form UK Magnox reactors, Gilsocarbon from AGRs (Advanced Gas Cooled Reactors) and NBG-10 and NBG-18 from future HTRs (High Temperature Reactors) were chosen. The manufacturing processes of these graphite grades are distinct, which results different microstructures, including differences in crystal orientations, in the final product.

The physical properties of graphite are dependent on the type and size of coke used and the manufacturing route employed. PGA was produced from a petroleum coke, which is a by-product of oil refining industry.[18, 54] It has needle-shaped coke particles and the PGA blocks were produced by an extrusion process, which tended to align the needle coke particles thus the crystallographic basal or layer planes tend to lie parallel to extrusion axis, giving rise to the anisotropic properties of PGA graphite.[54]

Gilsocarbon is produced from the naturally occurring asphalt pitch-coke which is excavated from Gilsonite veins.[55] The coke particles have an “onion skin” structure and the blocks were produced by a moulding process. NBG-10 is a semi-isotropic nuclear grade graphite developed by SGL and is manufactured by a process of extrusion and are produced from isotropic coke and pitch binder.[56] NBG-18 graphite is developed by a process of vibrating moulding, using the same constituents of NBG-10 graphite.

PGA and Gilsocarbon graphites are produced by British Acheson Electrodes Ltd (BAEL). NBG-10 and NBG-18 graphites are produced by SGL Group. All samples for the analysis were cut or trepanned out from a block of graphites which were supplied by the manufacturers to the research group.

3.1.2 Irradiated Graphite Providence

Irradiated graphite samples from the Oldbury Magnox Reactor 1 core were used throughout this investigation. A related pair of matching samples, in terms of irradiation history and properties was immersed in solution, representing typical repository conditions as described in Section 3.4.1. The composition of the solution simulating groundwater is shown in Table 12. The data collected was used to relate the leachability factor to the pH of the solution and the graphite irradiation history.

There are twenty six Magnox reactors which were commissioned around the world between 1956 and 1972 at the sites of eleven power stations.[57] All Magnox reactors are cooled by CO_2 gas and moderated by graphite.[57, 58] The pressure vessels of the reactors were constructed from steel except the last four reactors which feature pre-stressed concrete vessels. In general these reactors have provided reliable electrical power generation over their operating lives.[57] The core of each reactor is an assembly of machined graphite blocks and the core graphite bricks comprised of fuel channels, control devices, samples and coolant flow routes. Small gaps were left between the moderator blocks during assembling procedure to allow for the expansion of the graphite blocks. The cores are attached together with keys to produce a strong structure. [58] To contain the effects of thermal transients and dimensional changes induced by irradiation in graphite bricks the keys are designed to tolerate comparative movement, radially and vertically, between neighboring columns. Thermocouples are also inserted in each core to measure temperatures of the graphite material and channel outlet gas. The reactor core has typical inlet gas temperatures between 160 – 225 °C whilst outlet gas temperatures of between 345 – 370 °C.

The basic design of Oldbury reactor core has a height of 9.75 m and a radius of 6.8 to 7.2m, which depends on the thickness of the reflector. The active core is 8.6 m high and has a radius of 6.4 m.[57, 58] The individual bricks are 0.813 m in height and have a width of either 0.171 m or 0.221 m, resulting in about 10 bricks per channel core. To maintain the structure in position and to maintain the circumferential shape, support plates and a steel restraint are used.

Samples from fuel Channel Q09B5 West brick 4, 6 and 8 (L)ower and (U)pper (Upper refers to the top end of the brick and Lower refers to the bottom part of the brick) trepanning positions were chosen. The sample identification (string) Q09B5 describes the location and position of the sample inside the core channel.[57] The first three characters, Q09 indicates the standpipe position in the reactor and the channel position related to the standpipe indicated by the last two characters, B5. The letter ‘Q’ indicates the channel is located at the North of the core. In the ID the second and third numbers, 09 indicate the channel is positioned at the west. The second character is less than three then it reveals the channel is in Reactor 1. The fourth character, B specifies one of the eight sections within the standpipe. The last digit in the sample identification characters, ‘5’ shows the position of the channel within this section.

During the reactor lifetime many samples have been trepanned from the core using a milling cutter. Six of these samples were supplied from this project. Approximately 9 mm graphite is removed from each sample to remove any fission products associated with the graphite wall. The remaining part of the sample was cut into two discs; 12 mm in diameter and 6 mm in length. A schematic of the sampling is shown in Figure 10. Slice 2, i.e. centre position of ~9 mm [59] from the fuel channel wall were used for the leaching campaign, taken from brick 4 samples 1/2(L) and 2/2(U), brick 6 samples 5/2(L) and 6/2(U) and brick 8 samples 9/2(L) and 10/2(U). The nomenclature here for example 5/2(L) refers to the sample number, in this case 5 and the slice number in this case 2 which were taken at the upper lower (L) position of brick 6. During the

period of reactor operation, the samples received a fast neutron dose of between 5.6 - 6.8 dpa and they gained radiolytic weight losses of between 25% and 38%. Sample details are summarised in Table 10.

Table 10: Temperatures and Fast Neutron Dose for Oldbury Reactor 1 (2009) Trepanned Samples from Flattened Region Channels [60]

Sample ID	Brick	Trepanned Sample Height (m)	Temperature (°C)	DIDO Equivalent Dose (10^{20} n.cm^{-2})	Displacement per atom* (dpa)	%wt loss*
1/2	4L	2.66	294	45.56	6.0	33
2/2	4U	3.01	302	48.15	6.3	38
5/2	6L	4.26	329	51.49	6.8	33
6/2	6U	4.7	338	50.95	6.7	33
9/2	8L	5.86	356	45.55	6.0	25
10/2	8U	6.22	361	42.86	5.6	27

* Calculated by the author

The amount damage to a graphite core depends on four main reactor parameters. These are irradiation temperature, flux spectrum, flux intensity and irradiation time.[61] The temperatures and dose distribution as a function of trepanned samples height for the flattened region of channels in Oldbury Reactor 1 are shown in Figure 11. The distribution of the temperature is approximately linear over the length of the corresponding channels and varies from 294 °C at the bottom of brick 4 to 361 °C at the top of brick 8. Similar variation were also observed by Bridge, H, et al. [62] for a gas cooled reactor. In which the coolant flow required to prevent the temperature of the graphite moderator, the channel brick and the reflector blocks the reactor from exceeding its critical temperature at full power operating conditions. The temperature effect is a major factor in the control of the fission process and heat production of the reactor.[62] The thermal neutron dose distribution along the channel from brick 4 to brick 8 was found to be parabolic. This dose distribution is analogues with the result mentioned by Dent K. H., et al. and Bridge, H, et al. [62]

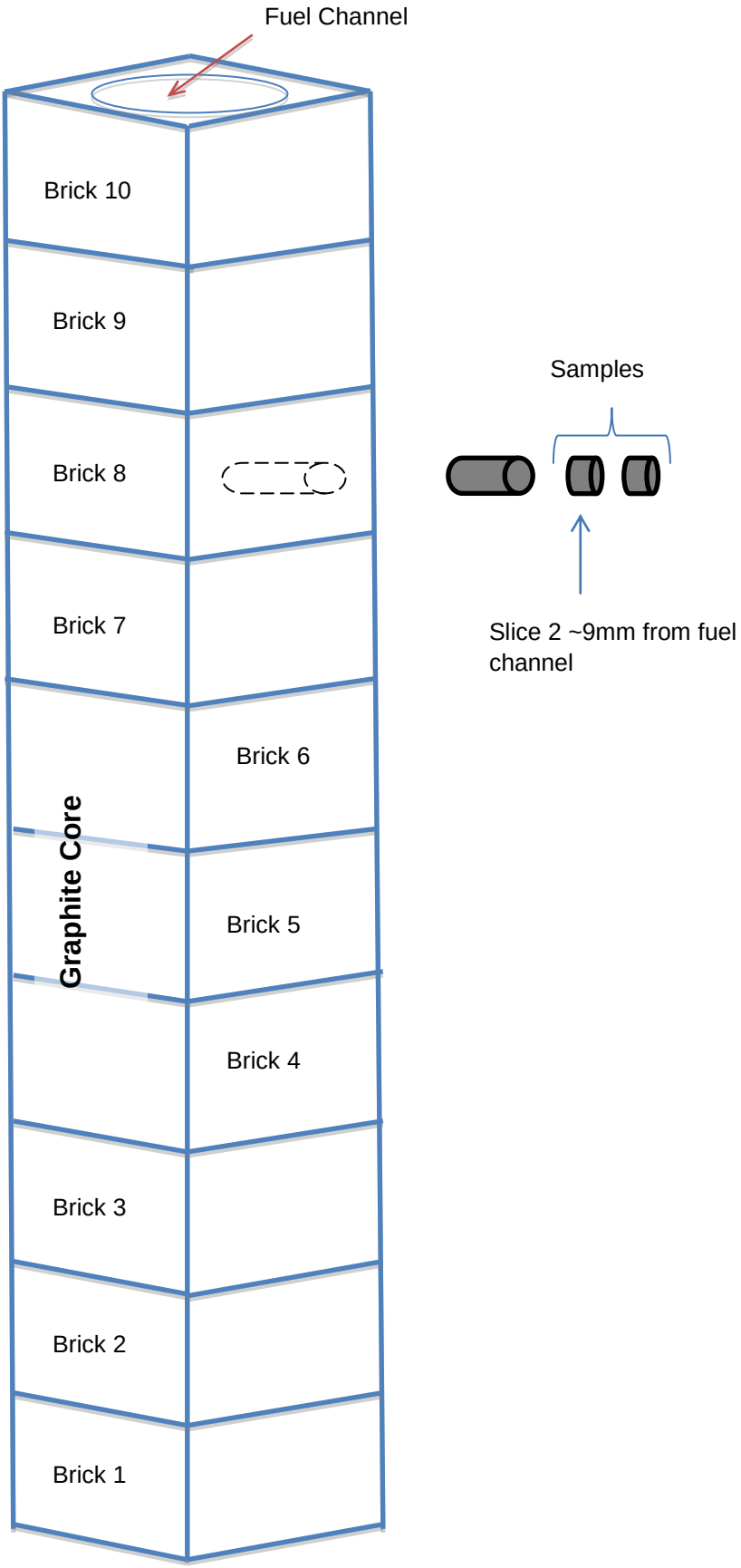

Figure 10: Scheme of sampling from graphite core brick (not to scale)

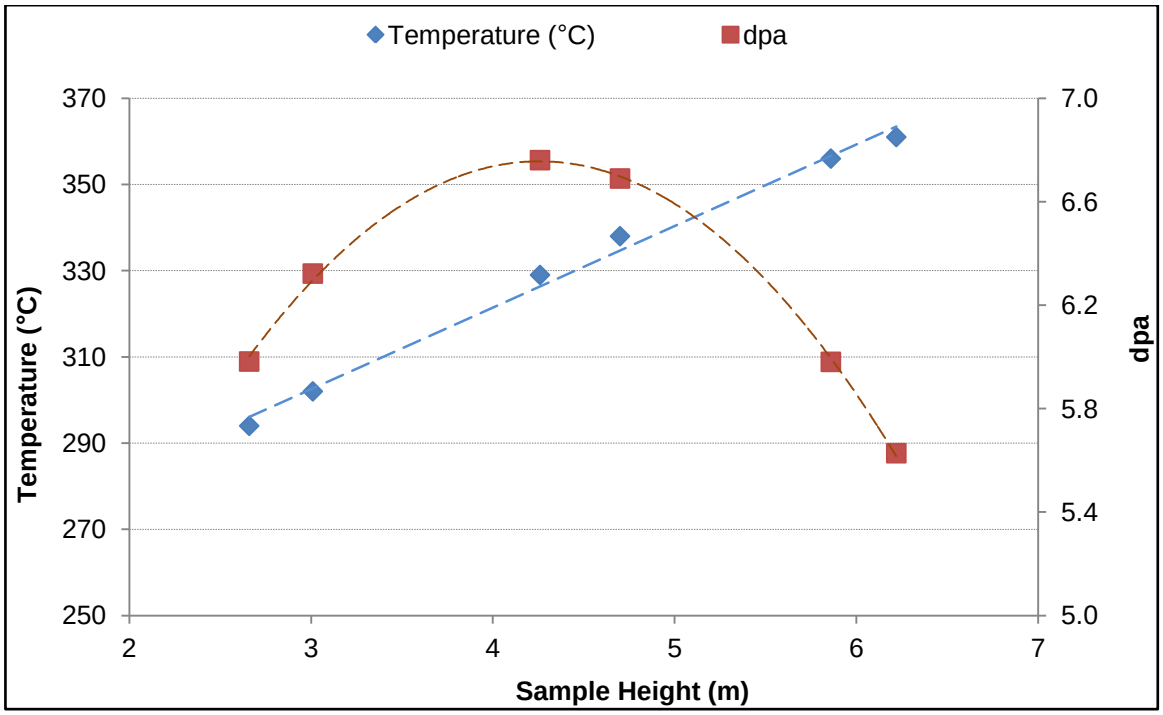

Figure 11: Temperatures and Doses as a function of Trepanned Samples height for Oldbury Reactor 1 from Flattened Region Channels

The magnitude of temperature range along the graphite channel wall is dependent on the shape of the heat transfer surface, entrance length and the length of the core. At the bottom of the core where the heat exchange rate of the coolant and the channels are high resulting lower temperature, however, around the top of the core the heat transfer between the different passages in the cluster is relatively poor and the temperature is high. The temperature difference also increases with the increasing coolant variation. The weight loss of the graphite is higher at the bottom of the core than at the top as it can be seen from Figure 12. This is due to the radiolytic oxidation of the graphite in the carbon dioxide coolant which is a strong function of gamma irradiation and gas pressure with a smaller dependence on temperature. Gamma dose tends to follow a similar profile in the core to the fast neutron dose. Radiolytic weight loss leads to significant degradation of physical, chemical and mechanical properties of the graphite.[3]

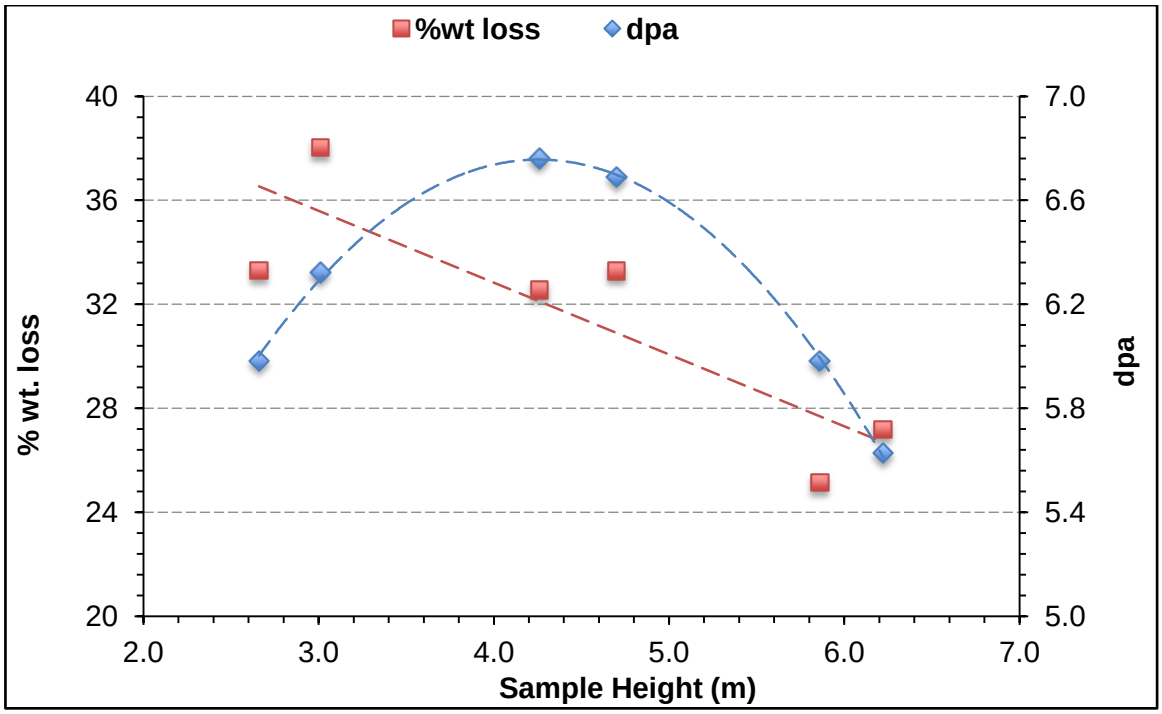

Figure 12: Weight Loss and Dose as a function of Sample Height of the Samples of Oldbury Reactor 1 graphite from Flattened Region Channels

3.2 MICROSTRUCTURAL METHODS

3.2.1 Sample preparation

PGA form UK Magnox reactors and NBG-10 from future HTR reactors were chosen for investigation. Unirradiated PGA graphite and irradiated and unirradiated NBG-10 graphite were characterised. The unirradiated specimens were about 10mm x10mm x 10mm in size. For Scanning Electron Microscopy (SEM) and Transmission Electron Microscopy (TEM) observations the sample graphites were polished. To produce a highly polished scratch-free surface the samples were ground with a selection of Silicon Carbide manually and then, polished with diamond pastes on polishing cloth. Finally, the samples were washed with water and ethanol to remove loose materials and were dried with an air blower. For TEM analysis, further grinding and polishing was done as it is described in section 3.3.3.

3.3 ANALYTICAL INSTRUMENTATION

To investigate the microstructure and the types and distribution of microporosity and impurities in graphite different high resolution microscopes have been employed.

3.3.1 Polarised Light Optical Microscopy

To understand the distribution of the different constituents, i.e., binder, filler and the coke particles and the types and distribution of porosity within the microstructure of virgin graphite, polarised optical microscopy was employed. During the observation of the graphite samples, the polarising filters were placed at 90° angles to each other.

Normal light from the sun or microscope lamp vibrates in all directions perpendicular to the axis in which the light travels. If this light is passed through a polariser, only light wave oscillating in one plane is transmitted, this light is called plane polarised. If this light is then passed through a second piece of polariser, which has been orientated so that the plane of polarisation is parallel to that of the first polariser, then the light will be transmitted. However, if the second polariser is then placed 90° about the axis of light travel, then no light is transmitted. In this situation the planes are called cross polarised.[63]

Figure 13 illustrates a schematic diagram of polarised light microscopy. The specimen is illuminated with plane polarised light. When this light is reflected form the surface, it undergoes a phase change and becomes elliptically polarised. The wavevector has a component at right angle to the plane of polarisation of the incident light. With a second polariser placed between the objective lens and the eyepiece, and the polarisation plane at 90° to the first polariser, the wavevector component, perpendicular to the plane of polarisation of the incident light, can be insulated by a transmitted intensity at the eyepiece. This phase change at the reflecting surface occurs if it has either an anisotropic reflection coefficient or multiple reflections are produced from an isotropic surface.[63]

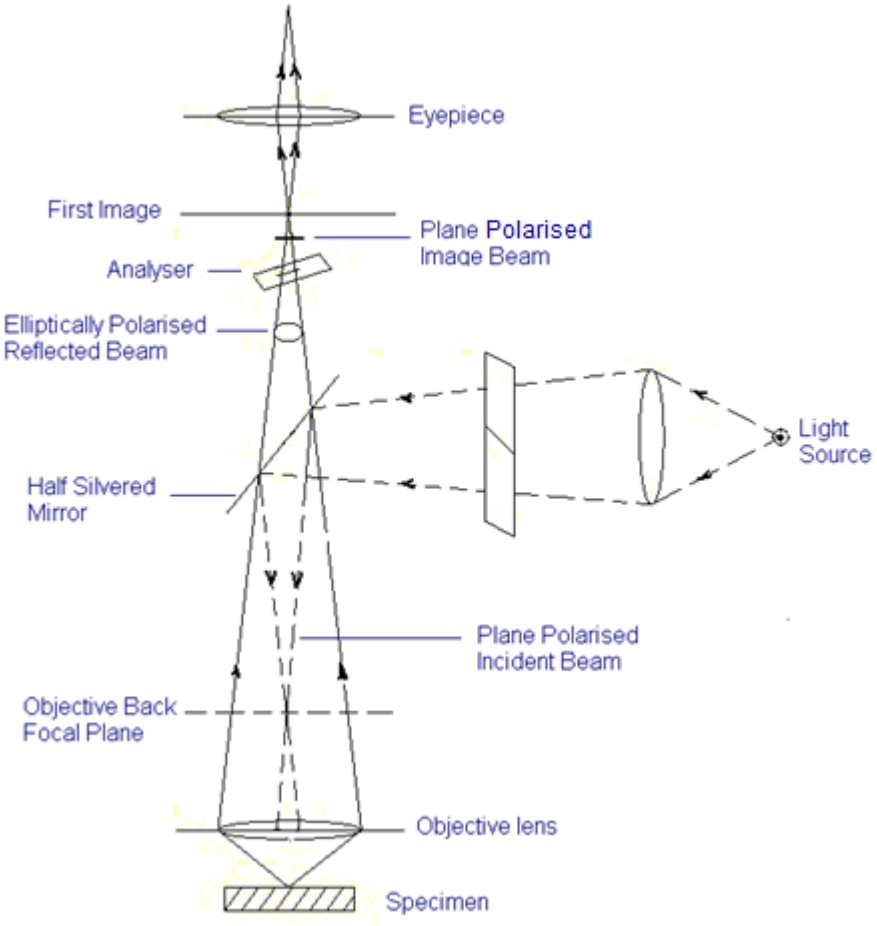

Figure 13: Schematic diagram of Polarised Light Microscopy

3.3.2 Scanning Electron Microscopy (SEM)

To investigate the microstructure and the types and distribution of microporosity observed on the basal plane of the graphite samples two scanning electron microscopes (Jeol200fx and ZESIS EVO 60) were used.

Scanning Electron Microscope (SEM) produces high-resolution images of a sample surface. The secondary electron image is dominated by surface topography. To produce a highly polished scratch-free surface the samples were ground with a selection of Silicon Carbide papers (from 800 grit to 4000 grit) manually and then, polished with diamond pastes on polishing cloth.

Scanning electron microscopes use a fine beam of electrons produced by an electron gun at the top of the column (Figure 14). Heating a fine tungsten filament or crystal with an electric current generates the electrons. A beam of electrons is drawn from the filament tip by applying a high voltage between the filament assembly and condensing lenses below it, the latter having central hole. By making the coil positive electrons are attracted to it and the voltage forces them

towards the coil but many miss it and go through the hole. The accelerated electrons are free to travel down the column and are focused into a small spot by the objective lens. The short wave length of the electron means the beam can be made into a very much smaller spot than could be achieved.[63]

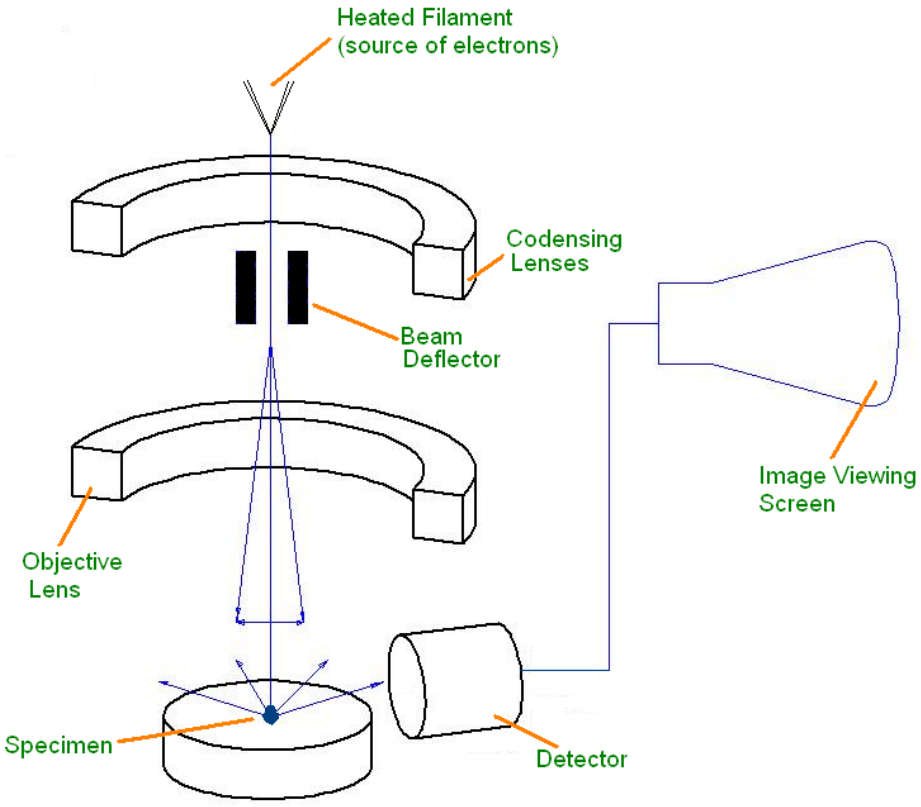

Figure 14: Schematic diagram of secondary electron microscope

Electromagnetic coils (beam deflector) used to deflect the beam so that it scans across the sample lines. Where it falls on the sample electrons are emitted and these secondary electrons can be detected in an electron detector. The signal is then amplified and used to form an image on a TV screen. Each scans line crosses on transect of the sample and then moves down so that the beam transverses the next transect. This is a raster and is used to build up a full image of the specimen. Because the number of electrons arising from the coincident spot on the specimen determines the brightness of each spot on the TV screen, the image appears to have shaded areas and bright areas. Thus the image resembles a 3-D map of the surface of specimen because contours and surface emission are what determines the image features. The resolution is determined by the size of the spot, because of the short wavelength of electrons can be made down to 0.5nm in the very best SEM. The magnification is determined by the lens in combination with the raster size – a smaller area is scanned and it is then magnified more.[63]

Figure 15 shows the different types of signals produce by an SEM when an incident beam interacts with atoms at the surface of the sample. It is rare that a single machine would have detectors for all possible signals. Most SEMs have detectors which can detect back scattered, secondary and characteristics X-ray electrons (EDX). Back scattered electrons (BSE) are often used in analytical SEM along with the spectra made from the characteristic X-rays. Because the intensity of the BSE signal is strongly related to the atomic number (Z) of the specimen; BSE images can provide information about the distribution of different elements in the sample. Characteristic X-rays are emitted when the electron beam removes an inner shell electron from the sample, causing a higher energy electron to fill the shell and release energy. These characteristic X-rays are used to identify the composition and measure the abundance of elements in the sample

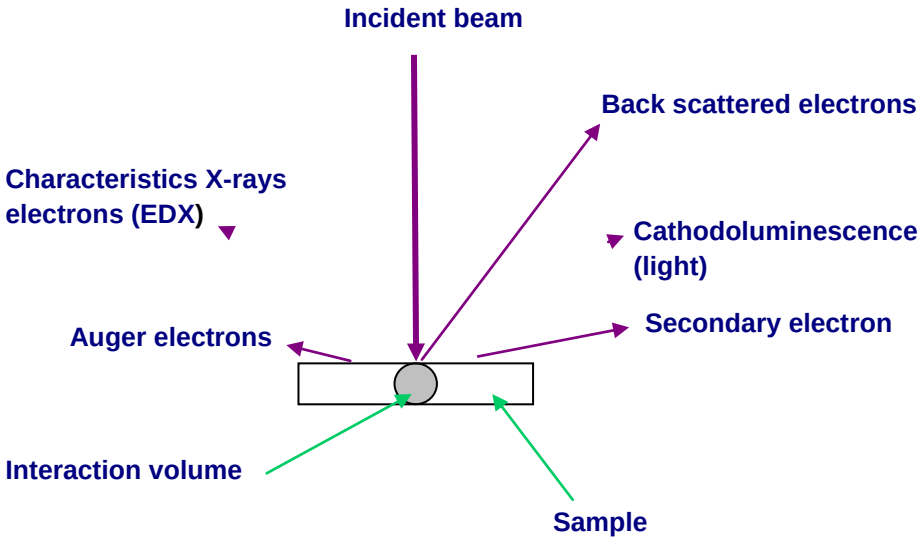

Figure 15: Schematic diagram of signals produced by SEM when the incident beam interacts with opaque material

3.3.3 Transmission Electron Microscopy (TEM)

The objective of the TEM examination was to understand the arrangement of crystallites within the microstructure and the types and distribution of microporosity contained within the graphite structure. The graphite samples were cut to a size of about 10 mm x 10 mm with a thickness of about 10 mm. Then, it was ground to a thickness of about 30 μm by polishing both sides of the graphite. A circular disc with a diameter of 3 mm was cut from this polished thin film graphite using a hollow diamond-impregnated drill and was glued on to 3.05 mm diameter molybdenum TEM disc with Araldite. Finally, the graphite disc samples were thinned to optical transparency using a Gatan PIPs (6 KeV) with an Ar ion beam.

3.3.4 X – Ray Diffraction

The crystalline purity, lattice parameters and crystallite size of virgin graphite was determined using X-ray Diffraction. Philips X'Pert PW3710 XRD equipment with generator power of 40 mA, 50 kV was used.

X-rays are an extremely short wavelength, high energy form of electromagnetic radiation. There are two types of X-rays, namely white x-rays and characteristic x-rays. Characteristic x-rays are used for the investigation of crystal structure by x-ray diffraction. Crystal lattice dimensions can be determined using techniques involving these x-rays. Characteristic x-rays are emitted when their electrons make transitions from higher to the lower atomic energy levels. When a material (sample) is irradiated with a parallel beam of monochromatic x-rays, the atomic lattice of the sample acts as a three dimensional diffraction grating causing the x-ray beam to be diffracted to specific angles (Figure 16). When x-ray photons collide with electrons, some photons from the incident beam are deflected away from the direction they originally travel. These are the x-rays that will be measured, as the scattered x-rays carry information about the electron distribution of the material.[64]

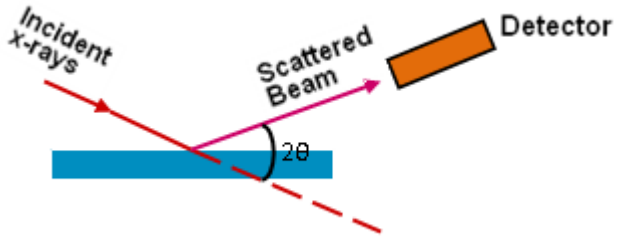

Figure 16: Schematic of scattering beam of x-rays

A detector called diffractometer measures the intensity of the diffracted x-rays. The apparatus is arranged so that both the crystal and the intensity measuring device rotate. The measuring device always moves at twice the speed of the sample, which keeps the intensity recording device at the correct angle. Therefore, it is possible to get the value of 2Θ directly from the plot.[64]

The atoms are represented as spheres and can be viewed as forming different sets of planes in the crystal. For a given set of lattice plane with an inter-plane distance of d, the condition for a diffraction to occur depends on the wavelength, λ and the angle of diffraction, θ. These factors are related to one another by Bragg's equation (eq.1), i.e.

$$2d\sin\theta = n\lambda \quad \ldots\ldots\ldots\ldots \text{ eq.1}$$

The Bragg law is fundamental to x-ray diffraction analysis and it is used for a 3D lattice. When x-rays are scattered from a crystal lattice, peaks of scattered intensity are observed which correspond to the following conditions:

1. The angle of incidence = angle of scattering.
2. The path-length difference is equal to an integer number of wavelengths.

The diffractometer used in this experiment uses copper as an x-ray source and it produces $K_{\alpha 1,2}$ and $K_{\beta 1,2}$ rays. The $K_{\beta 1}$ and $K_{\beta 2}$ ray were filtered using a slit. The $K_{\alpha 1}$ and $K_{\alpha 2}$ x-rays were used for the radiation and have a wavelength of 1.54060Å and 1.54443Å, respectively [64]. The peaks in x-ray diffraction pattern are directly related to the atomic distances.

The crystallite thickness can be calculated using, L_{002}, drawing on the Scherrer equation. The crystalline thickness perpendicular to the basal plane can be obtained by measuring the Full Width of the peak at Half Height (Maximum), FWHM and substituting in eq2.[64]

$$L_{002} = \frac{0.89\lambda}{\beta_{\frac{1}{2}(True)} \cos\theta_B} \quad \text{.....eq.2}$$

Where: L - Crystallite thickness

λ - x-ray Wavelength

$\beta_{½\,(True)}$ - Full Width at Half Maximum (FWHM) of the peak

θ_B - Angle at FWHM

3.3.5 Tomography

The x-ray tomography system employed in this investigation was Nikon Custom Bay. The instrument uses up to 320kV x-ray source and it has a resolution from 100's microns to about 3 - 5 microns.[65] The schematic diagram of Computed Tomography system is shown in Figure 17. The instrument consists of x-ray originator, collimator, sample holder and detector [65]. Collimator is used to narrow the x-ray beam to the slice that is going to be imaged. The detector is located opposite to the x-ray source and records the intensity that passed through the sample. Then, the transmitted x-ray beams will be converted into computable signals and the cross sectional image of the sample can be calculated.

During scanning the sample rotates and moves vertically while the x-rays passed through the sample at different angles and generate cross sectional slices of the sample being analysed. Due to the density difference inside the material, different absorptions will be generated.[66] The different compositions of the sample correspond to the number of different gray scales produced.

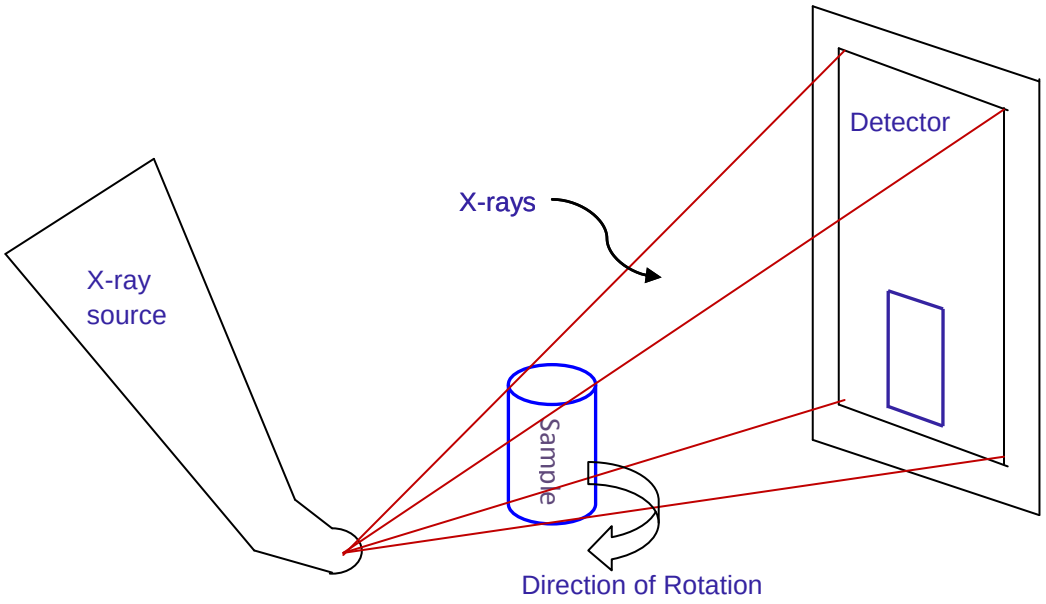

Figure 17: Schematic Diagram of Computed Tomography System

While the sample rotated through 360° the x-ray CT takes hundreds or thousands of 2D radiographs. The stacks of these 2D radiographs are then reconstructed into a 3D image using CT Pro 3D software. The main advantage of CT lies in the fact that a duplicate which is near to the object/ specimen will be recreated to show the internal structures such as cracks or voids and can be measured precisely without polishing or cutting the specimen [67]. Moreover, due to the intrinsic high contrast resolution of CT, features that differ by less than 1% in physical density can be distinguished [66, 67]. In some cases one can follow the change inside a material by analysing the slices. The other advantage of CT is the samples which are being analysed are stress free, no temperature regulation or needs any vacuuming, i.e., the analysis will be performed under real working conditions [67].

3.4 RADIOCHEMICAL METHODS

3.4.1 Sample Preparation for Leaching test on active graphite samples

The six fuel channel PGA graphite sample discs, of nominal dimensions 6 mm x 12 mm diameter and mass, 1g, were immersed in leachant solution volumes of 50 ml for ten specified time periods as outlined in Table 11. At periodic intervals, each leachant was renewed and the recovered leachates analysed. The chemical composition of the simulant water has been described by Wilkins et al. [68] and is shown in Table 12.

A modified version of the ANSI 16.1 standard [69], as described below, was used throughout the leaching trial. The ANSI 16.1 protocol determines the leachability of contaminants from encapsulated low-level radioactive waste samples. This standard provides a uniform procedure to measure and calculate the leachability factor of the radionuclides released from waste forms as a result of leaching in demineralised water for 5 days or more. The demineralised water was tested out and found to be of pH 6. It is slightly acidic as it absorbs carbon dioxide until it reaches equilibrium with the CO_2 in the atmosphere.

Table 11: Leachant Renewal Schedule

Leach Period	Leaching Interval Time (hours)	Total Time (hours)	Total Time (days)
1	2	2	0.1
2	5	7	0.3
3	17	24	1
4	24	48	2
5	24	72	3
6	24	96	4
7	72	168	7
8	336	504	21
9	672	1176	49
10	1008	2184	91

The standard test procedure was modified for application on solid graphite samples instead of monolithic cement based waste samples, and requires the total quantity of leachate to be removed from the leach container at the end of each leach period and replaced with fresh leachant. According to the procedure the samples should have dimensions of 49 mm diameter and 58 mm height, hence, a geometric surface area of approximately 12700 mm^2. It also recommends using a leachant volume of 10 times that of the volume of the sample equating to 1270 ml.

During this study the sample size and the volume of the leachate were different from that of the encapsulant, however as the ANSI standard requires a volume/surface area ratio to be at least that of 10:1, the leachant volumes used throughout this study were calculated to meet this requirement. The external surface area of the samples was calculated from the physical measurements of the specimens. In order to represent typical UK repository conditions based at

Sellafield, a simulated groundwater was used instead of demineralised water which is comparable to that of Drigg groundwater [68].

The six graphite samples underwent a 91 day leaching test as per ANSI 16.1. This solution had a starting pH of 7-8 and contained salts comparable to simulated repository Drigg groundwater (Table 12). [70]

Table 12: Original Simulated Groundwater Composition (Wilkins)

Compound	Deionised Water (g / l)
KCl	0.0066
$MgSO_4.7H_2O$	0.0976
$MgCl_2$	0.0810
$CaCO_3$	0.1672
Na_2SiO_3	0.0829
$NaNO_3$	0.0275
NaCl	0.0094
$NaHCO_3$	0.2424
pH	7.35

The samples were immersed in leachant solution, as shown in Figure 18, for ten specified time periods. After each period the leachant was renewed completely and analysed for release of contaminants. The samples were suspended in the leachant by a copper wire so that the whole surface area was covered by water. In total, sixty leachant samples were produced.

Figure 18: Leaching experiment set -up

3.4.2 Counting Efficiency

The counting efficiency is the effectiveness of a scintillation cocktail which is the percentage of emission events that produce a detectable signal of photons. It can also be described as the ratio of the counts per minute (CPM) to disintegrations per minute (DPM) expressed as a percentage (eq. 3).[71, 72]

$$\text{Counting efficency} = \frac{\text{Counts per minute}}{\text{Disintegration per minute}} \text{x } 100\ \% \quad \text{...eq. 3}$$

Counting efficiency depends on the type of isotopes to be measured, the sample composition and the ability of the scintillation counter.[71] Reduction in counting efficiency can originate from the loss of counts due to sample or cocktail characteristics. The loss of counts due to absorption of β-energy or photons by sample components or cocktail is known as quenching. [71] Due to quench, the energy spectrum produced from the radionuclide appeared to shift toward a lower energy (Figure 19 [71]). Quenching is divided into three categories, physical quenching, chemical quenching and colour quenching.[71]

Physical quench occurs when the radioisotope is not homogenously dissolved with the scintillator.[71, 72] The other case where physical quenching arises is when an obstacle exists such as activity on solid samples. The problem of physical quench may be avoided by mixing the solution properly. Chemical quench occurs when radioactive energy of the beta particle absorbed by compounds before it is converted to light or re-emitted.[71, 72] Therefore, chemical quench decrease the number of photons produced by each β-particle or the photons will not reach the scintillator. Subsequently, no light will reach the detector. Colour quench occurs when the wavelength range of the emitted light is absorbed by the colour of the scintillator or the

sample.[71, 72] Here the total quantity of light emitted is not changed, but the signal detected at the photomultiplier tube is reduced.

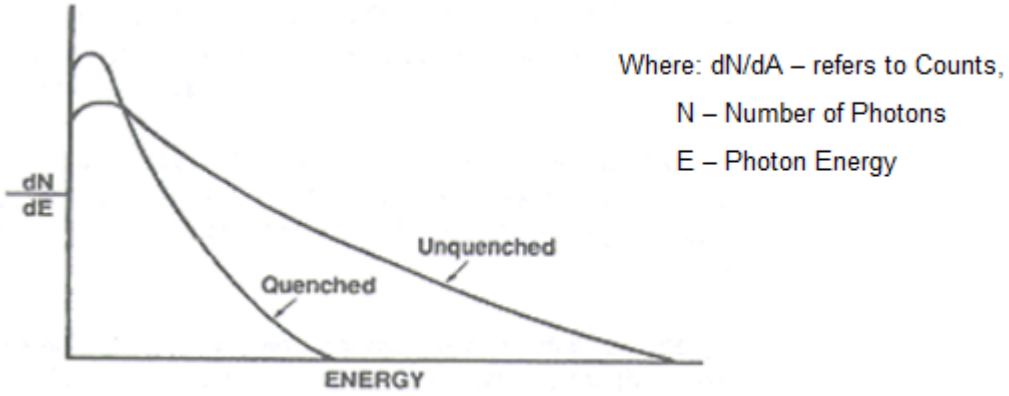

Figure 19: Effect of Quenching on an Energy Spectrum [71]

3.4.2.1 Quench Correction Methods

Quench effects can be reduced by applying the best possible effective sample preparation and setting the correct energy windows and optimising the counting windows.[71, 73] All beta activity measurements were carried out using Packard Tri-Carb 2250-CA LS spectrometer.

Using Internal Standards

Quench corrections using internal standard is the simplest and extremely accurate method but it is exhaustive or requires a long effort.[71-73] In this case a known activity of internal standard ($DPM_{(st)}$) will be prepared and an unknown sample will be prepared and its activity will be measured ($CPM_{(x)}$). Then, the known internal standard radioactive added to the unknown sample and the resulting activity will be measured ($CPM_{(st)} + CPM_{(x)}$). The mixture will increase the DPM by a known amount. The difference between the increase in DPM achieved and that expected is due to quenching, and permits the determination of counting efficiency [73] for that sample.

Activity of internal standard is given by $DPM_{(st)}$ which is expressed as $CPM_{(st)}$/efficiency

$$\mathrm{DPM}_{(\mathrm{st})} = \frac{\mathrm{CPM}_{(\mathrm{st})}}{\text{efficiency}} \ldots\ldots\ldots\ldots\ldots (a)$$

Activity sample is expressed by $CPM_{(x)}$

The activity of the mixture is given by:

$CPM_{(x+st)} = CPM_{(x)} + CPM_{(st)}$ .....(b)

Equation (a) and (b) gives:

$CPM_{(x+st)} = CPM_{(x)} + [DPM_{(st)} \times \text{Counting Efficiency}]$

Therefore,

$$\%\ \text{Counting Efficiency} = \frac{\text{CPM}_{(x+st)} - \text{CPM}_{(x)}}{\text{DPM}_{(st)}} \ldots\ldots\ldots\ldots \text{eq. 4}$$

Use of Quench Curves

This technique employs the use of a quench curve. The curve determines the relationship between a quench parameter and the counting efficiency. A quench curve is plotted using a series of standards in which the total radioactivity per vial is the same and the quantity of quench increases from vial to vial.[71, 72] After the activity in each standard is counted and the CPM is determined, the DPM value in each standard is calculated from the quench curve produced. For each standard the quench indicating parameter (QIP) is measured during the activity counting and a curve is drawn using the standard points. Hence, a relationship is made using the quench indicating parameter from the axis (X) and the % efficiency with the other axis (Y). Then, the counting efficiency is calculated using eq. 4 above for each vial. The quench curve drawn will be then used to determine the corresponding counting efficiency of unknown sample.

There are two QIP's for measuring quench which involve spectral analysis techniques. The Spectral Index of the Sample (SIS) is the first technique. This quench parameter is derived from the sample spectral endpoint.[71, 72] The SIS employs the use of sample radionuclide spectrum to investigate the quench of a solution. The spectrum corresponds to the probability distribution of the distinct energy of the beta-particles.[73] The average kinetic energy of all beta-particles can be calculated from this distribution. The SIS decreases as quench increases and the spectrum shift to lower energy.[71]

The second technique is the transformed Spectral Index of the External Standard (tSIE) and it is used to measure quench which is calculated from the Compton spectrum induced by an external ^{133}Ba gamma source in the scintillation cocktail.[71, 72] The source is placed under the sample vial and the tSIE value is determined from a mathematical transformation of this spectrum. The tSIE is a comparative value and scale from 0 (most quenched) to 1000 (unquenched).[71] Both SIS or/and tSIE will be measured during counting the activity of each standard. Then, from the measured CPM of the unknown sample and the counting efficiency the DPM value was calculated. Then, the quench curve can be drawn and can be used to determine the corresponding counting efficiency.

tSIE is not controlled by the sample atom and radioactivity in the vial and has a large active range.[72] This advantage makes it a very important and accurate means of tracking the quench of the cocktail. SIS can only be employed when the activity in the sample is greater than 500 CPM.[72] It uses the sample atom spectrum to track quench and it is most accurate technique for

samples which have a high count rate samples. Therefore, SIS must not be employed for samples with low activity since it is difficult to acquire an accurate sample spectrum.[73]

Direct DPM

Direct DPM is an automatic feature or program technique which is used to determine the counting efficiency and DPM of a sample. It is installed at the factory and it allows the counting and DPM calculation of various nuclides within the same LSC rack without changing the program if half-life correction is not employed.[71, 73] When using the Direct DPM method the user has to specify the counting time and the nuclide if half-life amendment is to be applied.

This technique gives best result if it is used for sample with an activity greater than 1000 CPM.[71] The Direct DPM permits analysis of any number of samples within one or more LSC racks [71]. The method is exceptionally simple to employ, there is no need for windows settings, can be used to correct chemical and colour quench, and is very important for short half-life nuclides when quench standards are not commercially obtainable.

The disadvantage of Direct DPM method is it cannot be used for dual labelled samples.[71] Dual labelled samples are samples of radionuclide decay with secondary events taking place with no clear beta/ gamma nuclides or a situation in which there are two radionuclides in the same sample. Moreover, Direct DPM method relies on the sample counts (>1000 CPM) and requires good counting data for precise results. Therefore, this technique cannot be employed for low activity samples.

Setting counting windows

The purpose of setting counting windows is to measure the only photons which originate from the radioactive sample. There are other measurements which are not the part of the standard solution activity such as background which originate from cosmic rays or radioactivity from the environment and contribution of neighbouring radionuclides as shown in Figure 20.[71] When a window is set only the counts with the original nuclear decay energy dissipated in the cocktail, i.e. the ones within the counting windows are measured, after subtracting the part of the background and the contribution of the activity count of neighbouring radionuclide.

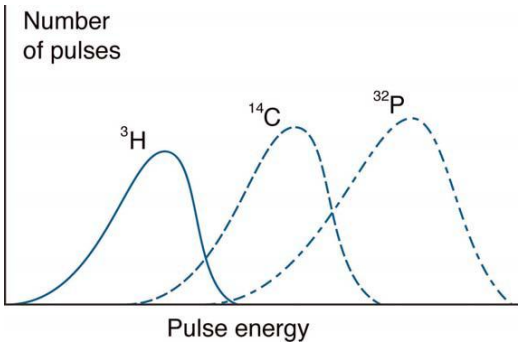

Figure 20: LSC energy spectrum of ^{3}H, ^{14}C and ^{32}P showing activity contribution of neighbouring radionuclides

In the ^{3}H and ^{14}C counting the number of photons produced is low and the spectrum position and shape changes depending on the quench.[71, 73] Consequently, CPM results may be invalid due to the unknown effect of quench, which varies from sample to sample. Each cocktail and sample has a distinctive quench level and the optimum window is different from the theoretical position. As a result the counting windows were set with a procedure described below:

- The lower limit is set so that the photon peak does not cause invalid counts in the counting window due to background counts and contribution of neighbouring radionuclides
- The upper limit of the window is set so that the spectrum lies below the upper value

Therefore, the determination of the counting efficiency and the corresponding quench correction performed for the investigation is described below:

3.4.2.2 ^{3}H Counting Efficiency Determination

In order to determine the effect of quenching on the counting efficiency of ^{3}H a set of six quenched standards is prepared by adding a quenching agent, i.e., simulated groundwater, into an internal standard with a known amount of activity. In conjunction with the standard samples two blank samples were prepared by adding 4 ml of simulated groundwater into a vial containing 16 ml of UG scintillation cocktail. Then, the background count rates were determined by counting the blank samples. Table 13 shows determination of counting efficiency of tritium. The counting efficiency found out to be about 38 %.

Table 13: ^{3}H counting efficiency determination

Cocktail Vol. (ml)	Vol. H_2O (ml)	Vol. Std (ml)	Activity (Bq)	CPSB (Bq)	B:2S%	tSIE	Efficiency (%)
16.0	3.9	0.1	16.1	6.1	2.3	458.4	37.8
16.0	3.9	0.1	16.1	6.1	2.3	458.2	38.0
16.0	3.9	0.1	16.1	6.2	2.3	456.8	38.6
16.0	3.9	0.1	16.1	6.1	2.3	458.9	37.7
16.0	3.9	0.1	16.1	6.1	2.3	457.7	37.8
16.0	3.9	0.1	16.1	6.1	2.3	458.2	38.0
						Average Efficiency	38.0

3.4.2.3 ^{14}C Counting Efficiency Determination

The counting efficiency of ^{14}C with a particular quench level must be measured to determine the activity of ^{14}C. The determination of the counting efficiency was done by counting a series of quenched reference standards of ^{14}C. The ^{14}C in the leachate was recovered as a precipitate of $BaCO_3$. Hence, the internal standard which is going to be used should be a solid standard. This method involves the counting of $BaCO_3$ suspended in a liquid scintillator adjusted for gel formation. Since the sample is solid and suspended in a gel the mixture of the cocktail, the standard and the simulated water will be affected by physical, colour and chemical quench. The effect of quenching due to the water (chemical quench) is expected but here there is an additional obstacle from the solid sample. The radioisotope should be homogenously dissolved with the scintillator and water but it is quite difficult to tell for sure.

The procedure of the sample preparation is described as follows. Six vials containing different amount of internal standard (Table 14) but with same amounts of a quenching agent, i.e., simulated groundwater was prepared. The internal standard, $BaCO_3$, was put into the counting vials containing 10 ml of Insta-Gel scintillation cocktail and, 4 ml of simulated groundwater was added. The ratio between the water and scintillator was 2:5. Homogenous mixing was obtained by warming the vial and shaking it thoroughly. A blank sample with a volume equivalent to the quenched standard solutions was also prepared to measure the background and used in the calculation to get the most possible accurate result.

The DPM value in each standard is known. Each standard is counted and the CPM is measured as shown in Table 14. From the standards in which the absolute radioactivity (DPM) per vial is different and the amount of activity of the vials the efficiency is calculated using eq. 4. Then, an

efficiency curve is fitted to the calculated points. A correlation is made using the mass of the sample on one axis (X) and the % efficiency on the other axis (Y) and the resulting graph is shown in Figure 21.

Table 14: ^{14}C counting efficiency determination

Sample #	Mass $BaCO_3$ (g)	Vol. H_2O (ml)	C-14 Activity (Bq)	CPSB (Bq)	B:2S%	tSIE	Efficiency (%)
1	0.0303	4	85.143	48	1.22	324.17	57
2	0.0493	4	138.533	78	1.21	311.37	56
3	0.0714	4	200.634	112	1.22	319.06	56
4	0.0984	4	276.504	148	1.23	318.83	54
5	0.1253	4	352.093	179	1.24	319.93	51
6	0.1544	4	433.864	232	1.23	323.86	53

From the graph it can be observed that the counting efficiency decreases when the mass of the internal standard increases. This reveals that the amount of mass that can be added into a particular vial cocktail affects the counting efficiency. Therefore, the graph shown in Figure 21 was used to select the amount (mass) of sample which is going to be used and the corresponding counting efficiency throughout experiment. Hence, a mass of 0.1 g and a counting efficiency of 54 % were used to investigate the activity of ^{14}C found in the leachates from the graphite waste.

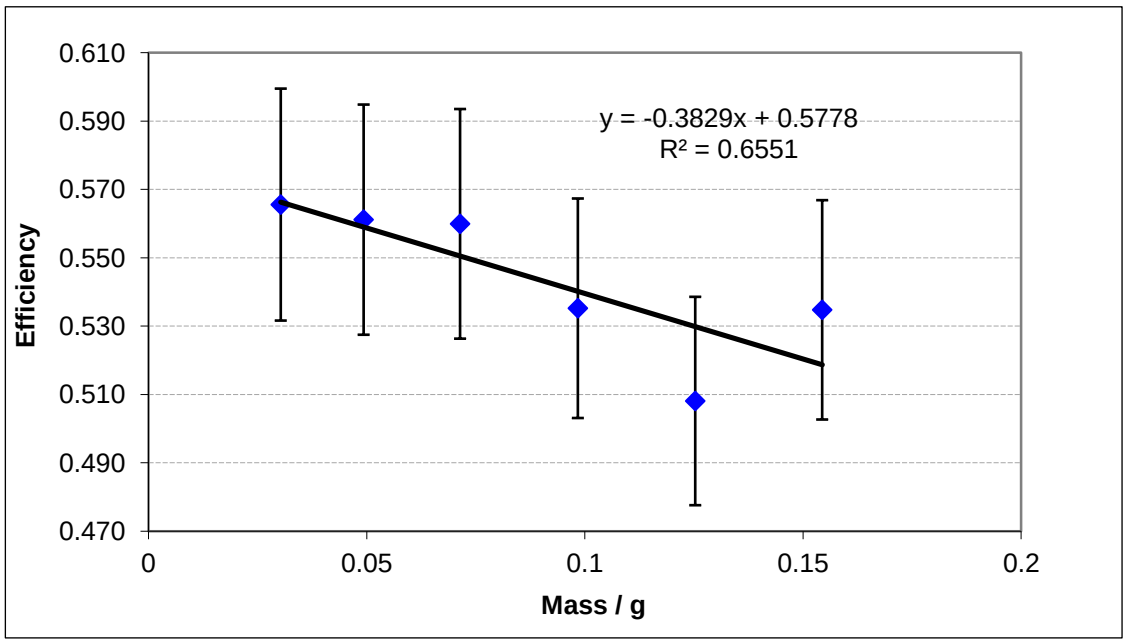

Figure 21: The effect of quench on counting efficiency of ^{14}C

3.4.2.4 Window Selection and Widow Optimisation

As described above setting the counting windows with lower level (LL) and upper level (UL) pulse height channel windows eliminates activity measurements which are not part of the standard solution activity such as background and the contribution of neighbouring radionuclides. To determine the LL and UL window of background count rates two blank samples were prepared using 16 ml UG scintillation cocktail and 4 ml of simulated groundwater and were counted for 120 minutes. The background counts were found within the window between about 0 - 4 keV energy range. The effective counting window optimisation procedure employed is similar to the procedure followed by Kong, T. Y., et al. [74].

The maximum energy window for ^{3}H is 0 – 18.6 keV [75]. In order to determine the LL and UL window of ^{3}H count rates two ^{3}H standard samples were prepared using 16 ml UG scintillation cocktail, 0.1 ml of ^{3}H standard and 3.9 ml of simulated groundwater and each solutions were counted for 120 minutes. After measuring the samples using LSC, to determine the LL the minimum window level was fixed at 0 kev. Then, the lower channel was increased progressively by 0.5 keV in order to optimise the counting windows. The optimum section is where there is minimum change but any change made to evaluate the LL was resulted in a significant change on the count. Hence, the LL of the counting window for ^{3}H is found to be 4 kev. To determine the optimised UL of the counting window the maximum level was set at 20 keV and progressively decreased by 0.5 keV. The UL of the counting window was found to be 18 keV. Therefore, the counting window of ^{3}H was defined by the LL and UL settings of 4 – 18 keV. The LS Counter software allows the user to select counting windows of interest. Then, for ^{3}H the three channels selected were: Channel A, 0 - 4 keV, Channel B 4 – 18 keV, and Channel C 18 - 2000 keV. The standard deviation (2S) of the measured values was considered as suitable, and was shown to be within 2 - 3 % of the average measured values.

^{14}C has a spectrum with a maximum energy of 156 keV [75]. The effectual channel window of the count assayed through the optimisation procedure. To evaluate the LL and UL window of ^{14}C count rates two standard samples were prepared using 10 ml Insta-Gel scintillation cocktail, 0.1 g of active $BaCO_3$ standard and 4 ml of simulated groundwater and the resulting mixtures were counted for 120 minutes.

After measuring the ^{14}C spectrum by using LSC, to determine the LL the maximum window level was fixed at 156 kev. Then, the lower channel was increased progressively by 0.5 keV in order to optimise the counting windows. In order to find the UL window, the lower channel was fixed at 18 kev and the maximum energy was decreased progressively by 0.5 keV from the maximum value 200 keV to optimise the UL of the counting window. The LL of the window was found out to be 18 and it was found that 96 % of total spectrum was distributed lower than 85 keV. The total counts were distributed within 67 keV. Therefore, the counting window of ^{14}C was defined by the LL and UL settings of 18 – 85 keV. The standard deviation (2S) of the measured values

was considered as appropriate, and was shown to be within 2 - 3 % of the average measured values. Therefore, the activity measured for ^{14}C from the samples was divided into three counting window channels. Channel A encompassed the energy window for ^{3}H and background. Channel B was assigned as a window from 18 keV to 85 keV. Channel C was assigned from 85 – 2000 kev. In this procedure, the effective counting windows were determined by using the spectrums of both ^{3}H and ^{14}C in order to maximise the counting efficiency and minimise the minimum detectable activity.

3.4.3 Cocktail Selection

When a radionuclide decays it results in the emission of two particles, an electron (beta particle) and a neutrino.[76] The energy released is a kinetic energy and it dissipates during collisions in a medium in which it is released. The energy is absorbed by the medium in three forms, heat, ionisation and excitation of the molecules of the solution.[76] In liquid scintillation method it is the excitation of the solution is that the base for engineering of scintillation cocktails.

Cocktail selection depends on the characteristics of the sample to be counted, the sample preparation procedure and the instrument it is going to be employed. Therefore, to get accurate and reproducible counting results one has to chose the right cocktail matching with a correct sample preparation procedure and instrument. When analysing aqueous samples the loading capacity of the cocktail will influence the limit of detection of the radionuclide being investigated.[76] Therefore, the cocktail(s) chosen for a particular analysis should be appraised to determine the sample to cocktail mixing ratio that will give the best result.

Liquid scintillation cocktail should be prepared from reagents that are low in natural radioactivity. For contamination counting cocktails with low background and high sample loading capacity are desirable. Most scintillation cocktails designed for aqueous samples contain surfactants, which emulsify the sample into the organic solvent. The best solvents for scintillation counting are the aromatic organics, such as toluene and xylene.[76] Hydrophobic compounds can be counted directly in such solvents, but hydrophilic materials, are completely insoluble in simple cocktails.[75] This requires the engineering of complex cocktails, capable of bringing hydrophilic sample molecules into close to organic solvents and the dissolved scintillators. Various other components are added to the cocktail in small amounts, which regulate the amount of quench to maintain overall solution clarity.[75] Because the surfactants and other additives are generally less effective at energy capturing than the solvent, emulsion cocktails are less efficient than pure solvent cocktails.

Hence, for the investigation Ultima Gold™ and Insta-Gel™ scintillation cocktails have been chosen.

Scintillation cocktail for total alpha and beta and total alpha and beta without ^{3}H analysis

For total alpha and beta, total alpha and beta without ^{3}H and ^{3}H analysis Ultima Gold™ scintillation cocktail have been chosen. Ultima Gold is a multipurpose LSC cocktail and a safer liquid scintillation cocktail for a wide range of aqueous and non-aqueous samples. It is chosen due to its high counting efficiency, slower diffusion rate into the plastic vials and higher detection efficiency for samples that exhibit severe quench.

Scintillation cocktail for ^{3}H analysis

Scintillation cocktail is a mixture of a solvent and a solute and when it interacts with the radiation emitted from the sample and a count is recorded. Ultima Gold had been chosen because it has an excellent sample holding capacity and it is an ideal choice for aqueous samples due to its low surfactant content. Duplicate samples containing a known amount of ^{3}H standard were processed parallel to the samples and analysed in order to correct for any reduction in counting efficiency due to the effect of quenching substances. Quenching occurs when the energy emitted by the radionuclide is not collected completely by the photomultiplier tube of the counting instrument.

Scintillation cocktail for ^{14}C analysis

Insta-Gel scintillation cocktail is used for counting ^{14}C beta emission using a Liquid Scintillation Counter. Insta-Gel Plus (1,2,4-Trimethylbenzene) is an almost water-insoluble hydrocarbon liquid based cocktail. It is excellent for the incorporation of water and aqueous soluble samples and organic samples due to its resistance to colour quenching and formation of a stable gel. It has very high sample holding capacity and ideal for counting large volumes of water and suspended solids.

3.4.4 Estimate of the Counting Error

Radioactive decay is a random event. The number of decay events per unit time is variable. The average behaviour of all nuclear decays in a simple can be described by means of counting statistics.[76] Counting statistics are used to express the probability of acquiring a given count within a certain confidence limit. Hence, the determination of the validity of a single count whether it is representative of the true count rate or not can be determined by applying counting statistics.

In nuclear counting, one can use probability to estimate the counting error associated with any determination or to what degree the observed value deviates from the true value (mean). This is achieved by calculating the standard deviation (S). For a normal distribution, the probability of an observed value falling within $\pm$ 1s is 68%. This is the confidence limit. In nuclear counting, it

is desirable to work with a higher confidence limit of $\pm$ 2s from the mean or 95.5% confidence.[76] This means that the probability of the observed count being within $\pm$ 2s from the mean will be 95.5% and 4.5% of the time the observed count will fall outside of this range.

3.4.5 Detection Limit Determination

Many standard and regulations have accepted Currie's expression for limit of detection. Currie defines two basic features of detection.[77] The first is that of deciding whether an observed signal is indeed a detected "true" signal. This conclusion is subject to two kinds of errors: deciding that the signal is true when it is not (α or Type I error), and failing to decide that it is true when it is true (β or Type II error). Type **I** errors (α) are used to create the idea of the Critical Level, $L_{c.}$ Critical level can be defined as a point above which a signal would be detected.[77] 5% is a tolerable value for α in nuclear counting.[76] This means, there is a probability of 5% deciding incorrectly that the signal is true when it is not. The correct decision is made 95% (1-α) of the time. Currie mathematical expression for L_c is:

$$L_c = 2.33\ B^{1/2}$$

Where: B - is the total counts of an appropriate blank counted for the same time as the sample.

This shows that the lower limit of detection is based upon the measurements of replicate blank samples. Blank is defined as a sample chemistry which is identical to the sample of activity, except that the activity is small when compared to the standard deviation of the blank (Currie 1968).[77] Once L_c is known with its known error level for α, then, the true net signal that can be detected (the Detection Limit) is defined as:

$$L_d = 4.65\ B^{1/2}$$

This formula is derived from the L_c and an acceptable level of β (Type ll error). An acceptable value for β is 5%; a 5% probability that a true signal will be missed. On the contrary, 1-β or 95% of the time the conclusion that a signal was there will be correct. Thus, L_d is determined by L_c and accounts for both Type l and a Type ll error.[76] For radioactivity calculations, 2.71 is often added to the L_d term to account for the zero blank case which corresponds to a 5% probability of a false negative. Sometimes, the number is simply rounded to 3 [76]. The resulting equation is shown in eq. 6.

The LLD values are calculated for each type of analysis. Values of detection efficiencies and other process parameters are used when possible and should be reflective of the actual conditions. Expressed mathematically, the equation of LLD for a paired sample and blank is:

$$LLD = L_c/K$$

Where: K = a series of factors multiplied together and grouped as one:

K = {(activity units)(efficiency)(aliquot size)(abundance)(count time)(chemical yield)(decay correction)} and applied where appropriate.

Hence, the LLD is the smallest activity of a sample that produces a net count above background with a 95% probability with no more than 5% probability of deciding that a blank is a true signal or false positive. Basically, LLD is equivalent to minimal detectable activity (MDA).

3.4.5.1 ^{3}H Minimal Detectable Activity

As discussed above (Section 3.4.5), the MDA (Minimum Detectable Activity) value, as defined in eq.6 below, determines a lower limit for the detected net activity which corresponds to a specific activity concentration for the sample being analysed. The Currie equation, i.e., eq.6 provides a generalized estimate of the MDA which is proportional to the standard deviation of the background counts σ_{bkgrd} at a specific volume of interest,

$$MDA = 2.71 + 4.65\,\sigma_{bkgrd} \quad \text{----- eq.6}$$

The MDA values are calculated for each type of analysis. Values of detection efficiencies and other process parameters are used when possible and should be reflective of the actual conditions. To a great degree, the selection of these parameters will be based on judgment and will require evaluation of experiment-specific conditions. So, eq.6 is modified to determine the MDA for ^{3}H analysis as shown in eq.7.

$$MDA = \left(\frac{\left(\frac{2.71 + \left(4.65\sqrt{(\text{Blank Average X Count time of Blank})} \right)}{Count time \text{ X } 60} \right)}{Efficiency} \right) \text{X} \left(\frac{1}{\text{Volume of QC/ Sample}} \right) \quad \text{----- eq.7}$$

3.4.5.2 ^{14}C Minimal Detectable Activity

The MDA value MDA for ^{14}C was calculated is based upon measurements of replicate blank samples and based on the Currie law (eq.6). Therefore, eq.6 is modified as shown in eq.8 to determine the MDA of ^{14}C analysis, an equation which includes all the parameters used in processing and analysing the samples.

$$MDA = \left(\frac{\left(\frac{2.71 + \left(4.65\sqrt{(\text{Blank Average X Count time of Blank})} \right)}{Count time \text{ X } 60} \right)}{Efficiency} \right) \text{X} \left(\frac{1}{\text{Recovery}} \right) \text{X} \left(\frac{\text{Mass of ppt produced}}{\text{Mass taken for LSC}} \right) \text{x} \left(\frac{1}{\text{Volume of QC/Sample}} \right)$$

.....

eq.8

3.5 ANALYTICAL INVESTIGATION

3.5.1 Gamma Spectroscopy

The activity of gamma emitting radionuclides was measured using Gamma spectroscopy. The spectrometer uses a High-Purity Germanium (HPGe) detector (Model GC10 connected to an Ortec DSPEC jr. digital gamma ray spectrometer and is operated using Ortec Gammavision-32 software Version 6). The advantage of using this detector is that it has an excellent Compton Suppression System (CSS) which allows reduction in Compton background and therefore higher resolution. The detection software also minimises any cosmic background.

The geometry of the container was defined by specifying the size of the container from the choice available within the software. The software also allows materials to be defined from using default entries. All aqueous sources are modelled and defined as water with a density of 1.00 g / cm^3, and all plastic materials were defined by selecting plastic from the default list. The software defines the plastic as a material made of 57% carbon, 34% oxygen, 9% hydrogen with a density of 0.94 g / cm^3.[65]

Gamma spectroscopy was used to quantify the activity of gamma releasing radionuclides. A small volume of solution (5 ml) was extracted from each leachate and used to measure total alpha-gamma and total alpha-gamma without tritium activity using a Liquid Scintillation Counter. A blank system and quality control samples were also run in parallel to the system containing graphite in order to calculate errors on the system and preparation and to determine the accuracy of the method respectively.

3.5.2 Liquid Scintillation Counting

One of the main issues that needs addressing when planning and carrying out decommissioning operations and disposing of irradiated graphite are the presence of radiological nuclides in the waste. Radionuclides which are the main concern include ^{3}H, ^{14}C, ^{133}Ba, ^{36}Cl, ^{63}Ni, ^{60}Co, ^{41}Ca, ^{55}Fe, ^{152}Eu, ^{90}Sr, and ^{137}Cs. There may also be some alpha emitting radionuclides of concern such as ^{238}Pu, ^{238}U, ^{239}Pu, ^{240}Pu, ^{241}Am and ^{241}Pu. Alpha emitting nuclides have a large nucleus and must have atomic nucleus that can support it. Therefore, it does not have enough energy to escape from the strong force of the nucleus. Due to this they cannot travel long distances and they are mostly bound near the surface of the graphite channel wall. Therefore, the majority of the alpha emitting radionuclides were removed when about 9 mm of the graphite nearest the channel wall is removed during sample preparation to clean the surface from Uranic impurities in the graphite, released fission products in reactor or/and from contaminations in the lab during post-irradiation examination. Therefore, during measuring of

the activity of the leachates in this investigation only the alpha particles which were transported deep into the graphite via the open pore network were measured.

The analysis of ^{14}C contained within the leachant solution was investigated using sample digestion, the measurement of total alpha and beta radiation was determined using liquid scintillation and investigation of ^{3}H was carried out by separation and analysis. Liquid Scintillation Counting also has the ability to determine the energy ranges of alpha emitting radionuclides. Alpha and beta events may be distinguished from one another in a liquid scintillator by examining the electronic signals that are produced at the photomultiplier tube anode of the detector. The signals produced are comprised of two components: the prompt component and the delayed component [78-80]. The magnitudes of these components in alpha and beta signals are different: the alpha signals are longer than the beta signals.

The radioactive decay of excited singlet and triplet states of the cocktail molecules produce photons on the cathode of the photomultiplier tube.[76] The fast exponential decay of excited singlet states produces the prompt component. The delayed component of the signal is produced when triplet states interact only with another molecule and emit photons. The collision process has a longer lifetime which causes the delay. The relative scintillation yield depends upon specific ionisation potentials. High specific ionisation potential causes a greater fraction of excited molecules in triplet states and, hence, causing the alpha signal to have a longer duration. The basis of alpha/beta separation by signal shape discrimination is the delay of these alpha signals. Most alpha radionuclides emit high-energy particles in the range of 4 – 6 MeV and betas have values below 2.5 Mev.[76] Separation of alpha from beta is essential because the interaction of alpha particle with the scintillator produces low scintillation or photon yield as compared to betas (approximately it is lower by a factor of 10) shifting their spectra into the beta region.[76]

3.5.3 Total Alpha and Beta

To measure the total alpha and beta activity released after each specific period of leaching time a small volume of solution (5 ml) was extracted from each leachate and was measured using a Liquid Scintillation Counter. A blank system and quality control samples were also run in parallel to the system containing graphite to calculate errors on the system and preparation and to determine the accuracy of the method respectively. The errors associated with the measurements were adjusted by subtracting the blank and background measurements from each leachate activity measurements. The efficiency was calculated by placing a known amount of activity (^{241}Am (for alpha) and ^{90}Sr (for beta) in a designated quality control vial and comparing the input and the output values. The quality of measurement data is directly impacted by the magnitude of the measurement uncertainty associated with it and it this uncertainty was measured to be approximately 6.6% based on a standard deviation (2σ).

3.5.4 Total Alpha and Beta without Tritium Analysis

The total alpha and beta without ^{3}H measurement was achieved by separating the ^{3}H by evaporation. The method involved separating the ^{3}H from the other radionuclides by taking a 5 ml volume of sample extracted from each leachate. This was then dried at a temperature of 125 °C until all the liquid phase evaporated completely. This process eliminates all the ^{3}H leaving only the heavy radionuclides as a solid. These heavy nuclides have a higher molecular mass and boiling point than ^{3}H, hence remain inside the vial after the digestion process. A 5 ml volume of $0.1HNO_3$ was next added and the resulting solution was mixed with 10 ml of scintillation cocktail. Nitric acid is a strong oxidising agent which dissolves the resulting solid particles. Any tritium left after drying is released on reacting with the nitric acid. The ensuing mixture was analysed using a liquid scintillation counter.

A blank system and quality control samples were also run in parallel to the system containing a virgin graphite sample in order to calculate errors on both the system and preparation in order to determine the accuracy of the method. The error was calculated by subtracting the blank and background measurements from each leachant activity measurement. The efficiency was calculated by placing a known amount of activity (^{241}Am and ^{90}Sr) in a designated quality control vial and comparing the input and the output values.The quality of measurement data is directly impacted by the magnitude of the measurement uncertainty associated with it and was found to be about 6.6% 2σ standard deviation.

3.5.5 Measurement of ^{3}H by digestion and distillation of leachant

One of the most significant short-lived radionuclides is ^{3}H, which arises from irradiated graphite and it has a half-life of 12.3 years. During irradiation most ^{3}H is generated from the activation of ^{6}Li (n, α) [3] and it also produced from fuel elements as a result of the fission process. ^{3}H is very mobile and is bound to graphite very loosely. Kinetic studies [81] showed the rapid exchange process between ^{3}H on to the graphite and the untritated reactor coolant hydrogenous components. Therefore, due to this (highly mobility of tritium) it diffuses quickly to reach pore surfaces where it may be adsorbed and then, may be absorbed by the coolant or untritated water during leaching. ^{3}H decays by beta minus directly to nonradioactive ^{3}He.

In the investigation the apparatus employs a dry-bed absorber system that is designed to separate ^{3}H, ^{14}C and ^{35}S. It uses a series of columns containing either silica gel or soda lime to trap moisture and air from the different species over a specified time. At the end of an experiment the absorbed water is removed from the silica gel column and the ^{3}H content measured by liquid scintillation counting.

For this investigation a simple digestion and distillation technique was used. This method has been chosen because it is inexpensive and easy to perform and the results obtained are reasonably accurate. The investigation involves heating 20 ml of a sample on a hot plate at 60°C for an hour. When the digestion of each cycle is completed the tritiated water is distilled off onto a Petri dish cover is collected and transferred to a vial. The process is repeated until 4 ml of distillate was collected from each sample. Then, the distillates are mixed with Ultima Gold liquid scintillator for assay.

3.5.6 Measurement of ^{14}C by digestion (wet oxidation) of leachant methods

Analysis of the leachants to measure ^{14}C involves digestion of the sample. Radioactive carbon radionuclide, ^{14}C, decays with a half-life of 5730 years by beta emission into ^{14}N [82]. ^{14}C is produced directly in three major ways: i. by transmutation of the $^{14}N(n, p) \rightarrow {}^{14}C$, an impurity which have been transported there during reactor operation or trapped inside the pores during manufacturing of the graphite, ii. via the reaction $^{13}C(n,\gamma) \rightarrow {}^{14}C$ which is a common isotope with abundance of compared to 98.89% for ^{12}C 1.1% original impurity inclusions in the graphite and iii. by the neutron activation during irradiation or/and the reaction $^{16}O(n, \gamma) \rightarrow {}^{17}O(n, \alpha) \rightarrow {}^{14}C$ which might have been carried around the circuit by the coolant gas during reactor operation.[82, 83] The production routes $^{13}C(n, \gamma) \rightarrow {}^{14}C$, $^{14}N(n, p) \rightarrow {}^{14}C$ and $^{17}O(n, \alpha) \rightarrow {}^{14}C$ have capture cross-section of between 0.0009-0.0014 barns, 1.8 barn and 0.235 barn respectively.[3, 82] So, $^{14}N(n, p) \rightarrow {}^{14}C$ and $^{17}O(n, \alpha) \rightarrow {}^{14}C$ could be considered the main routes due to their high cross-sections.[82, 83]

One of the principal aims of this investigation was to separate the ^{14}C from other beta-gamma emitters present in low level radioactive wastes from decommissioning graphite moderated reactors. ^{14}C and ^{3}H are the most significant β-emitters and the quantity of ^{14}C inside the specimens was determined by using radiochemical separation method in order to provide ^{14}C inventory data. The separation method used is based on an oxidation technique where carbon is trapped by NaOH. NaOH is highly reactive and forms sodium carbonate when it absorbs carbon dioxide released. Sodium carbonate is unstable because it is water soluble. Therefore, carbon dioxide trapped in this way needs further treatment. Hence, the resulting sodium carbonate should react with an alkali earth chloride (Calcium, Strontium and Barium) to precipitate out the carbonate. The alkali earth carbonates are stable towards oxidation and heat and insoluble in pure water. The sensitivity of this method is considered sufficient to achieve the required thresholds for the radiological characterisation of the radioactive materials in this study.[84]

The schematic diagram of the ^{14}C distillation apparatus used for the analysis is shown in Figure 22. 30 ml of deionised water was put into a round bottom flask and 5 g of potassium persulphate added to it. A citric acid was then added to this effluent to act as a ^{14}C carrier. A volume of 5 ml of aliquot was taken from each leachate and added to the solution, followed by 5

ml of 10 % silver nitrate. Then, the solution was oxidised for about an hour. Potassium persulphate and silver nitrate catalysts were add to accelerate the reaction. Concentrated sulphuric acid was added to initiate the reaction and the resulting solution was approximately 1M in sulphuric acid. The solution was heated under reflux to initiate oxidation and liberate carbon dioxide. The released carbon dioxide was trapped in sodium hydroxide. The redox reaction of the process is described from eq.9 to eq.11. The carbonate produced precipitated out by adding barium chloride into the solution.

After washing and drying, the precipitate was weighed to calculate the recovery. A mass of 1 ± 0.02 g was measured and was suspended in Insta-Gel scintillation cocktail for counting for ^{14}C beta emission using a Liquid Scintillation Counter. A blank system and quality control samples were also run in parallel to the system containing graphite in order to calculate errors in the system and method of preparation in order to determine the accuracy. Any errors in the activity analysis were adjusted by subtracting the blank and background measurements from each leachant activity measurement. The efficiency was calculated by using a known amount of ^{14}C activity. The quality of measurement is directly related to the measurement uncertainty associated with it and it was measured to be between about 1 - 7%.This value was calculated from the count results using a mathematical procedure, i.e., at 2σ standard deviation.

$C_6H_8O_7\,(aq) + CH_2O\,(aq) \rightarrow 7CO_2\,(g) + 4H_2\,(g) + H_2O\,(\ell)$ ------- eq.9

$CO_2\,(g) + 2NaOH \rightarrow Na_2CO_3 + H_2O\,(\ell)$ ------- eq.10

$Na_2CO_3\,(aq) + BaCl_2\,(aq) \rightarrow BaCO_3\,(aq) + 2NaCl\,(aq)$ ------- eq.11

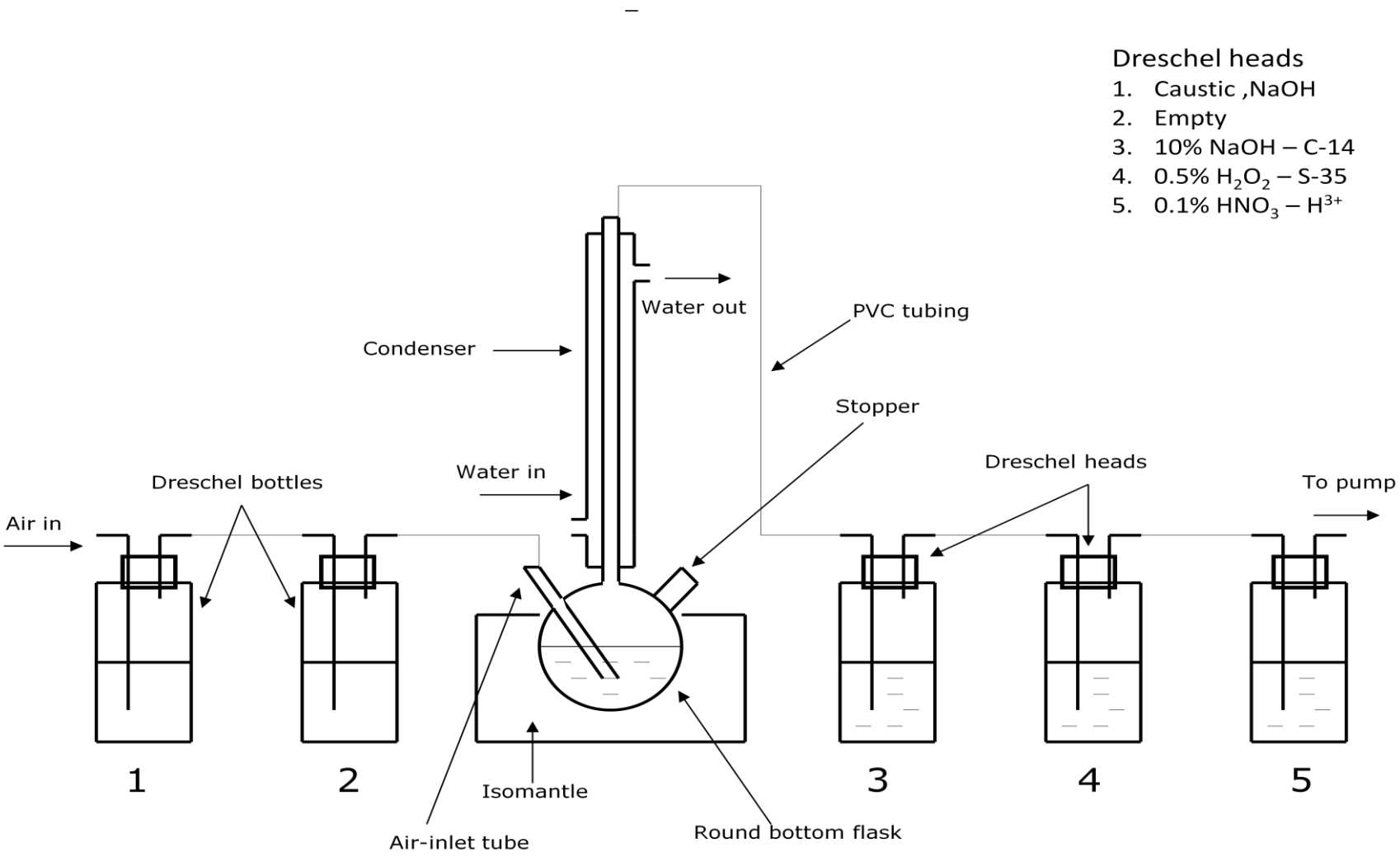

Figure 22: ^{14}C Distillation Apparatus Schematic Diagram

4. RESULTS AND DISCUSSIONS

4.1 MICROSTRUCTURAL RESULTS

4.1.1 Polarised Light Microscopy

In Polarised Light Optical Microscopy, to analyse samples such as graphite, the incident light must be shown from above because the specimens are opaque. In incident light polarisation both a polariser and an analyser are used together with a Bertrand lens. The polariser first polarises the light and the analyser is the second polarising filter. They are turned on angles and the angles precisely measured, i.e. 90^{o}C.

The polarised light micrographs which illustrates the microstructure of nuclear grade graphites PGA, NBG-10 and NBG-18 is shown in Figure 23. The aligned regions change from red to blue when the microscope stage is rotated 90°. As it can be seen the micrographs they (blue and red coloured particles) are perpendicular to each other. The colour of poorly aligned graphite regions changes very little during the polarisation process. In graphite the size of the filler particles observed is taken as the grain size of the material. Striking differences in the grain structure of these graphites can be observed by optical microscopy techniques.

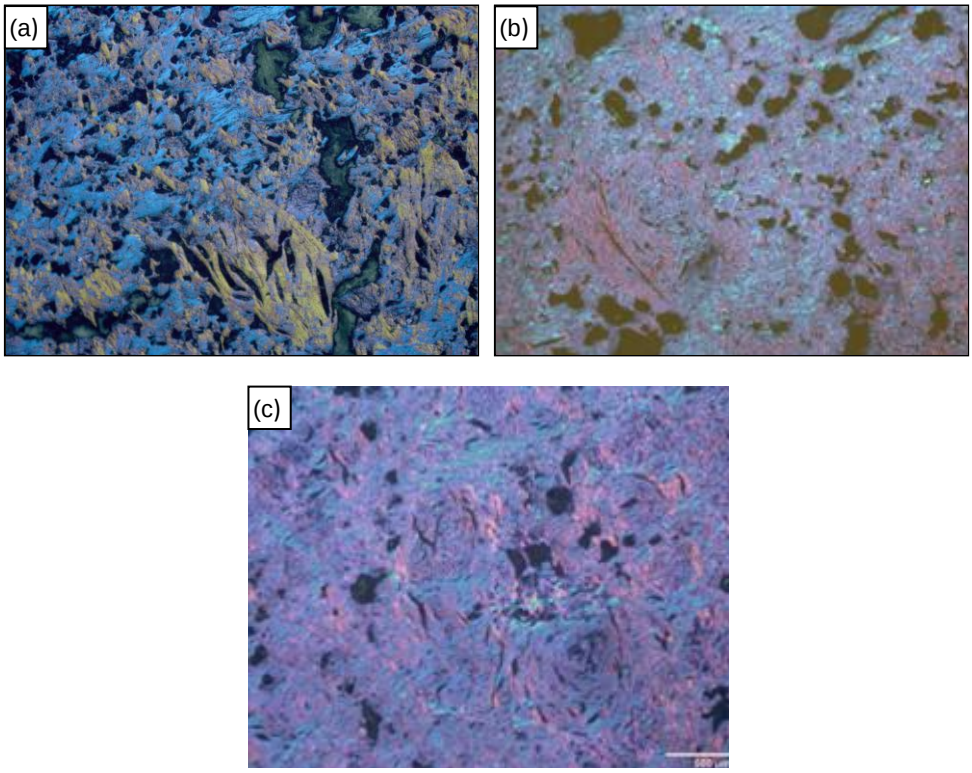

Figure 23: Polarised light optical micrographs of nuclear grade graphites: (a) PGA (b) NBG-10 and (c) NBG-18 all scaled to 500µm

PGA has more aligned coke particles than the other two graphites (this was confirmed by XRD analysis). Its pores are larger than NBG-10 and NBG-18 graphites (Figure 24) and are somewhat elongated. This might have been due to the characteristics of the coke particle which may determine the anisotropy of graphite. Moreover, the sizes of coke particles corresponding to the highly aligned regions might also results in a higher degree of anisotropy of the graphite.

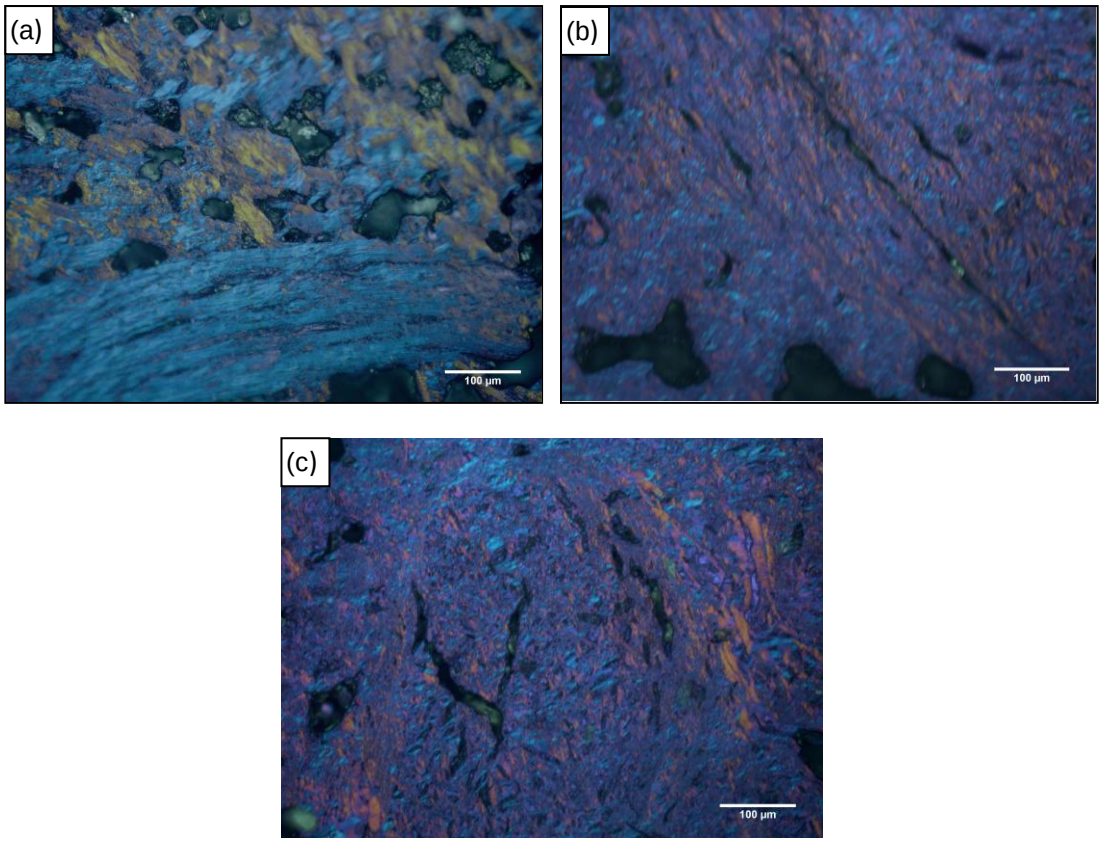

Figure 24: Polarised light optical micrographs of nuclear grade graphites: (a) PGA (b) NBG-10 and (c) NBG-18 all scaled to 100µm

PGA is anisotropic materials, i.e., has more than one refractive index and exhibits different degrees of light absorption in different directions within the crystal, resulting in the crystal showing a different colour, or different intensity of colour, when rotated 90° in plane-polarised light. Given the refractive index, n_i where i = 1,2,3..., the corresponding reflected light beams velocities produced by the incident light velocity C are given by eq.12:

$$\left.\begin{aligned} V_1 &= \frac{C}{n_1} \\ V_2 &= \frac{C}{n_2} \end{aligned}\right\} \quad \cdots\cdots\cdots\cdots\cdots\cdots \quad \text{eq.12}$$

Similarly, the relationship of velocity with wavelength, λ and frequency, f is give by eq.13:

$$v = \lambda f \text{.....}_{\text{eq.13}}$$

The wavelength of the light remains unchanged after reflection but the frequency changes and it is directly proportional to the velocity. Therefore, the lights produced after reflection will be different in colour.

The NBG-10 and NBG-18 graphites have an isotropic structure and the different intensity of colours at the reflecting surface is produced by phase change of multiple reflections. Isometric materials have only one refractive index. When a light ray is incident on the graphite which has a boundary of greater density than the current medium (air), the reflected ray undergoes a 180 degree phase change. The phase change is strongly frequency dependent. The measured phase difference is the combination of the phase change caused by the sample and phase shift due to the multiple reflections.

4.1.2 Scanning Electron Microscopy

Figure 25 shows Scanning Electron micrographs of (a) PGA, (b) NBG-10 and (c) NBG-18 graphites all scaled to 100μm. It can be seen that PGA has heterogeneous structure due to the distribution of binder phase and filler particles. NBG-10 and NBG-18 have a relatively homogeneous structure. Moreover, from SEM analysis PGA appears to be more porous than the other two graphites, this may be attributed to its lowest density as shown in Table 5.

The microscopic examination of these graphitised blocks samples of graphite appears to show the original filler grains incorporated in a graphitised binder structure. The apparent size of the filler particles is taken as the grain size of the materials. Generally, materials of finer grain size are stronger and more consistent in their properties than coarser materials.[13] It shows considerable porosity, with some long thin cracks, and some nearly spherical.

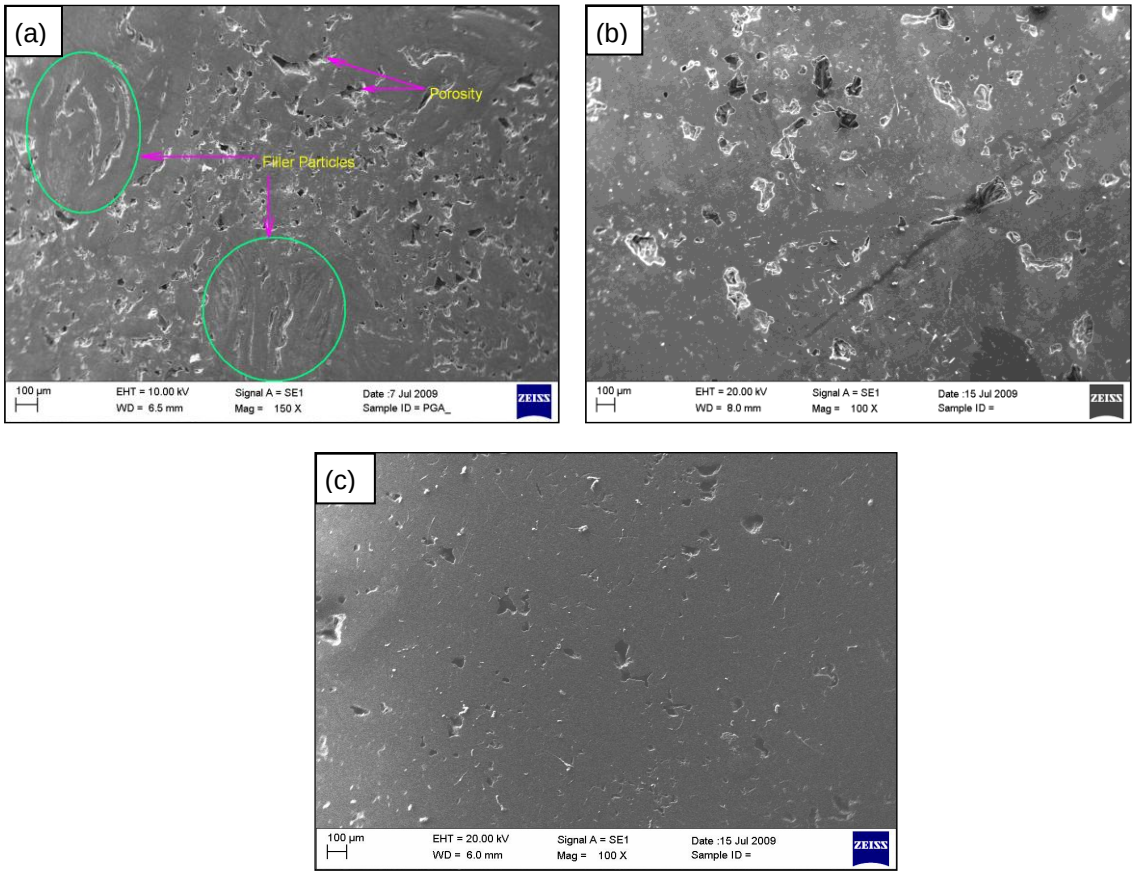

Figure 25: **Scanning electron micrographs (Secondary Electron Image (SEI)) of nuclear grade graphites: (a) PGA (b) NBG-10 and (c) NBG-18.**

The comparison between microstructure and pore distribution of unirradiated and irradiated NBG-10 nuclear graphite was obtained using SEM analysis and are shown in Figure 26 and Figure 27. The topography and morphology of the graphite have changed considerably after irradiation. Figure 27(a) and (b) show significant irradiation damage to the surface of the material which is inhomogeneous in comparison to unirradiated material.

A comparison of the change in pore microstructure and morphology are shown in the high resolution micrographs of Figure 26(c) and Figure 27(c). Prior to irradiation the graphite samples exhibits areas of oriented morphology, with the graphite crystals aligned and roughly equal in size. After irradiation the graphite crystals have become fragmented and are smaller. In addition, the graphite exhibits an amorphous structure.

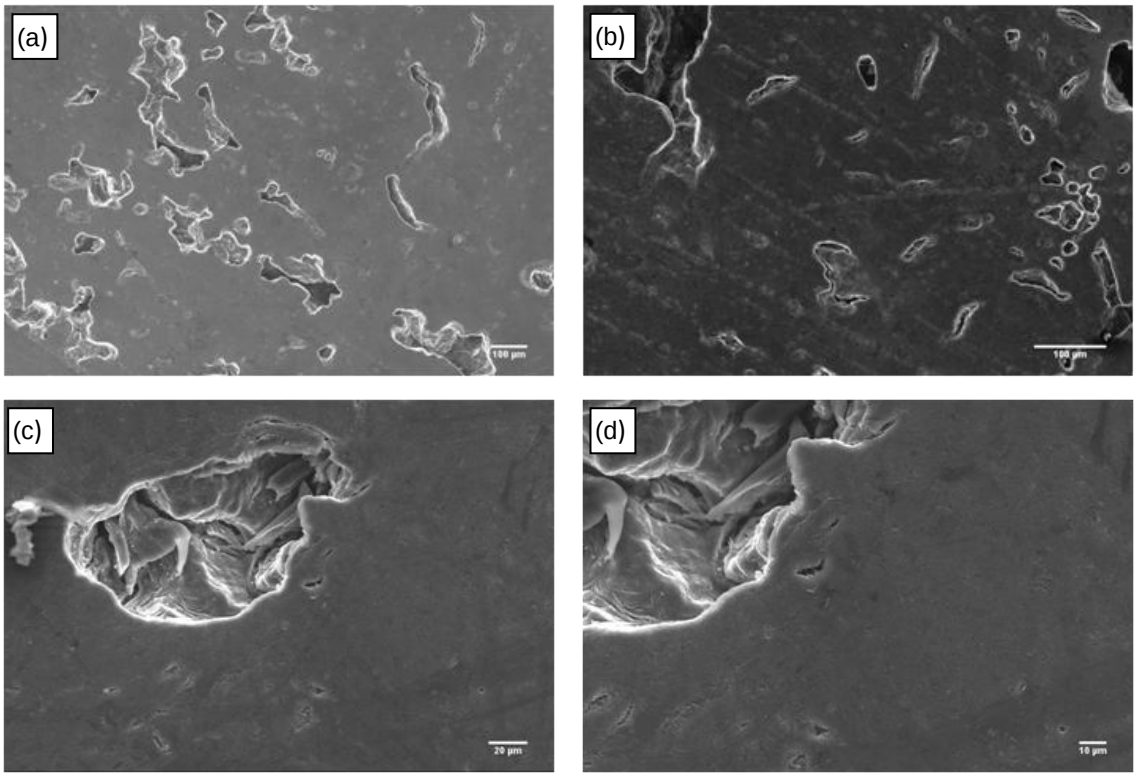

Figure 26: Scanning electron micrographs of unirradiated NBG-10 graphite. Scale: 100 - 10µm

A high resolution micrograph of NBG-10 is shown in Figure 27(d). The graphite exhibits a high degree of cracking within the porosity. These cracks have been observed within the structure of unirradiated graphite (Figure 27(d)) however, the occurrence and size had increased significantly after irradiation.

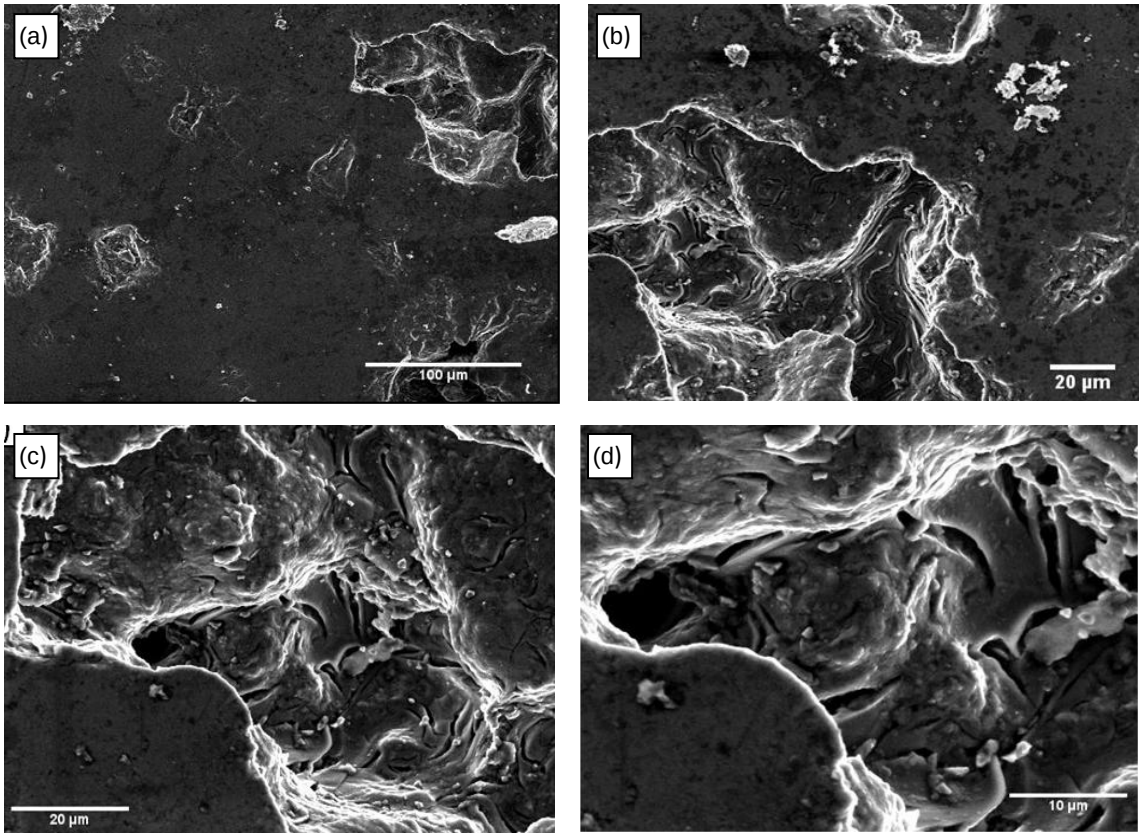

Figure 27: Scanning electron micrographs of NBG-10 graphite irradiated at 9.16dpa Scale: 100 - 10µm

Under neutron irradiation, expansion of the c-axis of graphite and contraction of the a-axis is speculated to occur.[12] This can lead to significant bulk dimensional changes and considerably alters the physical properties such as thermal conductivity, Young's modulus, Poisson's ratio, irradiation creep and electrical conductivity. Therefore, the knowledge of the crystallite structure and porosity distribution before exposure to irradiation is very important as it will help us to understand the affects of irradiated damage.

4.1.3 Transmissions Electron Microscopy

The pore space or porosity is an important factor that influences the transport rate of constituents towards the water phase both for monolithic and granular materials. Transport of water is easier in media with a high porosity than in a low porosity medium; therefore, a higher porosity generally leads to a higher release. In nuclear graphite, the bulk properties are governed by the porosity, in particular, the one in nanometre scale.[17] Therefore, it is the aim of this analysis to investigate the effect of irradiation on porosity of graphite.

Transmission Electron Microscopy of the typical microstructure of NBG-10 graphite is shown in Figure 28(a), (b) and (c). The microstructure of the sample graphite comprised of both graphitised and non-graphitised regions. The non-graphitised region consists of an aggregate of

small crystallites, each formed of a few graphite layer planes with some degree of parallelism and usually with many imperfections. These crystallites are generally randomly oriented.

During graphitisation the structure of graphite becomes dense and highly orientated [81]. The microstructural features of graphitised samples are seen in Figure 28(a) and the foil shows extensive Mrozowski microcracks and they are lenticular in shape. These microcracks run parallel to the graphite basal plane and about 20-60 nm in width. It was proposed that they were formed due to the thermal expansion coefficient difference along the grain and normal to the grain of graphite during slow cooling process of graphitisation [28, 85]. The graphite shows local areas of well ordered crystallites which are parallel to the basal plane such as those found on highly orientated pyrolytic graphites [81].

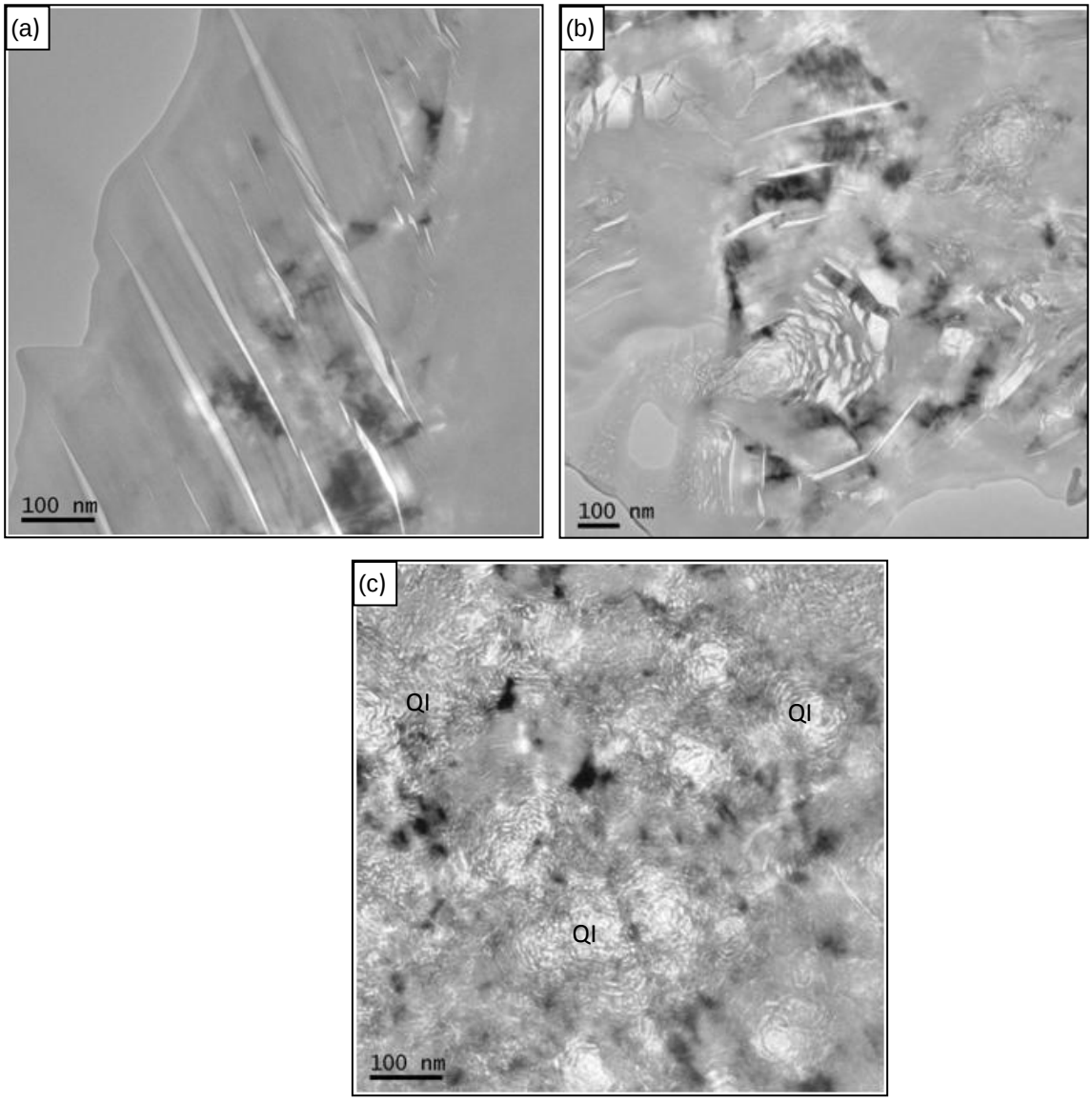

Figure 28: Transmission electron micrographs of NGB-10 nuclear grade graphite (a) Microcracks (b) graphitised and non-graphitised regions and (c) Quinoline Insoluble Particles (coalescence of quinoline insoluble (QI) particles) The scale bar is 100nm

Figure 29 shows the coalescence of small particles which were observed at the edge of the dimple created on the surface of TEM foil using electron beam milling. They are generally spherical in shape and are component of the quinoline insoluble (QI) (Figure 29(a) and (b)) particles of coal tar pitch and have been previously seen in carbon blacks produced during carbonisation of hydrocarbons.[54] The carbonisation mechanism of polyaromatic hydrocarbons is relatively straight forward. It starts by the breaking bonds between carbon and hydrogen and the removal of the hydrogen. Some of these hydrocarbons first go through an intermediate liquid or plastic stage known as “mesophase”, which occurs at high temperatures. This stage is at which the material shows the optical birefringence characteristic of crystals which have a lamellar arrangement with the long axes in parallel lines. During this melt stage**,** condensation takes place and large polyaromatic molecules are formed. These spherulitic liquid crystals gradually increase in size to build up sufficient mutual Van der Waals attraction to start promoting their alignment and crystallisation.[14]

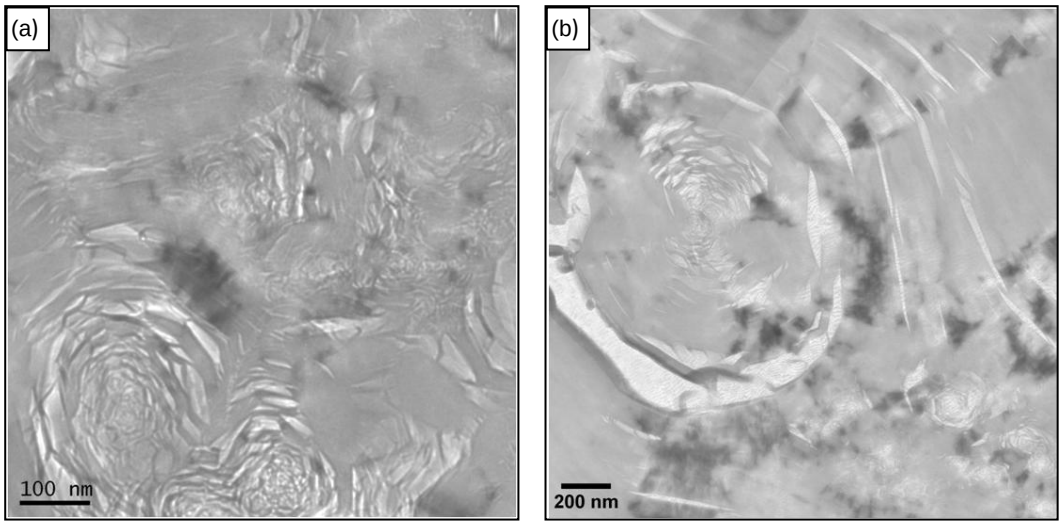

Figure 29: TEM micrograph of NBG-10 showing the coalescence of quinoline insoluble (QI) particles of coal tar pitch and cracks between the lamellas and bridged by crystallite – Scale bar 200 - 100nm

From Figure 30(a) it can be seen that the local arrangement of graphite layers can be disturbed by QI particles. QI particles (Figure 28(c)) are interfacial regions formed by the coalescence of mesophase spheres. Due to this association of QI and mesophase spheres the size of the mesophase spheres before coalescence appears to be greatly reduced by agglomerated QI particles.

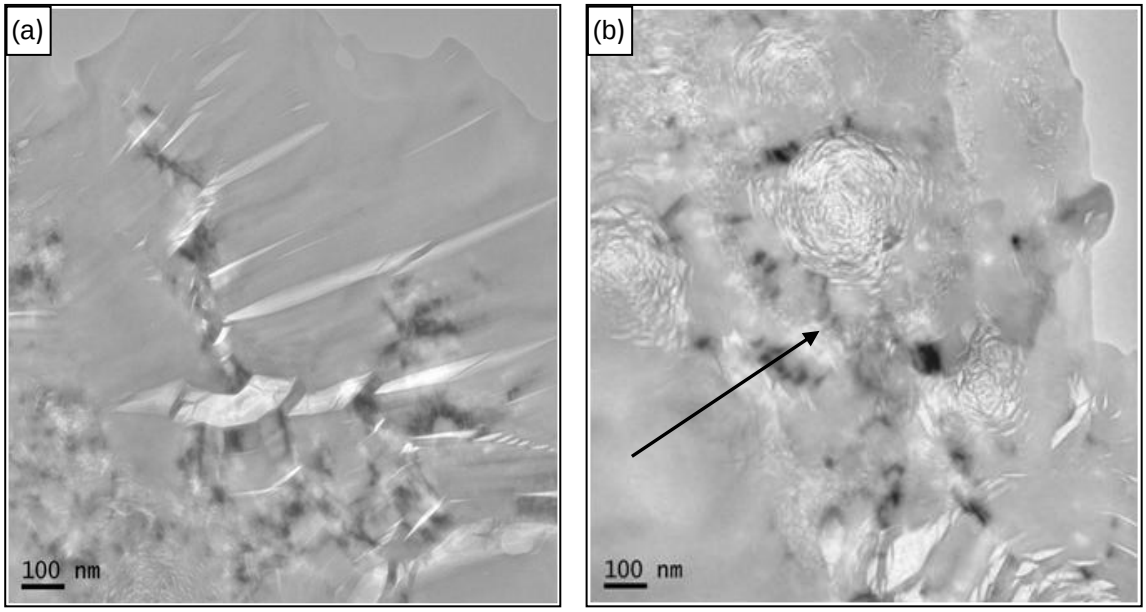

Figure 30: TEM micrograph of NBG-10 showing (a) crystallisation disturbance caused by QI particles and (b) arrow showing randomly oriented microstructures

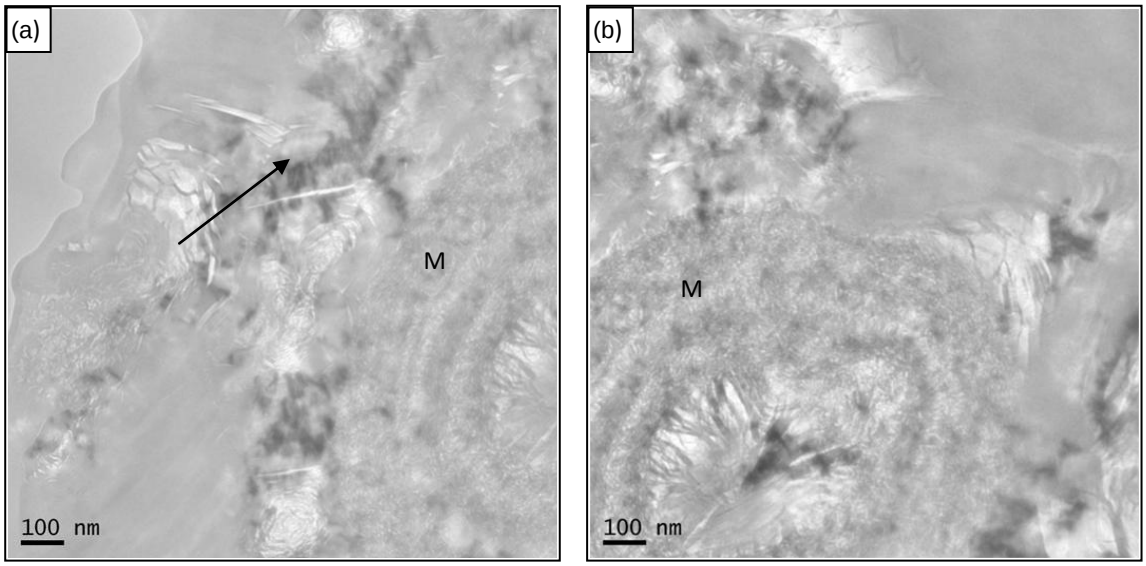

Figure 31: TEM micrograph of NBG-10 showing randomly oriented microstructures indicated by arrows and incomplete process of carbonisation indicated by the letter M – Scale bar 100nm

The other most important features are randomly oriented microstructures which are indicated by arrows in Figure 30(b) and Figure 31(a) and (b). These regions are formed between adjacent QI particles.

The other most intriguing microstructures are the areas which are labelled as M in Figure 31(a) and (b). They look like fishing net and these particles are arising from the incomplete process of carbonisation of the pitch and didn't get enough time at least to reach the mesophase stage.[14]

Agglomeration of QI particles were also observed in PGA graphite as it shown in Figure 32(a) and (b). Extensive Mrozowski microcracks (Figure 32(c)) were also observed a on the TEM foil and run parallel to the graphite basal plane. It also shows local areas of well ordered crystallites which are parallel to the basal plane. The lattice parameter size of PGA graphite layers is similar to that in NBG, but PGA has much bigger crystallite plane size.[86]

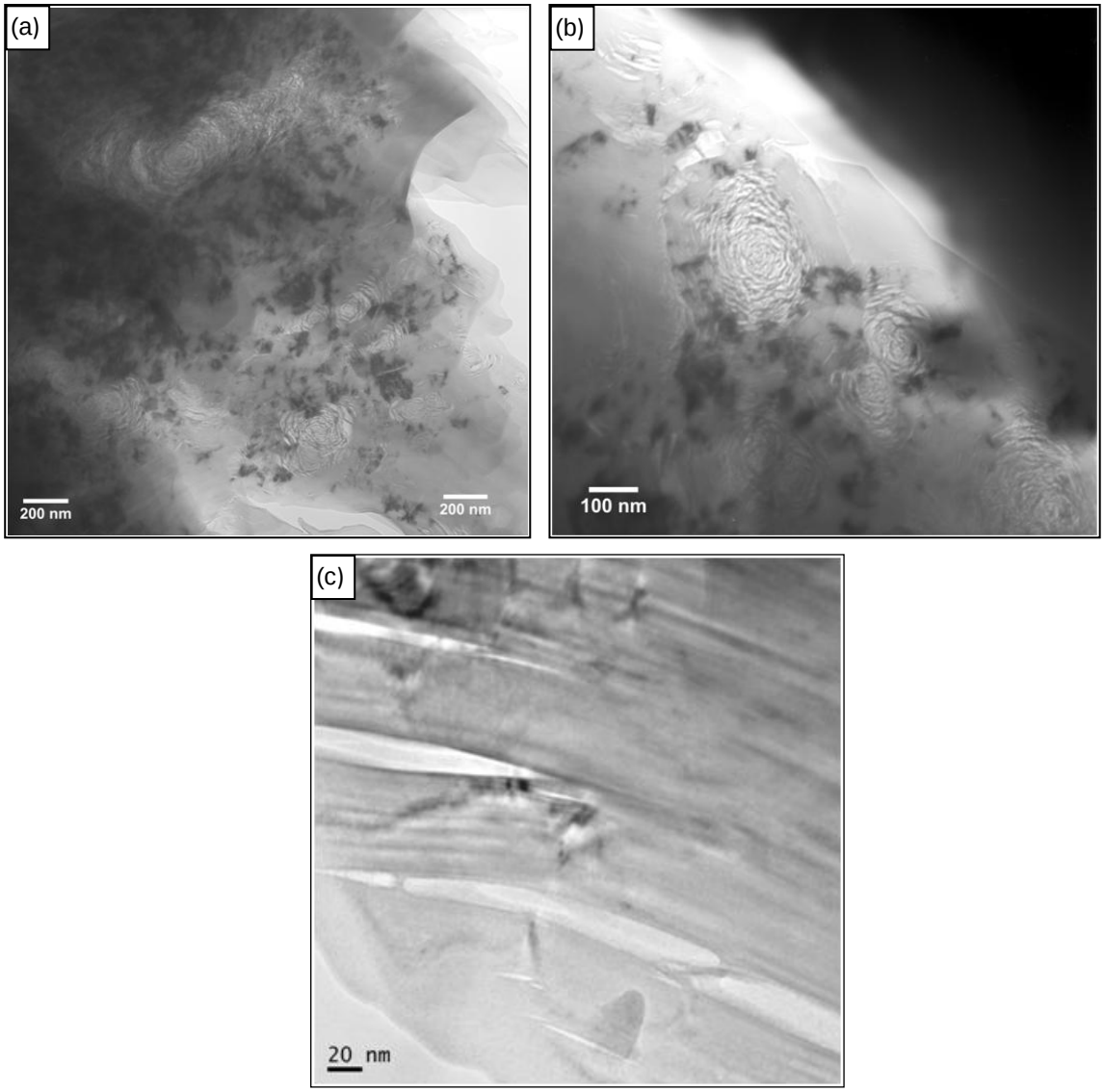

Figure 32: TEM micrograph of PGA showing (a) Quinoline Insoluble Particles (coalescence of quinoline insoluble (QI) particles) - scale bar 200nm (b) QI Particles - scale bar 100nm and (c) Microcracks - scale bar 20nm

Irradiated PGA Graphite

The principal objective of this investigation is to relate the physical properties of irradiated and radiolytically oxidised graphite samples to changes in their microstructure. Two interstitial channel samples and two fuel-channel samples taken at the same axial height were examined using Transmission Electron Microscopy (TEM) using dust/fragments resulting from the strength test.

Reactor graphite is a polycrystalline material; the crystallites are very small, and it is very difficult to produce large thin section suitable for transmission electron microscopy (TEM) particularly from irradiated material. One method of producing these samples is by using fragments or scrapings taken from a larger sample and to find some areas that are thin enough for TEM observation. To produce these tiny samples fragments or dust, a diametral compression testing was carried out on four larger graphite samples.

TEM micrographs and a corresponding selected area diffraction pattern of irradiated PGA nuclear grade graphite are shown in Figure 33. It shows graphitic characteristics of the graphite but the layer planes are randomly oriented caused by the bombardment of neutrons during irradiation.

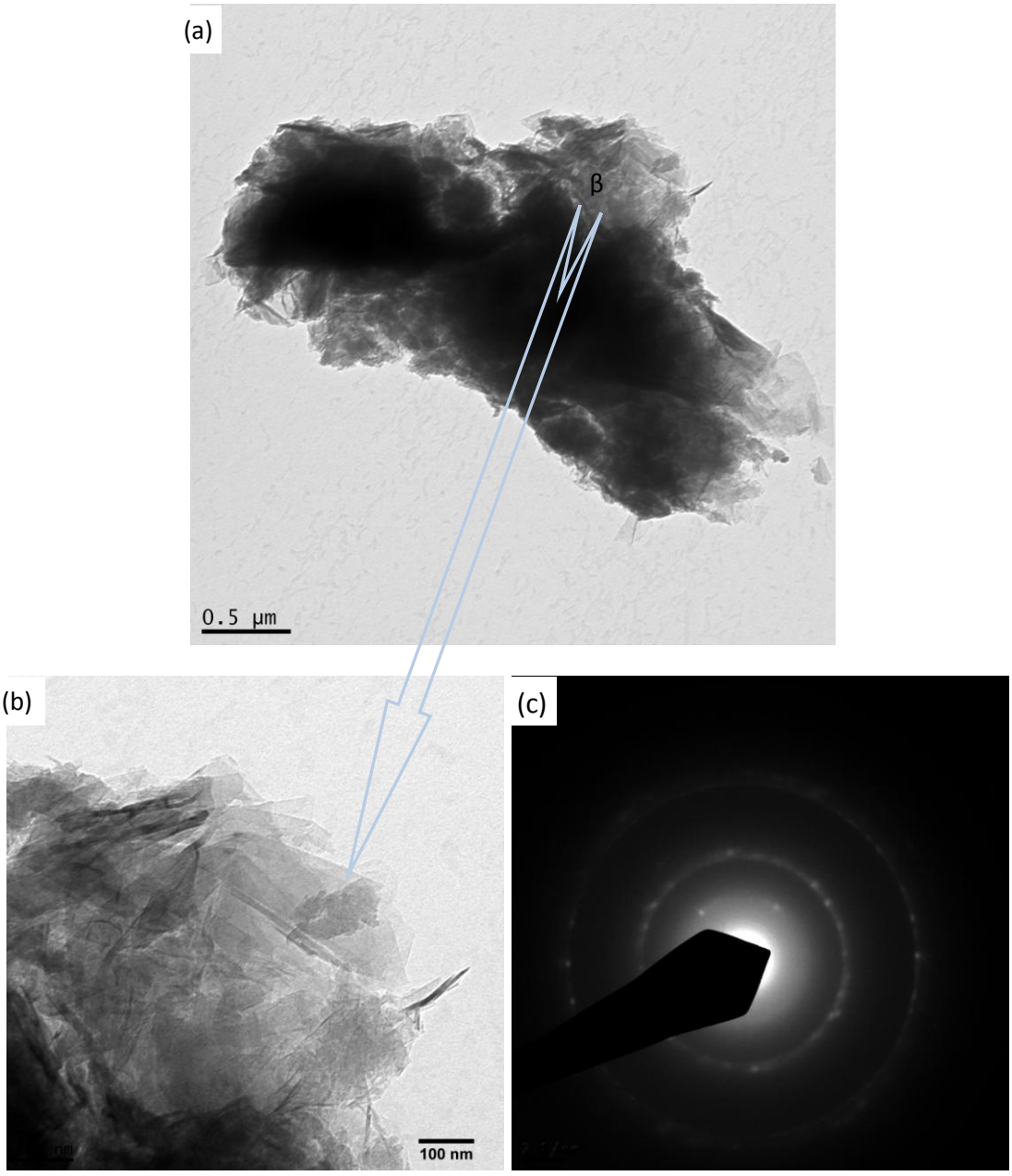

Figure 33: Transmission electron microscopy micrographs of irradiated PGA nuclear grade graphite (a) Large thin fragment scale bar is 0.5µm, (b) thin area labeled 'β' section from (a) scale bar is 100nm and (c)Diffraction pattern of thin area labeled 'β'

Figure 34 shows a micrograph from an irradiated polycrystalline specimen together with its corresponding diffraction pattern. The behaviour of defects is heterogeneous. The graphite was exposed to 6.69 dpa at a temperature of 338 °C and the defect size and concentration is varied with crystal perfection in the same specimen. During the analysis of irradiated graphite neither Mrozowski microcracks nor quinoline insoluble particles were observed and diffraction shown a breakdown of the crystalline structure in this region. The cracks may have been closed upon heating or by irradiation due to dimensional change of the graphite crystals.

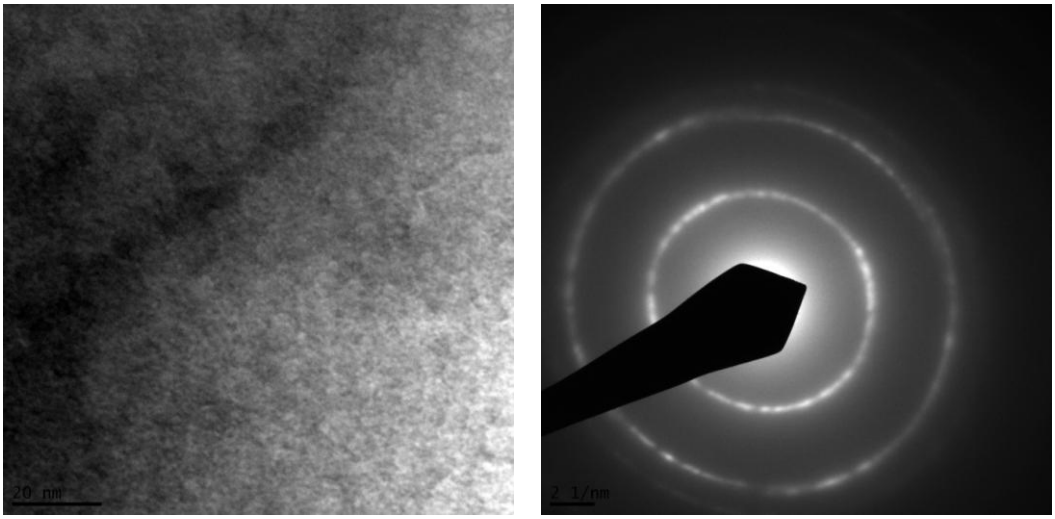

Figure 34: Transmission electron microscopy micrographs showing defects in PGA nuclear grade graphite irradiated at 6.69dpa at a temperature of 338°C together with corresponding diffraction pattern

4.1.4 X-ray diffraction

X-ray diffraction technique was used to determine degree of crystallinity, size and orientation of crystallites. The crystallites of the graphites are randomly oriented with respect to each other. Therefore, the scattering is the same in all directions so we only need to sample a one dimensional slice of the scattering, i.e., the angle is used to calculate the interplanar atomic spacing. Because every crystalline material will give a characteristic diffraction pattern and can act as a unique fingerprint. Figure 35 shows X-ray diffraction pattern of the three nuclear grade graphites samples used in the investigation all normalised to the (002) peak for comparison.

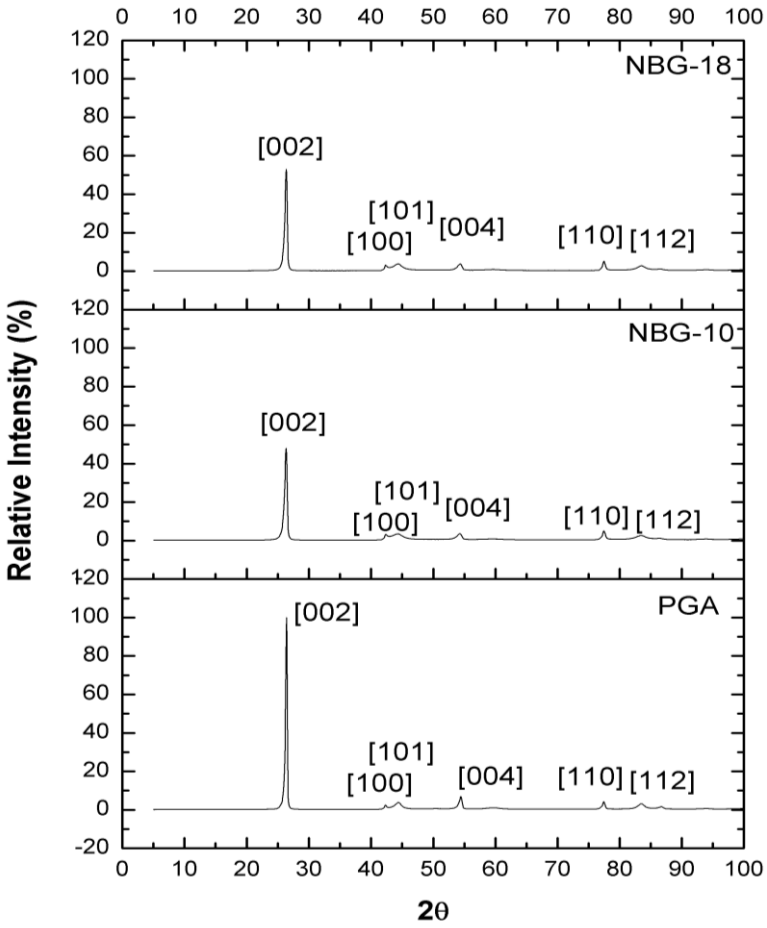

Figure 35: X-ray diffraction pattern of nuclear grade graphites PGA, NBG -10 and NBG -18, all normalised to the [002] peak

Since monochromatic $K\alpha_1$ wavelength radiation was not used profile fitting must be applied to correct the peak broadening error due to the $K\alpha_2$ wavelength. In addition, there are also strain broadening and instrumental broadening. These broadening errors must be corrected by superimposing the resulted x-ray diffraction patterns with a highly crystalline standard. Silicon was used as a standard because it is cheap, and readily available. It also has an infinitely large crystallite thickness. Note that the term 'infinitely large' used here is with relation to the wavelength, λ, which is approximately 1 Angstrom. Elementary diffraction theory assumes an infinitely thick perfect crystal.

Most profile fitting programs give FWHM, but for accurate size-strain broadening integral breadth as a measure of the peak width is better. Integral Breadth (β) is the width of a rectangle with the same height and area as the diffraction peak.

$$\text{IntegralBreadth} = \frac{\text{Area}}{\text{Height}}$$

Both the area and height of the peak were derived from the computer analysis. Both values are free from amorphous halo (background). Then, the calculated values were used to calculate the crystallite thickness using the Scherrer equation. For graphite x-ray diffraction patterns at (002) and (110) peaks are the standards which are used to calculate the crystallite parameters. These planes are chosen because the planes are parallel and perpendicular to the direction of extrusion respectively.

The crystal symmetry and the unit cell dimension of nuclear grade graphites namely Pile Grade A (PGA), NBG-10 and NBG-18 were derived from the analysis of X-ray diffraction patterns. The average crystallite thickness (L_c) and width (L_a) were also obtained. As it can be seen form Figure 36 PGA has a long and narrower diffraction peak at (002) while the NBG grades have broader and shorter peaks indicative of PGA has larger aligned crystallites.

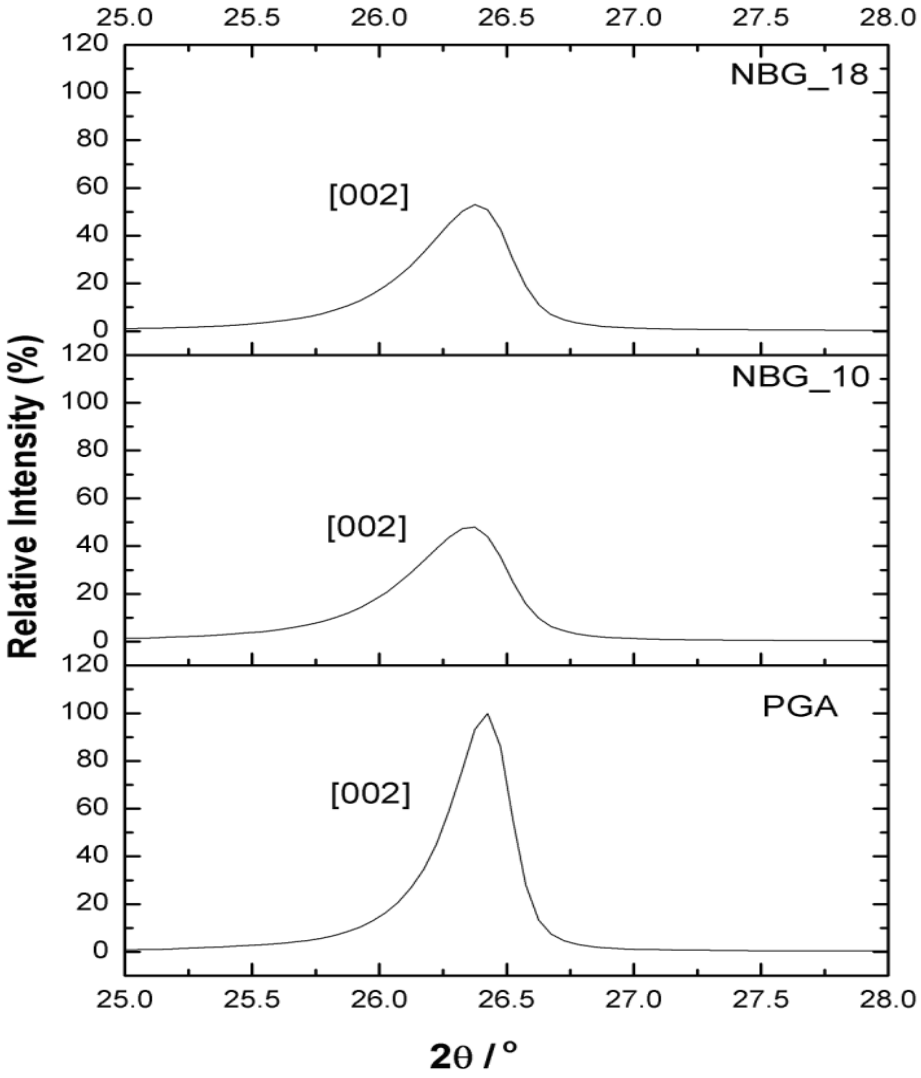

Figure 36: X-ray diffraction pattern of nuclear grade graphites PGA, NBG -10 and NBG -18 at [002] peaks, all normalised to the [002] peak of PGA

In order to examine the orientation alignment of the *c* and *a*-axis of the graphite and investigate the average layer diameter and thickness, X-ray diffraction spectra of the graphite (002) and (110) diffraction patterns were obtained separately. The thickness in the c-axis direction L_C was obtained from the widths of the (002) peaks and the distance L_a in the a-axis directions from the widths of the (110) peaks of each graphite, these are standard peaks for graphite. These x-ray diffraction spectra of the graphite were fitted with the x-ray diffraction spectra profile of silicon at (111) and (110) peaks respectively to correct broadening.

The results from these calculations are shown in Table 15. PGA has a typical crystallite size of 378Å and 292Å in *c*- and *a*- directions respectively, these are comparable with quoted reference values of 435Å and 400Å for the L_c and L_a of PGA respectively.[18] It may be noted, these Lattice spacings are larger than the other two graphites. Table 16 shows the calculations from lattice parameter measurements, all graphite grades show similar lattice spacings in the directions of L_a, $L_{a'}$ and L_c. The distance between neighbouring planes (L_c) is greater than the distance between atoms within the hexagon (L_a); therefore, this shows that the bonding between the atoms in the horizontal layers is greater than the bonding between the layers.

Table 15 : Crystallite dimensions (*c* and *a*) of nuclear grade graphites calibrated at (002) and (110)

	L_c (Å)	L_a (Å)
PGA {002}	378	-
PGA {110}	-	292
NBG-10 {002}	200	-
NBG-10 {110}	-	185
NBG-18 {002}	220	-
NBG-18 {110}	-	256

Table 16 : Lattice spacing of nuclear grade graphites calibrated using XRD

Material	a (Å)	c (Å)
PGA	2.463	6.732
NBG-10	2.462	6.743
NBG-18	2.463	6.737

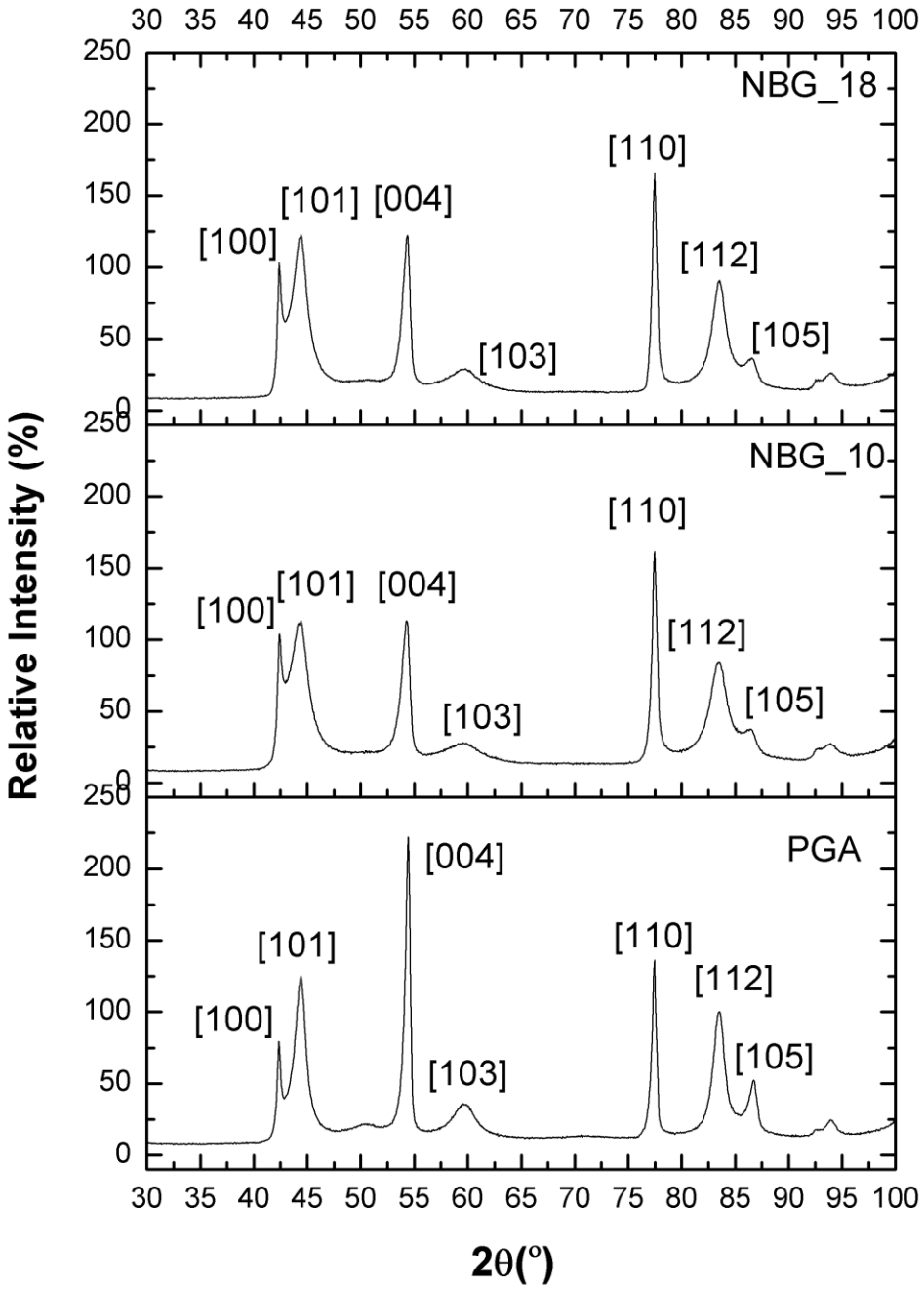

Figure 37: X-ray diffraction pattern of PGA, NBG -10 and NBG -18 nuclear grade graphites excluding [002] peak, all normalised to the [004] peak

The structure of graphite is hexagonal with four atoms in the unit cell as discussed earlier (section 2.2 Figure 2). However, this structure does not account for some faint lines that occur on the X-ray diffraction of the graphites shown in Figure 37. The hexagonal planes which form a perfect crystal structure are (00ℓ), (0k0), (h00) and (hk0), any family of planes which are not included in this family planes is not the part of the crystal structure. The extra lines in the diffraction pattern could have been assumed they are formed may be due

to defects in the graphite structure, but they are occurring at regular intervals (h0ℓ), i.e., (101), (103), (105)… and therefore, this assumption is not the case.

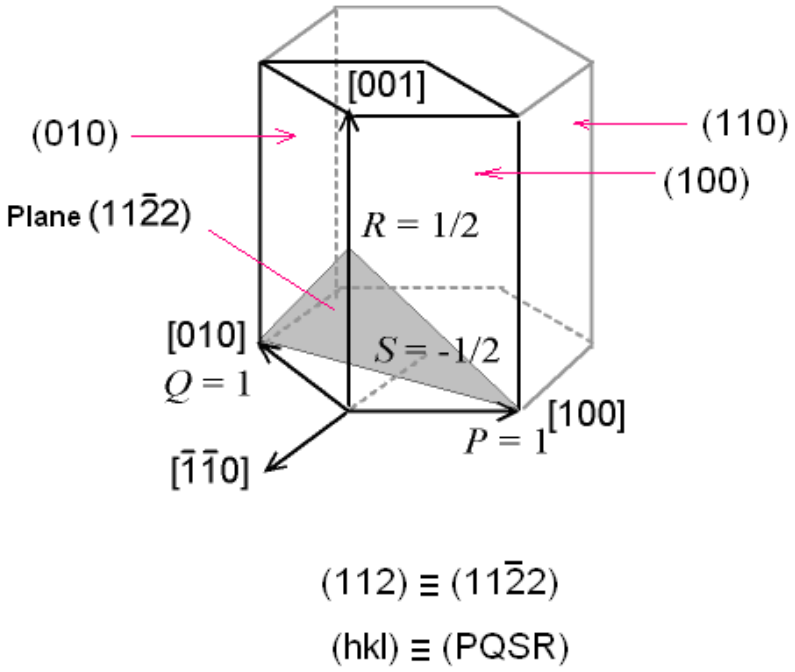

Figure 38: Hexagonal lattice structure showing (112) plane of a rhombohedral

In ordinary graphite structure (Figure 2) it consists layers of carbon atoms forming hexagons with shared edges; each layer has half its atoms directly above atoms in the layer below, and the other half above the centres of hexagons. The complete structure is formed by repeating these layers in such a way that alternate ones are similar. In Figure 2 such layers are shown by hard lines and broken lines. However, in Figure 3 it can be seen that there is a third type of layer which is shown by a different broken lines which is symmetrically related to the other two. Therefore, it can be imagined that these three layers repeat sequentially. The peaks (101), (103) and (105) correspond to diagonal planes in a crystal lattice and there are no such planes in a hexagonal lattice. In addition to this, the (112) peak in the X-diffraction pattern, Figure 37, is accounted for the (112) plane in rhombohedral lattice as shown in Figure 38. It can be concluded that the material consists hexagonal lattice with a small number of rhombohedral lattices. Lipson and Stokes [87, 88] also clearly showed that the rhombohedral lattice is fully accounted for the extra X-ray patterns found in graphite.

4.1.5 Tomography

The chemical purity of the original graphite very important, because it will determine the isotopes partly that become activated during neutron irradiation, and thus ascertain the radionuclide inventory which it may be disposed. The assessment of impurities in unirradiated graphite using XCT has been structured in three phases.

The first stage was to measure the amount of the total impurity in the two graphites. The next stage was to sub-classify the pores based upon the pore size, shape, and structure and high attenuation impurities. A region of interest (a cube of box) was cut out from the whole sample CT scan in order to reduce the dataset to a manageable size. The region of interest was segmented by separating the porosity and high attenuation impurities from the coke by setting a greyscale threshold. The final stage of the analysis was to get a distribution of high attenuation impurities in PGA graphite and the association of impurities with the pores.

The XCT scans were carried out on the graphite specimens using Nikon Metris 225/ 320 kV Custom Bay. The voxel size achieved for each scan was 12.01 x 12.01 x 12.01 μm^3. A single scan was performed on each specimen to achieve the data. All the scans on the samples were carried out with the same settings.

The scanning was performed with the 225 kV source and a tungsten x-ray source using a voltage of 55 kV and a current of 170 µA. The data acquisition was carried out with an exposure time of 1980 ms (0.5 frames per second). The number of frames per projection was 1 and the total number of projections was set to 2000, this has resulted in 1 hour and 6 minutes acquisition time. The resolution of the resulting radiographs was 12.01µm and it was calculated from the geometry of the acquisition conditions are a factor of the sample size and shape.

Reconstruction

For any sample the feature of interest has to be at least two voxels in size to be visualised clearly and the visualisation is also dependent on the attenuation resolution. For all scans the reconstruction settings were similar. The CT-Pro software from Nikon Metris was used for the reconstruction of the acquired data. The beam hardening correction setting was set to 2 (out of a range of 1–6) because the range represents number of iteration and a setting of 2 was suggested by Ramakrishna, K., et al.[67] During scanning the attenuation of the x-ray at any point depends on the material composition at that point and on the energy spectrum of the beam. But the x-ray beam emitting from the x-ray source contains photons at different energies which cause problems during reconstruction.

The energy spectrum of the x-ray beam hardens as it passes through a specimen and the attenuation at a certain point is generally higher for lower energy photons. As the specimen rotates and the x-ray beam travels in different directions to a particular point inside the specimen it results in different spectra; thus the attenuation will differ at the point of interest. This makes it complicated to assign a single value for the attenuation coefficient at that point. The issue of beam hardening is that for any source and detector pair the reconstruction procedure requires different spectra energy from the projection. This results in achieving wrong gradients of the linear attenuation coefficients in the CT cross section images, resulting a false

density or composition gradient in the scanned images. Therefore, rectification for this beam hardening effect is a must during analysis of CT scanned images.

The noise produced from the heat generated by detector and the resolution of the scanner reduces the quality of the image during reconstruction. To overcome this problem the CT-Pro software has six different noise reduction levels. So, the noise reduction was set at level two because the noise produced by the scanner is fairly low. Since the reconstruction data is dense and to interlace the upper and lower fields interpolation was used. In digital signal construction interpolation refers to the method of converting a sampled digital signal to a higher sampling rate using different digital filtering procedures.[89] The volume was reconstructed with a resolution quality of 100 % and a quality of 100 % to create a good quality image without any loss of resolution. The resulting reconstruction time was 54 minutes.

The reconstructed data is 32-bit resulting in there being a large amount of data to manipulate. To overcome this problem the data was reduced to 8-bit for visualisation and processing. This was achieved by loading the data set into the MATLAB software and then, converted from 32 bits to 8 bits and the greyscale was remapped from [0, 420] to [0, 255].

Visualisation

Avizo version 7.0 was used to visualise the images produced. The software was developed by Visualisation Science Group and is used mainly for segmentation and skeletonisation. The resulting images for the specimens are shown in results section.

4.1.5.1 PGA Graphite

Analysis of Whole Volume Sample

The analysis routine assumes that the pores in nuclear graphite can be categorised into 3 types [81]:

1. Lenticular pores - large cracks in filler particles that tend to lie parallel to the basal planes, and are formed by volumetric shrinkage during the calcination of the filler particles.
2. Gas evolution pores or gas entrapment pores – pores within the binder phase or matrix which forms during the mixing and baking stage of graphite manufacture.
3. Small narrow pores - slit-shaped pores in the binder phase or matrix that are formed as a result of either volumetric shrinkage during baking or by anisotropic contraction when cooling down from the graphitisation temperature

The advantage of CT over SEM is that the virtual micrographs of PGA graphite which are obtained by SEM and CT are shown in Figure 39. Physical surface visualisation using the SEM is difficult without grinding and polishing of the specimen. One can visualise surface features of a specimen using SEM but the bulk internal features such as information about distribution of pores, internal structures and impurities are obviously not possible to visualise or quantify. Figure 39(a) shows the 2D SEM micrograph of PGA graphite provides only information on the surface the sample. In contrast, Figure 39(b) is also a non-destructive analysing method and does not necessitate sample preparation to create cross-sectional images.

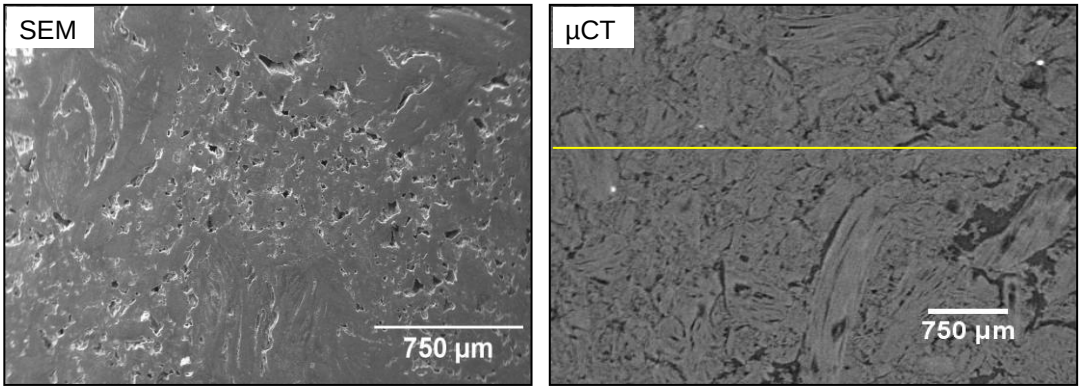

Figure 39: Micrograph of PGA nuclear graphite (a) SEM (b) µCT

Initial data reconstruction acquired using CT allows analysis of 2D image cross-sectional slice image and 3D tomographic virtual replica of the specimen to be constructed, which provides detailed information about distribution of pores, internal structures and impurities. For qualitative visualisation the coke, pores and impurities were identified from the structure using a greyscale thresholding technique based on a histogram analysis from the radiograph obtained from scanning. The different greyscale digital values represent the different physical densities of the features inside the material. Before any analysis the reconstructed images were filtered with median filter to reduce the noise that might have been caused by beam hardening. The median filter slightly reduced the edge sharpness of image of material but the change was insignificant.

A histogram of a typical PGA slice image is shown Figure 40(a) and it shows well-defined minima and maxima from which one can automatically define a threshold values. Figure 40(b) illustrates greyscale profile of PGA cross-sectional slice image (Figure 40(b) yellow line). The profile clearly indicates that there is distinctive difference among the features of the graphite, i.e., the coke, the pores and the impurities. The value of the thresholds that were derived from the histogram (Figure 40(a)) was applied to the entire stack for coherent segmentation. A change in threshold cutoff by 1 greyscale value results in a variation in porosity by approximately 0.39%.

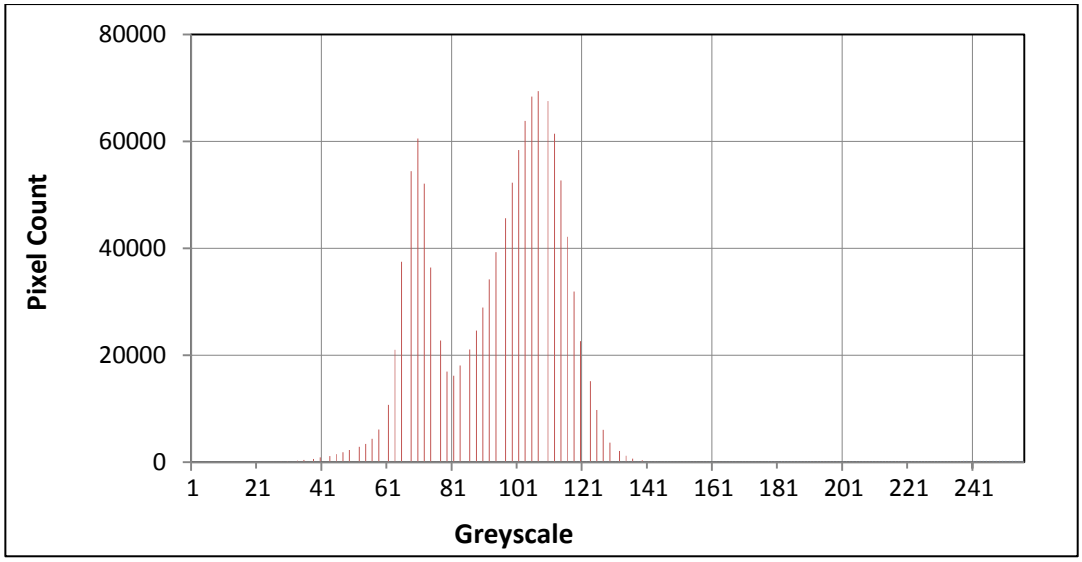

(a)

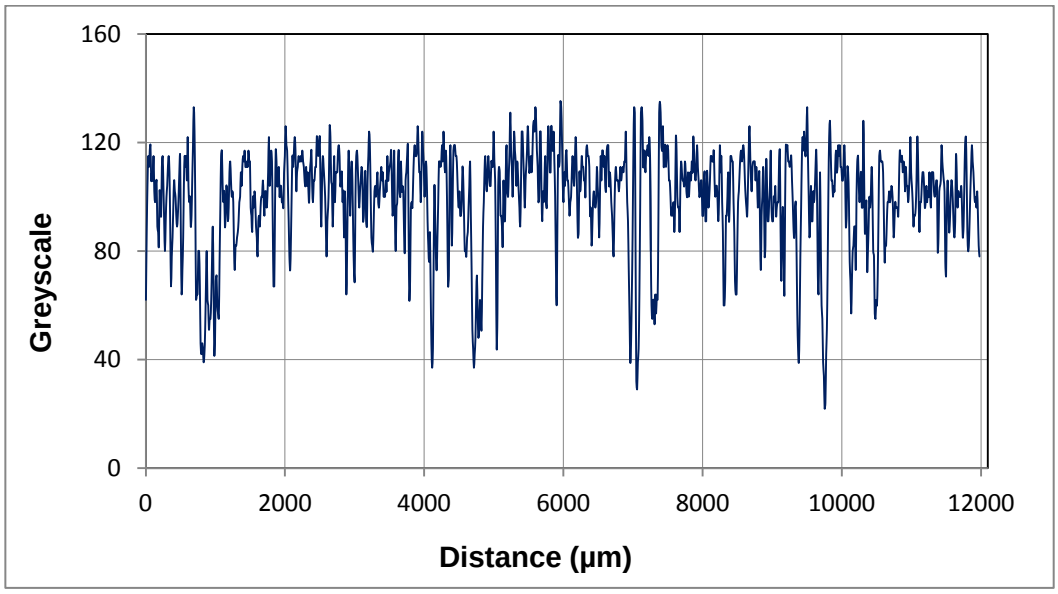

(b)

Figure 40 : Thresholding value with respect to greyscale distribution: (a) A greyscale value histogram of the median filtered raw image data (Figure 39b). (b) A profile of the greyscale values across the distance of the same image.

One can easily distinguish in Figure 39(b) the binder, the filler, the pores and the impurities by structure as well as brightness, and within the layers one can distinguish the distribution of different pores, e.g., gas evolution pores and lenticular pores.

The sensitivity of the CT equipment is capable of distinguishing the difference among the coke, the pores and the impurities. Moreover, one is able to differentiate differences in the pore structures inside the binder and the filler features but the structure of the binder or the filler themselves could not be analysed separately as they have the same gray scale.

The first analysis performed was to separate out and measure impurities by segmentation. Thresholding plays a critical role for the segmentation process. The greyscale was set by selecting the correct colour of interest using the greyscale values measured in Figure 40(a). One can also use the magic wand tool (if available), known simply as the Magic Wand. The Magic Wand is a selection tool and unlike other selection tools that select pixels in an image based on shapes or by detecting object edges, the Magic Wand selects pixels based on tone and colour.[90] Then, the remaining unlabelled impurities were selected by thresholding after the holes were filled. The brightness of the greyscale indicates x-ray absorption intensity of the carbon itself and any elemental impurities, elements with high atomic numbers or densities such as metals tend to be white in colour.

Figure 41: Impurities in PGA graphite

The filler and binder phases are both carbonaceous and they are gray in colour where as the pores and voids are dark or black. The skeletonisation and analysis was carried out on the whole sample and the total area assigned as impurities is shown Figure 41. The impurities were measured using a quantification tool to obtain the impurities ratio. The total impurities on the graphite were found out to be very low, about 0.01%.

Analysis of Reduced Cubic Volume Sample

An analysis of the type of pores and the ratio of their distribution was performed on three PGA specimens. The 3D tomographic virtual model constructed from the original graphite sample was reduced to a small cube (to reduce the data) to reduce the analysis time to a manageable period. The size of the reduced cube was 2.4 x 2.4 x 2.4 mm^3 in size and the constructed cube is shown in Figure 42(a). Figure 42(b), (c) and (d) shows 2D radiographic images of the graphite slice the XY-plane, YZ-plane and XZ-plane respectively. The pore distribution along the sample thickness was obtained from every slice, i.e. the labelling was made slice-by-slice selection. In addition to pore distribution the impurities were characterised from the examination of all the slice images. The 3D virtual selection of the high attenuation impurities inside the boundary box is shown in Figure 42(f).

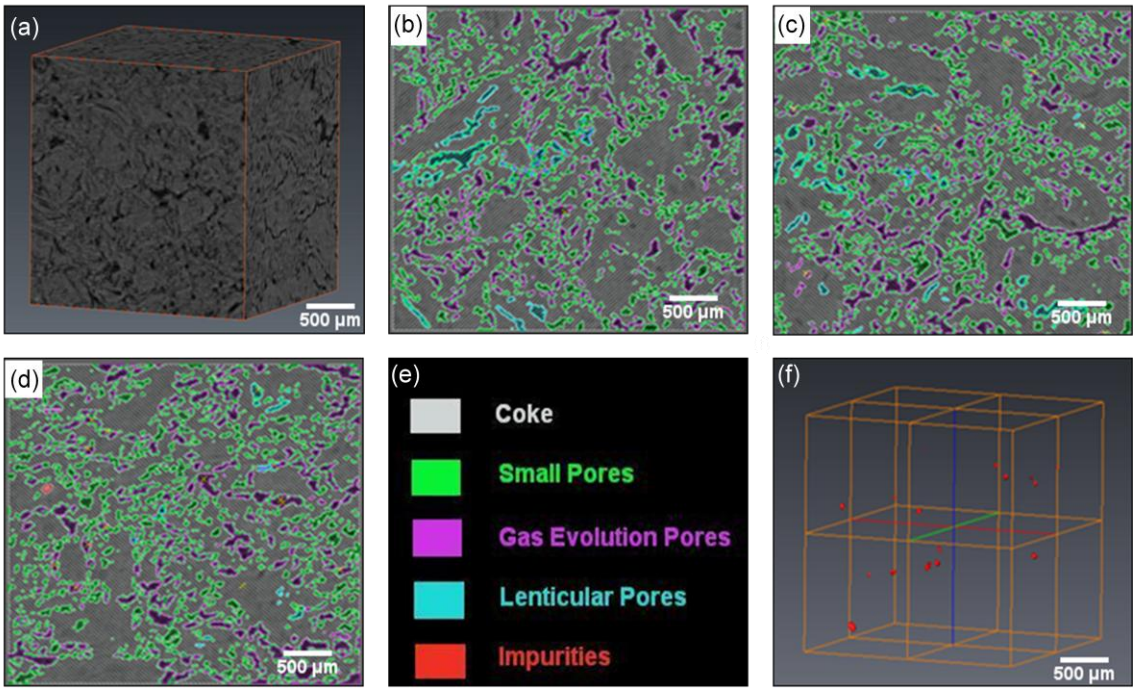

Figure 42: Labelling of PGA graphite (a) Reduced cube cut out of the main specimen (b) 2D radiographic cross-sectional image of the XY-plane), (c) YZ-plane, (d) XZ plane, (e) label of features and (f) 3D bounding box showing high attenuation impurities

By labelling the pores on each image slice, a pores distribution along the width and length direction can be recreated. Labelling was used in order to carry out the calculation and visualisation in image processing software package Avizo 7.0, which can make contour plot of the pixel value. The total pores in the cube sample then was statistically summarised. Based on the binarised image, the three dimensional features in the samples were created for visualization as shown in Figure 43. The analysis of the samples are summarised in tabulated form in Table 17.

Table 17: Quantitative analysis of PGA graphite features

Materials	Count	Volume	Deviation	Ratio (%)
Coke	5961979	10.3452	1.71	73.42
Small Pores	1192191	2.0687	1.31	14.68
Gas Evolution Pores	854250	1.4823	2.57	10.52
Lenticular Pores	111102	0.1928	2.66	1.37
Impurities	1079	0.0019	6.39	0.01

The average bulk porosity is about 26 % which is similar to the porosity values measured by other scientists [62, 91]. Figure 43(a) shows the whole specimen and the size of the cube slice cut out from it. The reconstructed cube slice is shown in Figure 43(b) and its virtual labelled model is shown Figure 43(c). The porosity distributions are typically divisible into three segments; small pores, gas evolution pores and lenticular pores and all represent the total pores found inside the graphite (Figure 43(d)). The two main pore regions are the gas evolution pores and lenticular pores and are shown in Figure 43(e) and (f). Gas evolution pores are interconnected pores with large pores throughout the pore system. The lenticular pores are recognisable by their distinct shape and orientation (Figure 43(g)); they tend not to be interconnected. Figure 43(h) shows the high attenuation impurities found in the cubic slice.

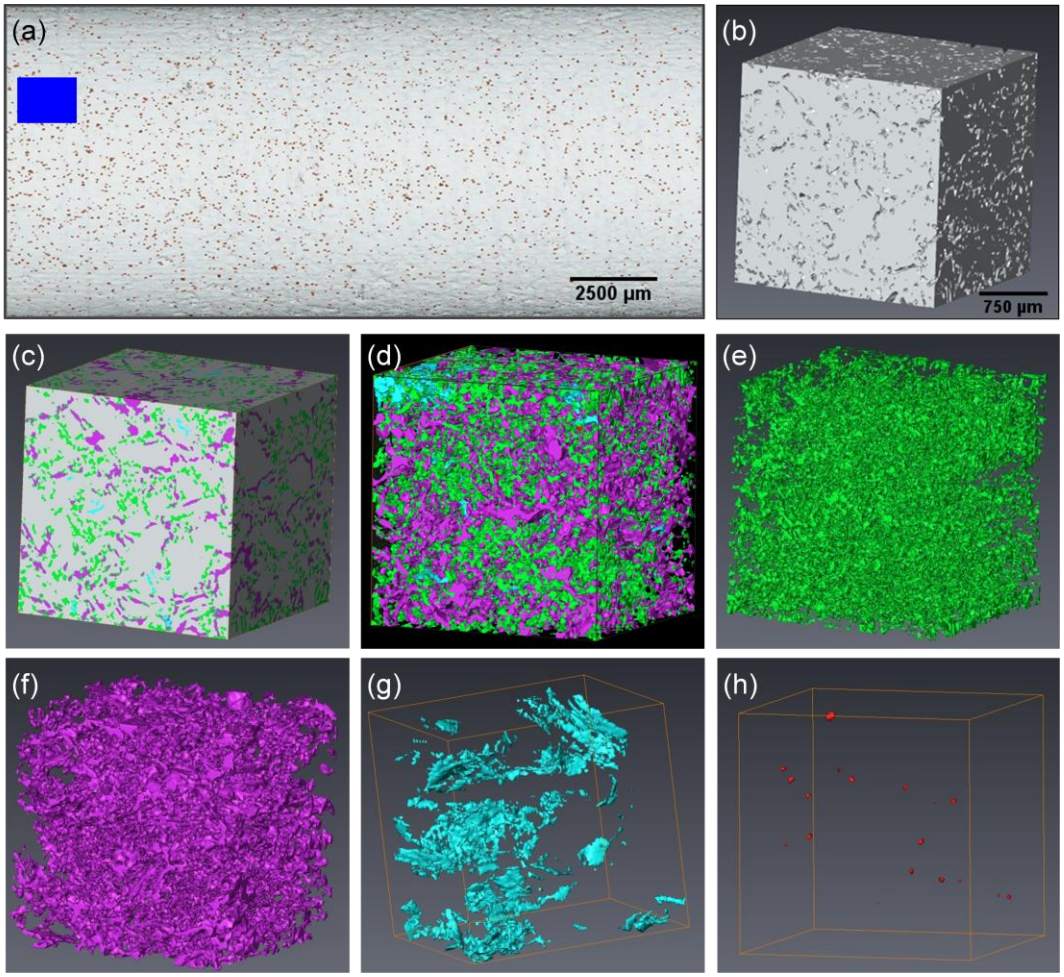

Figure 43: Segmentation and Skeletonisation of PGA graphite (a) reconstructed specimen, (b) Reconstructed slice, (c) virtual model, (d) all pores, (e) small pores, (f) gas evolution pores, (g) lenticular pores and (h) impurities

4.1.5.2 Gilsocarbon Graphite

The radiographs of PGA and Gilsocarbon graphite are shown in Figure 44. These micrographs show the different types of pores that are present in the two grades of graphite. The anisotropy of the PGA is apparent from the arrangement of porosity distributions in the three directions. In contrast, Gilsocarbon is denser, with less porosity, and the majority of the graphite crystallites are highly orientated, with less gasification pores evident. The distribution of pores is due to choice of raw materials and manufacturing process.

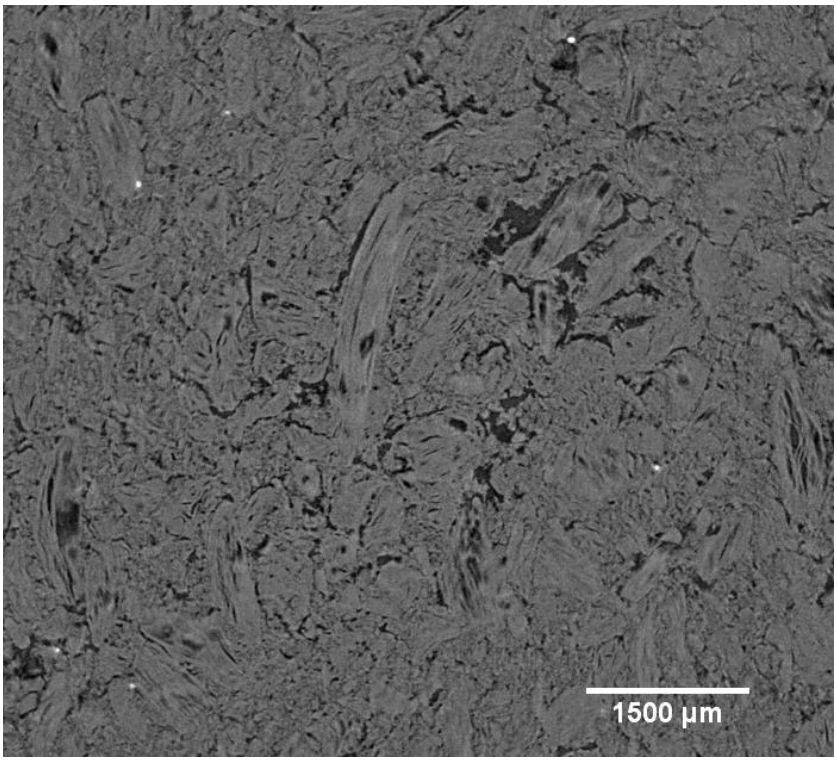

(a)

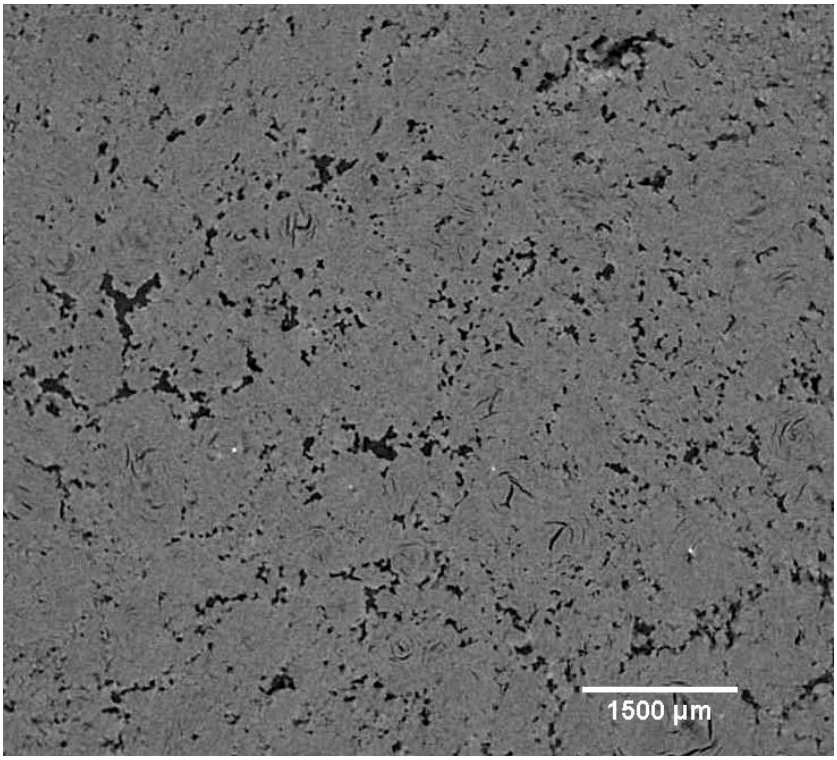

(b)

Figure 44: Radiographs of (a) PGA and (b) Gilsocarbon graphites

The analysis to measure porosity distribution and impurities by segmentation was also performed on three Gilsocarbon graphite samples and the average of the measurements was taken. The analysis was on the whole sample and on a small cube (2.4 x 2.4 x 2.4 mm^3) sliced out of the 3D tomographic virtual model of the original graphite samples. Then, the impurities were measured using quantification tool and the impurities ratio was quantified. The total impurities on the graphite were found out to be about 0.003%, which is much less than the impurities found on PGA graphite.

The analysis of the type of pores and the ratio of their distribution was also studied. The result of the analysis is shown in Table 18. It shows that the percentage (~11 %) of the pores is much less than that of the pores percentage of PGA graphite. This fact is apparent from the coke ratio as the Gilsocarbon has contained more coke.

Table 18: Quantitative analysis of Gilsocarbon graphite features

Materials	Count	Volume	Deviation	Ratio (%)
Coke	7193678	12.4618	1.53	89.028
Small Pores	115140	0.1995	1.71	1.425
Gas Evolution Pores	701712	1.2156	2.16	8.684
Lenticular Pores	69470	0.1203	2.46	0.860
Impurities	200	0.0004	6.04	0.003

4.1.5.3 Distribution of Porosity on PGA Graphite

The purpose of this section is to study the distribution of high attenuation impurities and to investigate whether the impurities are associated with the pores or not. The technique scatter plot with labels is used to plot the data which was obtained using Avizo software from the reconstructed CT scans. The x and y axes were plotted as horizontal and vertical data points, respectively and the z axis value as a label. The labeling will help us to distinguish between pores and impurities from impurity and impurity and pore and pore overlapping. As it can be seen from Figure 45 most of the high attenuation impurities are inside or very close to the pore. This shows that the impurities are accessible for the leachant to be leached out once they are activated with the bombardment of neutron flux.

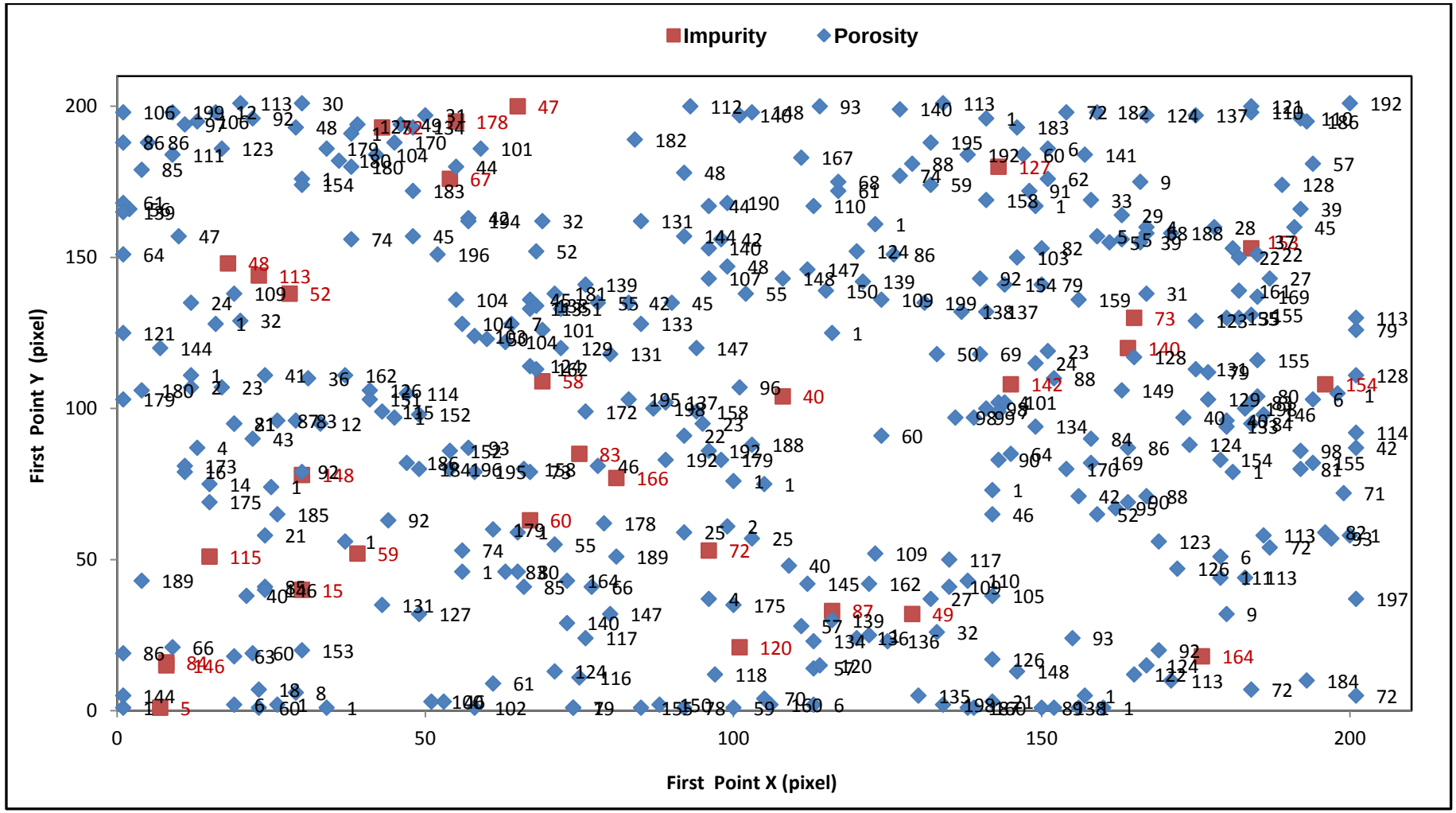

Figure 45: The Distribution of High Attenuation Impurities and Porosity.

4.1.6 EDX analysis

Energy dispersive spectroscopy (EDS) in combination with scanning electron microscopy (SEM) was used to identify the element or elemental composition of impurities inside nuclear graphite.

EDS is used to obtain a localised chemical analysis using the X-ray spectrum scattered by a solid sample when it interacts with a focused beam of electrons. In principle, elements from atomic number 4 (Be) to 92 (U) can be identified but not all instruments have the ability to measure all these elements [92]. The determination of the concentrations of the elements present involves the identification of the lines in the spectrum. The quantitative analysis requires measuring line intensities for each element in the sample and comparing it with the same elements in Calibration Standards of known composition.

When an incident beam from the gun interacts with the sample atoms, with slight loss of energy it will be scattered in different directions and angles. From these scattered electrons some of them will be directed back out of the sample and can be detected by the detector. Then, the signal received by the detector will be amplified and used to form an image on a TV screen. Thus, the image produced by the back scattered electrons (BSE) shows the surface of the specimen as black and white because the average mean atomic number of the sample in the interaction volume is what determines the image features. When the atomic number of an atom which interacts with the beam is higher, the positive charge of its nucleus is greater and an interaction that produces a BSE is more likely. Therefore, the BSE signal carries some information about sample composition but will not carry as much information about the sample topography.

For this analysis Philips XL30 FEGSEM was used. This instrument has a range of detectors which are used to investigate samples surface topography and composition. It is equipped with a backscattered detector (BSD) sensitive as low as 6.5 keV can be used to give topographical, orientation and atomic number contrast [93]. It is also equipped with a Bruker energy dispersive spectroscopy (EDS) analytical system with a silicon drift diode detector. It also incorporates a HKL electron backscattered diffraction system with Nordlys II camera which can provide us information about the sample [93]. The microscope has resolution of about 3 nm.

Graphite is manufactured using coke extracted from pitch coke and pitch derived from crude oil and contains different kinds of impurities that were originally incorporated with the coke or introduced into it during manufacturing processes. The graphite goes through a variety of purification processes but it still contains a significant amount of impurities.

To minimise contamination and to make the sample surface free from any inclusion which may be introduced during preparation the samples were prepared by fracture. The measuring was made using EDS attached to a FEGSEM and the presence of impurities within PGA and

Gilsocarbon samples have been investigated. All image and spectra were gathered using the same electron energy, magnification and integration time. The performance of the instrument was calibrated using a reference material, i.e., Cobalt, before any analysis. For the analysis, the experimental parameters were: spot size of 3, accelerating voltage of 20 kV and a beam current of 150 pA. The total acquisition time was 240 s and the analysis was done with a 1.5 Å probe.

The BSE micrograph of PGA graphite is shown in Figure 46. The impurities are appearing as white particles in BSED image and the graphite with black contrast. The technique x-ray mapping was employed and it has enabled a single element to be mapped according to its position on the secondary electron image. For the analysis one bright spot was selected at a time, and was analysed for elemental composition and their relative concentration was also determined. Once an impurity is selected and its back scattered image was taken. Then, it was checked whether it is integral to the graphite by switching to the secondary electron image mode.

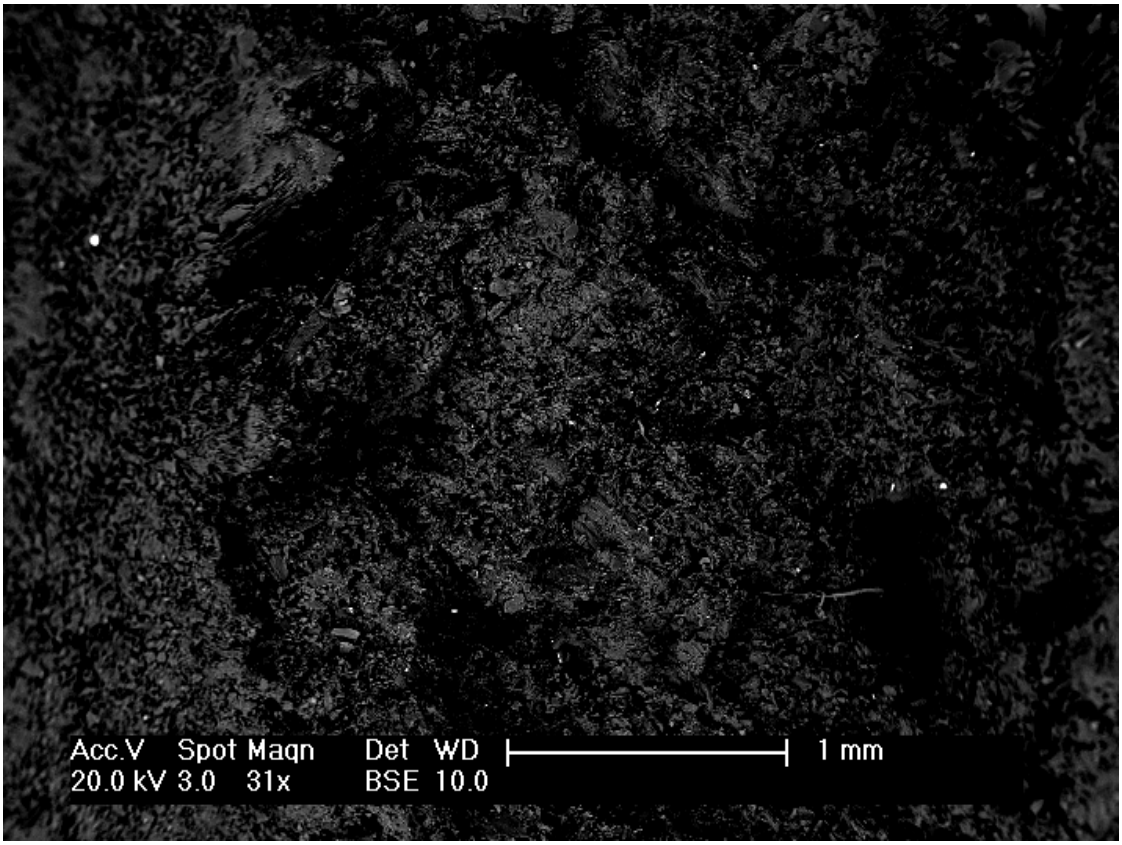

Figure 46: Back scattered electrons (BSE) micrograph of PGA graphite showing impurities as white dots - Scale bar 1 mm

Figure 47 shows a selected impurity from the sample. It was magnified (as shown Figure 48) and its secondary electron image was taken as shown in Figure 49 to see whether it is integral to the sample or a foreign material. As it can be observed from Figure 49 the impurity is

constituent of the graphite microstructure. The excited states from the impurity are displayed as a spectrum for the identification of elements in as it can be observed in Figure 50.

The EDX spectrum (Figure 50) shows peaks corresponding K_α series Carbon (C) at 0.239 keV, K_α series Oxygen (O) peak at 0.479 keV, K_α series Magnesium peak (Mg) at 1.279 keV and K_α series peak of Silicon (Si) at 1.5726 keV. The associated semi-quantitative measurement of the elements and their concentration in the impurity are presented in Table 19. As reported on the table four elements were detected. The carbon peak is the graphite substrate contribution; the excess oxygen is the stoichiometry of the impurity which can be attributed to the fact that silicon is bound to oxygen, creating an oxide phase. Moreover, the oxygen peak is also the result of the contributions of the oxygen reacted with magnesium to form the compound magnesium oxide.

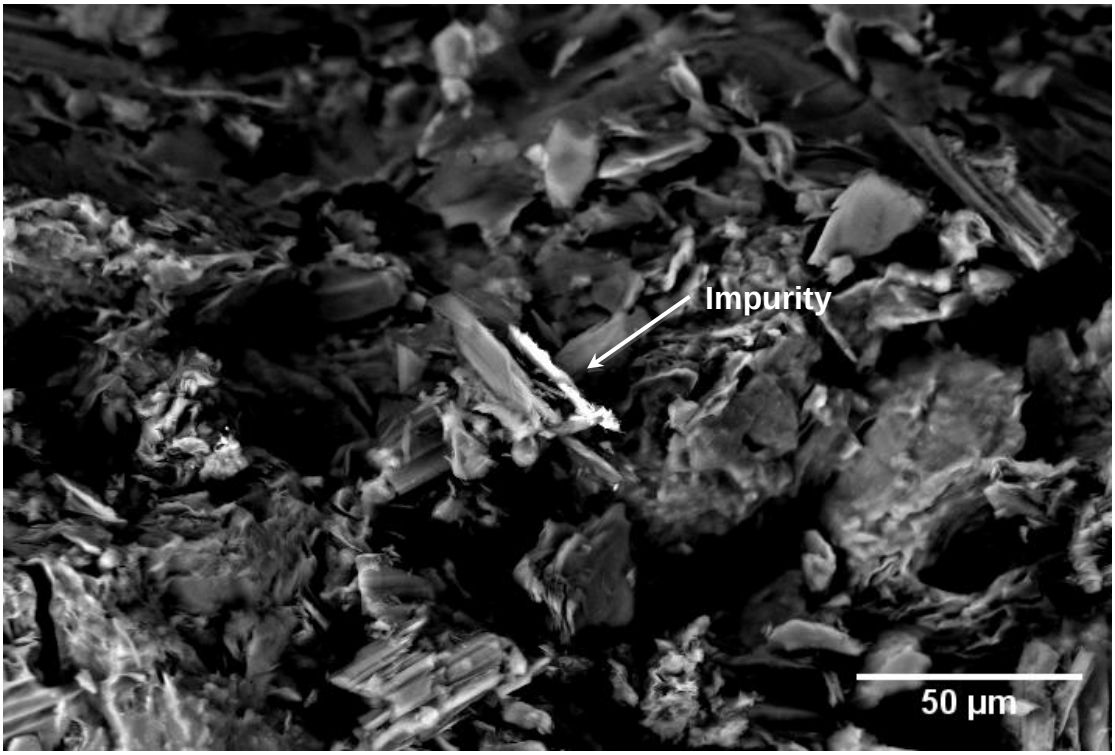

Figure 47: Back scattered electrons (BSE) micrograph of PGA graphite showing a selected impurity – Scale bar 50 µm

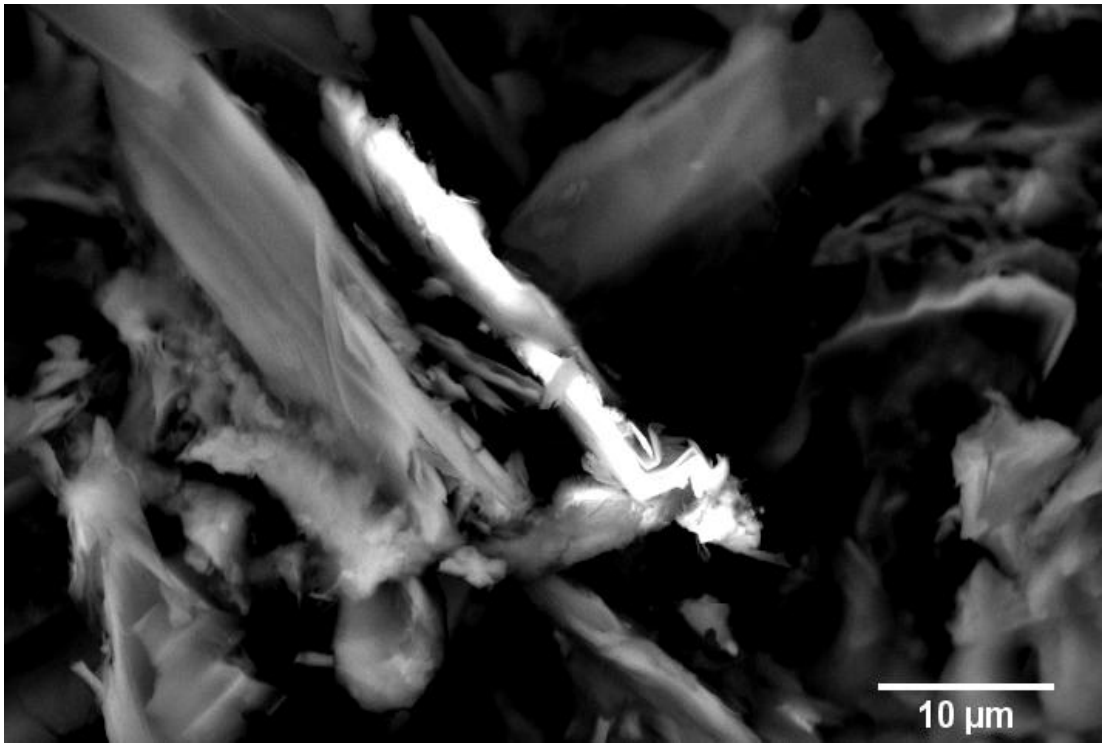

Figure 48: Back scattered electrons (BSE) micrograph of PGA graphite showing a selected impurity – Scale bar 10 µm

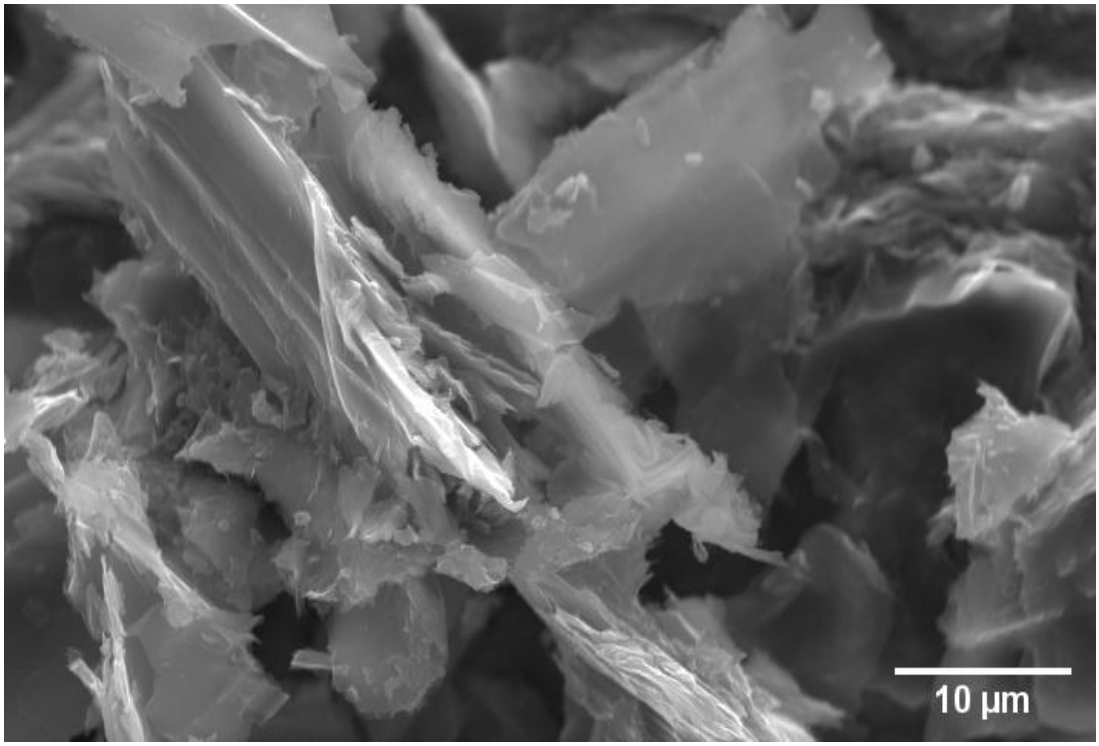

Figure 49: Secondary electrons micrograph of PGA graphite showing a selected impurity – Scale bar 10 µm

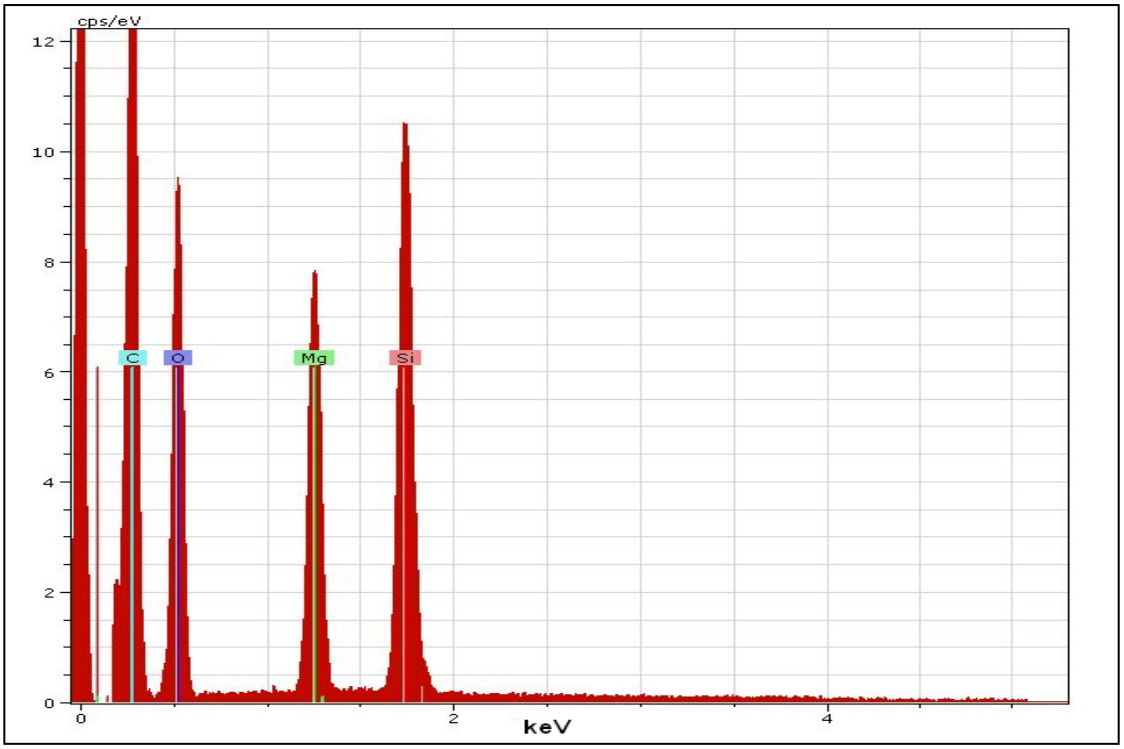

Figure 50: Energy dispersive x-ray spectrum of elements in an impurity from graphite showing K_α series peaks of Carbon (C), Oxygen (O), Magnesium (Mg) and Silicon (Si).

Table 19: Energy dispersive x-ray semi-quantitative measurement of elements in an impurity from graphite

Element	series	[wt.-%]	[norm. wt.-%]	[norm. at.-%]
Silicon	K-series	26.39	16.56	9.59
Magnesium	K-series	20.24	12.70	8.50
Carbon	K-series	47.11	29.57	40.05
Oxygen	K-series	65.59	41.17	41.86
	Sum:	159.33	100	100

Figure 51 show another impurity from the graphite substrate. The impurity is shown as white entity shown mainly in the graphite. Figure 52 was produced by magnifying the same impurity. The secondary electron microscope micrograph of the same area of Figure 52 reported on Figure 53, and it reveals that the impurity is a constituent of the graphite. Figure 54 displays the excited x-rays from the impurity on the sample shown as a spectrum for the identification of elements. The spectrum reveals that the most dominant element detected is Aluminium (Al).

The semi-quantitative analysis result of the elements and their concentration in the impurity is reported in Table 20.The aluminium K_α series peak is at 1.3675 keV and the impurity also contains traces of magnesium, silicon and oxygen which are accounted for less than 1 at.% all together. The peak at 0.239 keV corresponds to the K_α series carbon (C) and it is the contribution of the graphite substrate.

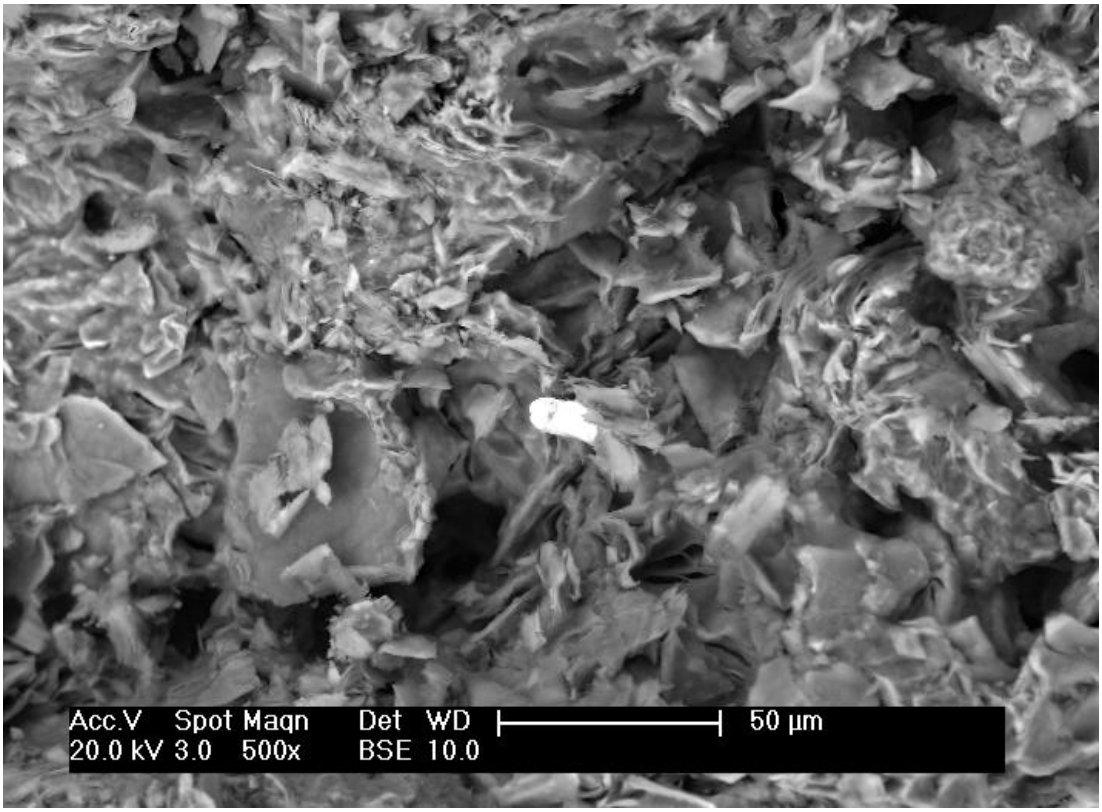

Figure 51: Back scattered electrons (BSE) micrograph of PGA graphite showing a selected impurity – Scale bar 50 µm

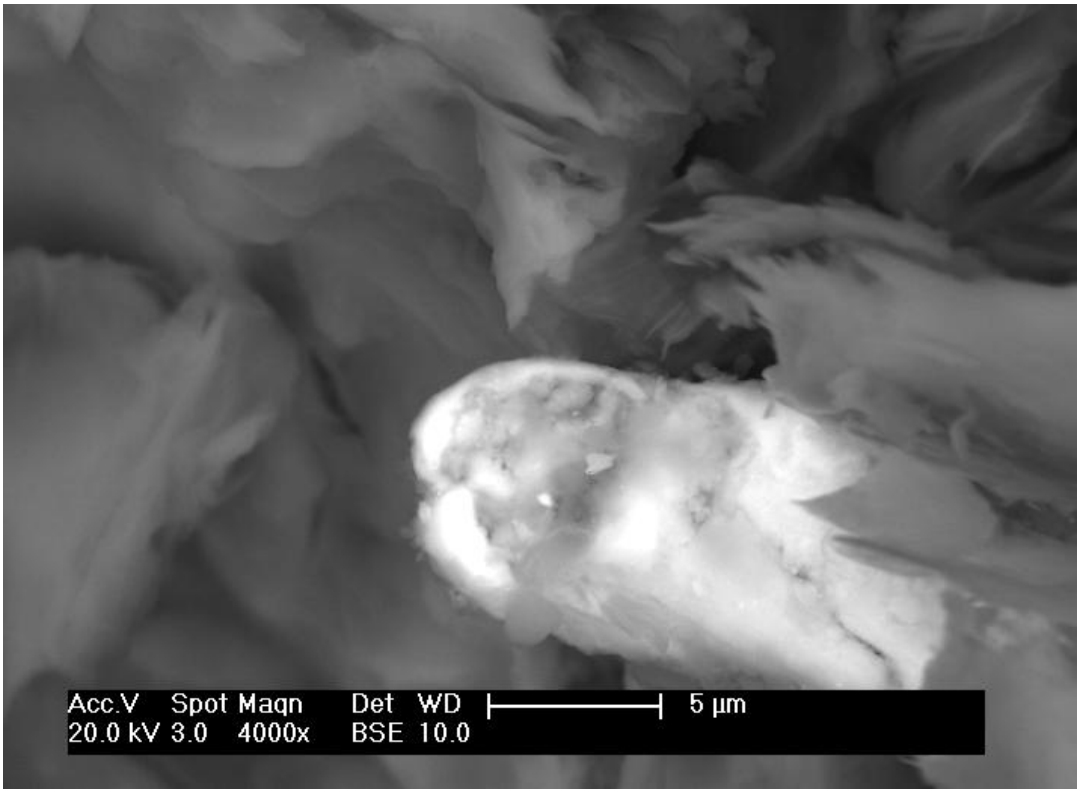

Figure 52: Back scattered electrons (BSE) micrograph of PGA graphite showing a selected impurity – Scale bar 5 µm

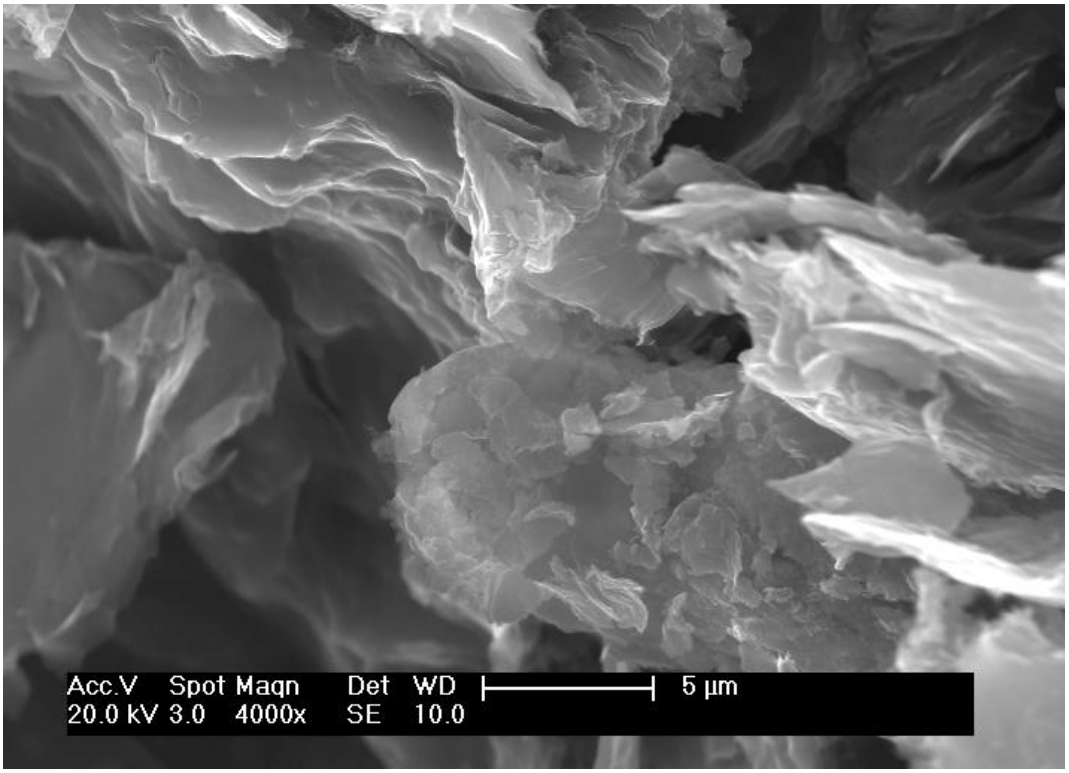

Figure 53: Secondary electrons micrograph of PGA graphite showing a selected impurity – Scale bar 5 µm

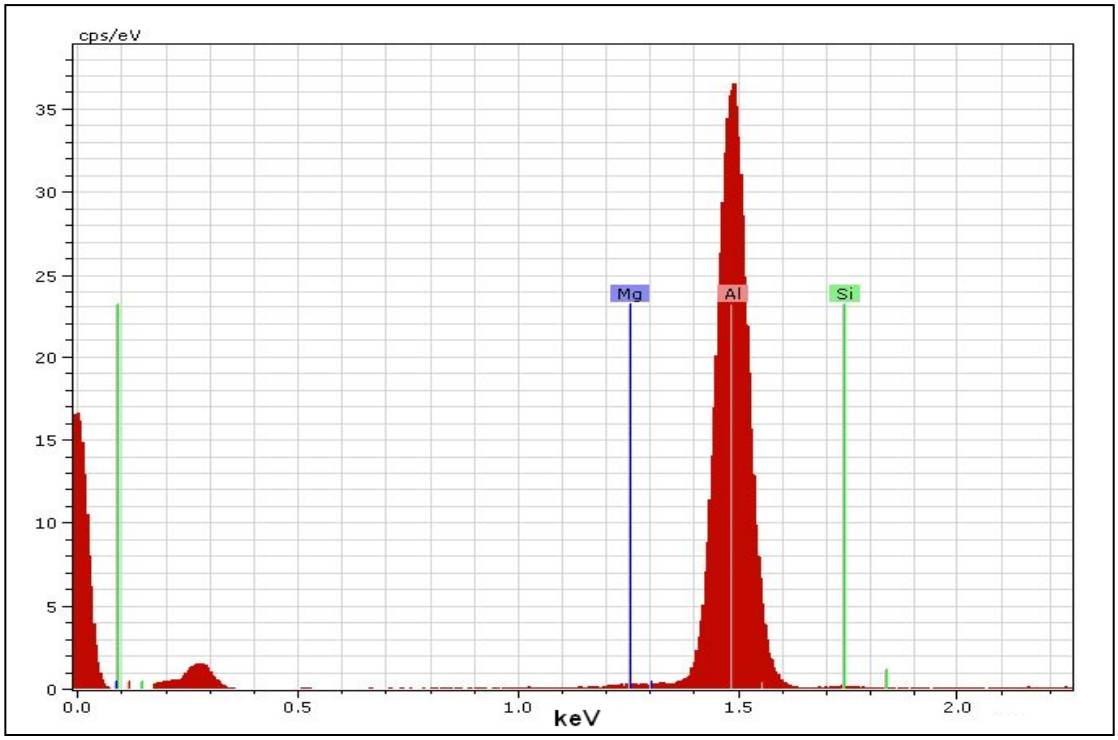

Figure 54: Energy dispersive x-ray spectrum of elements in an impurity from graphite showing K series peaks of Aluminium (Al)

Table 20: Energy dispersive x-ray semi-quantitative measurement of elements in an impurity from graphite

Element	series	[wt.-%]	[norm. wt.-%]	[norm. at.-%]
Silicon	K-series	0.06	0.07	0.05
Aluminium	K-series	56.46	65.96	46.36
Magnesium	K-series	0.02	0.023	0.018
Carbon	K-series	29.03	33.91	53.54
Oxygen	K-series	0.03	0.031	0.04
	Sum:	85.60	100	100

The BSE micrograph of an impurity in PGA graphite is shown in Figure 55. The impurity is appearing as white particle in BSE micrograph and the graphite with black contrast. The secondary electron microscope micrograph of the same area of Figure 55 is reported on Figure 56, and it reveals that the impurity is an integral part of the graphite. Simultaneously the dispersed x-rays from the impurity were displayed as a spectrum for the identification of elements in Figure 57. The spectrum reveals that the most dominant element detected is Iron (Fe). Iron is very stable carbide former [94] and as it can be seen clearly from Figure 55 it is chemically bonded with the graphite.

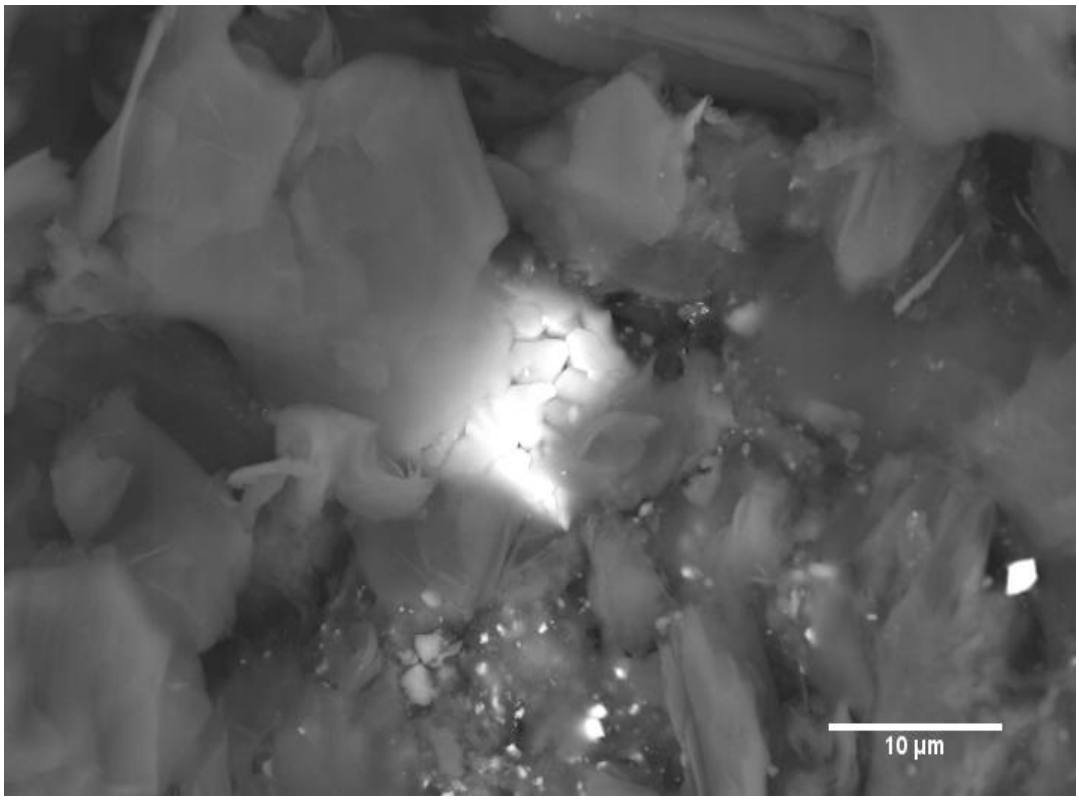

Figure 55: Back scattered electrons (BSE) micrograph of PGA graphite showing a selected impurity – Scale bar 10 µm

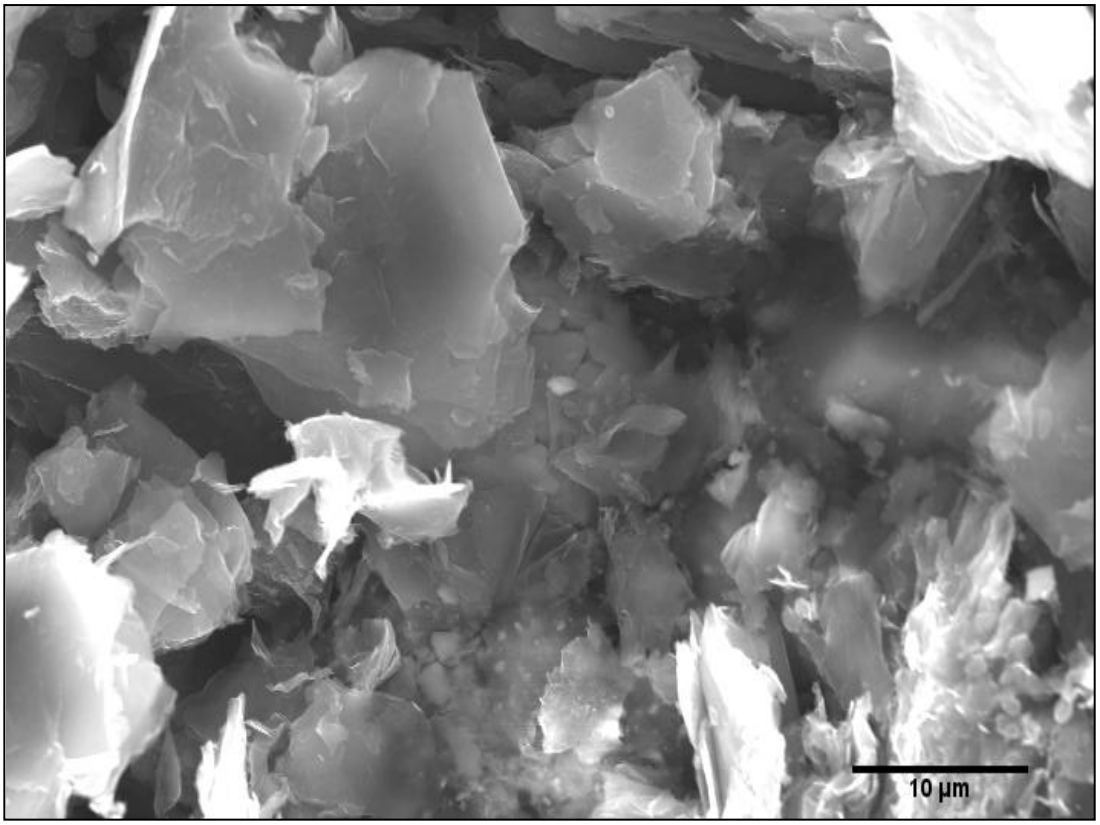

Figure 56: Secondary electrons micrograph of PGA graphite showing a selected impurity – Scale bar 10 µm

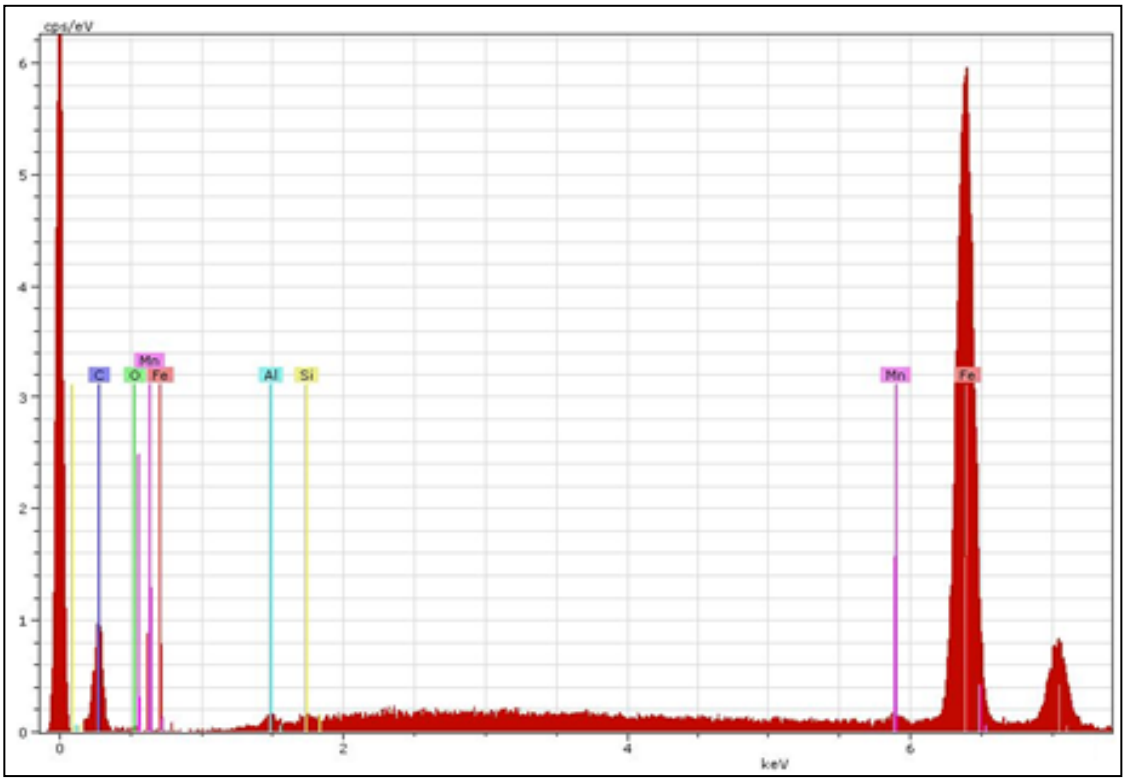

Figure 57: Energy dispersive x-ray spectrum of elements in an impurity from graphite showing K_{α} series peaks of Iron (Fe)

The elements and their concentration in the impurity is shown in Table 21.The iron K_α series peak is at 5.829 keV and the impurity also contains traces of manganese K_α series peak at 5.385 kV, aluminium K_α series peak at 1.368 and silicon K_α series peak at 1.573 which are accounted for less than 1 at.% all together. The peak at 0.239 keV corresponds to the K_α series carbon (C) and it comes from the emitted scattered electrons from the graphite sample.

Table 21: Energy dispersive x-ray semi-quantitative measurement of elements in an impurity from PGA graphite

Element	Series	[wt.-%]	[norm. wt.-%]	[norm. at.-%]
Carbon	K-series	6.89	7.090626	26.16
Iron	K-series	88.94	91.82341	72.87
Aluminium	K-series	0.08	0.085591	0.14
Silicon	K-series	0.02	0.023208	0.04
Manganese	K-series	0.95	0.977127	0.79
Oxygen	K-series	3.78E-05	3.9E-05	0.00
	Sum:	96.86422	100	100

The material also displayed a mineral impurity containing a variety of elements as its constituent. Figure 58 shows the EDX image of the impurity, this procedure produces a white particle directly on the electron image. Figure 59 shows the same area of the EDX image but an image produced by secondary electron. The purpose of the later procedure is to confirm whether the compound is ingrained in the graphite. The scattered x-rays from the sample were shown as a spectrum for the detection of elements in Figure 60. The spectra were analysed in standard mode and the related semi-quantitative information about the elements and their concentration is reported in Table 22. The dominant peaks in the spectrum of the impurity were identified as the K_α series peaks of oxygen, calcium (Ca), silicon and aluminium.

During a 240 sec scan of the impurity in the graphite the EDX spectrum (Figure 60) shows clear peaks corresponding to the oxygen K_α series peak at 0.479 keV, calcium (Ca) K_α series peak at 3.700 keV, silicon K_α series peak at 1.573 keV and aluminium K_α series peak at 1.368 keV. The impurity also contains traces of iron K_α series peak at 5.829 keV, titanium (Ti) K_α series peak at 4.514 keV, sulphur (S) K_α series peak at 2.314 keV, potassium (K) K_α series peak at 3.314 keV, sodium (Na) K_α series peak at 1.029 keV, magnesium K_α series peak at 1.279 keV, chlorine (Cl) K_α series peak at 2.629 keV and zinc (Zn) K_α series peak at 8.629 keV. The peak at 0.239 keV

corresponds to the K_α series carbon (C) and it comes from the emitted scattered electrons from the graphite sample. The carbon peak is the graphite substrate contribution and the oxygen is the stoichiometry of the impurity which can be attributed to the fact that silicon is bound to oxygen, creating an oxide phase. Moreover, the oxygen peak is also the result of the contributions of the oxygen reacted with other reactive metals such as iron forming an oxide phase.

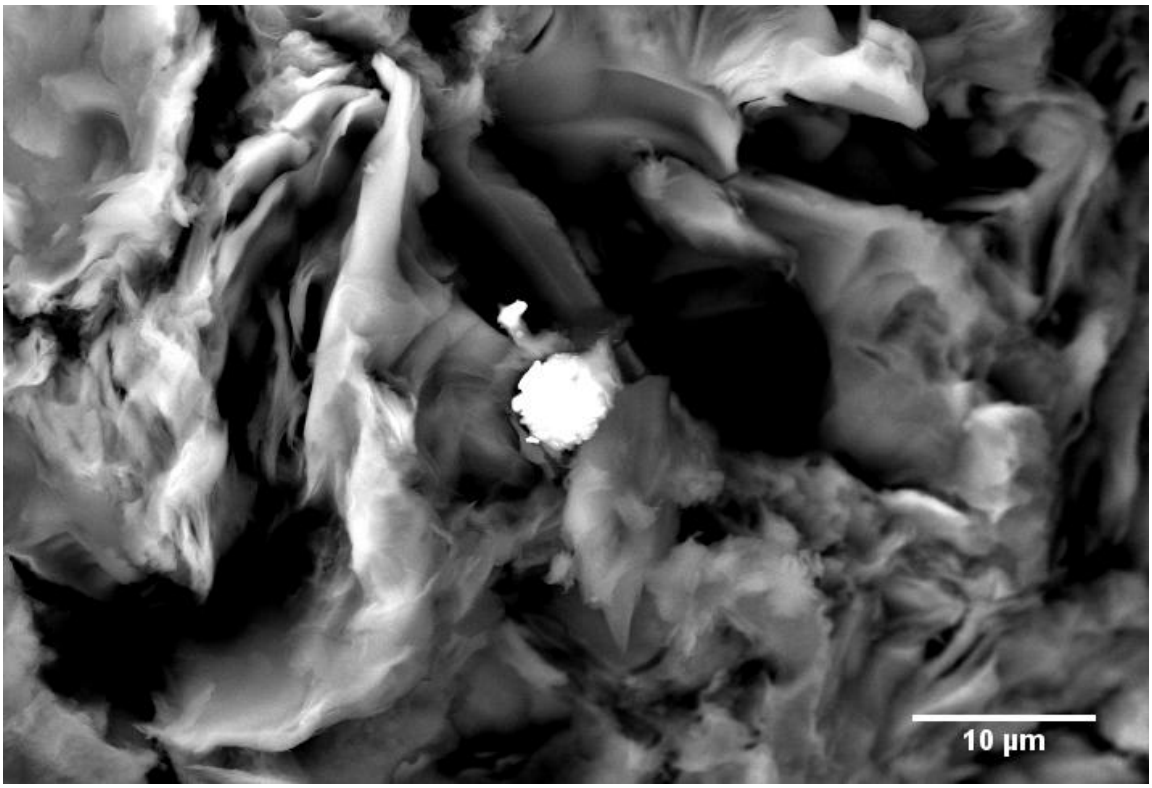

Figure 58: Back scattered electrons (BSE) micrograph of PGA graphite showing a selected impurity – Scale bar 10 µm

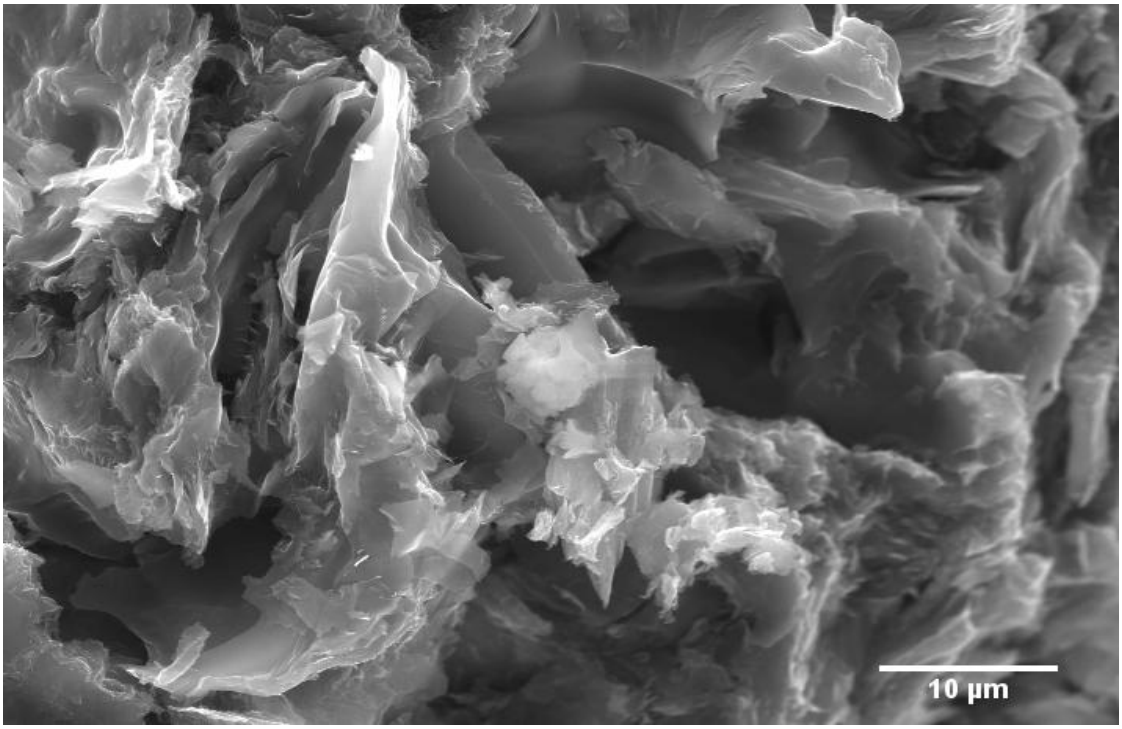

Figure 59: Secondary electrons micrograph of PGA graphite showing a selected impurity – Scale bar 10 µm

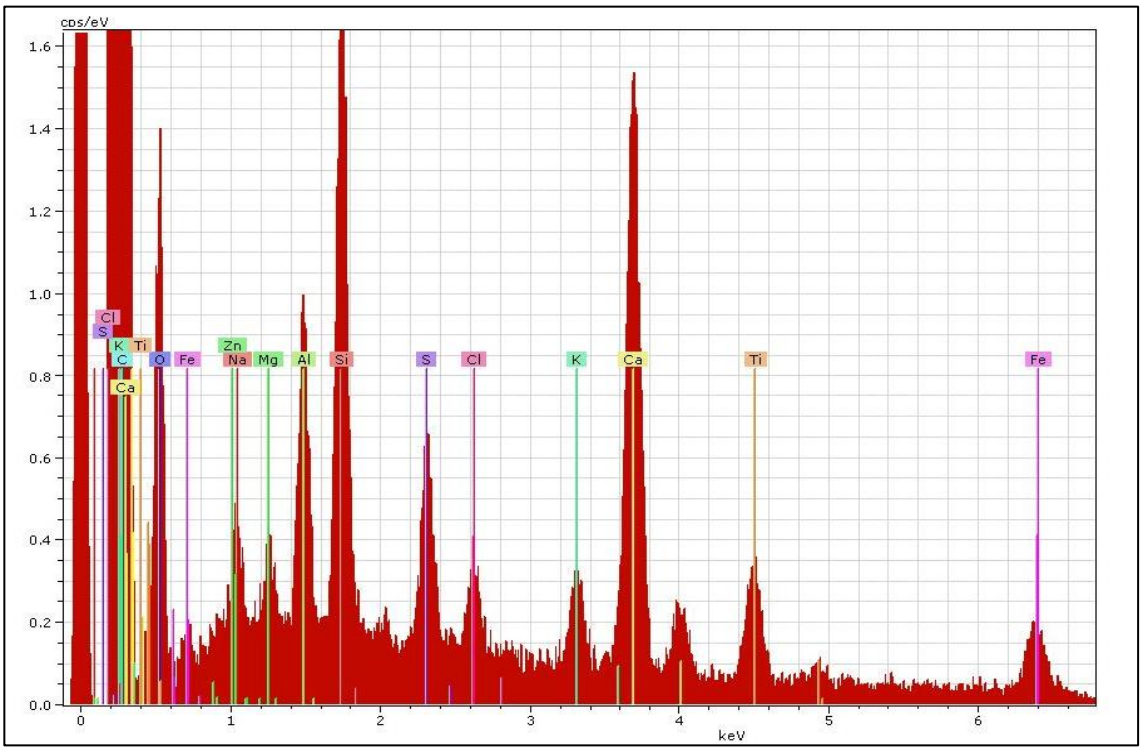

Figure 60: Energy dispersive x-ray spectrum of elements in an impurity from graphite showing K series peaks of Carbon (C), Oxygen (O), Calcium (Ca), Silicon (Si), Aluminium (Al), Iron (Fe), Titanium (Ti), Sulphur (S), Potassium (K), Sodium (Na), Magnesium (Mg), Chlorine (Cl) and Zinc (Zn).

Table 22: Energy dispersive x-ray semi-quantitative measurement of elements in an impurity from PGA graphite

Element	Series	[wt. %]	[norm. wt. %]	[norm. at. %]
Silicon	K-series	3.71	3.71	1.96
Magnesium	K-series	0.63	0.63	0.39
Carbon	K-series	58.77	58.77	72.47
Sodium	K-series	0.82	0.82	0.54
Aluminium	K-series	1.83	1.83	1.00
Sulphur	K-series	1.25	1.25	0.58
Chlorine	K-series	0.61	0.61	0.25
Potassium	K-series	0.97	0.97	0.37
Calcium	K-series	5.94	5.94	2.20
Titanium	K-series	1.98	1.98	0.61
Iron	K-series	2.45	2.45	0.65
Zinc	K-series	0.69	0.69	0.16
Oxygen	K-series	20.35	20.35	18.84
	Sum:	100	100	100

To sum up, it is interesting to see that graphite consists of many thousand “platelets”. Some of the impurities are trapped within these platelets and some of them are chemically bonded with the graphite. In reactor core radionuclides located within the bulk graphite could arise from the activation of these impurities which were integral with the original graphite components. Therefore, using EDX analysis it was possible to determine some of the impurities which could be the origin of some of the radionuclides which were leached into the leachate from the active specimens. For instance, Titanium and Iron could produce ^{59}Co which could be a source ^{60}Co, Chlorine impurity which is responsible for ^{36}Cl, Cesium which might produce ^{133}Cs which could be a source of ^{134}Cs and Calcium which could be a source of ^{46}Sc.

Similar tests were carried out on Gilsocarbon nuclear grade graphite. The analysis was carried out with the same parameters as for PGA graphite investigation. The spectra were analysed in standard mode and simultaneously electron energy loss spectra was acquired for the elemental identification. Then, the related semi-quantitative information about the elements and their concentration was analysed. The most abundant elements in the material matrix are iron, calcium and aluminium impurities. Small amounts of magnesium, oxygen and chlorine were also detected. The concentration of the impurities in Gilsocarbon is low compared to PGA graphite.

4.2 LEACHING RESULTS

4.2.1 Measurement of Total Gamma Activity

The gamma emitting radionuclide content in the graphite leach samples was determined from the fingerprint analysis produced and by matching the energies of the prints with the graphite library (file containing all radionuclide and their corresponding energy levels). The values for the parameters of half-life, gamma ray energy and abundance that are used for the fitting are not absolute, but are experimentally determined and therefore depend on the source used. Thus, the library values were verified against databases like NUDAT (Brookhaven National Laboratory database). The complexity and time required to obtain the assays on isotopic content for individual radionuclides differed very much. For example, assays on content of tritium and actinides require up to 10 hours or more which would lead to excessive experimental time and expense. As a reasonable compromise, the measurements were carried out continuously for four hours for each sample.

For each analysis, leachate samples were placed in 150 ml polyethylene bottle and the activity release was measured for each sample. For the analysis the whole sample volume of each individual leachate sample was used. The size and construction of the container for each sample was specified to the assessment code before each count to establish the geometry and material of the container.

As it can be seen from Figure 61 the principal radionuclides present in terms of activity were ^{60}Co, ^{137}Cs, ^{134}Cs, ^{155}Eu, ^{133}Ba and ^{46}Sc, the dominant radionuclides are ^{60}Co, ^{134}Cs and ^{133}Ba which together account for about 91% of the total activity. The 91 % can be broken down into 73.4 % ^{60}Co, 9.1 % ^{134}Cs and 8.1 % ^{133}Ba.

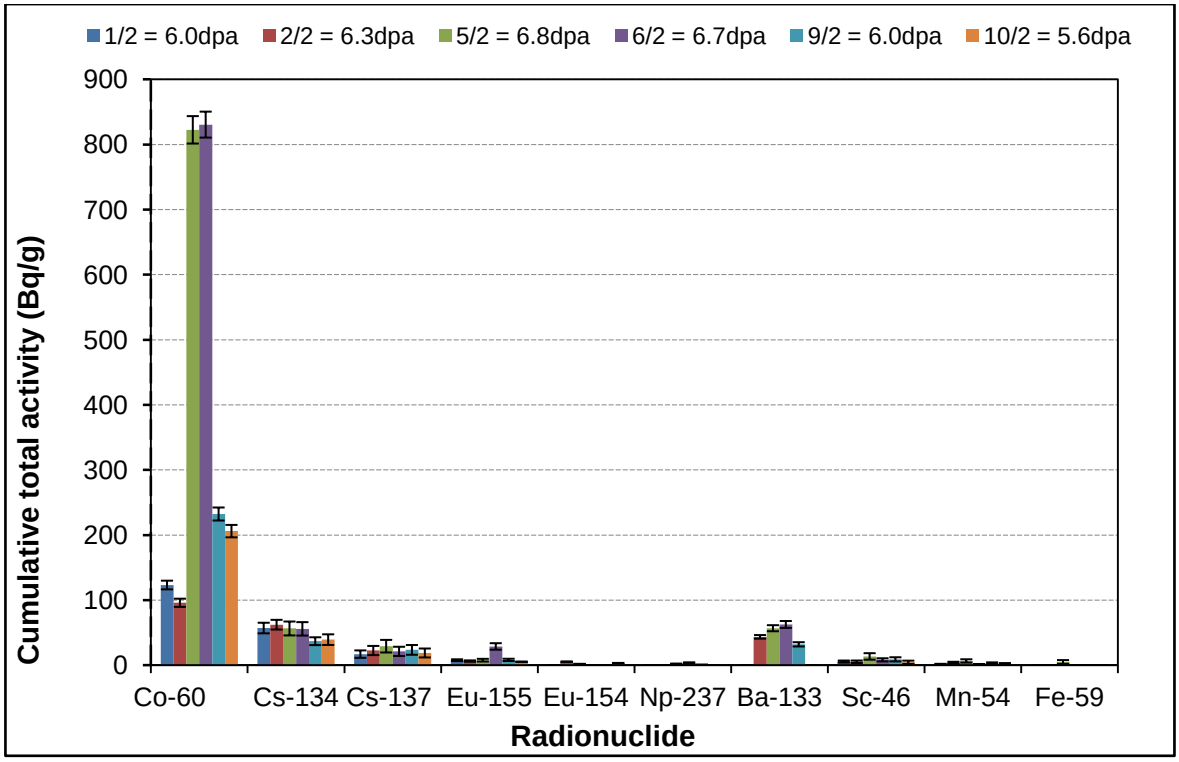

Figure 61: Bar graph showing gamma emitter radionuclides and corresponding activity release measured using Gamma Spectroscopy for all six samples

The cumulative total activity release (sum of activity for each period) of each species detected is shown in Figure 62 to Figure 67. The release of the activity from each sample was shown to vary, but in general samples which were exposed to a high radiation flux, i.e., located at mid-channel height, show the highest abundance of leached radionuclides, with over 72% of the total accounted activity.

The summary of solubility, the possible origin and possible entrainment of radionuclides is shown in Table 23. The time for cumulative total release start to get plateau and the corresponding cumulative total release is also summarised in Table 24.

Table 23: Solubility, origin and possible entrainment of radionuclides

Radionuclide	Solubility in Water at 25 °C (mg/L) [95]	Possible Origin fission Product	Possible nonradioactive Impurity	Possible origin entrainment	Impurity Origin
^{60}Co	8.745e+004	Fe or/and Ti	^{59}Co	• Neutron irradiation • During manufacturing	• Structural materials • Coke impurity
^{134}Cs	5.707e+004	^{133}In	^{133}Cs	• Fission Product • During manufacturing	• Fuel element • Coke impurity
^{133}Ba	5.476e+004	^{133}Cs	^{133}Cs, ^{132}Ba	• Fission Product • During manufacturing	• Fuel element • Coke impurity
^{137}Cs	5.707e+004	^{137}Te		• Fission Product	• Fuel element
^{155}Eu	4.741e+004	^{155}Nd	^{153}Eu	• Fission Product • During manufacturing	• Fuel element • Coke impurity
^{46}Sc	8.432e+004		^{45}Sc, ^{43}Ca	• During manufacturing	• The coke
^{3}H	3.950e+003		^{6}Li	• Fission Product • During manufacturing	• Fuel element • Coke impurity
^{14}C	Insoluble		^{14}N, ^{17}O ^{13}C	• From atmosphere • During manufacturing	• From the atmosphere • The Coke

Table 24: Time for cumulative release to plateau versus Cumulative release to plateau

Cobalt-60 (^{60}Co)

Sample ID/ dose	Initial rate of release (Bq/g)	Time for cumulative release to plateau (days)	Cumulative release to plateau (Bq/g)
1/2 = 6.0dpa	0.0	49	89.2
2/2 = 6.3dpa	5.5	49	77.0
5/2 = 6.8dpa	0.0	49	568.0
6/2 = 6.7dpa	0.0	49	724.4
9/2 = 6.0dpa	0.0	49	224.2
10/2 = 5.6dpa	0.0	49	154.1

Cesium-134 (^{134}Cs)

Sample ID/ dose	Initial rate of release (Bq/g)	Time for cumulative release to plateau (days)	Cumulative release to plateau (Bq/g)
1/2 = 6.0dpa	31.5	4	48.8
2/2 = 6.3dpa	34.4	4	53.5
5/2 = 6.8dpa	32.1	4	52.5
6/2 = 6.7dpa	27.8	4	49.4
9/2 = 6.0dpa	16.0	4	25.6
10/2 = 5.6dpa	19.9	4	30.7

Barium-133 (^{133}Ba)

Sample ID/ dose	Initial rate of release (Bq/g)	Time for cumulative release to plateau (days)	Cumulative release to plateau (Bq/g)
1/2 = 6.0dpa	0.0	90*	6.1
2/2 = 6.3dpa	0.0	90*	53.2
5/2 = 6.8dpa	0.0	90*	95.3
6/2 = 6.7dpa	0.0	90*	100.6
9/2 = 6.0dpa	0.0	49	32.1
10/2 = 5.6dpa	0.0	0	0.0

*End of the experiment and no sign of plateau

Cesium-137 (^{137}Cs)

Sample ID/ dose	Initial rate of release (Bq/g)	Time for cumulative release to plateau (days)	Cumulative release to plateau (Bq/g)
1/2 = 6.0dpa	9.2	3	13.7
2/2 = 6.3dpa	13.3	3	19.2
5/2 = 6.8dpa	9.4	3	15.9
6/2 = 6.7dpa	10.1	3	19.6
9/2 = 6.0dpa	10.9	3	18.6
10/2 = 5.6dpa	9.6	3	15.5

Europium-155 (^{155}Eu)

Sample ID/ dose	Initial rate of release (Bq/g)	Time for cumulative release to plateau (days)	Cumulative release to plateau (Bq/g)
1/2 = 6.0dpa	0.0	91*	11.7
2/2 = 6.3dpa	0.0	91*	9.3
5/2 = 6.8dpa	0.0	91*	10.3
6/2 = 6.7dpa	0.0	91*	37.2
9/2 = 6.0dpa	0.0	91*	10.4
10/2 = 5.6dpa	0.0	91*	7.5

*End of the experiment and no sign of plateau

Scandium-46 (^{46}Sc)

Sample ID/ dose	Initial rate of release (Bq/g)	Time for cumulative release to plateau (days)	Cumulative release to plateau (Bq/g)
1/2 = 6.0dpa	0.0	49	5.6
2/2 = 6.3dpa	0.0	49	5.4
5/2 = 6.8dpa	0.0	49	13.5
6/2 = 6.7dpa	0.0	49	8.3
9/2 = 6.0dpa	0.0	49	9.0
10/2 = 5.6dpa	0.0	49	4.6

Tritium (^{3}H)

Sample ID/ dose	Initial rate of release (Bq/g)	Time for cumulative release to plateau (days)	Cumulative release to plateau (Bq/g)
1/2 = 6.0dpa	0.7	7	2.4
2/2 = 6.3dpa	0.5	7	1.7
5/2 = 6.8dpa	0.5	7	6.2
6/2 = 6.7dpa	0.6	7	9.1
9/2 = 6.0dpa	0.6	7	1.2
10/2 = 5.6dpa	0.2	7	0.4

Carbon-14 (^{14}C)

Sample ID/ dose	Initial rate of release (Bq/g)	Time for cumulative release to plateau (days)	Cumulative release to plateau (Bq/g)
1/2 = 6.0dpa	0.0	21	10.4
2/2 = 6.3dpa	1.8	21	11.7
5/2 = 6.8dpa	7.4	21	23.4
6/2 = 6.7dpa	4.1	21	11.9
9/2 = 6.0dpa	0.6	21	18.0
10/2 = 5.6dpa	3.5	21	14.2

The radioactive nuclide cobalt-60 decays by beta decay to the stable isotope nickel-60 (^{60}Ni) and it has a half-life of 5.27 years.[91] A possible route for ^{60}Co (Figure 62) generation is the neutron reaction ^{59}Co (n,γ)→^{60}Co [60]. ^{60}Co is produced both directly as a fission product and via neutron capture from nonradioactive Cobalt-59 (^{59}Co). ^{59}Co has a high sensitivity nucleus with a 100% natural abundance.[96] Inside the bulk graphite block volume, ^{60}Co is generated through activation of ^{59}Co impurities while at the surface layers and/or from ^{59}Co transported into the graphite by water vapour mixture.[60] It also created when structural materials, for instance steel or titanium, are exposed to neutron irradiation. The generation of ^{59}Co from impurities or structural materials is shown in decay equation eq.14.[97]

$$^{59}\mathrm{Ti} \xrightarrow{\beta^-} {}^{59}\mathrm{V} \xrightarrow[130\mathrm{ms}]{\beta^-} {}^{59}\mathrm{Cr} \xrightarrow[0.74\mathrm{s}]{\beta^-} {}^{59}\mathrm{Mn} \xrightarrow[4.6\mathrm{s}]{\beta^-} {}^{59}\mathrm{Fe} \xrightarrow[44.5\mathrm{s}]{\beta^-} {}^{59}\mathrm{Co} \quad \text{..... eq.14}$$

The samples which were exposed to a high radiation flux, i.e., located in the centre of the core were found to release a high amount of ^{60}Co contaminant. The release increases as the time period increases, probably the leaching of radionuclides present on the surface of the graphite and inside the volume. The release mechanism depends on the location of the contaminant. ^{60}Co contaminant has high solubility as shown in Table 23 but it took 49 days for the cumulative total release to plateau. Here the impurities (as water vapour or fission products from structural materials) may have travelled through the graphite open pore network before being deposited and activated. Then, during the leaching experiment the leachant may have taken some time to travel through the open porosity and interact with the radionuclide. Moreover, radiolytic oxidation leads to graphite weight loss which will have opened the closed porosity and it could be the reason for the upper brick samples releasing more activity than the lower brick samples.

The radionuclide cesium-134 (^{134}C) is generated in graphite through activation of ^{133}Cs.[3] ^{133}Cs is the only naturally occurring isotope of cesium, with a 100% natural abundance [96]. The likely production route of the nuclide ^{134}C are possibly the fission reaction of fuel element or/and from the activation of nonradioactive ^{133}Cs impurity which may have been integral to the original graphite.[3] Since the radionuclide ^{137}Cs was detected it confirms that this specie may have arise from partly as a result of fission reactions.[3, 51] The production of ^{133}Cs as a fission product is shown in eq.15 [61, 97]. Indium–133 (^{133}In) is a fission product and does not exist naturally. ^{134}C produce ^{134}Ba by beta decay (β^-) directly, emitting gamma ray [97].

$$^{133}\mathrm{In} \xrightarrow[180\mathrm{ms}]{\beta^-} {}^{133}\mathrm{Sn} \xrightarrow[1.45\mathrm{s}]{\beta^-} {}^{133}\mathrm{Sb} \xrightarrow[2.5\mathrm{m}]{\beta^-} {}^{133}\mathrm{Te} \xrightarrow[12.5\mathrm{m}]{\beta^-} {}^{133}\mathrm{I} \xrightarrow[28.8\mathrm{h}]{\beta^-} {}^{133}\mathrm{Xe} \xrightarrow[5.2\mathrm{d}]{\beta^-} {}^{133}\mathrm{Cs} \quad \text{… eq.15}$$

The samples which were taken from the centre and lower core positions release a high amount of ^{134}Cs contaminant but the samples which are taken from the lower bricks of the core, i.e. 1/2 and 2/2, release slightly more than the centre brick samples (Figure 63). The cumulative release increases as the time period increases until it reaches a period of four days when it starts to plateau (Table 24). The release is very fast as compared to the other radionuclides; this may suggest that the contaminant is bound to the surface of the graphite. Moreover, as shown in Table – 20 the solubility of the radionuclide is high resulting a shorter leaching period. Experimental errors in measurements of ^{60}Co and ^{134}Cs activities in the samples were within the range 1 - 10%.

^{133}Ba and ^{155}Eu could originate from impurities in the graphite and/or fission product released from the fuel [51]. ^{133}Ba has a half-life of about 10.51 years and does not exist naturally but can be produce from ^{132}Ba. ^{132}Ba is a naturally occurring isotope of Barium with an abundance of 0.101 % [98], it produces the nuclide with a production mode ^{132}Ba (n, γ) →^{133}Ba. It also produces the metastable phase ^{133m}Ba via a decay mode ^{132}Ba (n, γ) →^{133m}Ba. Then, it produces ^{133}Ba through isometric transition, ^{133m}Ba (n, γ) →^{133}Ba [99, 100]. The principal method for the production of ^{133}Ba is^{133}Cs, via the decay mode ^{133}Cs (p, n) → ^{133}Ba nuclear reaction, i.e., from nonradioactive impurity ^{133}Cs or via fission product ^{133}Cs produced by decay mode described on eq.15 and it decays into ^{133}Cs by electron capture [101].

The cumulative total release of ^{133}Ba is shown in Figure 64.[61] The release of activity from the samples which were exposed to a high radiation flux, i.e., 5/2 and 6/2, located in the centre of the core show the highest abundance of leached radionuclides as can be seen from Figure 64. The solubility of ^{133}Ba is very high (Table 23) but leaching of the contaminant increases as leaching time increases. This implies that the leachant has had to travel through the open pore network and it took some time to clean these pores and react for the leaching to occur.

Europium-155 (^{155}Eu) is a fission product with a half-life of 4.76 years.[102] A small amount of ^{155}Eu is also produced by repetitive neutron capture of nonradioactive ^{153}Eu.[101] ^{153}Eu of the naturally occurring europium is with 52.2% natural abundance.[96] It also generated from the fission product ^{155}Nd and the generation of this radionuclide is shown in eq.16a & 16b.[97] The activity release of ^{155}Eu in to the leachant is shown in Figure 66. The release of this radionuclide increases as the time period increases. ^{155}Eu has high solubility with water (Table 23) and the majority of the samples release fairly similar amount of ^{155}Eu contaminant. However, in the case of one of the samples (ID: 6/2) the release was noted to be significantly higher. This may be due to the opening of pore network, due to radiolytic oxidation of the graphite. Moreover, some of the pores may have been closed due to neutron irradiation sealing in radionuclides related to impurities or fission products; hence, it may have taken some time for the leachant to travel through these partly closed pores and to interact with the radionuclide.

$$^{155}Nd \xrightarrow[8.9s]{\beta^-} {}^{155}Pm \xrightarrow[41.5s]{\beta^-} {}^{155}Sm \xrightarrow[22.3m]{\beta^-} {}^{155}Eu \quad \ldots\ldots \text{ eq.16a}$$

or

$^{153}Eu\ (n, \gamma) \rightarrow {}^{155}Eu$ …… eq.16b

The ^{137}Cs radionuclide is a fission product and the only mechanism of the generation of this species is described in eq. 17.[97] ^{137}Cs undergoes beta decays to produce ^{137m}Ba, then to nonradioactive ^{137}Ba by emitting gamma radiation with a half-life of 2.55 min.[102] The release of this radionuclide from the graphite samples increases as the time of leaching increases and starts to plateau after three days (Figure 65). The release is very quick with a high mobility rate, suggesting the contaminant is bound to the surface of the graphite and not bound to the interior. The active material ^{137}Cs is very reactive and has a very high solubility with water (Table 23) and this may be the reason for the radionuclide to leach out very quickly and (3 days as summarised in Table - 5) reach equilibrium.

$$^{137}Te \xrightarrow[2.49s]{\beta^-} {}^{137}I \xrightarrow[24.5s]{\beta^-} {}^{137}Xe \xrightarrow[3.818m]{\beta^-} {}^{137}Cs \quad \ldots\ldots \text{ eq. 17}$$

The radionuclide Scandium-46 (^{46}Sc) has many route of formation, but the main routes are three given their abundance and reaction cross-section. ^{46}Sc arises from impurities and its production mechanism is through isometric transition of $^{46m}Sc\ (n, \gamma) \rightarrow {}^{46}Sc$ or/and $^{43}Ca\ (\alpha, p\gamma) \rightarrow {}^{46}Sc$ or/and $^{45}Sc\ (n, \gamma) \rightarrow {}^{46}Sc$.[101] ^{45}Sc is a naturally occurring form of Scandium with 100% abundance and the main production route [98]. Similarly ^{43}Ca is a stable isotope of calcium with a natural abundance of 0.135%.[96] ^{43}Ca can also be produce form ^{43}Sc through electron capture (β^+) [101]. In the isometric transition of $^{46m}Sc\ (n, \gamma) \rightarrow {}^{46}Sc$, ^{46m}Sc is produced by electron capture via the decay mode $^{45}Sc\ (n, \gamma) \rightarrow {}^{46m}Sc$.[101] So, ^{46}Sc may be produced from both ^{43}Ca and ^{45}Sc impurities. ^{46}Sc decays by beta minus emission to ^{46}Ti, with a half-life of 83.8 days.[101]

The leaching of this species is shown in Figure 67. The mechanism of the release of this radionuclide is unusual within this set of experiments. No release was observed for the first three days and it started to leach as a daughter product. The solubility of ^{46}Sc in water is very high (Table 23) but the leaching increases as leaching period increases. This may be because the contaminant was trapped in the open pore network and the initial three days in the leachate may have resulted in other impurities inside the pores being washed off before allowing the leachant to move freely and interact with ^{46}Sc. The samples which were exposed to a higher radiation flux, i.e. 5/2 and 6/2, and the sample which have been trepanned from the bottom brick and taken from the upper brick position, i.e. 1/2, have a high release of ^{46}Sc radionuclide. The release of the radionuclide from the samples increases as the time period increases and start to

plateau after 49 days (Table 24). The detected concentrations of ^{137}Cs and ^{46}Sc are low and the uncertainty of these radionuclides analysis is high.

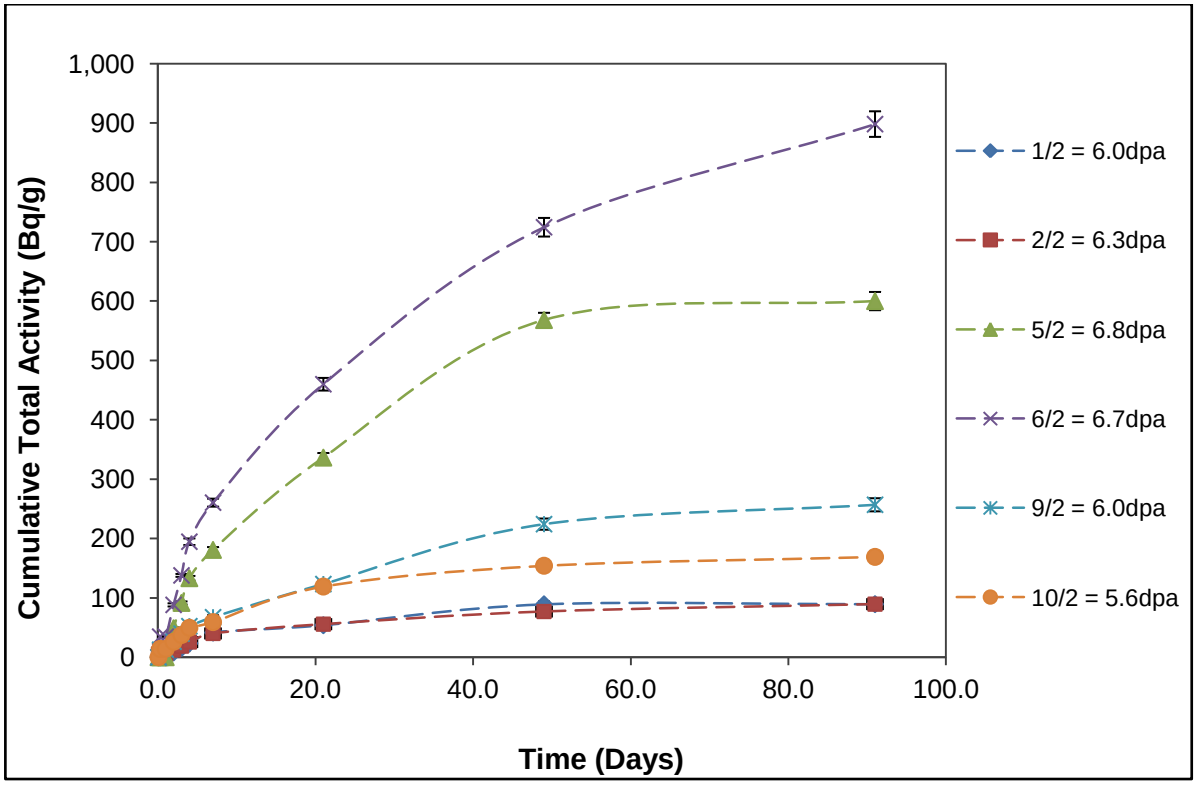

Figure 62: Cumulative total activity release of ^{60}Co measured using gamma spectroscopy

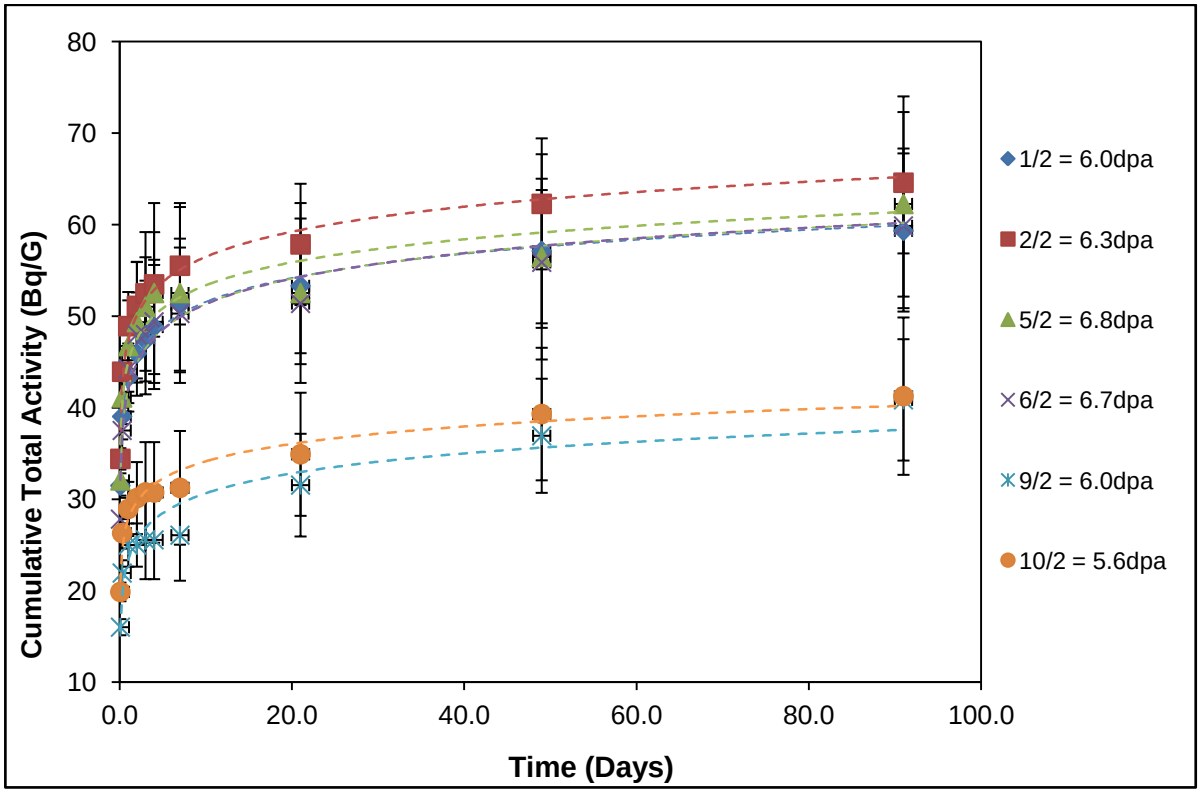

Figure 63: Cumulative total activity release of ^{134}Cs measured using gamma spectroscopy

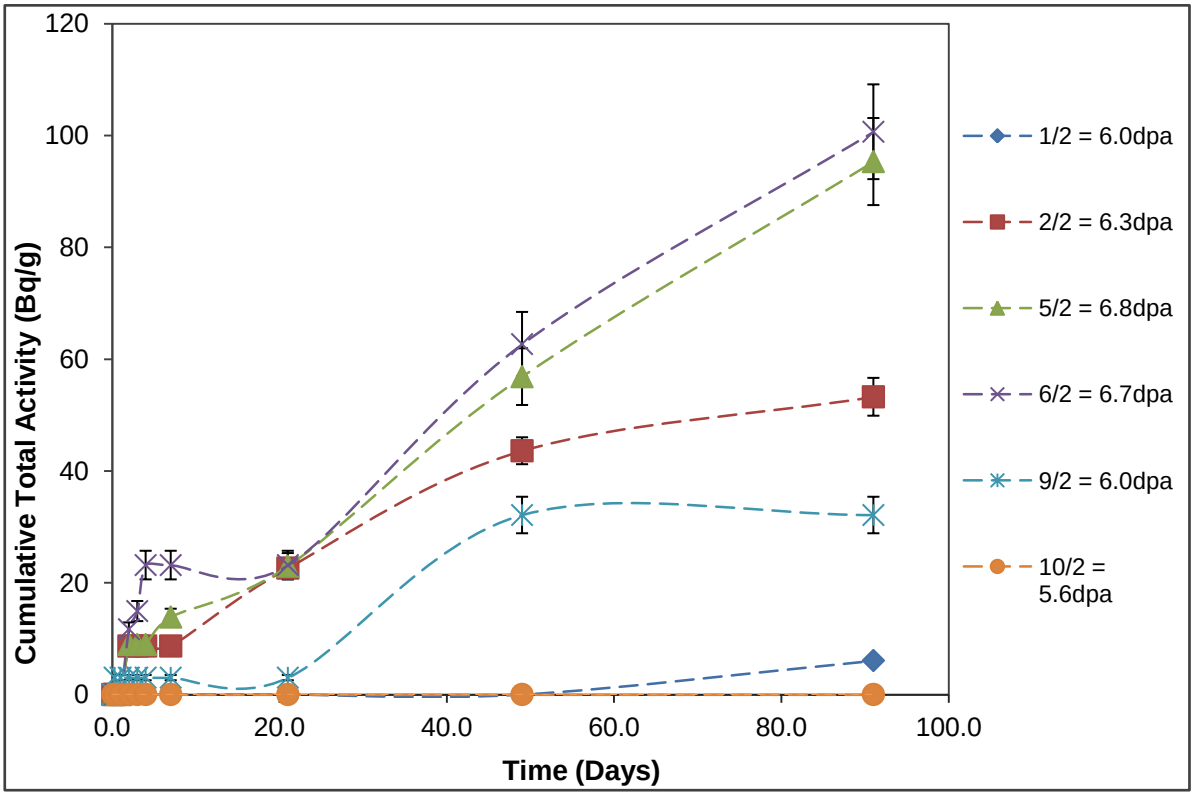

Figure 64: Cumulative total activity release of ^{133}Ba measured using gamma spectroscopy

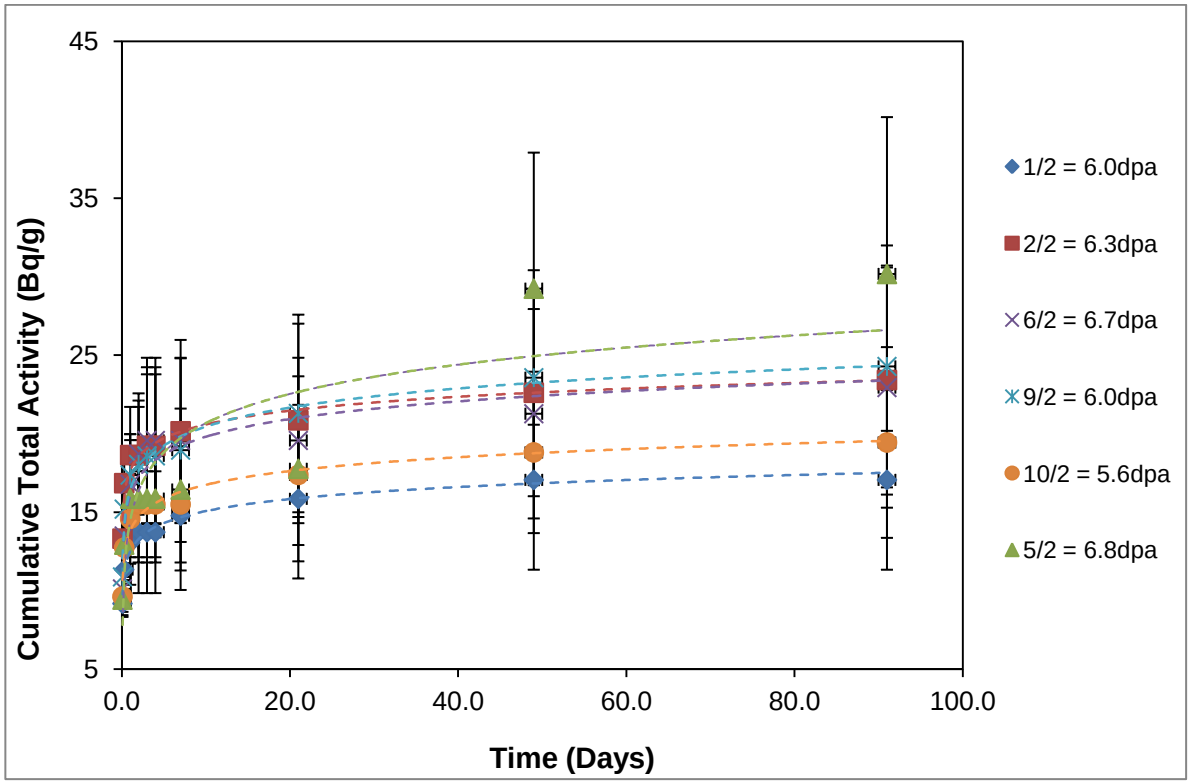

Figure 65: Cumulative total activity release of ^{137}Cs measured using gamma spectroscopy

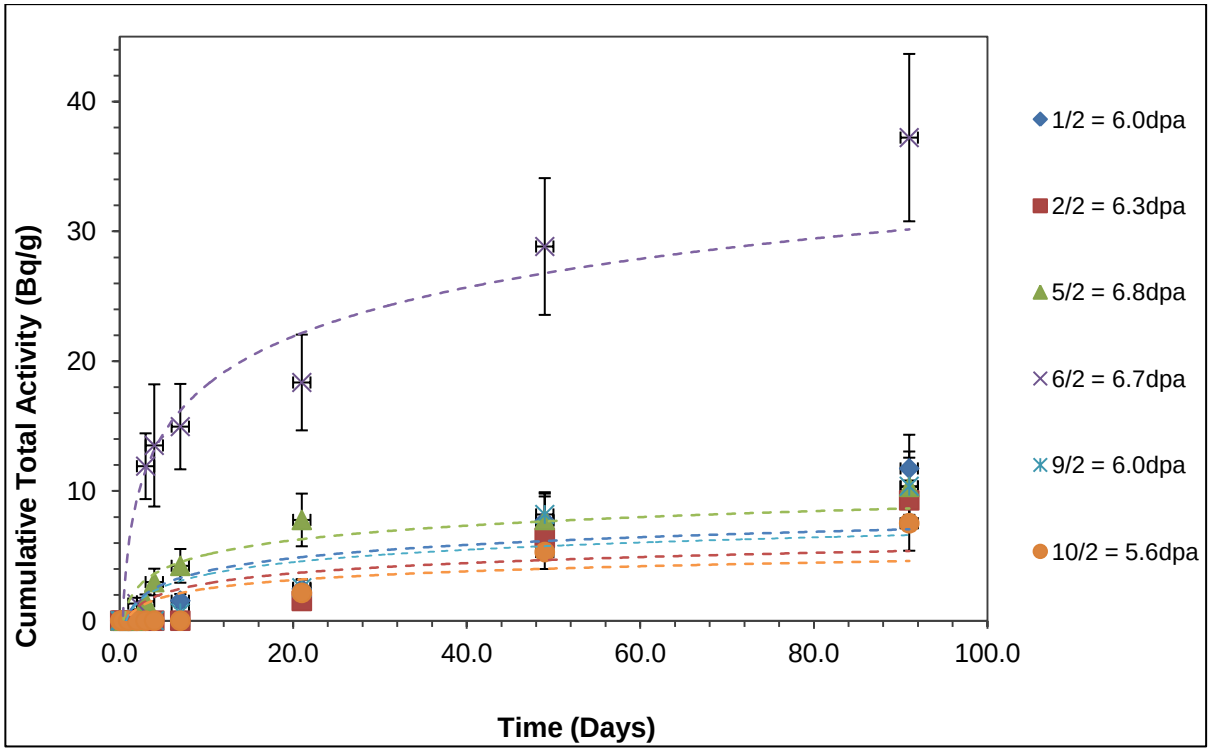

Figure 66: Cumulative total activity release of ^{155}Eu measured using gamma spectroscopy

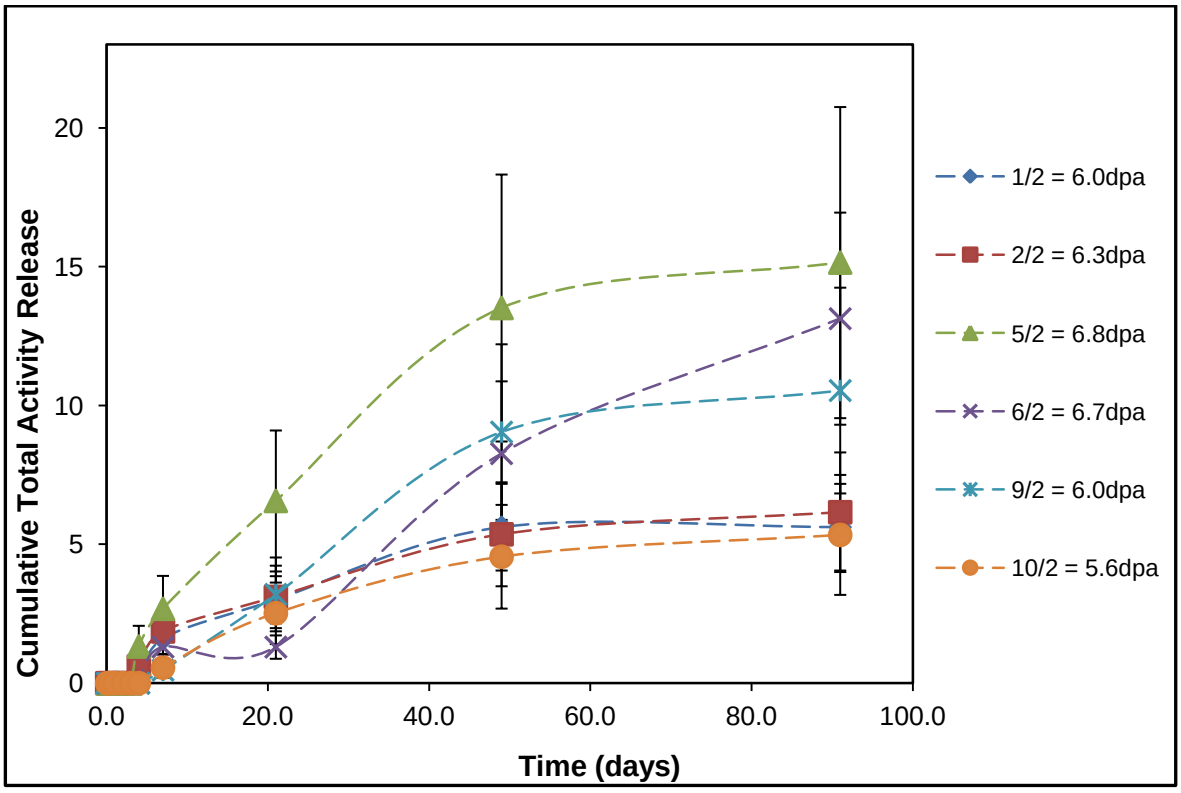

Figure 67: Cumulative total activity release of ^{46}Sc measured using gamma spectroscopy

4.2.2 Measurement of total alpha and beta radiation by liquid scintillation

It is seen from Figure 68 that the samples which were taken from the centre of the core and exposed to a high radiation, i.e., 5/2 and 6/2, are the ones with highest amount of leached radionuclides. These two samples contribute about 52% of the total activity. There is an initial high release of activity which reaches a plateau after approximately 21 days. This may be because the leachate specimen containing many radionuclides located within the bulk arising from the activation of impurities, which were integral with the original graphite components and from other reactor materials which have been activated elsewhere in the core before being carried around the circuit in the coolant gas into the graphite porosity network. In this case the activity may have leached out from both the graphite surface and internal porosity surfaces and transported via the complex porosity network.

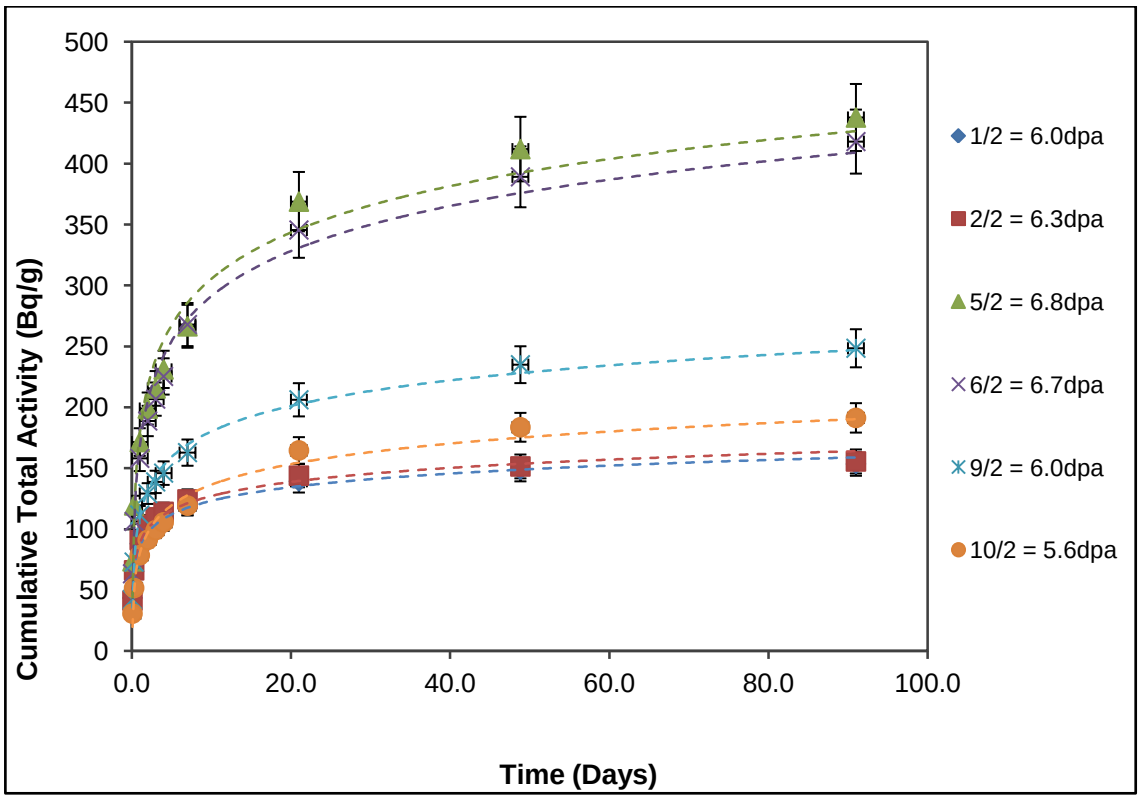

Figure 68: Cumulative total beta activity release measured using liquid scintillation

4.2.3 Measurement of total alpha and beta radiation without ^{3}H using liquid scintillation

Preliminary results are shown in Figure 69 and indicate there is an initial high release of activity that starts to reach equilibrium as it reaches approximately 21 days. The release of the activity may have been from both the graphite surface and internal porosity surfaces transported via the complex porosity network. Samples from the centre of the core, which were exposed to the highest radiation, produced the highest amount of leached radionuclides. These samples are identified as 5/2 and 6/2 and contribute about 77% of the total ^{3}H activity. Comparing this result

with the activity in Figure 68 there is about 277 Bq difference between the total beta release and the beta release with tritium removed.

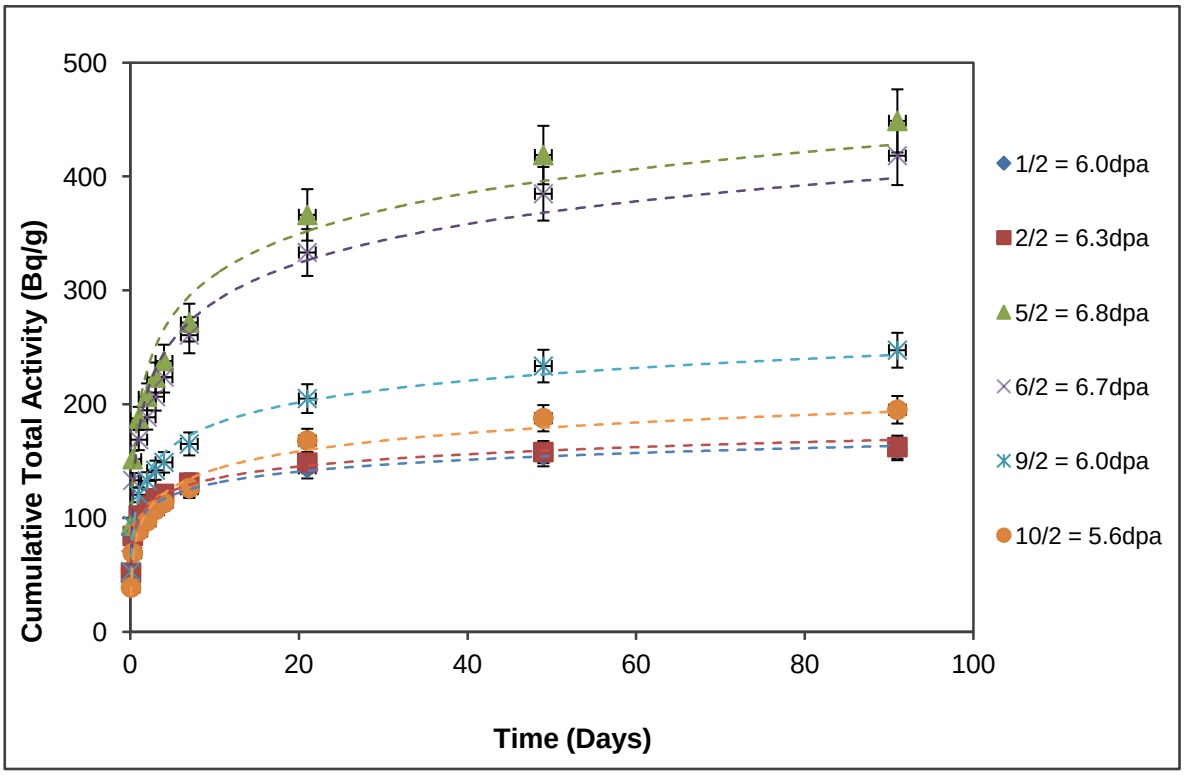

Figure 69: Cumulative total beta without ^{3}H activity release measured using liquid scintillation

4.2.4 Measurement of ^{3}H by digestion and distillation of leachant

The cumulative total release of ^{3}H from the irradiated graphite samples is shown in Figure 70. Over the 91 days of the experiment approximately 275.33 ± 18.20 Bq (from a 50 ml sample) of ^{3}H was measured using a Liquid Scintillation Counting. This value was derived from measurements taken on the most active sample. From Figure 70 it can be observed that the rate of leaching of ^{3}H increase as the time of leaching increases and starts to plateau after about 7 days (Table 24). Samples with highest amount of leached radionuclides are the ones which were trepanned from the middle of the core. The initial rise may possibly indicate the leaching of the contaminant is from the surface of the graphite and it may be due to its very high solubility as discussed in Table 23. The background activity level of ^{3}H in the laboratory was found to be below the detection limits (minimum detectable activity is 0.2 Bq).

The amount of activity found at this stage is similar to the activity release produced by interpolating total alpha and beta activity release result with alpha and beta without ^{3}H activity result (Figure 68 and Figure 69) that is shown in Figure 71. The difference is approximately 20% and may be due to the existence of weak beta emitting radionuclides.

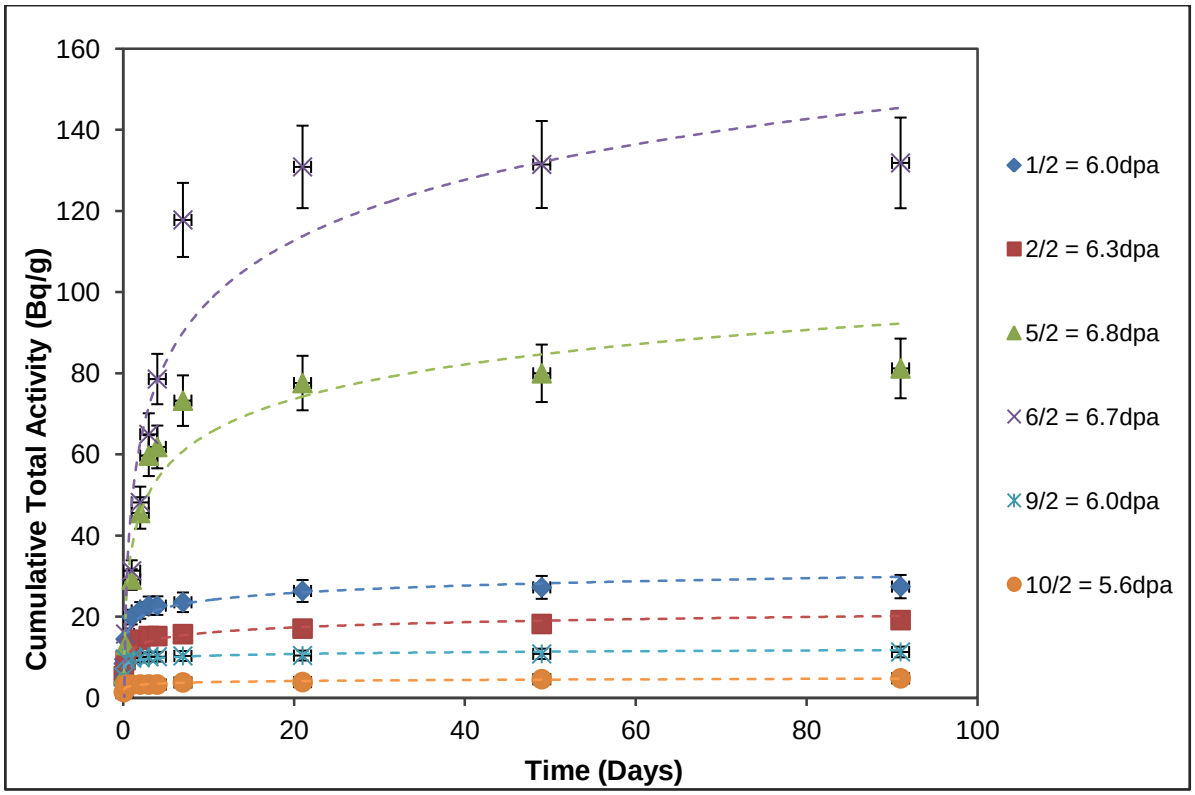

Figure 70: Cumulative total ^{3}H activity release measured using liquid scintillation

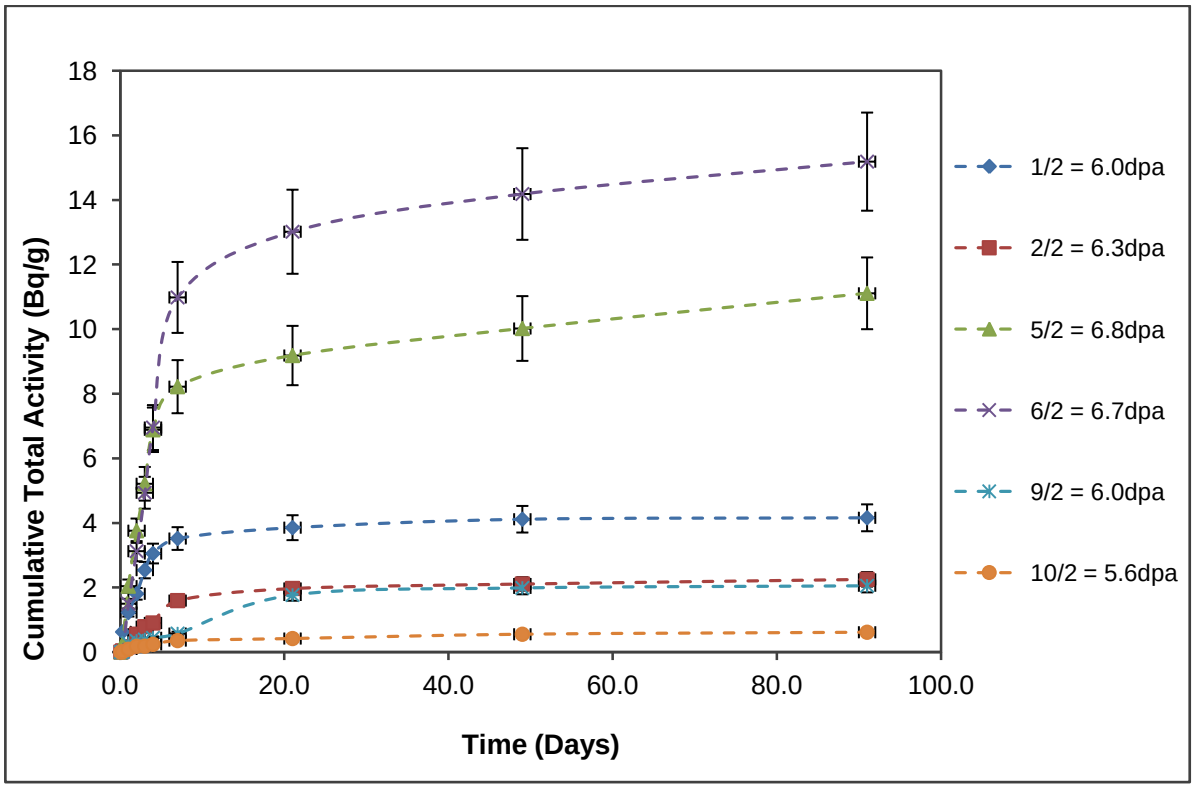

Figure 71: Graph showing result found by interpolating cumulative total alpha and beta and total alpha and beta without ^{3}H activity release

4.2.5 Measurement of ^{14}C by digestion (wet oxidation) of leachant

The quantities of ^{14}C obtained in the experiments are shown in Figure 72.The background levels of the blank and the laboratory was below detection limits (Minimum detectable activity is 0.2 Bq). Over the 91 days of the experiment about 106.26 ± 7.01 Bq cumulative activity (in sample size of 50 ml) of ^{14}C containing carbon dioxide was captured using a 0.1M sodium hydroxide dreschel bottle from the most active sample. The highest amounts of radionuclide leached is from the samples which were trepanned from the centre core bricks (i.e. 5/2 and 6/2) and exposed to highest radiation.

It can be seen from Figure 72, that the rate of leaching of ^{14}C increase with increasing time and plateaus after about 21 days (Table 24). The leaching period for ^{14}C (21 days) is longer than for ^{3}H (7 days). ^{14}C is mainly produced from carbonaceous deposits which are integral to the original graphite pores and surfaces, and from nitrogen impurity found in the form of gas which has accumulated on the surface of the graphite or nitrogen gas which is trapped within closed pores during calcination procedure during graphite manufacturing.[97] During leaching the leachant have to travel through the internal porosity via the complex porosity network which may result in a longer leaching time. ^{14}C can make a bond with the graphitic lattice structure.[3, 83] Therefore, this chemical formation may have a significant effect on the solubility of the nuclide and its chemical reaction rate with water. But ^{3}H which was adsorbed at the pore surfaces will be released when it makes contact with hydrogenous molecules in the leachant. Since it is bound to the surface it leaches out more quickly than ^{14}C radionuclide.

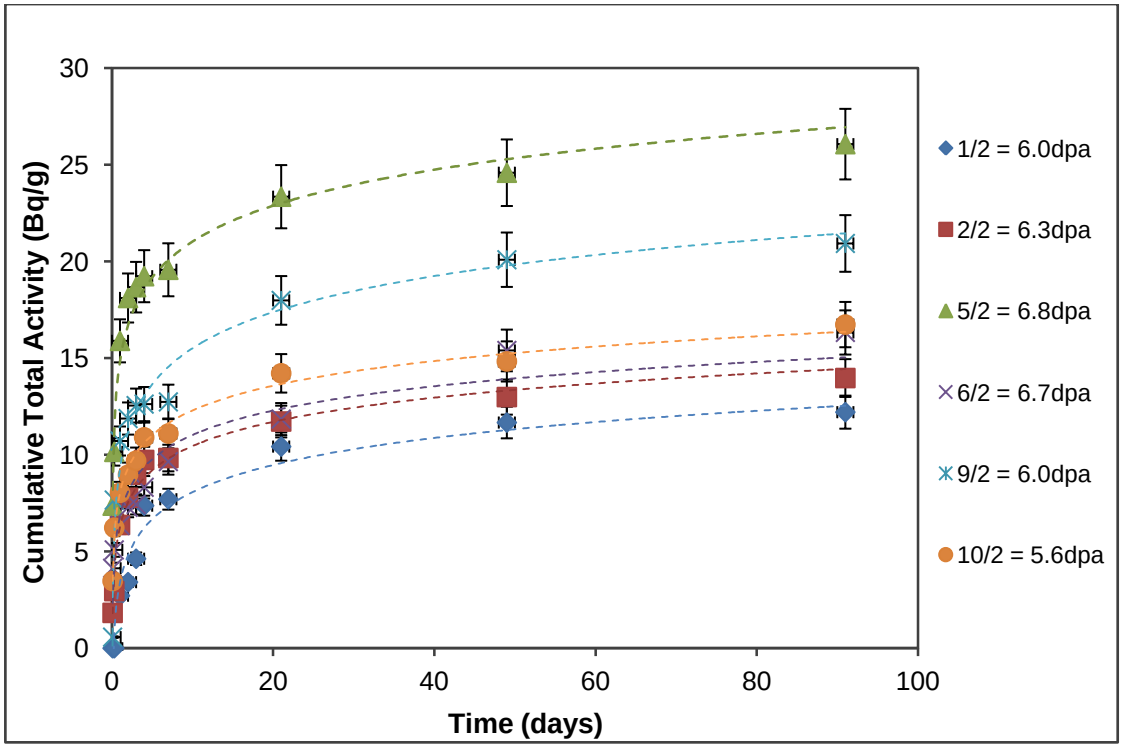

Figure 72: Cumulative total ^{14}C activity release measured using Liquid Scintillation

4.2.6 Leaching Rate of Graphite Specimens

The investigations carried out for mechanisms of leaching and measured rates have not produced extensive information in this area. The information on the chemistry of leaching reported in literature around 25 years ago and due to this it is very scarce.[103] Therefore, the purpose of this investigation is to document the results of the leach tests *conducted* on the samples of graphite obtained from the Oldbury Reactor 1. The information produced will help (1) to obtain data and compare information with other studies which have been conducted and published by other scientists and organisations, (2) to understand better the processes determining leaching behaviour and (3) to determine critical leaching parameters for further encapsulation and modelling investigation. The idea is to use short-term data to extrapolate to long times by utilising the data from different leachate experiments, modelling the effective leaching rate coefficient for leaching of radionuclides from a finite cylinder.

The cumulative fractional leach radioactivity of ^{3}H and ^{14}C found in the leachates are shown in Figure 73 and Figure 74. Data presented for the graphs were derived from the following equations [83, 104]:

$$F = \frac{\sum A_n}{A_0} \quad \ldots\ldots\ldots\ldots\ldots \; eq.18$$

$$R = \frac{F}{t_n}$$

$$L = \frac{R.V}{S} \ldots\ldots\ldots\ldots\ldots\ldots .. eq.19$$

Where:

F = Cumulative fraction of radionuclide released in a given leachant renewal period

A_n = Radioactivity in the leachate released during the leachant renewal period *n, Bq.g*$^{-1}$

V = Volume of specimen, cm^3

A_0 = Initial radioactivity inventory in the graphite specimen, *Bq.g*$^{-1}$

M = Mass of specimen, g

R = Cumulative fractional leach rate for the period, day^{-1}

S = Exposed surface area of specimen, cm^2

t = Duration of leachant renewal period, days

L = Cumulative leach rate of graphite per unit surface area of specimen, cm.day^{-1}.

To measure the initial radionuclide inventory[(a)] of the irradiated graphites before leaching tests two graphite samples from the same reactor was taken and combusted using Carbolite® furnace. The detailed procedure of combustion and analysis is detailed elsewhere [100]. The inventories of ^{3}H and ^{14}C in these specimens averaged 44 kBq/g and 64 kBq/g respectively. Moreover, the samples were separately characterised for density[(b)] using immersion method

(a) Total initial radionuclide measurements were done by Rob Worth, University of Manchester, UK.
(b) Density measurement were provided by National Nuclear Laboratory, Sellafield, UK

and their weight was measured before immersion and Table 25 shows the characterisation results for the six samples.

The cumulative fraction of inventory leached is calculated using eq. 18, i.e., by adding the leached fractions in each leach period. It is interesting to see that the greatest leach rates for ^{14}C do not follow the neutron irradiation history of the samples. Samples which were exposed to a slightly lower dose have released much more contamination. As it can be seen from Table 25 most samples which have a higher density have released much more activity. But, it is difficult to speculate the exact reason for the cause of this difference between the release behaviour of these samples.

For ^{3}H the samples which have the highest leach rates are the one which were exposed to high neutron dose and are the one of which located at the centre of the reactor core channel (Table 26). On average about 0.13 % of ^{3}H and 0.19 % ^{14}C of the inventory have leached out from the irradiated graphites during the 91 day period.

The incremental leach rates (calculated using eq. 19) are reported in Figure 75 and Figure 76. Each best fit curve to the series of data points exhibits a characteristic initial sharp fall, possibly due to leaching of nuclides present on the surface of the graphite, followed by a more progressive decline towards apparent equilibrium. The results of the leach tests are summarised in Table 27 and the cumulative fractions of activity released for ^{3}H and ^{14}C nuclides into the simulated groundwater at day 91 is summarised in Table 28.

The feasible mechanisms for the observed decline in leach rates with time could be due to the depletion of the ^{3}H and ^{14}C supply and the solubility of the radionuclide in water. The ^{14}C activity was not depleted during the leaching. Nevertheless, a significant fraction of ^{3}H was depleted from graphite samples. The reason for the depletion could be as mentioned above, the activity may have depleted due to the reactivity of ^{3}H, i.e., it may react with the leachant quickly or it is may be more readily available to react with the leachant.

The other interesting point is that the samples have almost the same dose (dpa), but the leach rate of the samples is different. This shows that weight loss and density change have played a major role on the release of radionuclide. Moreover, the order of the leaching rate of ^{14}C is greater than that of ^{3}H. This reveals that the amount of ^{14}C activity release is slower than the release of ^{3}H.

Table 25: Characterisation Results

Brick position	Slice	Weight (g)	Density by Immersion (g/cm^3)	Volume* (cm^3)	Thickness (cm)	Diameter (cm)	Surface* Area (cm^2)
4L	1/2	0.7239	1.2778	0.5665	0.5064	1.1935	4.1361
4U	2/2	0.8027	1.2151	0.6606	0.6053	1.1788	4.4243
6L	5/2	0.6905	1.2630	0.5467	0.4735	1.2125	4.1128
6U	6/2	0.8721	1.2397	0.7035	0.6062	1.2156	4.6360
8L	9/2	0.9651	1.3374	0.7216	0.5999	1.2376	4.7381
8U	10/2	0.7480	1.3934	0.5368	0.4769	1.1971	4.0448

* Calculated by the author

Table 26: Temperatures and Fast Neutron Dose for Oldbury Reactor 1 (2009) Trepanned Samples from Flattened Region Channels [60]

Sample ID	Brick	Trepanned Sample Height (m)	Temperature (°C)	DIDO Equivalent Dose (10^{20} $n.cm^{-2}$)	Displacement per atom* (dpa)	%wt loss*
1/2	4L	2.66	294	45.56	6.0	33
2/2	4U	3.01	302	48.15	6.3	38
5/2	6L	4.26	329	51.49	6.8	33
6/2	6U	4.70	338	50.95	6.7	33
9/2	8L	5.86	356	45.55	6.0	25
10/2	8U	6.22	361	42.86	5.6	27

* Calculated by the author

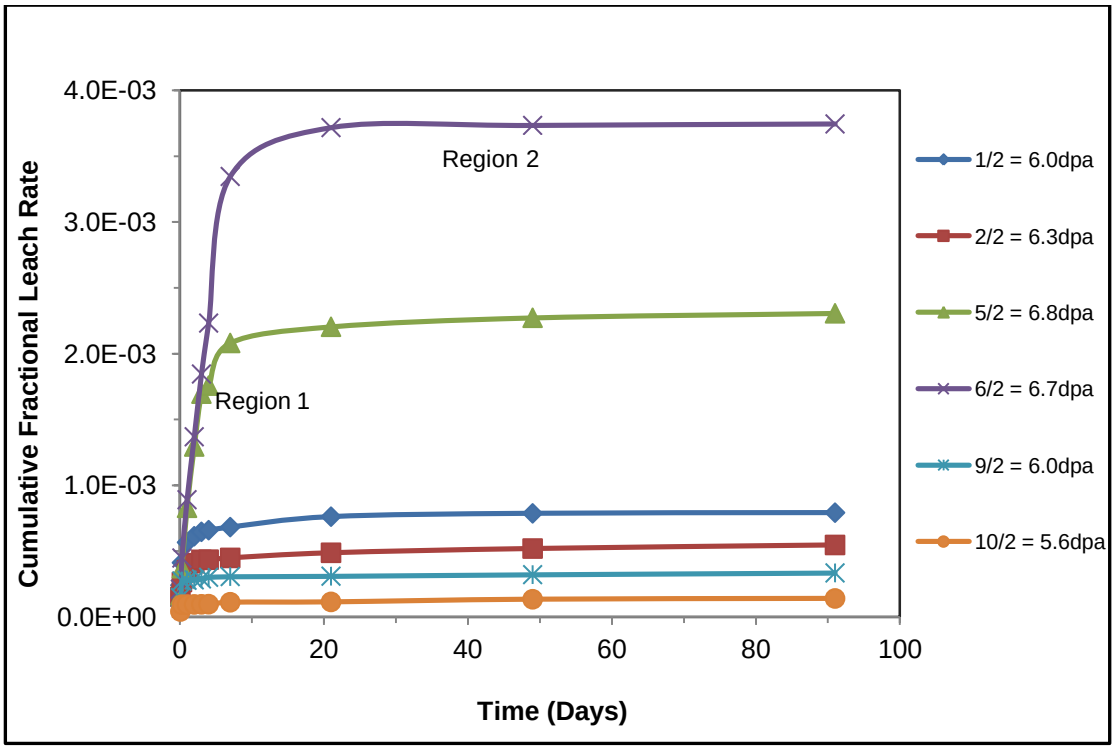

Figure 73: Cumulative Fraction of ^{3}H Activity Leached in Simulated Groundwater at 20 ± 5°C

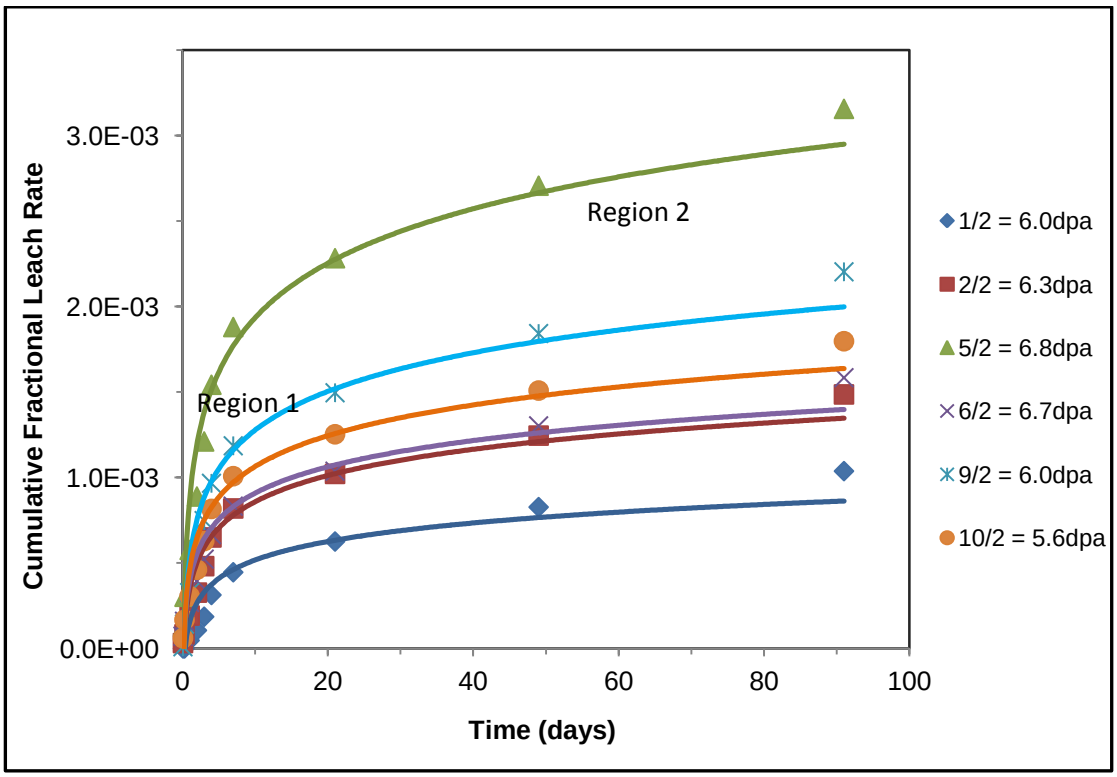

Figure 74: Cumulative Fraction of ^{14}C Activity Leached in Simulated Groundwater at 20 ± 5°C

Table 27: Incremental Leach Rates at Day 91

Sample	Density by Immersion (g/cm^3)	Surface* Area (cm^2)	%wt loss	Incremental Leach Rate	
				^3H	^{14}C
				$cm.day^{-1}$	$cm.day^{-1}$
1/2 = 6.0dpa	1.2778	4.1361	33	8.46×10^{-8}	6.86×10^{-7}
2/2 = 6.3dpa	1.2151	4.4243	38	1.11×10^{-7}	8.56×10^{-7}
5/2 = 6.8dpa	1.2630	4.1128	33	1.31×10^{-7}	1.42×10^{-6}
6/2 = 6.7dpa	1.2397	4.6360	33	1.25×10^{-7}	1.02×10^{-6}
9/2 = 6.0dpa	1.3374	4.7381	25	1.01×10^{-7}	1.31×10^{-6}
10/2 = 5.6dpa	1.3934	4.0448	27	9.09×10^{-8}	9.12×10^{-7}

Table 28: Cumulative Fraction of Activity Leached at day 91

Sample	Cumulative Fraction of Activity Leached	
	Cumulative Fraction of ^3H Activity	Cumulative Fraction of ^{14}C Activity
1/2 = 6.0dpa	7.91×10^{-4}	8.87×10^{-4}
2/2 = 6.3dpa	5.46×10^{-4}	1.24×10^{-3}
5/2 = 6.8dpa	2.31×10^{-3}	2.71×10^{-3}
6/2 = 6.7dpa	3.75×10^{-3}	1.30×10^{-3}
9/2 = 6.0dpa	3.34×10^{-4}	1.93×10^{-3}
10/2 = 5.6dpa	1.39×10^{-4}	1.51×10^{-3}

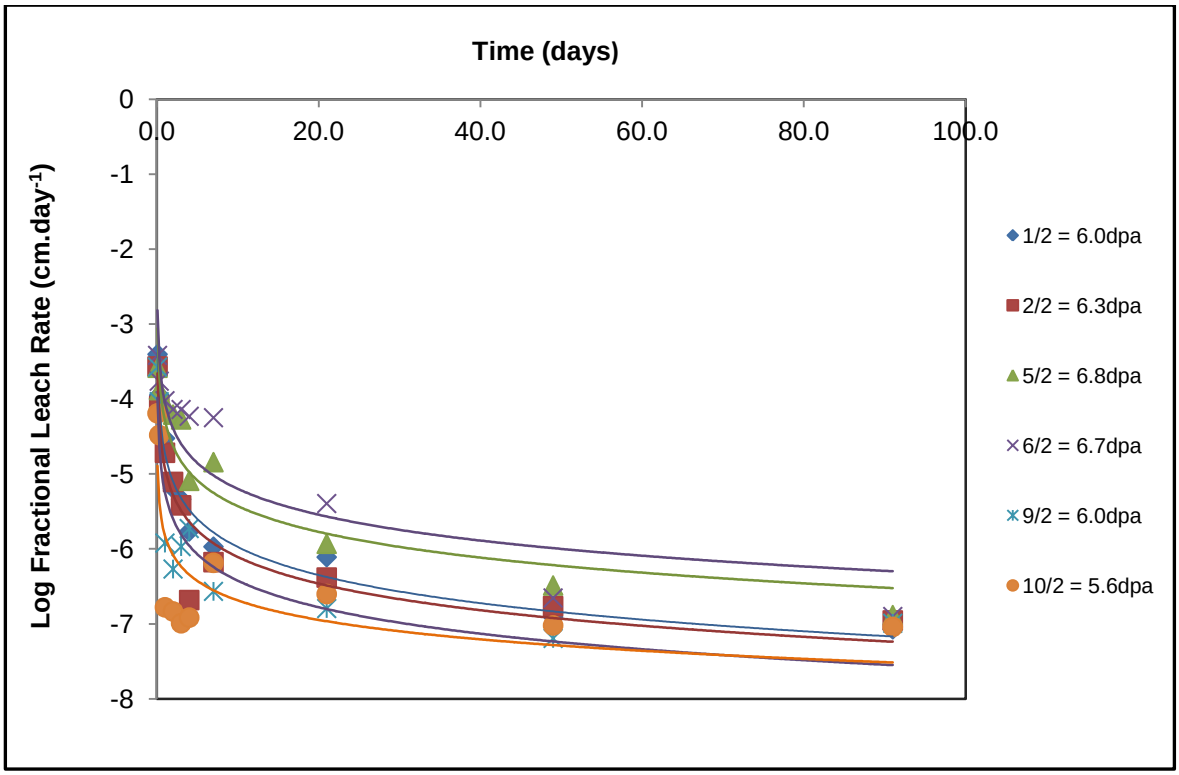

Figure 75: Fractional Leach Rate of ^{3}H in Simulated Groundwater at 20 ± 5°C

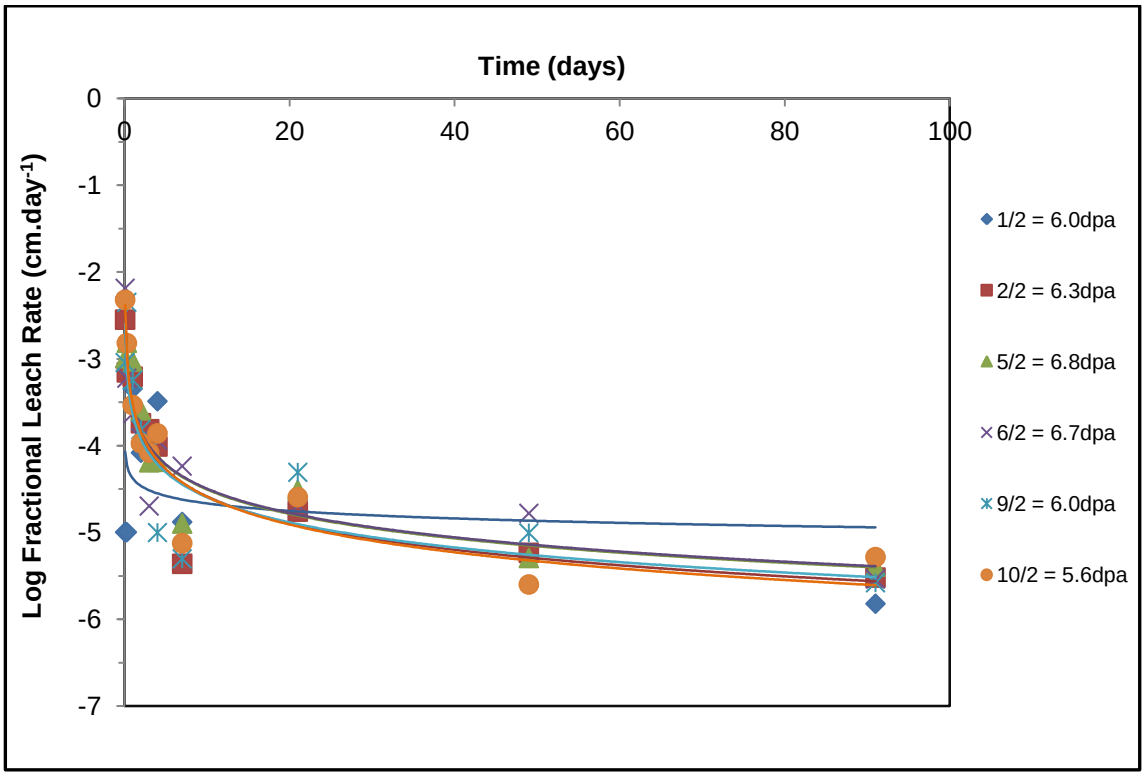

Figure 76: Fractional Leach Rate of ^{14}C in Simulated Groundwater at 20 ± 5°C

4.2.6.1 Determination of leaching mechanism

The determination of leaching mechanism methods used to evaluate diffusion controlled release are frequently referred to as either "monolith leach tests" or "tank leaching tests."

Two primary test methods are used for evaluation of monolithic materials. The first test method is the American Nuclear Society Method 16.1 (ANS 16.1, 1986).[69] The second test method is a recent derivation of ANS 16.1 that has been adopted in The Netherlands as NEN 7345 (1994).[105]

The Dutch diffusion leaching test NEN 7345 was employed to assess the mechanism of release of radionuclides from waste that is monolithic in form. The test applies Fick's second law of diffusion (eq. 20) for evaluating leaching behaviour, calculation of effective diffusion coefficient, and long-term leaching predictions.

$$\frac{\partial A}{\partial t} = D_e \frac{\partial^2 A}{\partial x^2} \dots\dots\dots eq.20$$

$where$:

D_e - effective diffusion coefficient [m^2/s]

A - Radionuclide concentration available in the solid phase

t - Leaching period [days] and

x - Distance from the surface [m]

In practice the NEN 7345 test is very similar with the American Nuclear Society Method 16.1 (ANS 16.1). In both test methods a molded and cured test specimen of defined geometry is immersed in deionised water (leachant). The leachant is then replaced by fresh leachant after specified period and the resulting leachant is sampled for chemical assay. The main difference between the tests is the basis for data reduction (the renewal periods are 0.25, 1, 2.25, 4, 9, 16, 36 and 64 days), and the calculation of effective diffusion coefficients and other parameters are provided. In addition, the diffusion models require that the cumulative fraction leached in any test is related to the ratio of the sample geometric surface area to geometric volume (S/V).

To estimate the effective diffusion coefficient, D_e Crank (1989) [106] have used a one dimensional semi-infinite linear diffusion model based on data obtained from both monolithic specimens and compacted granular material. The model requires the following boundary conditions for leaching test to be fulfilled:

- the material is homogeneous in composition
- over the duration of the test no depletion has occurred
- leachant replacement cycles are frequent enough to make sure the leachate remains dilute relative to leachate saturation element of interest, and

- monolithic samples maintain physical integrity (e.g., no cracking or disintegration) during testing

Crank [106] has developed a solution of Fick's law of diffusion (eq. 21) for the above conditions from a product with semi-infinite dimensions, in which the initial concentration is uniformly distributed in the product and the concentration on the surface between the product and the leachate is constant with respect to time:

$$\frac{A - A_1}{A_1 - A_0} = erf\left\{\frac{x}{2\sqrt{D_e t}}\right\} \ldots\ldots\ldots\ldots\ldots eq.21$$

where:

$A = A(x,t)$ - concentration as a function of location within the solid test specimen and time

A_1 - constant concentration at x=0

A_o - initial concentration in the product which must be uniformly distributed

D_e - the effective diffusion coefficient

t - Time [s], and

x - Distance from the surface [m], positive values

The resulting diffusion equation derived from eq.21 for the boundary condition is:

$$D = \frac{\pi A_t^2}{4t(\rho A_0)^2} \ldots\ldots\ldots\ldots\ldots\ldots eq.22$$

where:

D or D_e - diffusion coefficient for component x in the product [m^2/s]

A_t - cumulative release of the component [mg/m^2]

t - Leaching period time [s]

A_0 - maximum leachable quantity [mg/kg], and

ρ - Bulk density of the product [kg/m^3]

The NEN 7345 test uses specimens with a minimum diameter of 40 mm which is immersed in leachant in a closed vessel.[105] But Serne, R.J, et al. [107] prepared various sizes of cylindrical grout samples to test the effect of sample size in diffusion of contaminants from monolithic samples. They have showed that there is no significant difference in the diffusion coefficient (leach rate) between the various sized samples when leached in groundwater or deionised water.

The analysis of the determination of the diffusion mechanism of contaminants was provided by Todorović and Ecke (2004).[108] They have used weakly bound chlorine to study the leaching

of components from solid matrix and information on the physical properties of the matrix. They have analysed the leaching activities of the elements to determine whether the leaching of chlorine from the solid matrix is diffusion controlled or not. The investigation concluded that the diffusion controlled leaching behaviour is distinguished by the cumulative fractional release following a 0.5 slope on a log release vs. log time release plot. Rearranging eq. 22 yields:

$$A_t = \rho A_0 \left(\frac{4D_t t}{\pi}\right)^{\frac{1}{2}}$$

and after logarithmic transformation:

$$log\left(\frac{A_t}{A_0}\right) = \frac{1}{2}\log(t) + \ log\left\{\rho\left(\frac{4D_t}{\pi}\right)^{\frac{1}{2}}\right\}$$

Regression analysis (NEN 7345, 1995) was used to determine how much the curve deviated from 0.5 slope. If slope of a leaching curve or its part is within 0.5±0.15 interval, then leaching during the test or its part is diffusion controlled. The detailed derivation of this diffusion criteria is reported by Soldatove, 1997.[109] Subsequently, the effective diffusion coefficient is calculated using the total availability of a contaminant as determined using the NEN 7341 (1994) [50] as the driving force for diffusion.

The mechanism of leaching is thought to be diffusion controlled process. The permeability of a material determines how easy a leachant enters the specimen, and how fast radionuclides will be released over time. Water tends to flow around products with a low permeability rather than to enter it. Consequently, this is why products with a low permeability are more likely to show diffusion controlled release.[102]

Therefore, to determine whether the leaching is diffusion controlled or whether it depends on other mechanisms a graph was constructed using cumulative leach fraction data. The determination of the controlling leaching mechanism is based on the gradient of the linear regression of the logarithm of cumulative leach fraction versus the logarithm of time [105]. Then, the criterion for diffusion was applied to determine the process, i.e., if the gradient of the graph is less than 0.35 the controlling leaching mechanism will be the surface wash–off, if the gradient values are between 0.35 and 0.65 the controlling mechanism will be the diffusion, and higher gradient values signifies the dissolution mechanism.[105]

The result of the linear regression for all samples for the analysis is shown Figure 77 and Figure 78 for ^{3}H and ^{14}C, respectively. From Figure 77 it can be observed that the gradient values for all samples are less than 0.35 which indicate that the controlling leaching mechanism for leaching of ^{3}H from the graphite is surface wash–off. For ^{14}C it can be observed that the gradients of the graphs are between 0.35 and 0.65. This reveals that the leaching of the

radionuclide is due to surface wash-off and diffusion, and dissolution did not take place at all. This can be explained more clearly using incremental leach fractions graph of ^{3}H and ^{14}C which is expressed as cm.day^{-1} on log scale versus time graph as shown in Figure 79 and Figure 80, respectively. From both radionuclides incremental leach graphs, it can be observed that the leaching pattern can be divided into two regions. Region 1 demonstrates initial release of radionuclides and then a reduction in the release take place over a longer period of time (Region 2). ^{3}H shows an initial rapid release of radionuclides within the first 7 days and a drastic reduction in the release observed over a longer period of time. In contrast, ^{14}C showed an initial rapid release of radionuclides and there is more release when measured at day 21. Then, a reduced rate of release observed over a longer period of time.

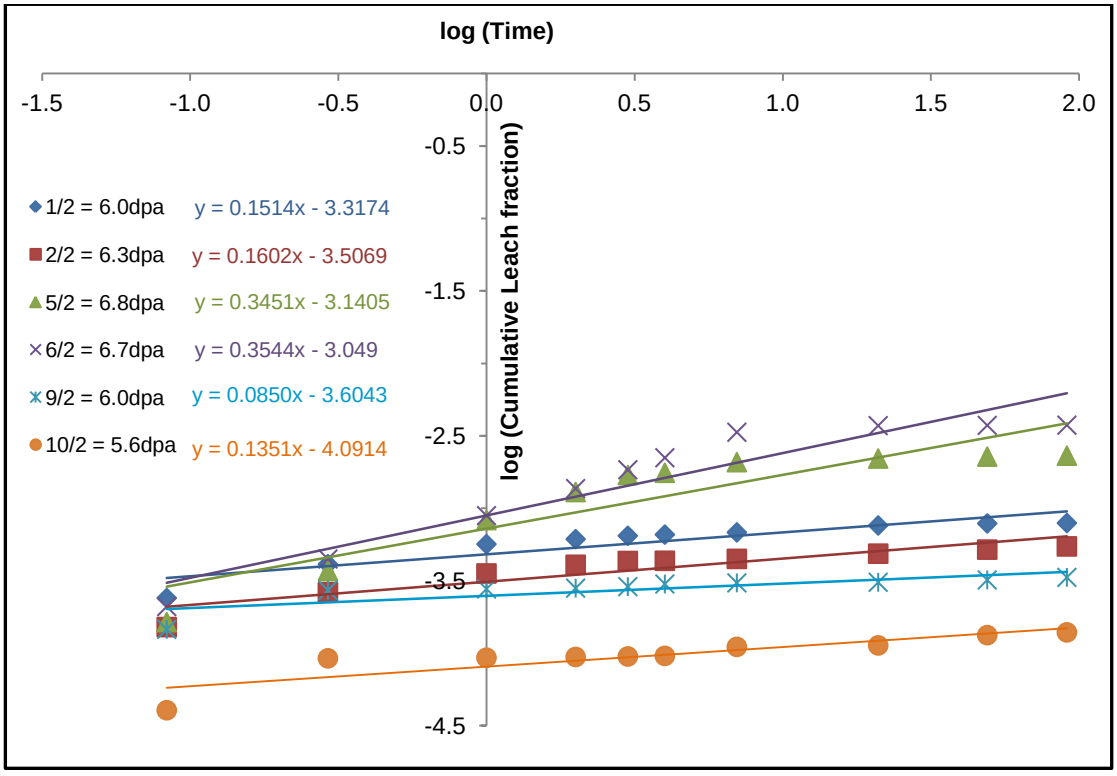

Figure 77: Linear Regression Graph of the Logarithm of Cumulative Leach Fraction of ^{3}H versus the Logarithm of Time

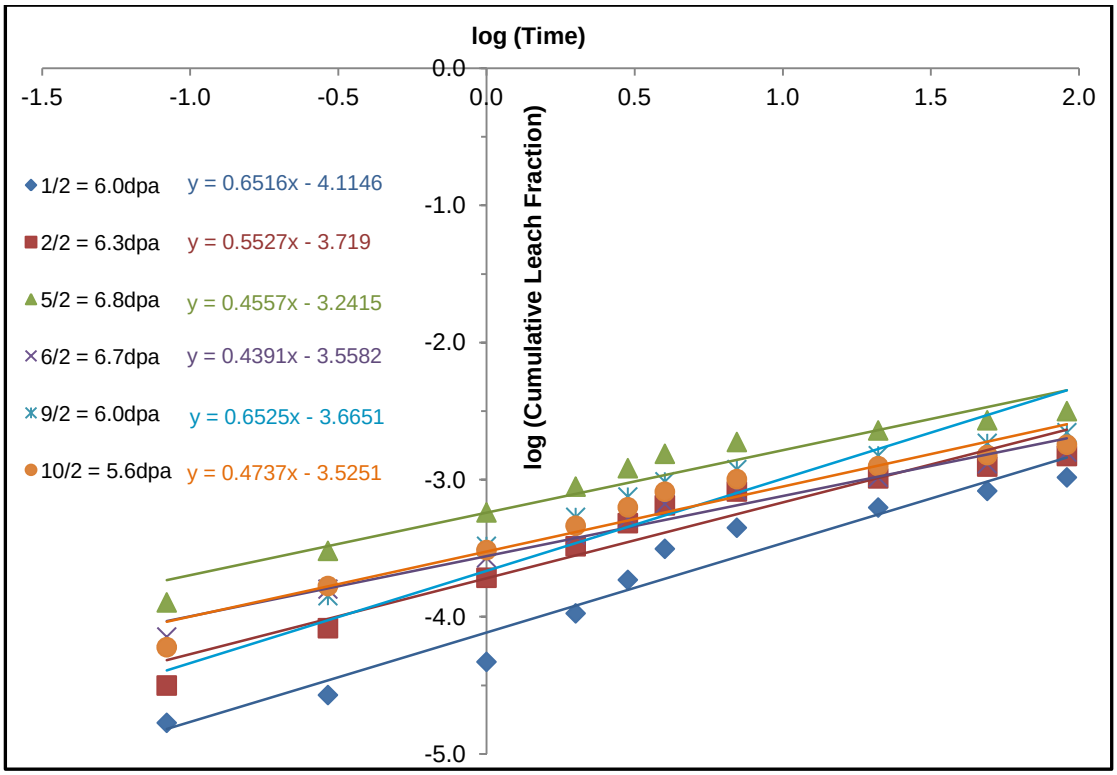

Figure 78: Linear Regression Graph of the Logarithm of Cumulative Leach Fraction of ^{14}c versus the Logarithm of Time

4.2.6.2 Leaching Factor/ Effective Diffusion Coefficient

The mechanism of diffusion is very complex due to the microstructure of the graphite and the presence of impurities/contaminants which may affect the rate of leaching. In addition the diffusion can also be influenced by the variation in temperature in the laboratory, the chemical composition of the leachant solution, the change in chemistry of the leachant due to the radionuclides diffused out and the effect of radiation.

Hespe, E. D. [83, 110] from IAEA suggested that leach factor or diffusion coefficients may be used to compare leaching data. Assuming the diffusion is the primary mechanism a straight line relationship should exist between the terms:

$$\frac{\sum A_n}{A_0} \Big/ \frac{S}{V} \; and \; \sqrt{t_n} \qquad (a)$$

the quantity of radionuclide leached out from a unit surface area during time, t_n is given by (Crank, 1975 [106]):

$$A_n = 2A_0 \frac{\sqrt{Dt_n}}{\sqrt{\pi}} \qquad (b)$$

Thus, from (a) and (b):

$$m = 2\frac{\sqrt{D}}{\sqrt{\pi}}\ x\ \frac{S}{V}$$

Where:

m = Gradient/ slope of the straight line

D = Leaching factor/ Effective Diffusion Coefficient

Therefore,

$$D = \frac{\pi m^2 V^2}{4S^2}$$

Figure 79 shows the fractional leach activity of ^{3}H radionuclides from all six samples studied versus square root of leaching time. As it can be observed from the figure, for all leaching test samples, there is an initial fast release during the first period and then has reached approximately to its equilibrium. This behaviour reveals the presence of one value of diffusion coefficient for the fast component and for the very slow component the value of the diffusion coefficient is close to zero or very low. But for ^{3}H as it can be observed from Figure 79 there an initial fast release. The diffusion coefficient for ^{3}H nuclide reported in Table 29 is the only for the initial fast release and the average diffusion coefficients of each sample.

The fractional leach activity of ^{14}C radionuclide from all six samples studied versus square root of leaching time is shown in Figure 80. It can be observed from the figures for all leaching tests there is an initial fast release during the first period followed by slow leaching in the subsequent periods. This behaviour reveals the presence of two different values of diffusion coefficients for the fast and slow components or the region where the leaching is approaching equilibrium. So, the calculated diffusion coefficient for ^{14}C nuclide reported in Table 29 is the average values of these two components diffusion coefficients and the average diffusion coefficients of each sample. From the data (Table 29) it can be deduced that ^{3}H have larger value of diffusion coefficients than ^{14}C radionuclide and can diffuse out more readily than ^{14}C.

Table 29: Diffusion coefficient value ^{14}C radionuclide leached from irradiated graphite waste

Radionuclide	Average Diffusion ($m^2.s^{-1}$)	Diffusion ($cm^2.s^{-1}$)
^{3}H	5.83×10^{-9}	5.83×10^{-5}
^{14}C	1.75×10^{-13}	1.75×10^{-9}

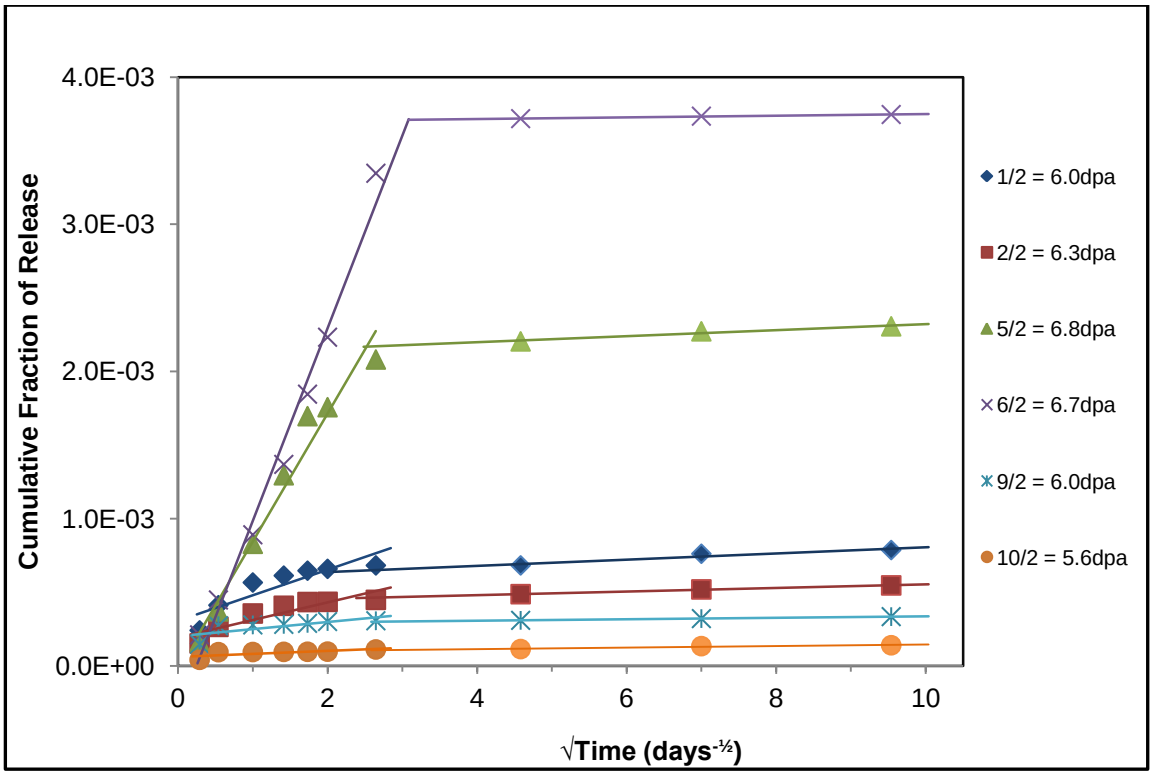

Figure 79: Cumulative Fraction of ^{3}H Activity Leached in Simulated Groundwater at 20 ± 5°C

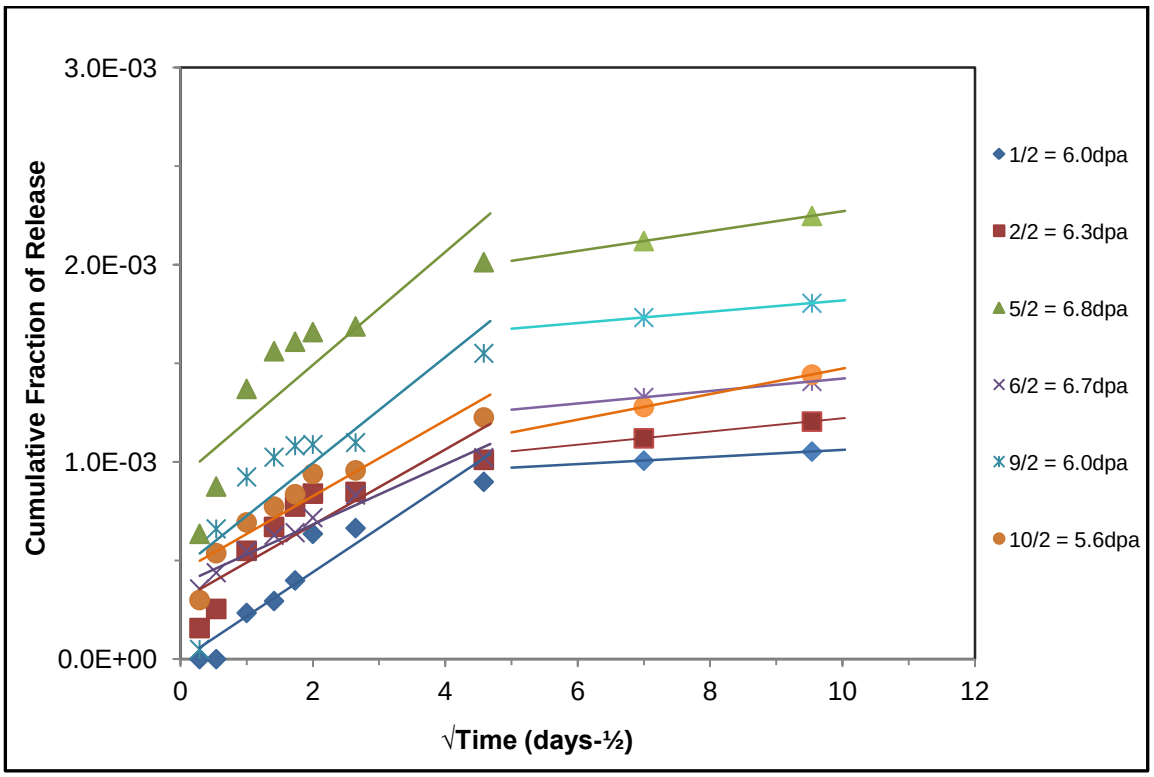

Figure 80: Cumulative Fraction of ^{14}C Activity Leached in Simulated Groundwater at 20 ± 5°C

4.2.6.3 Comparison with previous studies

It is of importance to compare the ^{3}H and ^{14}C leaching data of our studies with those obtained by White et al. (1984) [51] and Gray and Morgan (1988 &1989) [103, 104]. It is a special of interest to compare our investigation with White et al. since both tests were carried out on Magnox reactor graphite. White et al. used Hanford simulated groundwater while Gray and Morgan used demineralised water as a leachate in their experiment.

To enable comparison, both White et al. and Gray and Morgan have used samples cut from the inner-most bar retrieved from a reactor. But moderator bars are exposed to the maximum neutron fluence in the reactor and received different dose under reactor operation. Therefore, the graphite is not homogeneous, thus, a small sample from one bar may not be representative of the average of the material surrounding it. Hence, to minimise this uncertainty we have used six samples retrieved from one channel wall but from different brick and reactor position.

The ^{14}C data obtained in our investigation is scattered showing similar characteristics with the result observed by White et al. performed on CEGB Magnox reactor graphite at 25 °C and pressure of 1 bar. The temperature and pressure in the laboratory was controlled at 20 ± 5 °C throughout the entire work and the cause for scattering of the data can only be attributed to the slow rate of release of ^{14}C from the graphite matrix.

The average cumulative leach fraction results of ^{3}H and ^{14}C found (Table 30) are similar to the results obtained by White et al. (Table 31). The value of ^{14}C attained by the author is slightly higher; this implies that the irradiated graphite samples used for this investigation, in general, are much more reactive. The mean initial radionuclide inventory for ^{14}C obtained by White et al. was 21 kBq/g and as mentioned above the samples used in this experiment have a mean activity of 64 kBq/g, which lends support to the argument. From the results it was observed that the leach rates are decreased by factors of 15 to 140 after 91 days. This is very similar to the reduction observed by White et al. who have found a reduction by factors of 50 to 100 after 100 days.

In contrast, the cumulative fractional ^{3}H activity obtained is less than from the value discovered by White et al., but the result is relatively good given the initial inventory difference; 220 kBq/g which is 5 times more active than the initial radionuclide inventory obtained by the author. The difference on the initial inventory and cumulative leach fraction may be influenced by weight loss which may have been produced by of radiolytic oxidation. As discussed in section 3.1.2 the graphites involved in the leaching experiment have suffered a weight loss of up to 38 % during operating time. The weight loss is originate from the open pore structure opening up by oxidation and at the higher weight losses by opening up of much of the closed porosity in the graphite [82]. For instance, it was reported that (Morgan, W.C, 1988 [103]) the graphite samples which were used by Gray and Morgan may have been suffered 2 % weight loss. Therefore,

weight loss is a significant factor that should be taken account of in inventory estimations and leaching investigation.

The cumulative leach fraction data obtained by Gray and Morgan (1988) [104] from an investigation performed on Hanford graphite (3.6×10^{-5} to 9.2×10^{-5} of inventory) at 20°C are far more less than from the amount found in our experiment (1.04×10^{-3} to 3.16×10^{-3} of inventory). But it is in good concurrence with their investigation result they have performed and obtained on graphite from French G-2 reactor (1989) [103] (2.6×10^{-3} to 8.5×10^{-3} of inventory). The reasons for these similarities and difference in the results obtained can be due to the experimental methodologies followed, differences in test duration, temperature, sample size, sampling frequency and/ or the leachant used.

Table 30: Average Cumulative Fraction and Average Incremental Leach Rate of Activity Leached at day 91 from all samples

Radionuclide	Simulated Groundwater at Day 91	
	Cumulative Fraction of Activity Leached	Incremental Leach Rate ($cm.day^{-1}$)
^{3}H	1.31×10^{-3}	1.07×10^{-7}
^{14}C	1.88×10^{-3}	1.03×10^{-6}

Table 31: Cumulative Fraction and Incremental Leach Rate of Activity Leached at day 100 obtained by White et al.

Radionuclide	Simulated Groundwater at Day 100	
	Cumulative Fraction of Activity Leached	Incremental Leach Rate ($cm.day^{-1}$)
^{3}H	4.8×10^{-3}	2.7×10^{-6}
^{14}C	1.4×10^{-3}	6.0×10^{-7}

5. CONCLUSIONS

Irradiation induced damage to the nuclear graphite crystal structure have been shown to cause disruption of the bonding between the basal planes leading to *c*-axis expansion and *a*-axis contractions. Moreover, from the TEM analysis closure of Mrozowski cracks has been observed. The bulk properties are influenced by both this dimensional change coupled with by the porosity distribution, in particular, at the nanometre scale. This is due to fast neutron irradiation. The crystallites shrink and swell, resulting in contraction of crystal related lenticular porosity.

Graphite consists of many thousands of platelets. Some of the impurities are trapped within these platelets and some of them are chemically bonded with the graphite structure. In reactor core radionuclides located within the bulk irradiated graphite could arise from the activation of these impurities which were integral with the original graphite components. Therefore, using EDX analysis it was possible to determine some of the impurities which could be the origin of some of the radionuclides which were leached into the leachate from the active specimens. For instance, titanium and iron which might be sources of ^{59}Co, chlorine impurity which is responsible for ^{36}Cl, Cesium which is a source of ^{133}Cs and Calcium which could be a source of ^{46}Sc.

The tests which were carried out on Gilsocarbon nuclear grade graphite shows the most abundant elements in the material matrix are iron, calcium and aluminium impurities. Small amounts of magnesium, oxygen and chlorine were also detected. The concentration of the impurities in Gilsocarbon is low compared to PGA graphite. The total impurities on the graphite were found out to be about 0.003 %, which is much less than the impurities found in PGA graphite (0.01 %). Moreover, the percentage of Gilsocarbon pores (~11 %) is much less than that of the pores percentage of PGA graphite (~26 %). This fact is apparent from the coke ratio as the Gilsocarbon has contained more coke and is more dens. Therefore, knowledge of the crystallite structure and porosity distribution is very important; as it assists in gaining an understanding of the affects of irradiated damage and the location of and the mechanism of leaching of radionuclides.

A procedure for the evaluation of the leaching properties of radionuclides from irradiated graphite waste has been developed based on a standardised diffusion leaching test. The procedure employs simulated Drigg groundwater as a leachant using semi-dynamic technique for the production of leachate specimens. From gamma spectroscopy analysis the principal radionuclides present in terms of activity were ^{60}Co, ^{137}Cs, ^{134}Cs, ^{155}Eu, ^{133}Ba and ^{46}Sc. The dominant radionuclides are ^{60}Co, ^{134}Cs and ^{133}Ba which together account for about 91 % of the total activity. The 91 % can be broken down into 73.4 % ^{60}Co, 9.1 % ^{134}Cs and 8.1 % ^{133}Ba. Analysis of total beta and total beta without tritium activity release from Magnox graphite was measured using liquid scintillating counting. The results show that there is an initial high release of activity and decreases when the leaching period increases. This may be due to the depletion of contaminants which were

absorbed by the pore networks and the surface. During the leaching test approximately 275.33 ± 18.20 Bq of ^{3}H and 106.26 ± 7.01 Bq of ^{14}C was released into the leachant within 91 days.

The result of the linear regression analysis for all samples shows that the controlling leaching mechanism for ^{3}H radionuclide from the graphite is surface wash–off. For ^{14}C the initial controlling leaching mechanism is surface wash-off followed by diffusion which is the major transport mechanism. The amount released depends on the time-dependent diffusion of constituents from the products towards the water phase. The fractional leach activity of ^{14}C radionuclide versus square root of leaching time relationship reveals that the radionuclide has two different values (5.90 x 10^{-14} and 2.91 x 10^{-13}. The values which are given in Table 29 are the average values of these coefficients) of diffusion coefficients, i.e., the initial fast release during the first period followed by slow leaching in the subsequent periods.

The radionuclides released during leaching tests may arise from the activation of impurities that are integral with the original graphite components, other radionuclides arise from other reactor materials, which has then been activated elsewhere in the core before being carried around the circuit in the coolant gas. This latter activation material may be associated with the graphite component internal porosity surfaces transported via the complex porosity network.

Radiolytic oxidation leads to graphite weight loss which opens much of the closed porosity. Weigh loss is likely to significantly affect the leaching of elements from the irradiated graphite. From the result obtained in most cases the leaching of radionuclides from the samples increases as a function of the irradiation dose received by samples (the middle core brick samples to release more activity than the other brick samples). It is an intriguing observation to see that the release of ^{134}Cs, ^{137}Cs and ^{155}Eu differs from the release behaviour of the other elements. Because the release of these radionuclide from the samples is independent of the position samples in the core and the dose received. For instance, samples which were taken from the centre and lower core positions released a high amount of ^{134}Cs contaminant but the samples which are taken from the lower bricks of the core, i.e. 1/2 and 2/2, released slightly more than the centre brick samples. Similar characteristics were observed for the other two radionuclides.

Leaching predictions of both ^{3}H and ^{14}C from the graphite based on diffusion leaching test data agree well with previous leaching test data obtained by White, I. F., et al. (1985) conducted on CEGB Magnox reactor graphite and with Gray and Morgan (1989) result obtained using an irradiated graphite from French G-2 reactor.

To conclude, main contribution of this investigation to knowledge is that using EDX analysis it was possible to determine some of the impurities which could be the origin of some of the radionuclides which were leached into the leachate from the active specimens. From the Tomography investigation it was made possible to measure the amount of impurities and the distribution of

pores. Moreover, the controlling leaching mechanism of ^{3}H and ^{14}C radionuclides has been determined and it is also successful in determining their leaching rate.

6. RECOMMENDATION

- In the research the student has used TEM samples from scraping of tensile compression test. But if the facility is set up here at UoM, it will be good to prepare active samples with Focused Ion Beam (FIB) and distinguish the result obtained with sample prepared manually.
- Here a sample of 12 mm in diameter and with a height of 20 mm was used to characterise the sample with Tomography. If the sample size has decreased to a few milimeters it will save time and labour.
- Timeframe for leaching is very important, therefore, if leaching tests are conducted the time allocated should be sufficient to repaeat experiments and process results at least between each bath tests.

7. REFERENCE

1. Wise, M., *Management of UKAEA Graphite Liabilities.* Nuclear Energy, 2000. **39**(4): p. 249-257.
2. Telling, R.H. and M.I. Heggie, *Radiation Defects in Graphite.* Philosophical Magazine, 2007. **87**(31): p. 4797-4846.
3. Bradtec Decon Technologies, L., *Graphite Decommissioning Options for Graphite Treatment, Recycling, or Disposal, including a discussion of Safety-Related Issues*, E.P.R.I. (EPRI). Editor. 2006.
4. IAEA, *Characterization, Treatment and Conditioning of Radioactive Graphite from Decommissioning of Nuclear Reactors* W.T. Section, Editor. 2006, IAEA: Vienna. p. 71.
5. Jones, A.N., et al., *Review of the Characterisation of Nuclear Graphites in UK Reactors Scheduled for Decommissioning.* IAEA TECDOC, In press , 2009.
6. Bush, R.P., I.F. White, and G.M. Smith, *Carbon-14 Waste Management*. 1982.
7. Podruzhina, T., *Graphite as Radioactive Waste Corrosion Behaviour Under Final Repository Conditions and Thermal Treatment*, in *FZJ Report* 2004: Jülich.
8. Takahashi, R., et al. *Investigation of Morphology and Impurity of Nuclear Grade Graphite and Leaching Mechanism of Carbon-14*. in *IAEA Technical Committee Meeting on Nuclear Graphite Waste Management* 1999. Manchester, United Kingdom.
9. Marsden, B.J. and A.J. Wickham. *Graphite disposal options - A comparison of the approaches proposed by UK and Russian reactor operators*. in *Nuclear Decommissioning 1998*. 1998. London: Professional Engineering Publishing.
10. Kelly, B.T., *GRAPHITE - THE MOST FASCINATING NUCLEAR MATERIAL.* Carbon, 1982. **20**(1): p. 3-11.
11. IAEA. *Technical Committee Meeting* in *Nuclear Graphite Waste Management*. 1999. Manchester: IAEA Austria.
12. Kelly, B.T., *The Physics of Graphite*. 1981, London: Applied Science Publishers.
13. Reynolds, W.N., *PHYSICAL PROPERTIES OF GRAPHITE*, ed. A.E.A.T. plc. 1968, LONDON: ELSEVIER PUBLISHING CO. LTD
14. Pierson, H.O., *Handbook of Carbon, Graphite, Diamond and Fullerenes - Properties, Processing and Applications*. 1993: William Andrew Publishing/Noyes.
15. Goncharov, V.V., *Graphite in reactor design.* The Soviet Journal of Atomic Energy, 1958. **3**(11): p. 1257-1267.
16. Zuo, K., et al., *Development of nuclear-pure natural flake graphite.* Gaojishu Tongxin/High Technology Letters, 1997. **7**(6): p. 44-48.
17. Jones, A.N., et al., *Microstructural Characterisation of Nuclear Grade Graphite.* Journal of Nuclear Materials, 2008. **381**(1-2): p. 152-157.
18. Nightingale, R.E., *Nuclear Graphite*. 1962, New York: Academic Press.

19. Ubbelohde, A.R.a.L., F. A., *Graphite and Its Crystal Compounds*. 1 ed. 1960, Oxford: Oxford University Press. P. 1-46.
20. Clayton, A.M., Harper, A & Wheatley, C J *Behaviour of Chlorine in Nuclear Graphites.* Nuclear Engineering and Design, 1996(3): p. 145.
21. Marsden, B.J. *Reactor Core Design principles AGR and HTR*. 2008: Nuclear Graphite Research Group, School of Mechanical, Aerospace and Civil Engineering, The University of Manchester.
22. Reed, D.L., *THE COMPARISON OF CARBON-ATOM DISPLACEMENT RATE IN GRAPHITE IN THE DRAGON REACTOR, THE PETTEN HTR AND LOW ENRICHMENT HTR. Project DRAGON*, in *Other Information: UNCL. Orig. Receipt Date: 31-DEC-71; Related Information: OECD High Temperature Reactor Project Dragon Report. Now open access.* 1967. p. Medium: ED; Size: Pages: 42.
23. Marsden, B.J. *Dosimetry and Units*. 2008: Nuclear Graphite Reserach Group School of Mechanical, Aerospace and Civil Engineering, The University of Manchester.
24. Marsden, B.J. *Reactor Core Design Principles Air- Cooled and Magnox*. 2008: Nuclear Graphite Reserach Group School of Mechanical, Aerospace and Civil Engineering, The University of Manchester.
25. Wikipedia, t.f.e. *Advanced gas-cooled reactor*. 2013 25 February 2013 [cited 2013 5 March 2013]; Available from: https://en.wikipedia.org/wiki/Advanced_gas-cooled_reactor#cite_note-2.
26. Wickham, A.J. and B.J. Marsden, *Characterisation, Treatment and Conditioning of Radioactive Graphite from Decommissioning of Nuclear Reactors.* IAEA TECDOC-1521,, 2006.
27. Weir, C.G., *Chapelcross Melt-Out and Recovery Operations Active Working on Reactors*, ed. B.N.E. Society. 1971, London. pp 23-9
28. Simmons, J.H.W., *Radiation Damage in Graphite*, ed. Pergamon. Vol. Chapter 2. 1965, Oxford
29. Marsden, B.J., et al., *Dimensional and Material Property Changes to Irradiated Gilsocarbon Graphite Irradiated Between 650 and 750 °C.* Journal of Nuclear Materials, 2008. **381**(1-2): p. 62-67.
30. Kelly, B.T., W.H. Martin, and P.T. Nettley, *Dimensional Changes in Pyrolytic Graphite under Fast-Neutron Irradiation.* Philosophical Transactions of the Royal Society of London. Series A, Mathematical and Physical Sciences, 1966. **260**(1109): p. 37-49.
31. Ammar, M.R., et al., *Characterization of graphite implanted with chlorine ions using combined Raman microspectrometry and transmission electron microscopy on thin sections prepared by focused ion beam.* Carbon. **48**(4): p. 1244-1251.
32. Chi, S.H. and G.C. Kim, *Comparison of the oxidation rate and degree of graphitization of selected IG and NBG nuclear graphite grades.* Journal of Nuclear Materials, 2008. **381**: p. P9-14.
33. Telling, R.H., et al., *Wigner Defects Bridge The Graphite Gap.* Nature Materials, 2003. **2**(5): p. 333-337.

34. Kelly, B.T., *Basal Plane Contraction in Graphite Due to Mono-Vacancies.* Nature, 1965. **207**(4994): p. 257-259.
35. Walker, P.L., *Chemistry and Physics of Carbon*. The Study of Defects in Graphite, ed. P.A. Thrower. Vol. 5. 1969, New York: Marcel Dekker, Inc. P.217-315.
36. Walker, P.L., *Chemistry and Physics of Carbon*. Dislocations and Stacking Faults in Graphite, ed. S. Amelinckx, Delavignette, P. and Heersch, M. Vol. 1. 1965, London: Edward Arnold (Publishers) Ltd. P.6-14.
37. Henson, R.W. and W.N. Reynolds, *Lattice parameter changes in irradiated graphite.* Carbon, 1965. **3**(3): p. 277-287.
38. Kelly, B.T. and R.E. Taylor, *The Effect of Defects on the Thermal Conductivity of a Graphite Crystal.* Carbon, 1968. **6**(2): p. 219-219.
39. Thrower, P.A., *Vacancy and interstitial loops in graphite produced by high temperature irradiation and annealing.* Carbon, 1968. **6**(2): p. 211-211.
40. Fujita, F.E. and K. Izui, *OBSERVATION OF LATTICE DEFECTS IN GRAPHITE BY ELECTRON MICROSCOPY, PART I.* Journal Name: J. Phys. Soc. Japan; Journal Volume: Vol: 16; Other Information: Orig. Receipt Date: 31-DEC-61, 1961: p. Medium: X; Size: Pages: 214-27.
41. Jackson, A., *Nuclear Issues.*
42. von Lensa, W., *CARBOWASTE: New EURATOM Project on 'Treatment and Disposal of Irradiated Graphite and other Carbonaceous Waste'*, in *Proceedings of the 4th International Topical Meeting on High-Temperature Reactor Technology*, HTR2008, Editor. 2008: Washington D.C., USA.
43. FZJ, *CARBOWASTE Treatment and Disposal of Irradiated Graphite and Other Carbonaceous Waste Grant agreement no.: 211333*. 2008.
44. Quade, U. *Packaging requirements for graphite and carbon from the decommissioning of the AVR in consideration of the German final disposal regulations*. in *Technologies for Gas Cooled Reactor Decommissioning, Fuel Storage and Waste Disposal*. 1998. Vienna
45. HOLT, G. *The decommissioning of commercial Magnox gas cooled reactor power stations in the United Kingdom*. in *Technologies for Gas Cooled Reactor Decommissioning, Fuel Storage and Waste Disposal*. 1998: IAEA-TECDOC Vienna.
46. NDA, *Final Waste Issues Group Report*. June 2007.
47. NDA, *Final Waste Issues Group Report*. 2007.
48. Izumi, J., et al., *14CO and 12CO Separation on Na-X Using Pressure Swing Adsorption at Low Temperatures.* Adsorption, 2005. **11**(0): p. 817-821.
49. http://www.corwm.org/pdf/FullReport.pdf, C.o.R.W.M., *Managing our radioactive waste safely*. 2006, CoRWM
50. 7341, N., *Determination of Availability for Leaching of Inorganic Components from Granular (Wastes) Material, .* Netherlands Energy Research Foundation, Petten, The Netherlands., 1994. **Final Version,**.
51. White, I.F., et al., *Assessment of Graphite management modesfor graphite form reactor decommissioning*, in *CEC*, E. Commission, Editor. 1984.

52. Chambers, A.V., et al. *The diffusion of radionuclides through waste encapsulation grouts*. in *Materials Research Society Symposium Proceedings*. 2006.
53. Godbee, H.W., et al., *DIFFUSION OF RADIOISOTOPES THROUGH WASTE SOLIDS.* Trans. Amer. Nucl. Soc., 12: 450-1(Nov. 1969).; From 17th Conference on Remote Systems Technology, San Francisco, Calif. See CONF-691102., 1969.
54. Wen, K.Y., T.J. Marrow, and B.J. Marsden, *The microstructure of nuclear graphite binders.* Carbon, 2008. **46**(1): p. 62-71.
55. Kretchman, H.F., *The Story of Gilsonite*. 1957, Salt Lake City: American Gilsonite Company.
56. Brocklehurst, J.E., *The dilation of neutron irradiated graphite exposed to liquid sodium.* Carbon, 1968. **6**(4): p. 545-548.
57. Ellis, A. and K. Staples, *The management of magnox graphite reactor cores to underwrite continued safe operation.* SPECIAL PUBLICATION-ROYAL SOCIETY OF CHEMISTRY, 2007. **309**: p. 3.
58. Pick, M., *Magnox graphite core decommissioning and disposal issues.*
59. hagos, B., *Provide access to active research facilities to the DIAMOND project*. 2010, National Decomissioning Agency: National Nuclear Laboratory. p. 11.
60. Bushuev, A., Y.M. Verzilov, and V. Zubarev, *Radionuclide characterization of graphite stacks from plutonium production reactors of the Siberian group of chemical enterprises.* 2001.
61. R.R.Kinsey, e.a., *The NUDAT/PCNUDAT Program for Nuclear Data, paper submitted to the 9 th International Symposium of Capture-Gamma_ray Spectroscopy and Related Topics,* . 1999: Budapest, Hungary,.
62. Dent, H.K., E. Long, and , and K. Prince, *The Graphite Structure*, in *The Design of Gas-Cooled Graphite-Moderated Reactors*, D.R. Poulter, Editor. 1963, OXFORD UNIVERSITY PRESS: LONDON.
63. Flewitt, P.E.J., Wild, R. K., *Physical Methods for Materials Characterisation*. Graduate Student Series in Materials and Engineering, ed. B. Cantor. 1994, London: Institute of Physics Publishing. 517.
64. Cullity, B.D., *ELEMENTS OF X-RAY DIFFRACTION*. 3rd Edition ed. Metallurgy and Materials - Addison-Wesley, ed. M. Cohen. 1956, Reading, Massachusetts: Addison-Wesley Publishing Company, Inc. 514.
65. Bell, S., S. Judge, and P. Regan, *An investigation of HPGe gamma efficiency calibration software (ANGLE V. 3) for applications in nuclear decommissioning.* Applied Radiation and Isotopes, 2012.
66. Langford, R.M., *Focused ion beams techniques for nanomaterials characterization.* Microscopy Research and Technique, 2006. **69**(7): p. 538-549.
67. Ramakrishna, K., K. Muralidhar, and P. Munshi, *BEAM-HARDENING IN SIMULATED X-RAY TOMOGRAPHY.*

68. Wilkins, M.J., *The influence of microbial redox cycling on radionuclide mobility in the subsurface at a low-level radioactive waste storage sit.* Geobiology, 2007. **5**(3): p. 293 - 301.
69. American Nuclear Society, *Measurement of the leachability of solidified low-level radioactive wastes by a short-term test procedure, method ANSI/ANS-16.1 (1986).* American Nuclear Society, 1986,.
70. Wilkins, M.J., et al., *The influence of microbial redox cycling on radionuclide mobility in the subsurface at a low-level radioactive waste storage site.* Geobiology, 2007. **5**(3): p. 293-301.
71. PerkinElmer Inc. *Quench, counting efficiency, and quench correction,* http://www.perkinelmer.com/Resources/TechnicalResources/ApplicationSupportKnowledgebase/radiometric/quench.xhtml. 1998-2012, [cited 20/06/2012].
72. L'Annunziata, M.F., *Handbook of radioactivity analysis*. 2012: Academic Press.
73. PerkinElmer Life and Analytical Science. *Features and Benefits Guide for Tri-Carb Liquid Scintillation Analyzers,* http://shop.perkinelmer.co.uk/content/manuals/gde_tricarbfeatures.pdf. 2005 [cited 17/09/2011].
74. KONG, T.Y., et al., *Development of Dual Counting Analysis and Exposure Possibility Evaluation for Carbon-14 at Korean Nuclear Power Plants.*
75. Packard Instrument Company, *Liquid Scintillation Analysis;*. 1986.: Science and Technology, Rev. C,.
76. Passo and Cook and G.T.C. C.J. Passo, *Handbook of Environmental Liquid Scintillation Spectrometry: A Compilation of Theory and Methods* 1994, Packard, : Meriden, U.S.A.
77. Currie, L.A., *The limit of precision in nuclear and analytical chemistry.* Nuclear Instruments and Methods, 1972. **100**(3): p. 387-395.
78. Hwang, H.-Y., et al., *Standardization of radionuclide by [beta](LS)-[gamma] coincidence counting using the geometry-efficiency variation method.* Applied Radiation and Isotopes, 2006. **64**(10-11): p. 1119-1123.
79. Jaubert, F., I. Tartes, and P. Cassette, *Quality control of liquid scintillation counters.* Applied Radiation and Isotopes, 2006. **64**(10-11): p. 1163-1170.
80. Kossert, K. and A. Grau Carles, *The LSC efficiency for low-Z electron-capture nuclides.* Applied Radiation and Isotopes, 2006. **64**(10-11): p. 1446-1453.
81. Particular, G.L.A.R.o.I.A.L.D.W., P.A. Reference to the Decommissioning of Graphite Moderated Reactors. EPRI, CA: 2008., and 1016772.
82. Marsden, B.J., Hopkinson, K., L and Wickham, A., J *The Chemical Form of Carbon-14 within Graphite.* 2002(Issue 4).
83. Bradbury, D., and Wickham, A.J. , *Graphite Leaching: A Review of International Aqueous Leaching Data With Particular Reference to the Decommissioning of Graphite Moderated Reactors. EPRI,*, B.D.T. Ltd., Editor. 2008: Palo Alto, CA.
84. *Nuclear - Grade Graphite From Coal.* 2004.

85. Jenkins, G.M., *The thermal expansion of polycrystalline graphite.* Journal of Nuclear Materials, 1964. **13**(1): p. 33-39.
86. Hagos, B.A., Jones, A. N., Marrow, T. J. and Marsden, B. J. , *Characterisation and Treatment of Irradiated Graphite*, in *DIAMOND '09*. 2009, DIAMOND University Consortium: National Railway Museum, York. p. Paper 28.
87. Lipson, H., Stokes, A. R, , *A New Structure of Carbon*. 1942, Nature Publishing Group.
88. Lipson, H., Stokes, A. R., *The Structure of Graphite.* Proceedings of the Royal Society of London. Series A, Mathematical and Physical Sciences, 1942. **181**(984): p. 101-105.
89. Crochiere, R.E.a.R., L.R.,, *Multirate Digital Signal Processing,*. 1st ed. 1983, Englewood Cliffs, NJ,: Prentice-Hall.
90. Photoshop. *The Magic Wand Tool In Photoshop, http://www.photoshopessentials.com/basics/selections/magic-wand-tool/*. 2012, [cited 14/08/12].
91. Chemicool. *"Cobalt",*. Chemicool Periodic Table, 16 Oct. 2012, [cited 20/12/2012,]; Available from: <http://www.chemicool.com/elements/cobalt.html>.
92. Jones, S.S., *Experimental techniques for electron microscopy studies of gas reactions with polycrystalline graphites.* Carbon, 1970. **8**(5): p. 673.
93. STS, S.S., Inc. *Philips XL 30*. 2011 [cited 11/02/2013]; http://www.semtechsolutions.com/node/124/philips-xl-30-sem].
94. Tzeli, D. and A. Mavridis, *Theoretical investigation of iron carbide, FeC.* The Journal of chemical physics, 2002. **116**: p. 4901.
95. ChemSpider. *Chemical Structure*. [cited Jan 20, 2013]; Available from: http://www.chemspider.com/Chemical-Structure.94815.html
96. *Naturally occurring isotope abundances: Commission on Atomic Weights and Isotopic Abundances report for the International Union of Pure and Applied Chemistry in Isotopic Compositions of the Elements* in *Pure and Applied Chemistry,*. 1989,, 1998 IUPAC.
97. Hacker, C., *RadDecay, Evaluated Nuclear Structure Data File, National Nuclear Data Center, Brookhaven National Laboratory, Upton, NY 11973-5000* 2007, Griffith University,: Brisbane, Australia.
98. Rosman, K.J.R.a.T., P.D.P. , *International Union of Pure and Applied Chemistry in Isotopic Compositions of the Elements 1997.* Pure and Applied Chemistry,, 1998,. **70,** : p. 217.
99. Horsley, G.W., *THE PURIFICATION OF GRAPHITE BY TREATMENT WITH HALOGENS AT TEMPERATURES UP TO 1000$sup 0$C. Project DRAGON*, in *Other Information: UNCL. Orig. Receipt Date: 31-DEC-70; Related Information: OECD High Temperature Reactor Project Dragon Report. Now open access.* 1962. p. Medium: ED.
100. Kenneth Barbalace. *Periodic Table of Elements - Ba - Barium,*. 1995, [cited 2013, 13/02/2013,]; Available from: http://EnvironmentalChemistry.com/yogi/periodic/Ba-pg2.html.
101. BÉ, M., et al., *Table of radionuclides (Vol. 1-A= 1 to 150).* Bureau International des Poids et Mesures, France: Sèvres, 2004.

102. Dubey, V.S., C.E. Mandeville, and M.A. Rothman, *Decay of Eu^{155}, Sm^{153}, Sn^{125}, and Br^{82}.* Physical Review, 1956. **103**(5): p. 1430-1441.
103. Gray, W.J. and W.C. Morgan, *Leaching of/sup 14/C and/sup 36/Cl from irradiated French graphite*. 1989, Pacific Northwest Lab., Richland, WA (USA).
104. Gray, W.J. and W.C. Morgan, *Leaching of 14C and 36Cl from Hanford Reactor Graphite*, P.N. Labs, Editor. 1988.
105. Nen, E.A., *7375. 2004.* Leaching charasteristics of moulded or monolithic building and waste materials. Determination of leaching of inorganic components with the diffusion test. The tank test, 2004.
106. Crank, J., *The mathematics of diffusion*. 1979: Oxford university press.
107. Serne, R.J., R.O. Lokken, and L.J. Criscenti, *Characterization of grouted low-level waste to support performance assessment.* Waste Management, 1992. **12**(2): p. 271-287.
108. Ecke, J.T.a.H., *LEACHING TESTS FOR ASSESSMENT OF MOBILITY OF INORGANIC CONTAMINANTS FROM SOLIDIFIED INCINERATION RESIDUES - LITERATURE REVIEW.* Division of Waste Science and Technology, Luleå University of Technology, Luleå, Sweden. , 2004.
109. Soldatov, V.S., *Chapter 20 - Leaching of products*, in *Studies in Environmental Science*. 1997, Elsevier. p. 841-894.
110. Hespe, E.D., *Leach Testing of Immobilized Radioactive Waste Solids: A Proposal for a Standard Method.* Atomic Energy Reviews, 1971(9): p. 195 -207.
111. Hagos, B., et al., *Characterisation and treatment of irradiated graphite waste.*
112. Hagos, B., et al., *Microstructural analysis of irradiated nuclear graphite waste.*

8. APPENDIX

Terminologies

Calcination: A thermal treatment process in absence of air applied to ores and other solid materials to bring about a thermal decomposition, phase transition, or removal of a volatile fraction.

Combustion: is the term used to describe the burning of material, i.e. a self-sustaining oxidation reaction in air or oxygen. Graphite is reported to have a sublimation temperature in excess of 3300K at atmospheric pressure, showing that a very high temperature is required to combust it in air.

Incineration: a waste treatment process of burning combustible waste to reduce its volume and yield an ash residue. Incineration is a process whereby a material is placed in a special facility designed to wholly oxidise it.

Oxidation: simply the name for the chemical reaction of a material with oxygen. in chemistry it is called termed redox processes; to indicate the elevation of a cation to a greater valence state, and in some cases to represent reaction with materials other than oxygen.

Wigner energy: created inside nuclear reactors that use graphite as a neutron moderator. When the graphite is bombarded with neutrons from the reactor core, crystalline dislocations occur as a result of the Wigner effect, causing the graphite rods to swell and begin storing the energy. This energy is problematic for nuclear reactors, because it can be spontaneously and rapidly released from the graphite in the form of heat, and unplanned excess heat is not a desirable situation within a nuclear reactor.

Decommissioning: The final phases in the life cycle of a nuclear installation and it is process f removing a reactor from active status.

Maintenance: A stage in the process of decommissioning a nuclear site.

Disposal: In the context of solid waste, disposal is the emplacement of waste in a suitable facility without intent to retrieve it at a later date.

Waste Management/ Repository: Is the emplacement of waste in a suitable facility with the intent to retrieve it at a later date

Defueling: is a special operation of removing or offloading of a reactive fuel from the core. Once removed it must never be re-used and must placed into a dedicated de-fuelling tanker/bowser. The fuel may be recycled after process of separation.

Chemiluminescence: Random single photon events which are generated as a result of the chemical interaction of the sample components. Except at high rates, most chemiluminescence events are excluded by the coincidence circuit.

Chemical Quenching: a reduction in the scintillation intensity seen by the photomultiplier tubesdue to materials present in the scintillation solution that interfere with the processes leading to the production of light. The result is fewer photons per keV of beta particle energy and usually a reduction in counting efficiency.

Cocktail: the scintillation fluid; a mixture of 3 chemicals (solvent, emulsifier, and fluor) which produces light flashes when it absorbs the energy of particulate radioactive decay.

Compton Scattering: Elastic scattering of photons (x/?-rays) by electrons. In each such process the electron gains energy and recoils and the photon loses energy. This is one of the three ways photons lose energy upon interacting with matter, and is the usual method with photons of intermediate energy and materials of low atomic number. Named for Arthur H. Compton the American physicist who discovered it in 1923

CPM: Counts per minute. This is the number of light flashes or counts the LSC registered per minute. The number of decays produced by the radioactivity is usually more than the number of counts registered.

Discriminator: An electronic circuit which distinguishes signal pulses according to their pulse height or voltage. It is often used to exclude noise or background radiation counts.

DPM: Disintegration per minute. The sample's activity in units of nuclear decays per minute.

Efficiency: The ratio, CPM/DPM, of measured counts to the number of decays which occurred during the measurement time.

Fluor: A chemical component of the liquid scintillation cocktail that absorbs the

	UV light emitted by the solvent and emits a flash of blue light.
Fluorescence:	The emission of light resulting from the absorption of incident radiation and persisting only as long as the stimulating radiation is continued.
Luminescence:	A general term applied to the emission of light by causes other than high temperature.
PMT:	The Photo-Multiplier Tube is an electron tube that detects the blue light flashes from the fluor and converts them into an electrical pulse.
Photo luminescence:	Delayed and persistent emission of single photons of light following activation by radiation such as ultraviolet.
Pulse:	Electrical signal of the PMT; its size is proportional to the radiation energy absorbed by the cocktail.
Quenching:	Anything which interferes with the conversion of decay energy emitted from the sample vial into blue light photons. This usually results in reduction in counting efficiency.
QIP:	The Quenching Index Parameter is a value that indicates the sample's level

9. PAPERS AND JOURNALS

1. Hagos, B., A. N. Jones, B. J. Marsden, and T. J. Marrow. "Characterisation and treatment of irradiated graphite waste." (2009) [111]
2. Hagos, B., A. N. Jones, T. J. Marrow, and B. J. Marsden. "Microstructural analysis of irradiated nuclear graphite waste." (2010). [112]